ISSN 1349-0087

SPring-8 Research Frontiers

2003

Editor's Note

Since the inauguration of SPring-8 in October 1997, five issues of SPring-8 Research Frontiers have already been published. During this period, many beamlines were constructed one after another and experiments using synchrotron radiation were made available for wider scientific fields step by step. As a result, outstanding scientific achievements have increased gradually but steadily.

The editorial board made some editing changes this time. First, the cover was changed to depict an image of dynamic development of synchrotron radiation science. Secondly, this sixth issue is simply entitled "2003," although it covers advances made during the two consecutive research terms, the second half of 2002 (2002B) and the first half of 2003 (2003A), as in the previous issues. Thirdly, each report is limited to two pages, and 58 reports are carried in this issue; the number of reports increased by about 40% from the previous issue. And finally, we made efforts to enrich the facility status section with more useful information.

We invited eight specialists from the Proposal Review Committee to serve as the Editing Coordinators for their respective research fields:

Life Science - *Prof. Keiichi Fukuyama* (Osaka University)
Materials Science: Structure - *Prof. Makoto Sakata* (Nagoya University)
Materials Science: Electronics & Magnetism - *Assoc. Prof. Toyohiko Kinoshita* (The University of Tokyo)
Chemical Science - *Assoc. Prof. Tsunehiro Tanaka* (Kyoto University)
Earth & Planetary Science - *Prof. Tetsuo Irifune* (Ehime University)
Environmental Science - *Dr. Momoko Takemura* (Toshiba Co., Ltd.)
Industrial Application - *Prof. Tokuhiko Okamoto* (Ritsumeikan University)
Instrumentation & Methodology - *Prof. Masaharu Nomura* (KEK)

We would like to express our most sincere appreciation to Editing Coordinators for their efforts in preparing the introductory overview and providing comments on each research field. We would also like to express our gratitude to users and staff members of SPring-8 for contributing their reports to SPring-8 Research Frontiers.

SPring-8 Research Frontiers will be sent on request. Its full text is also available on the SPring-8 Website: http://www.spring8.or.jp/

CONTENTS 2003

Preface

This issue presents the highlights of research crops harvested at six-year-old SPring-8. In FY2003, SPring-8 started a new scheme to support two national scientific projects: the Protein 3000 Project and the Nanotechnology Researchers Network Project launched by MEXT (Ministry of Education, Culture, Sports, Science and Technology) in 2002.

Protein-structure analysis, or structure biology, is a potential research field in utilization of SPring-8. If you look at the list of topics in the SPring-8 Homepage, you will find the dominance of topics of this field. Now, 12 beamlines (out of 46 operating beamlines) are available for this purpose: some are dedicated and some shared for other purposes.

The Nanotechnology Support Program can probably be connected with most fields of materials science, although the funds for the Project are allocated to the limited number of proposals. One of the fields on which SPring-8 puts emphasis is the precision powder diffraction. The sophisticated analysis method combined with precision data available at SPring-8 reveals the electronic structure of molecules or crystals with a small amount of a sample. This method casts light to structure determination of new materials which are usually obtained in a small amount in a form of powder or microcrystal.

The report on a study of a mechanism of an intelligent catalyst for automobiles, featured in Environmental Science in the previous issue, gave engineers a solid confidence that they can convince their company to install the catalyst on commercial cars.

A particle composed of five quarks were first discovered at SPring-8 on a laser inverse Compton beamline, which is called here Laser Electron Photon (LEP). It was fortunate for SPring-8 to operate such a beamline. This peculiar beamline is not for synchrotron radiation in a usual sense and even its existence might harm the quality of synchrotron radiation. Technology of SPring-8 has made LEP compatible with other SR beamlines.

Top-up operation started in May 2004. Many users appreciate it very much with expectation that precision would be improved by constant emission. The report on the technical aspects for realizing the top-up operation is also contained in this volume.

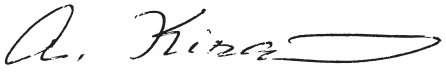

Akira Kira
Director General
SPring-8 / JASRI

Scientific Frontiers

LIFE SCIENCE

Synchrotron radiation, especially that from third-generation light sources, is now indispensable for the structural studies of biological macromolecules and the requirement of synchrotron radiation is rapidly growing. To fulfill this, at SPring-8, five undulator beamlines and seven bending magnet beamlines have been constructed for Life Science research. The beamlines for structural genomics, BL26B1 and BL26B2, are most recently in operation, at which mounting crystals and diffraction measurements are automated in cooperation with the sample mounting robot. In addition, various new equipment and software for beamlines have been developed. A new monochromator crystal was set up at BL41XU, which gives much higher brilliance with a higher energy resolution than before and a new imaging-plate detector system in BL44XU, which allows data collection for crystals with a very large unit cell (>1000 Å). Also the use of a user-friendly beamline control system as well as a high-speed data collection system has facilitated more efficient data collection at BL38B1, particularly for application to the MAD technique.

At SPring-8, a number of new structures of biologically important molecules were determined last year. The structure of the cytochrome b_6f complex, a membrane protein complex that functions in electron transfer and proton pumping in photosynthesis, was elucidated at 3 Å resolution. The structures of human cardiac troponin and the c-Myb-cEBPβ-DNA complex brought breakthrough in the fields of bioenergetics and transcription, respectively. The structures of the importin-β complex with a transcription factor showed how the factor is imported into nuclei while the structures of LolA and LolB proteins reveal the transport mechanism of lipoproteins. The structural information of cytosine deaminase and phosphodiesterase may lead to the clinical applications. The dynamic aspects of proteins clarified using laser were presented for hemoglobin and bacteriorhodopsin, which gave insight into the mechanisms of respective biological functions.

The National Project on Protein Structural and Functional Analysis by MEXT of Japan (Protein 3000 Project) is in the second year at SPring-8, and a number of structures has been solved and registered progressively using five beamlines.

Keiichi Fukuyama

Structure of the Cytochrome b_6f Complex of Oxygenic Photosynthesis

The photosynthetic unit of oxygenic photosynthesis is organized as two large multimolecular membrane complexes, photosystem II (PSII) that extracts low-energy electrons from water and photosystem I (PSI) that raises the energy level of such electrons using light energy to produce a strong reductant, NADPH. The two photosystems operate in a series linked by a third multiprotein complex called the cytochrome b_6f complex (Fig.1). The cytochrome b_6f complex is a membrane-spanning protein complex embedded in the thylakoid membrane of photosynthetic organisms. The molecular weight of the complex is 220,000 as a dimer with 26 transmembrane helices. The b_6f complex controls the electron transfer between the plastoquinol reduced by PSII and the electron carrier protein plastocyanin that associate with PSI. Coupled with the electron transfer, the b_6f complex also generates a transmembrane proton gradient for ATP synthesis. The crystal structures of the cytochrome b_6f complex [1,2] complete the description of the architecture of the oxygenic photosynthetic electron transport chain, since three-dimensional structures have been provided for PSI and PSII [3-5].

The structure of the b_6f complex from cyanobacterium *M. laminosus* was determined by the isomorphous replacement method using Pb and Pt derivatives and multiwavelength anomalous diffraction from native iron atoms. X-ray diffraction data from native crystals and complex crystals with the quinone-analogue inhibitor DBMIB were collected at the Osaka University beamline **BL44XU** of SPring-8. The highest resolution data of 3.0 Å from the complex crystal with another analogue inhibitor, TDS, was collected at the SBC beamline 19ID, APS. The initial model was developed into a 3.4 Å map of the native complex. Final refinement was carried out with a dataset from a co-crystal with TDS (Figs. 2, 3).

Viewed along the membrane normal, the b_6f complex is 90 Å × 55 Å within the membrane side, and 120 Å × 75 Å on the lumen (*p*) side (Fig. 2). A prominent feature of this structure is an extended quinone exchange cavity between the monomers, which exchanges lipophilic plastoquinone in the bilayer center, and also mediates the electron and proton transfer across the complex. The heme-binding 4 transmembrane helices core of the b_6f complex is almost identical to that of the analogous bc_1 complex in the respiration chain of the mitochondrial membrane. However, there are three prosthetic groups recently found in the b_6f complex that are not present in the bc_1 complex: a high spin heme *x* covalently bound to the cyt b_6 polypeptide by one thioether bond, and the pigment molecules, chlorophyll *a* and β-carotene. Heme *x* occupies the binding site of the *n*-side bound quinone in the bc_1 complex. The presence of heme *x* in contact with heme b_n and a plastoquinone in the cavity suggests the mechanism of ferredoxin-mediated cyclic electron transfer (dotted line in Fig. 1) that uses classical elements of the Q-cycle mechanism [1,2].

The quinone-mediated redox connection between the (*p*) and (*n*) sides of the complex can be visualized through (a) a plastoquinone molecule close to heme *x* on the *n*-side, and (b) a quinone analogue inhibitor, TDS, on the *p*-side of the other monomer that surrounds the cavity (Fig. 3). The position of TDS in the b_6f complex is similar to that of the *p*-side inhibitor myxothiazol in the bc_1 complex. Another *p*-side inhibitor, DBMIB, is bound near Glu in the conserved sequence in the *p*-side peripheral loop. Both of these inhibitors are >10 Å from the closest histidine ligand of the [2Fe-2S] cluster of Rieske ISP,

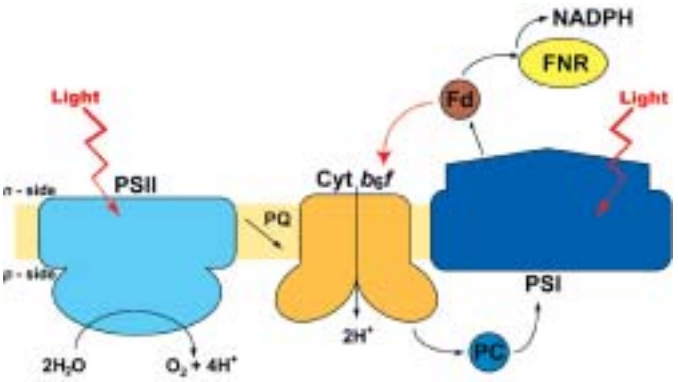

Fig. 1. Integral membrane protein complexes and electron carrier proteins responsible for electron transport and proton translocation in oxygenic photosynthesis.

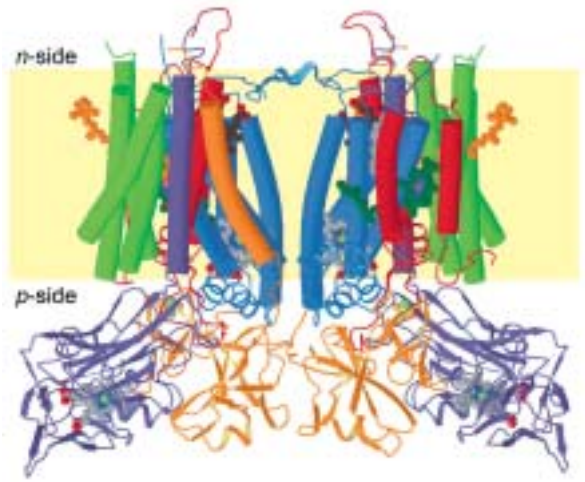

Fig. 2. Side view of eight-subunit dimeric cytochrome b_6f complex. Hemes *bn*, *bp* and *f* (grey), heme *x* (dark brown), chlorophyll a (dark green), β-carotene (orange), cyt b_6 (blue), subunit IV (red), cyt *f* (purple), iron-sulfur protein (orange), and small subunits (light green).

and cannot form an H-bond with the histidine ligand as does stigmatelline in the bc_1 complex.

The [2Fe-2S] cluster is 29 Å from the heme Fe of its electron acceptor, cyt *f*. In the case of the bc_1 complex, the positional change of the [2Fe-2S] cluster to a more c_1-proximal position in different crystal forms suggests that Rieske ISP mediates the electron transfer between the membrane-bound quinol and cyt c_1 by shuttling between the membrane-proximal and c_1-proximal states. However, only a single membrane-proximal position for the Rieske ISP has been observed in the b_6f complex. Together with the different positions of cytochrome *f* and its heme relative to cyt c_1, this implies the difference in trajectory between Rieske ISP and cyt *f*.

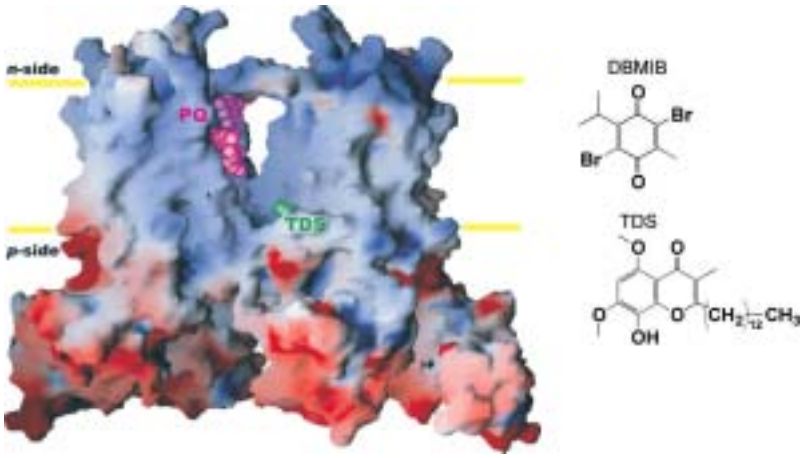

Fig. 3. Molecular surface of the complex mapping the electrostatic potential. Plastoquinone (PQ) and Q-analogue inhibitor (TDS) are drawn in the cavity as a cpk model, and the chemical formulas of inhibitors are shown on the right.

Genji Kurisu*

Institute for Protein Research, Osaka University

E-mail: GKurisu@bio.c.u-tokyo.ac.jp

**Present address* : Department of Life Sciences, The University of Tokyo

References

[1] G. Kurisu, H. Zhang, J.L. Smith and W.A. Cramer: Science **302** (2003) 1009.
[2] D. Stroebel *et al.*: Nature **426** (2003) 413.
[3] P. Jordan *et al.*: Nature **411** (2001) 909.
[4] A. Zouni *et al.*: Nature **409** (2001) 739
[5] N. Kamiya and J.-R. Shen: Proc. Natl. Acad. Sci. USA **100** (2003) 98.

Assembly of Transcriptional Regulatory Factors, c-Myb and C/EBPβ from Separated Sites on a Promoter

Assembly of stereospecific, multiprotein complexes on enhancers and promoters is a key step in transcriptional activation. Recent X-ray analyses of high-order complexes comprised of transcription factors bound to DNA have concentrated exclusively on cases in which interactions between transcription factors enhance their cooperative binding to adjacent sites on a promoter. In many eukaryotic genes, however, transcription factors bind to promoters at sites distant from one another, yet act synergistically to activate transcription. It has been proposed that DNA looping mediated by their interaction brings transcription factors scattered along the DNA into sufficiently close proximity to enable them to form nucleoprotein complexes. Here we address this problem in the case of the synergistic *trans*-activation of myeloid genes by c-Myb and C/EBPβ bound distantly from each other to the DNA .

The c-Myb transcriptional regulator is involved in the proliferation and differentiation of hematopoietic cells. Specifically, it cooperates with a C/EBP (CAAT/enhancer-binding protein) family member to induce myeloid cell differentiation. c-Myb has three tandem subdomains (R1, R2 and R3), each bearing a helix-turn-helix (HTH)-related motif, in its DNA-binding domain [1,2], whereas C/EBP family members contain a bZip-type motif for DNA binding. The *mim-1* promoter is a well-characterized c-Myb target gene promoter and this gene is a marker for granulocyte differentiation. Its promoter region includes the binding sites for c-Myb and C/EBP family members, which are critical for transcriptional regulation, separated by an intervening sequence of ~ 80 base pairs. Avian myeloblastosis virus (AMV) v-Myb, an oncogenic mutant of c-Myb, has no synergistic capacity with C/EBP for *trans*-activation of the *mim-1* gene, resulting in the inhibition of granulocyte differentiation and induction of leukemia.

To establish the structural basis of the *trans*-activational synergy between c-Myb and C/EBP family members, we analyzed the complex structures including c-Myb or AMV v-Myb, C/EBPβ and the promoter DNA. Because the X-ray crystallographic analysis of a DNA-loop-containing multiprotein –DNA complex seemed to be quite difficult, combinational X-ray crystallography experiments and atomic force microscopy (AFM) analyses were carried out [3]. X-ray diffraction data were collected on a RIKEN beamline **BL45XU** [4]. In the c-Myb (R1R2R3)–C/EBPβ (bZip)–DNA complex (Fig. 1), c-Myb–C/EBPβ intercomplex interactions were observed between the R2 subdomain of c-Myb bound to one DNA fragment and the C-terminal leucine-zipper part of C/EBPβ bound to another DNA fragment. On the c-Myb side, a hydrogen bond between a backbone amide of c-Myb R2 and a DNA minor groove phosphate, which plays an important role in the c-Myb–DNA interaction [5,6], becomes stabilized by a hydrogen-bonding network provided by C/EBPβ binding. These findings led us to assume an interaction between c-Myb and C/EBPβ separately bound to the native promoter DNA, with an intervening DNA loop, as shown in Fig. 2, where the *mim-1* promoter was used as a native promoter.

The oncogenic mutation points noted in the AMV v-Myb map near the interaction site with C/EBPβ, and the c-Myb–C/EBPβ interactions were disrupted in the crystal of the AMV v-Myb (truncated R1R2R3)–C/EBPβ(bZip)–DNA complex [3]. The data on Myb–C/EBPβ

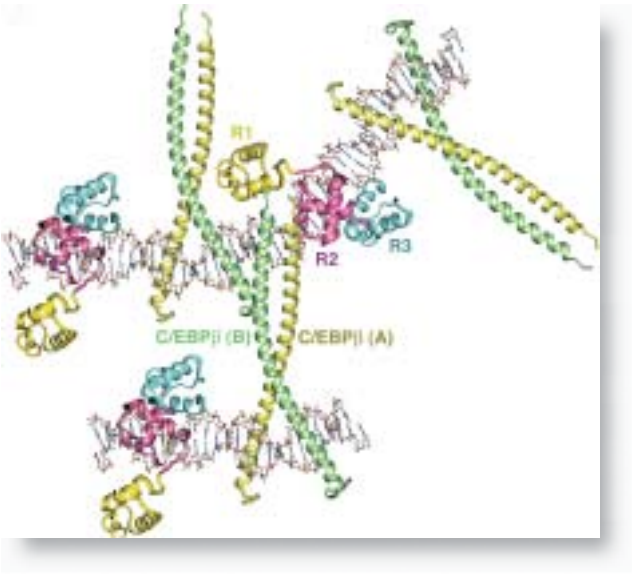

Fig. 1. Overview of three closely packed c-Myb–C/EBPβ–DNA complex molecules [3]. α-helical regions within the proteins are shown as ribbons; the remaining parts are shown as tubes. c-Myb R1, R2 and R3 and C/EBPβ chains A and B are respectively in dark yellow, pink, blue, yellow and green. The DNA molecules are shown in a stick representation.

interactions in crystals were consistent with those from the GST pull-down experiments in solution using GST-fused c-Myb or AMV v-Myb, and radioisotope-labeled C/EBPβ or its mutants [3]. The proposed DNA loop formation in the c-Myb–C/EBPβ–*mim-1* DNA complex was confirmed by using the AFM method. The AFM observations indicated that about 75% of the c-Myb and C/EBPβ-bound *mim-1* promoter DNA exhibited DNA looping, whereas the AMV v-Myb and C/EBPβ-bound *mim-1* promoter DNA had no DNA looping (Fig. 3). From the luciferase *trans*-activation assays, the aforementioned c-Myb–C/EBPβ interaction was shown to be critical for the cooperative *trans*-activation of the *mim-1* gene by c-Myb and C/EBPβ [3].

In transcriptional regulation, two factors are considered to be involved: the stabilization of the regulatory factor–DNA complex and the stereospecific assembly of these proteins on the looped or deformed DNA. For the stabilization of protein–DNA interactions, a direction-sensitive protein backbone amide–DNA phosphate hydrogen bond, whose formation depends on the protein conformation and which is surrounded by the sidechains of adjacent residues interacting with DNA minor groove atoms and/or partner protein atoms, seems to be critical [5,6]. For the stereospecific assembly of regulatory

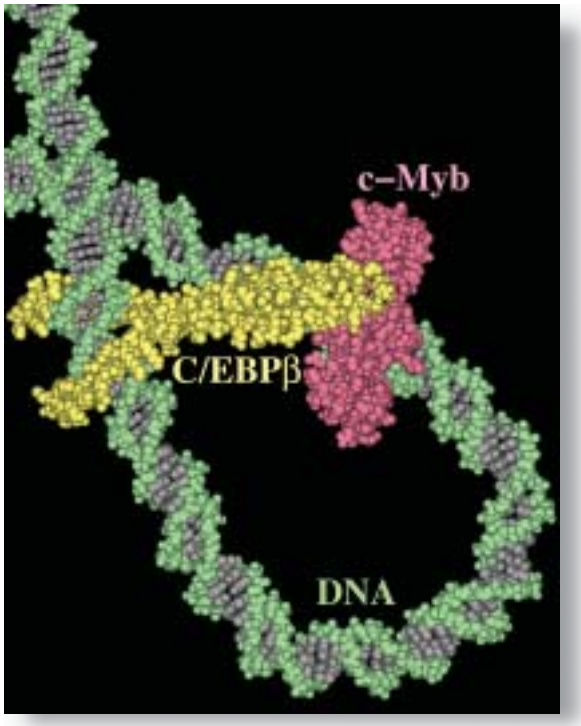

Fig. 2. A modeled structure of the complex composed of c-Myb, C/EBPβ and the *mim-1* promoter DNA, showing DNA loop formation [3,6].

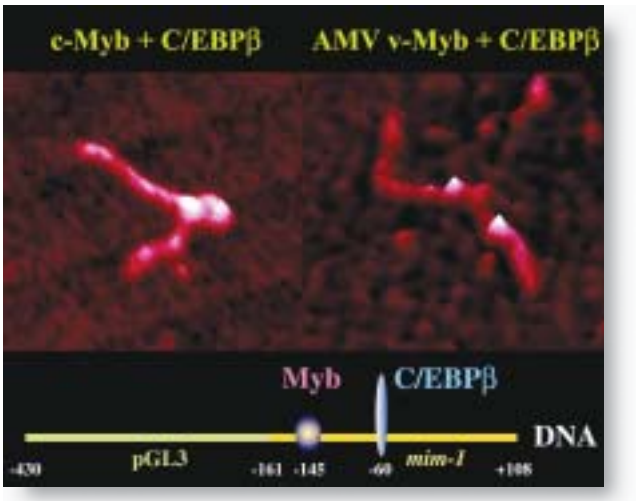

Fig. 3. Representative AFM images of *mim-1* promoter DNA complexes with c-Myb and C/EBPβ (left), and with AMV v-Myb and C/EBPβ (right) [3,6]. The bottom scheme shows the DNA construct used for the AFM experiments. The *mim-1* promoter with the separated c-Myb and C/EBPβ-binding sites was fused to the pGL3 vector.

factors, particularly protein-induced DNA looping, there are few examples for which structure/function relationships have been analyzed. The present study provides important clues that increase our understanding of the regulation of *trans*-activation mediated by distantly bound transcription factors and the dysregulation caused by oncogenic mutations. It is expected that extensive studies in the future will elucidate the entire molecular mechanism of enhanceosome or repressosome formation.

Tahir H. Tahirov[a,c], Ko Sato[a,b] and Kazuhiro Ogata[a,b,c]

(a) Kanagawa Academy of Science and Technology (KAST)
(b) Yokohama City University School of Medicine
(c) SPring-8/ RIKEN

E-mail: ogata@med.yokohama-cu.ac.jp

References

[1] K. Ogata *et al.*: Cell **79** (1994) 639.
[2] K. Ogata *et al.*: Nature Struct. Biol. **2** (1995) 309.
[3] T.H. Tahirov *et al.*: Cell **108** (2002) 57.
[4] T.H. Tahirov *et al.*: Acta Cryst. D **57** (2001) 1655.
[5] T.H. Tahirov *et al.*: Cell **104** (2001) 755.
[6] K. Ogata, K. Sato and T.H. Tahirov: Curr. Opin. Struct. Biol. **13** (2003) 40.

Structure of the Core Domain of Human Cardiac Troponin in the Ca^{2+}-Saturated Form

Muscle contraction is caused by interactions between two major contractile proteins, myosin and actin, which are polymerized to form the muscle thick filament and the thin filament, respectively. In the skeletal and cardiac muscles, contraction is controlled by intracellular Ca^{2+} concentration, and troponin, the sole Ca^{2+}-receptive protein in the myofilament, plays the key role in the regulation of the sliding action between these two filaments. Troponin (Tn), with a relative molecular mass of approximately 80 kDa, is composed of three polypeptide chains, TnT, TnI and TnC, and together with tropomyosin (Tm), is located in the polymerized-actin at a Tn:Tm: actin ratio of 1:1:7 (Fig. 1) [1]. The molecular basis of Ca^{2+} regulation was initially established by S. Ebashi and co-workers in the 1960's, although the mechanism by which troponin works has remained elusive because high resolution structural information have not been available. Since troponin is fairly flexible, the molecule evades packing in a crystalline lattice for a long time.

We have determined the crystal structure of the core domain of troponin [2], which was reconstituted from *Escherichia coli*-expressed recombinant human cardiac Tn subunits, after dozens of crystallization trials for more than 10 years. Diffraction data were collected at beamlines **BL41XU**, **BL44B2** and **BL45PX** and the structure was determined by the multiwavelength anomalous dispersion (MAD) method. The overall architecture of the core domain of troponin is shown in Fig. 2. Notably, the core domain is further divided into structurally distinct subdomains, denoted as the regulatory head and the IT arm, that are connected by linkers, making the entire molecule highly flexible. The IT arm has an asymmetric and elongated structure (~ 80 Å) including a parallel α-helical coiled-coil formed between TnT (H2(T2)) and TnI (H2(I)). On the other hand, as suggested previously [3,4], the amphiphilic α-helix, H3(I), binds specifically to a conserved hydrophobic patch of the Ca^{2+}-saturated amino-terminal lobe of TnC, forming the regulatory head. The segment H3(I) is located between the two putative actin/Tm-binding sites, the inhibitory region (IR, residues 137 - 148) and the carboxyl terminus of TnI (C-TnI, residues 169 - 210), which are both essential for the inhibitory binding of TnI at a low sarcoplasmic Ca^{2+} concentration. Thus this segment works as a molecular switch that transmits the initial signal of Ca^{2+} binding to TnC and to the other components of the thin filament .

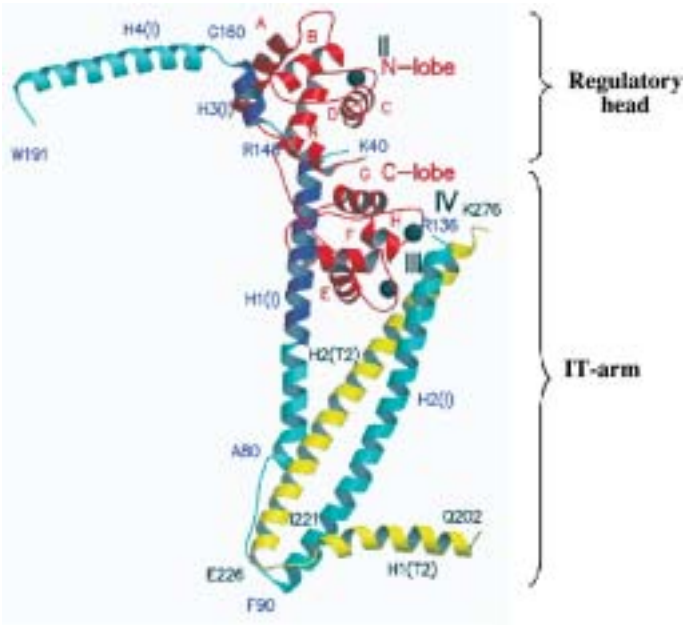

Fig. 2. Ribbon representation of the crystal structure of the core domain of human cardiac troponin. TnC and TnT are in red and yellow, respectively. TnI is in cyan, except for the two stretches of amphiphilic helices (TnC-binding sites) that are in blue. The three Ca^{2+} ions bound to the Ca^{2+}-binding sites (II to IV) are represented by black spheres [2].

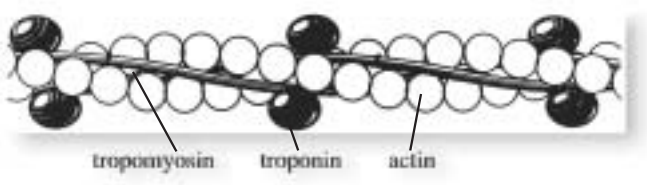

Fig. 1. Molecular arrangement of the proteins within the muscle thin filament.

Troponin is anchored to the thin filament mainly through Tm binding to two distinct portions of TnT, specifically the amino terminus (TnT1, residues 1 -1 82) and the carboxyl terminus (C-TnT, residues 272 - 288), irrespective of sarcoplasmic Ca^{2+} concentration [1]. On the basis of the present structures, the separation between TnT1 and C-TnT is estimated to be about 60 Å (Fig. 3), although the structures of

these components are currently unknown. During Ca^{2+} regulation, the carboxyl terminal portion of TnI (denoted as TnI_{reg}, residues 137 - 210) undergoes major changes both with regard to position and conformation. At high Ca^{2+} concentrations, TnI_{reg} associated with the N lobe of TnC detaches from actin/Tm, as observed from the present crystal structure. On the other hand, at low Ca^{2+} concentrations, TnI_{reg} must form an extra attachment to actin/Tm, so that the Tm strand is anchored to the actin filament. The IT arm may have an important role in the regulatory process. This subdomain is large, rigid and conserved between the species and bridges the two Tm-anchoring regions without directly interacting with actin/Tm. Moreover, the location is interesting. The IT arm resides immediately upstream of the Tm-anchoring site (C-TnT) and the mobile TnI_{reg}. An intriguing possibility is that the formation of a third attachment by TnI_{reg} could cause a minute rotation of the IT arm around the pivotal point; that is, the carboxyl terminal of the coiled-coil. The formation of the third attachment itself, as well as the rotation of the IT arm, may alter the properties of the Tm strand in the actin filament.

The nature of the changes remains to be elucidated. A plausible explanation is that the strain imposed on the Tm strand is altered depending on Ca^{2+} concentrations; thereby the mobility and/or the flexibility of the Tm strand may be changed. Changes in the properties of the tropomyosin strand may modify the accessibility of the myosin head to actin. In the present work we firstly propose a hypothesis that explains the mechanism by which troponin works on the basis of its atomic structure. The crystal structure additionally provides an opportunity to visualize sites of genetic disorders in the troponin molecule that are associated with cardiac dysfunctions [5].

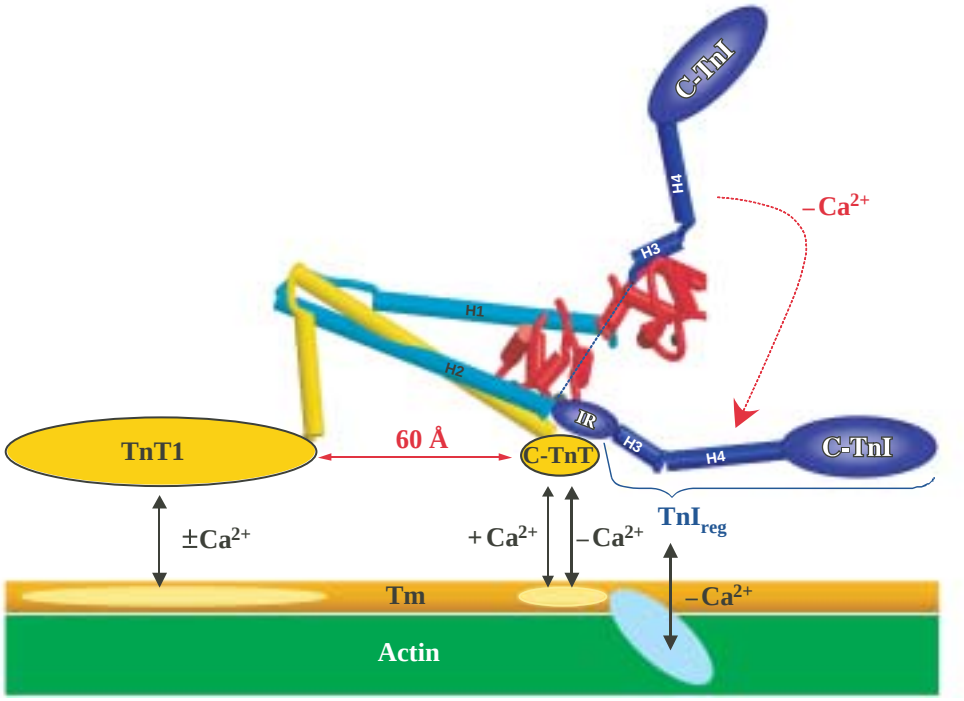

Fig. 3. Schematic representation of interactions between Tn and other thin filament components [2].

Soichi Takeda[a,b]

(a) Department of Cardiac Physiology, National Cardiovascular Center Research Institute
(b) SPring-8 / RIKEN

E-mail: stakeda@ri.ncvc.go.jp

References

[1] I. Ohtsuki *et al.*: Adv. Protein Chem. **38** (1986) 1.
[2] S. Takeda, A. Yamashita, K. Maeda and Y. Maéda: Nature **424** (2003) 35.
[3] S. Takeda *et al.*: Eur. J. Biochem. **246** (1997) 611.
[4] D. Vassylyev *et al.*: Proc. Natl. Acad. Sci. USA **95** (1998) 4847.
[5] D. Fatkin and R.M. Graham: Physiol. Rev. **82** (2002) 945.

Actin Filament Capping Protein (CapZ): The Story After Crystal Structure Elucidation

Capping protein (CP), or CapZ in muscle cells, binds the fast growing B-end of an actin filament, thereby blocking the addition and removal of monomeric actin molecules at the B-end. In ordinary cells, various actin-binding proteins accelerate polymerization at B-ends and depolymerization at P-ends (Fig. 1), specifying the location and translocation of cellular organelles. This molecular movement, named the actin dynamics, requires CP, which reduces the number of uncapped B-ends and increases growth rate.

We started the protein crystallographic study of this protein, because we wanted to exploit the possibility of preparing actin minifilaments. Since CapZ is a naturally occurring protein that inhibits the elongation of actin filaments, knowledge of the capping mechanism could enable us to control filament length. A good start was made possible by the work by Obinata and coworkers, who established a good *E. coli* expression system for this protein [1].

We crystallized recombinant chicken muscle CapZ and collected diffraction data at beamlines **BL45XU-PX** and **BL44B2**, and determined the structure at 2.1 Å resolution [2]. The obtained structures of α and β subunits of CapZ show striking resemblance, although they have no significant homology in the amino acid sequences. The two subunits assemble tightly with a pseudo two-fold symmetrical geometry through an extended hydrophobic surface.

Previous mutagenesis experiments indicated that the C-terminus of each subunit may be responsible for actin binding. Our crystal structure (Fig. 2) showed that 33 residues of the C-terminus of the β-subunit have no specific interaction with the main body of the protein, whereas 27 residues of the C-terminus of the α-subunit may have weak interactions with the main body. Each of the C-terminus contains a stretch of an amphipathic α-helix and is "anchored" by a conserved arginine residue, Arg-259 for α-tentacle and Arg-244 for β-tentacle, to the main body.

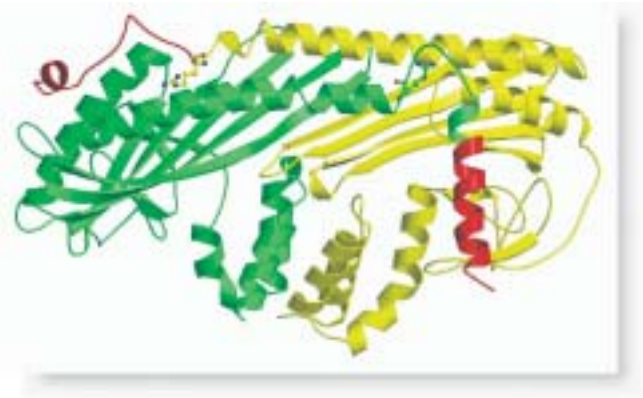

Fig. 2. A ribbon representation of the crystal structure of chicken muscle CapZ. The C-terminus (red) of each subunit, α- (yellow) and β- (green) subunits, of the hetero-dimeric molecule is responsible for actin binding. Arg-259 (α) and Arg244 (β), in ball-and-stick representation, may function as pivots.

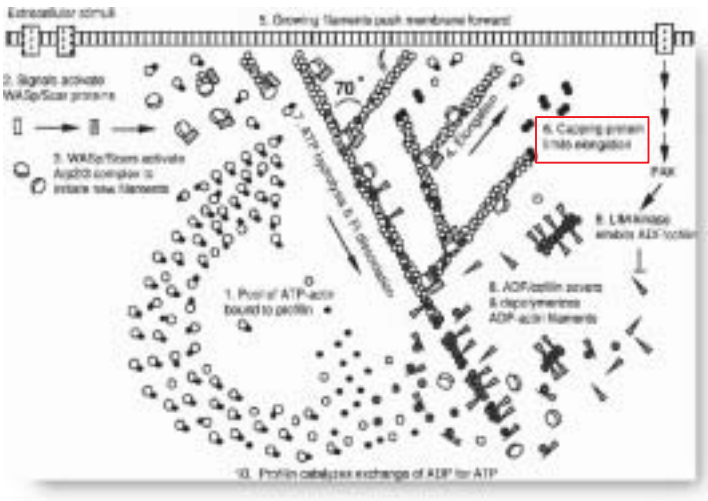

Fig. 1. Capping protein (CP) in the actin dynamics, which is a molecular movement driven by the polymerization and depolymerization of actin. The actin dynamics plays crucial roles in many cellular functions. CP is indispensable for this dynamics; it reduces the number of growing ends at the leading edge, thereby increasing the rate of forward movement [6].

On the basis of these observations, we proposed a "tentacle" model for the actin capping of CapZ. Actin binding is made possible predominantly by a pair of tentacles, which may protrude from the main body of the protein (Fig. 3). It is also postulated that the hydrophobic side of the α-helix within each tentacle functions as an interface to the surface of actin subunits, whereas the manner of binding of a pair of tentacles to the B-end of an actin filament remains elusive, largely due to the lack of information on the CapZ-binding site on the actin filament.

Immediately after obtaining the crystal structure, we started systematic mutation

and deletion experiments of chicken muscle CapZ [3] and yeast CP [4] in collaboration with John Cooper's laboratory in St. Louis. We believe that mutagenesis experiments should be useful only after the crystal structure is obtained.

In both chicken muscle CapZ and yeast CP, mutants lacking both tentacles did not show any capping activity, indicating that the pair of tentacles are the major actin-binding regions. CapZ (CP) with only the α-tentacle did show capping activity with a reduced affinity (by a factor of 400 in chicken CapZ, 7 in yeast CP), mainly due to the increased off-rate. On the other hand, CapZ (CP) with only the β-tentacle did not show a significant capping activity. These data indicate that the pair of tentacles are functionally independent and nonequivalent to each other.

An interesting information about the posture of the α-tentacle came from the study of interaction between CapZ and another protein S100B. Although the peptide corresponding to the α-tentacle specifically interacts with S100B, CapZ (with an intact α-tentacle) does not [5]. This indicates that, in solution, the α-tentacle does not protrude out from the main body of the protein, rather it lies down on the surface of the protein.

Our understanding on how CapZ caps the B-end of an actin filament is far from complete. We do not know in which posture CapZ binds the B-end, or whether each tentacle interacts with one actin monomer or two. More importantly, we should keep in mind that an actin filament, particularly its B-end, is dynamic. Our preliminary computer simulation (T. Oda & Y. Maéda) based on our atomic model of an actin filament indicates that the separation between two end monomers must be always fluctuating. This may be consistent with the fact that, with CapZ, the main body is well built and hydrophobic interactions between the two subunits are extremely tight, being suitable to bear the tearing force.

Our understanding of functional aspects of CapZ is also not complete. We do not know yet how CapZ is removed from the B-end. We also do not know much about the mechanism by which CapZ targets the actin filament in a muscle cell, that is, the nature of the interaction between CapZ and proteins to be targeted.

It is, however, clear that our elucidation of the crystal structure has opened up a new era in the study of the capping mechanism of CapZ at the B-end of an actin filament.

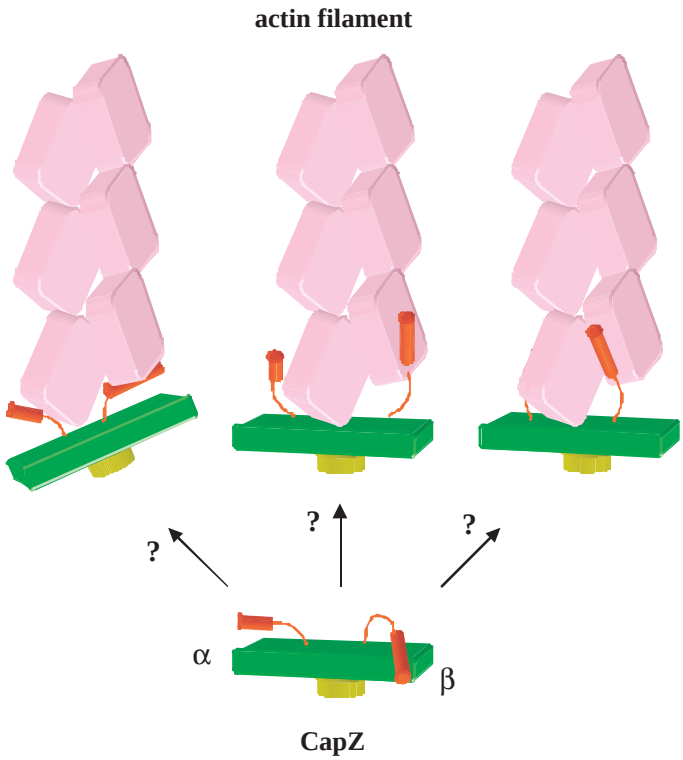

Fig. 3. Schematic drawings of the possible modes of binding of the capping protein to the actin filament (speculative models) [2].

Yuichiro Maéda[a,b] and Atsuko Yamashita[a]

(a) SPring-8 / RIKEN
(b) ERATO Actin Filament Dynamics Project

E-mail: ymaeda@spring8.or.jp

References

[1] Y. Soeno *et al.*: J. Muscle Res. Cell Motil. **19** (1998) 639.
[2] A. Yamashita, K. Maeda and Y. Maéda: EMBO J. **22** (2003) 1529.
[3] M.A. Wear *et al.*: Curr. Biol. **13** (2003) 1531.
[4] K. Kim, A. Yamashita, M.A. Wear, Y. Maéda and J.A. Cooper: J. Cell Biol. **164** (2004) 567.
[5] M.A. Wear and J.A. Cooper: J. Biol. Chem. **279** (2004) 14328.
[6] T.D. Pollard *et al.*: Ann. Rev. Biophys. Biomol. Struct. **29** (2000) 545.

Structure of Transcription Factor SREBP-2 and Importin-β Complex

Many proteins including histones, gene regulatory proteins, and RNA-processing proteins are imported into the nucleus from the cytosol. Nuclear import receptors bind to these proteins to be transported and enter the nucleus from the cytosol through the nuclear pore. Each protein family is transferred by a receptor protein that is specialized for the transport of a group of proteins, which have a similar fold.

A sterol regulatory element-binding protein (SREBP), a nuclear transcription factor, is a gene regulatory protein. SREBPs synthesized on ribosome particles are located on the endoplasmic reticulum (ER) membrane (Fig. 1). When cells are deprived of cholesterol, a membrane protein, designated the SREBP cleavage-activating protein (SCAP), is accumulated in the ER membrane to interact with SREBPs. SCAP escorts SREBPs to a post-ER component to reach the Golgi apparatus, which contains various proteases. Site-1 protease (S1P) catalyzes the first cut in the luminal loop, followed by a second cleavage at site 2 within the first membrane-spanning segment. This proteolytic process liberates a transcriptionally active N-terminal fragment of 480 residues from the membrane, designated the active form of a SREBP. The active form of a SREBP enters the nucleus and activates the transcription of a number of genes that control the synthesis and uptake of cholesterol (2). Thus, the transcriptional regulation of cholesterol metabolism is largely dependent on the nuclear transport of the active form of a SREBP. It was recently reported that SREBP-2 enters the nucleus through the direct interaction with importin-β via the helix-loop-helix-leucine-zipper (HLHZ) domain of SREBP [1,2] (Fig. 2). We have determined the structure of importin-β complexed with the active form of SREBP-2 [3].

The crystal belongs to the orthorhombic space group of $P2_12_12_1$ with unit cell dimensions of a = 101.0 (9), b =113.2 (8), c = 240.0 (4) Å. Diffraction experiments were carried out at beamline **BL44XU**. Then the SAD phasing method utilizing the anomalous scattering signal of Se atoms from the SeMet-substituted SREBP-2 crystal was applied. Phases were improved by solvent flattening and histogram matching using the DM program. However, the electron density map did not have sufficient quality for model building, particularly around the 100 residues of the N-terminus. Successive Fourier refinements showed a clear electron density that corresponds to the SREBP-2 dimer and the SREBP-2. Bulk solvent correction and anisotropic B-factor correction were applied during the course of the refinements. After each refinement cycle, the structural model was manually revised using the simulated annealed omit map. The final R- and free R-factors were 23.7% and 29.6%, respectively, in the resolution range of 20 ~ 3.0 Å (F > 0). The r.m.s. deviations for bond length and bond angle from the ideal values are 0.008 Å and 1.427 degrees, respectively. No residues are in the disallowed region in the Ramachandran plot.

This is the first structure in which the HLHZ domain in complex with a protein, but not DNA, is visualized and in which

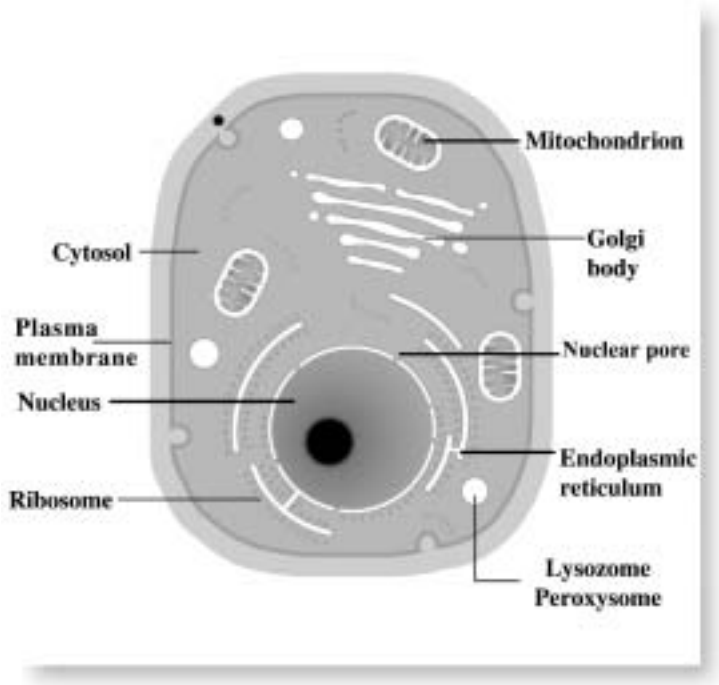

Fig. 1. Schematic drawing of an animal cell.

importin-β is observed to bind to the dimeric form of proteins (Fig. 3). Importin-β utilizes characteristic long helices, the significance of which are not understood, in a manner analogous to a pair of chopsticks to pick up SREBP-2. Importin-β alters its conformation, showing a pseudo two-fold symmetry on its surface structure, to accommodate a symmetric dimer molecule. This structure provides a model for dimeric cargo recognition by importin-β, and suggests that transcriptional regulation by SREBPs including proteolysis, nuclear import and SRE recognition is efficiently and accurately performed without the dissociation/reassociation reactions of SREBP dimers.

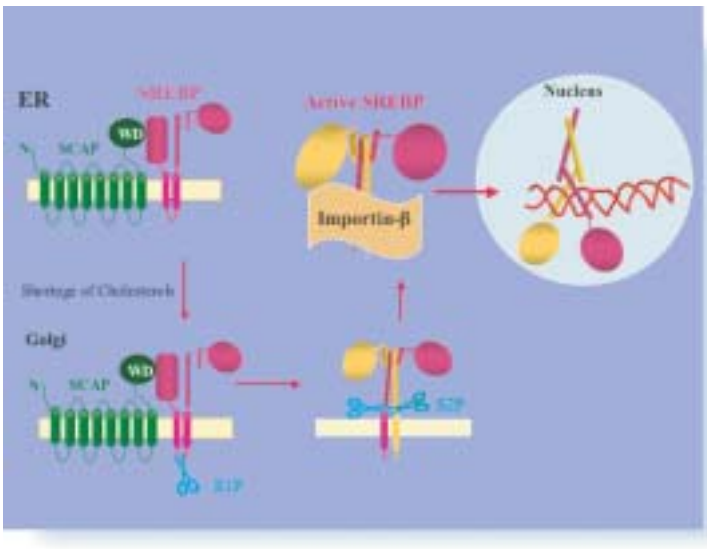

Fig. 2. Nuclear import of SREBP from ER.

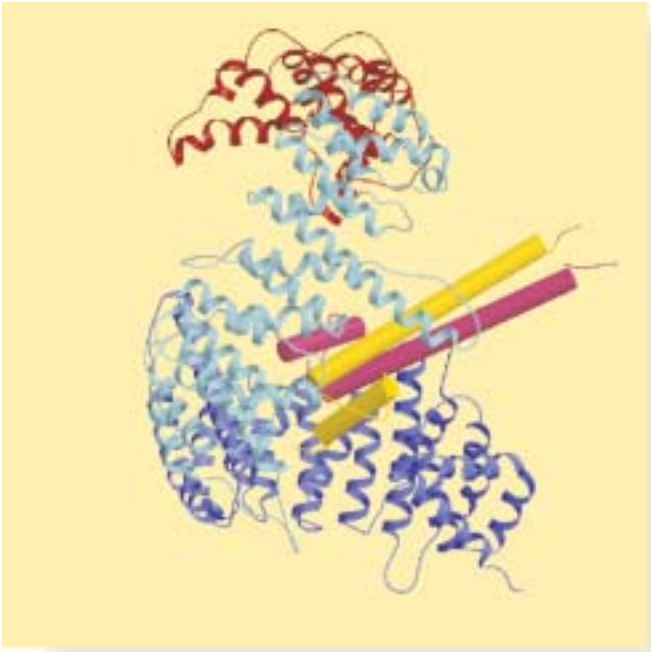

Fig. 3. Structure of importin-β complexed with the HLHZ domain of SREBP-2. Importin-β and SREBP-2 are depicted in ribbons and sticks, respectively.

Soo Jae Lee[a,b] and Tomitake Tsukihara[a]

(a) Institute for Protein Research, Osaka University
(b) Graduate School of Frontier Biosciences, Osaka University

E-mail: tsuki@protein.osaka-u.ac.jp

References

[1] E. Nagoshi *et al.*: Mol. Biol. Cell. **10** (1999) 2221.
[2] E. Nagoshi and Y. Yoneda: Mol. Biol. Cell. **21** (2001) 2779.
[3] S.J. Lee, E. Yamashita, A. Nakagawa, T. Tsukihara and Y. Yoneda: Science **302** (2003) 1571.

Crystal Structures of Bacterial Lipoprotein Localization Factors, LolA and LolB

Bacterial lipoproteins possessing a lipid-modified cysteine residue at the N-terminus are anchored on membranes because of their hydrophobic nature. Lipoproteins matured on the inner membrane are sorted and localized to their respective membranes. The transportation of such hydrophobic lipoproteins from the inner membrane to the outer membrane through the aqueous periplasm is mediated by the Lol system, which is widely distributed in Gram-negative bacteria. The LolCDE complex in the inner membrane belongs to the ATP-binding cassette (ABC) transporter superfamily and releases outer-membrane-specific lipoproteins using the ATP energy [1]. The released lipoproteins form a water-soluble complex with a periplasmic lipoprotein carrier, LolA [2]. The LolA-lipoprotein complex crosses the periplasm to the outer membrane, where a lipoprotein receptor, LolB, is present [3]. Upon the interaction of the LolA-lipoprotein complex with LolB, lipoproteins are spontaneously transferred from LolA to LolB, and finally localized on the outer membrane. To elucidate the molecular mechanism of lipoprotein transport by the Lol system, the crystal structures of LolA and LolB from *Escherichia coli* were determined using diffraction data collected at beamlines **BL38B1** and **BL44B2** [4].

The structure of LolA is characterized by an eleven-strand antiparallel β-sheet forming an unclosed β-barrel and three α-helices (α1-α3) plugging the β-sheet (Fig. 1) [4]. The long loop is located outside the β-sheet. An additional strand forms a parallel β-sheet with the barrel. The side chain of Arg43 is oriented toward the interior of the molecule due to the unusual *cis* peptide bond, and is hydrogen bonded to the main chain of residues in the α1- and α2-helices, thereby causing the tight fixation of the helices to the β-sheet. The inner surfaces of the β-sheet and three α-helices consist of aromatic residues and form a hydrophobic hollow cavity (Fig. 1). The cavity of LolA is a possible binding site of the lipid moiety of the lipoprotein. The plugging α-helices are expected to control opening and closing upon the accommodation and release of lipoproteins, respectively.

The structure of LolB also comprises an antiparallel β-sheet covered by three α-helices (α1-α3) as shown in Fig. 2 [4]. Surprisingly, the molecular structure of LolB is very similar to that of LolA, despite the low sequence identity of 8% between these two proteins. However, the position and orientation of the three α-helices are largely different from those of LolA. The cavity of LolB is also hydrophobic, but it opens outside

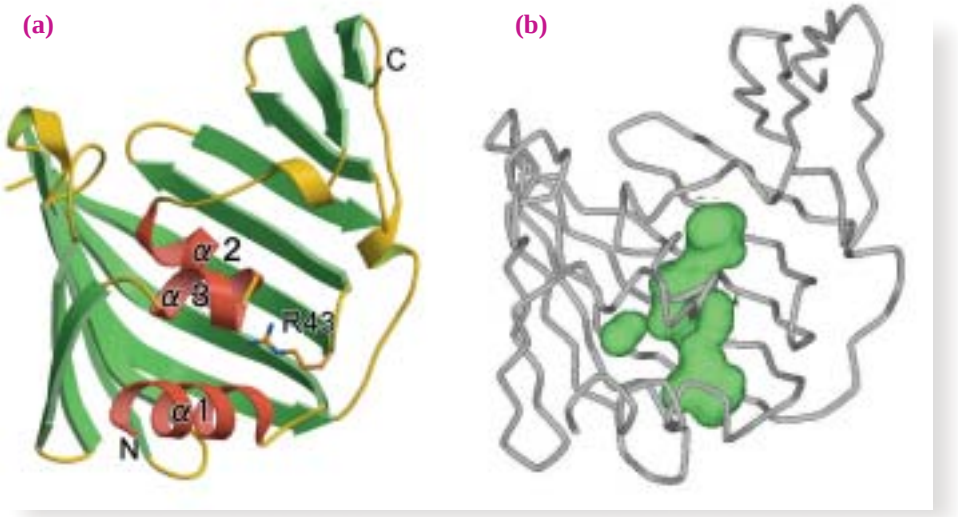

Fig. 1. Crystal structure of LolA. Ribbon presentation of the overall structure with α-helices (α1-α3) in red and β-strands in green **(a)** and the hydrophobic cavity in green **(b)**.

to contact with the solvent region. Polyethylene glycol monomethyl ether (PEGMME) used for crystallization is observed in this cavity, which might show a plausible binding mode of the lipid moiety of the lipoprotein.

These structural differences between two proteins cause the affinity difference for lipoproteins. Lipoproteins are energy-independently transferred from LolA to LolB by this affinity difference in the periplasmic space where ATP is not consumed. This result leads us to further insights on how the ATP-energy controls trafficking events beyond lipid membranes and how these insights can be generalized for other biological processes.

The localization of lipoproteins between membranes is a very important event in pathogenic bacteria which have various lipoproteins and Lol proteins, since lipoproteins induce the immunoresponse of host cells. Lol proteins are indispensable for the growth of all Gram-negative bacteria, and lack of any members is lethal for bacteria. Therefore, the insight on the structures of LolA and LolB is useful for designing effective antibiotics targeting to the proteins.

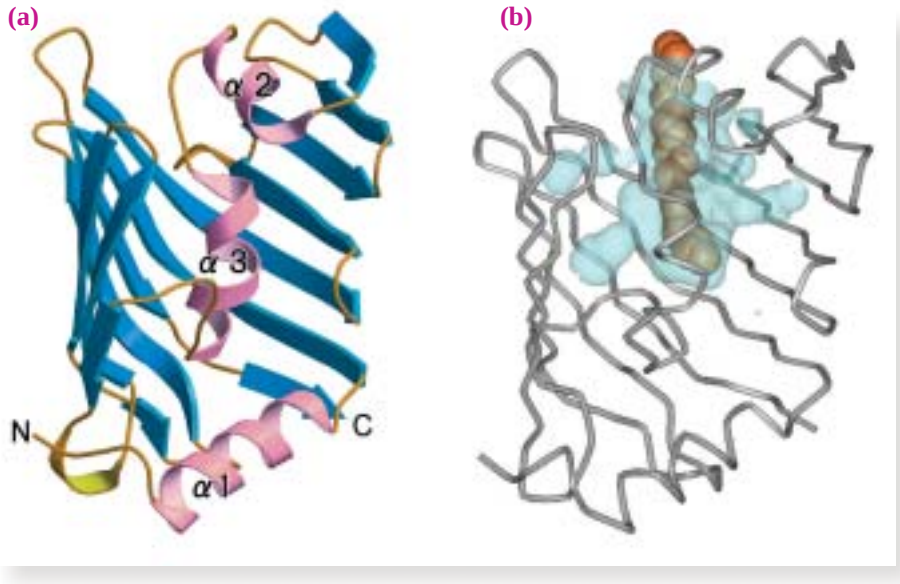

Fig. 2. Crystal structure of LolB. Ribbon presentation of the overall structure with α-helices (α1-α3) in pink and β-strands in blue **(a)** and the hydrophobic cavity in light blue **(b)** in which the PEGMME molecule bound to the cavity is shown as a CPK model in orange.

Kazuki Takeda[a] and Kunio Miki[a,b]

(a) SPring-8 / RIKEN
(b) Graduate School of Science, Kyoto University

E-mail: miki@kuchem.kyoto-u.ac.jp

References

[1] T. Yakushi *et al.*: Nature Cell Biol. **2** (2000) 212.
[2] S. Matsuyama *et al.*: EMBO J. **14** (1995) 3365.
[3] S. Matsuyama *et al.*: EMBO J. **16** (1997) 6947.
[4] K. Takeda, H. Miyatake, N. Yokota, S. Matsuyama, H. Tokuda and K. Miki: EMBO J. **22** (2003) 3199.

Crystal Structure of the Catalytic Domain of Human Phosphodiesterase 5 with Bound Drug Molecules

In 1992, nitric oxide (NO) was recognized by Science magazine as a molecule of the year and ever since NO has become an increasingly popular target of investigation. Why has such a small molecule received so much attention? It is primarily because of the extraordinary biological effects and medically relevant processes mediated by NO. NO exerts part of its effect by binding to the heme of guanyl cyclase which leads to the production of cyclic GMP (cGMP; Fig. 1). In the immune system, macrophage cells produce cGMP and NO as part of the oxidative cytotoxic arsenal resulting from macrophage stimulation (i.e., infection).

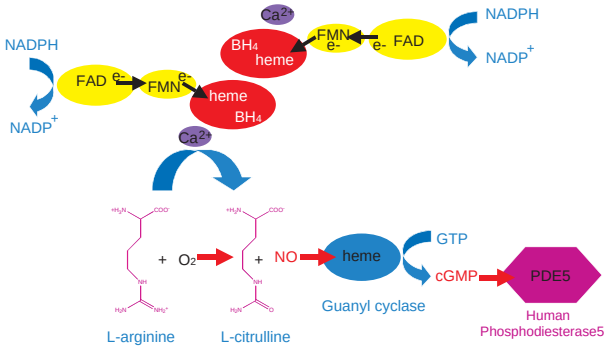

Fig. 1. Schematic representation of how PDE5 functions.

Phosphodiesterases (PDEs) are a superfamily of enzymes which degrade the intracellular second messengers cGMP and cyclic AMP (cAMP). As essential regulators in cyclic nucleotide signaling with diverse physiological functions, PDEs are drug targets for the treatment of various diseases including heart failure, depression, asthma, inflammation, and erectile dysfunction. Of the twelve PDE gene families, the cGMP-specific PDE5 is the principal cGMP-hydrolysing activity in the human corpus cavernosum tissue. It is well known as the target of the drugs sildenafil citrate (Viagra®, Pfizer), tadalafil (Cialis®, Lilly-ICOS), and vardenafil (Levitra®, Bayer & GlaxoSmithKline) for the treatment of erectile dysfunction. Despite the pressing need to develop selective PDE inhibitors as therapeutic drugs, only cAMP-specific PDE4 structures have been available [1]. To discover PDE inhibitors by rational structure-based drug design, we have determined the three-dimensional structures of the catalytic domain (residues 537-860) of human PDE5 complexed with the three drug molecules, sildenafil, tadalafil and vardenafil [2], at SPring-8 beamline **BL44B2** and at PSL (Pohang Light Source).

The catalytic domain of PDE5 has three helical subdomains, an N-terminal cyclin-fold region, a linker region and a C-terminal helical bundle (Fig. 2). The overall topology is similar to that of the homologous PDE4, although PDE5 has only 23% sequence identity with PDE4 in the catalytic region. The active site of PDE5 is located at the center of the C-terminal helical bundle domain. The substrate pocket is approximately 10 Å deep, with a narrow opening and a wide inner space, giving a total volume of about 330 Å^3. It is composed of four subsites, a metal binding site (M site), core pocket (Q pocket), hydrophobic pocket (H pocket), and lid region (L region) (Fig. 3(a)). Overall, the M site and Q pocket are similar to those of PDE4, but the H pocket and the L region show significant structural differences from those of PDE4 (Fig. 4).

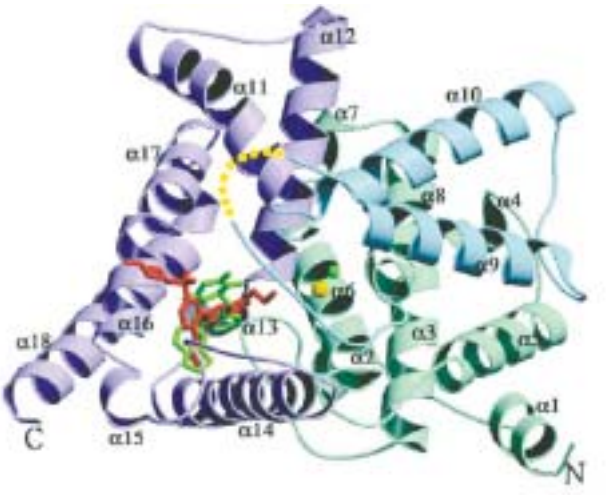

Fig. 2. Overview of PDE5 complex structure. The catalytic domain of the PDE5 molecule can be divided into three subdomains: N-terminal cyclin-fold domain (residues 537-678 in gray), linker helical domain (residues 679-725 in light green) and C-terminal helical bundle domain (residues 726-860 in violet). The bound sildenafil and tadalafil molecules are overlapped and shown by stick models (red and green, respectively) [2].

The binding mode of tadalafil is different from that of sildenafil (Figs. 3(a) and 3(b)). Tadalafil makes no interaction with the L region of the protein. The Q pocket also makes different interactions between the two ligands. The Oe atom of Gln forms a single, not bidentate, hydrogen bond with NH of tadalafil. The H pocket, occupied with an ethyloxy group in the sildenafil complex, is filled with the methylenedioxyphenyl group of tadalafil. The more extensive interactions with the H pocket may be one of the reasons that tadalafil maintains a high affinity without binding to the L region. A comparison of the structures of the three complexes suggests obvious modifications (for example, changing the ethyloxy group of sildenafil to fit to the H pocket) of the inhibitors in order to improve their binding affinity and selectivity. Vardenafil shows a binding mode very similar to that of sildenafil.

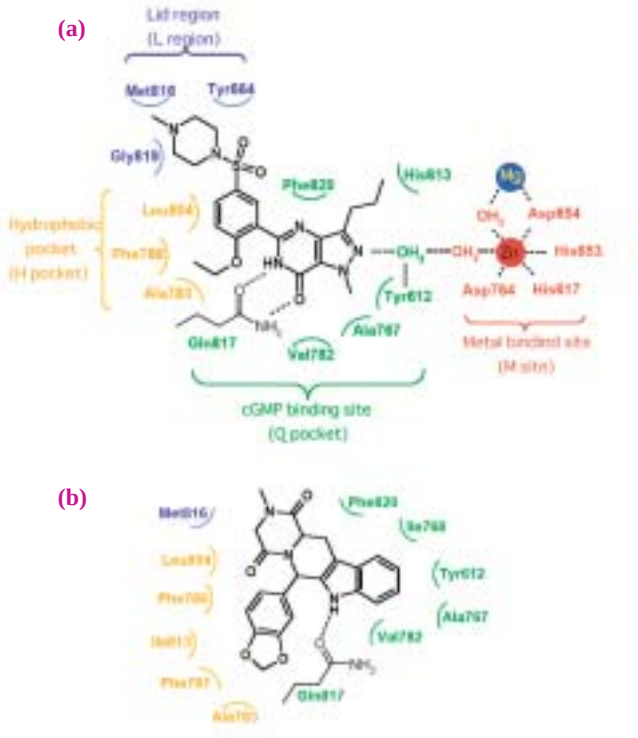

Fig. 3. **(a)** Schematic representation of interactions made by the sildenafil in complex with PDE5. Residues in four subsites are colored differently: M subsite in red, Q subsite in green, H subsite in yellow and L region in blue. The hydrogen-bonding interactions are only shown in dashed lines. **(b)** Schematic representation of interactions made by the tadalafil in complex with PDE5. The colors used are the same as those in **(a)** for the residues in four subsites.

In conclusion, we have presented here the three-dimensional structures of PDE5 complexed with the three inhibitors in clinical use, sildenafil, vardenafil, and tadalafil. Our study provides the first clear picture of the different binding modes of these ligands in the active site of PDE5. We believe that these structural studies will assist the discovery of potent and selective PDE inhibitors that exhibit improved pharmacological profiles.

Fig. 4. Comparison of PDE5 and PDE4 active sites. Superimposed structures of PDE5 and PDE4 showing a difference in folding at the active site. The backbone worm presentations of PDE5 and PDE4 are shown in red and blue, respectively. To emphasize the structural difference, only the backbone traces of aa.304-325 of PDE5 and aa.660-680 of PDE4 are saturated with their respective colors. The stick model of sildenafil is shown in yellow, and that of zardaverine in green [2].

Sam-Yong Park[a], Kwang Yeon Hwang[b] and Young Ho Jeon[b]

(a) Protein Design Laboratory, Yokohama City University
(b) Crystal Genomics, Inc., Korea

E-mail: park@tsurumi.yokohama-cu.ac.jp

References

[1] Xu R. X. *et al.*: Science **288** (2000) 1822.
[2] B.-J. Sung, K.Y. Hwang, Y.H. Jeon, J.Il Lee, Y.S. Heo, J.H. Kim, J. Moon, J.M. Yoon, Y.-L. Hyun, E. Kim, S.J. Eum, S.-Y. Park, J.-O. Lee, T.G. Lee, S. Ro and J.M. Cho: Nature **425** (2003) 98.

Crystal Structure of Yeast Cytosine Deaminase

Cytosine deaminase (CD) catalyzes the deamination of cytosine to uracil and that of 5-methylcytosine to thymine (Fig. 1). The antimetabolite 5-fluorouracil (5-FU) is one of the most active chemotherapeutic agents for cancer treatment, but it has limited efficacy due to gastrointestinal and hematological toxicities. Due to its ability to convert nontoxic 5-fluorocytosine (5-FC) into 5-FU and its absence in mammalian cells, the combination of 5-FC with CD in enzyme-prodrug gene therapy has been shown to effectively control tumor growth and is currently being evaluated in clinical trials. Here we have determined the yeast CD structure at 1.6 Å resolution at beamlines **BL12B2** and **BL41XU** [1,2].

The protein structure is composed of a central five-stranded β-sheet (β1- β5) sandwiched by six α-helices (αA - αF) (Fig. 2(a)). Surprisingly, even though yeast CD shares a higher sequence identity to cytidine deaminases (CDAs), its closest structural match is the subdomain 2 of the AICAR transformylase domain, due to the common αD helix and the same direction of the β5 strand (Fig. 2(b)). The strong conservation of tertiary structures suggests that these enzymes are descendants of a single ancestral gene, and thereby define a new superfamily.

Interestingly, the 426-residue hexameric *E. coli* CD belongs to superfamily, whereas the 158-residue dimeric yeast counterpart is grouped into the CDA superfamily [3]. The active site of yeast CD contains one tightly bound zinc ion, which is tetrahedrally coordinated by His^{62}, Cys^{91}, Cys^{94}, and a bound inhibitor (Fig. 3). The complex structure reveals that yeast CD converts the inhibitor 2-hydroxypyrimidine into 4-(R)hydroxyl-3,4-dihydropyrimidine, which is enantiomeric to the configuration observed in *E. coli* CD. Therefore, the crystal structures of bacterial and fungal CDs provide an excellent example of convergent evolution, in that they have evolved from unrelated ancestral proteins but have achieved the same deamination reaction.

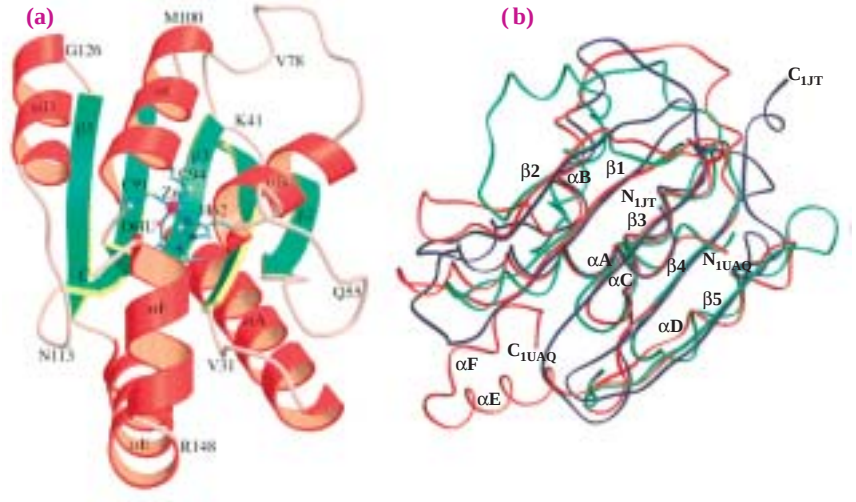

Fig. 2. **(a)** The monomeric structure of yeast CD with the zinc ion shown as a magenta sphere with its ligands and the inhibitor (DHU) as ball-and-stick representations. **(b)** Structural superposition of yeast CD (red), *B. subtilis* CDA (blue), and the subdomain 2 of AICAR transformylase (green) [4].

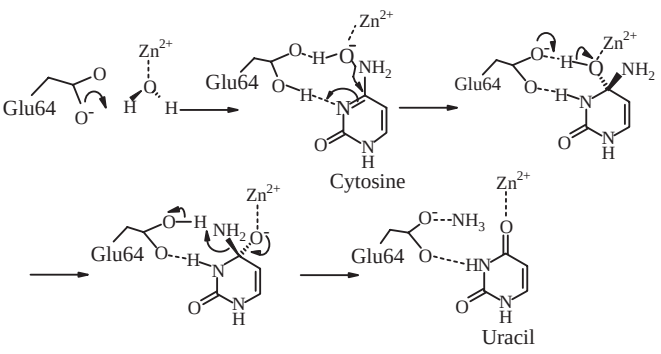

Fig. 1. Proposed catalytic mechanism for yeast CD.

Based on structural studies, we propose a deamination mechanism for yeast CD (Fig. 1). The substrate binds to an active site and induces a closed conformation to sequester the reaction from the solvent. The water molecule activated by the zinc ion attacks the C^4 atom with the assistance of Glu^{64} serving as a proton shuttle. The product uracil moves toward the zinc ion for ligation and this would weaken its interaction with the C-terminal tail, allowing its release from the active site. The active site architectures of yeast CD and CDAs are strikingly similar. However, they contain unique substrate-recognition residues, in particular, C-terminal tails.

The presence of an αD helix in yeast CD leads strands β4 and β5 to be parallel and this results in the C-terminal tail moving back sharply towards the active site to accommodate only the cytosine base within the same molecule (Fig. 4(a)). On the other hand, the lack of an αD helix in *B. subtilis* CDA leads strands β4 and β5 to be antiparallel and this results in an opposite direction for the C-terminal tail, which enlarges the active site of the adjacent molecule to accommodate a larger cytidine substrate (Fig. 4(b)).

Previous studies have demonstrated that yeast CD has a greater therapeutic potential than the bacterial enzymes in the enzyme-prodrug strategy. The C^5 atom of the pyrimidine ring is adjacent to a hydrophobic cluster and faces toward Phe^{114}, with a distance of 4.1 Å. When a fluorine atom is attached to an aromatic ring, it will make it very hydrophobic. Therefore, the hydrophobic cluster in yeast CD should enhance the binding of 5-FC. On the other hand, the C^5 atom faces toward Asp^{314} in *E. coli* CD, with a distance of 3.6 Å between C^5 and Asp314 $O^{\delta 1}$. Close contact with such a polar residue would be unfavorable to 5-FC binding. These structural observations are consistent with enzyme kinetic measurements.

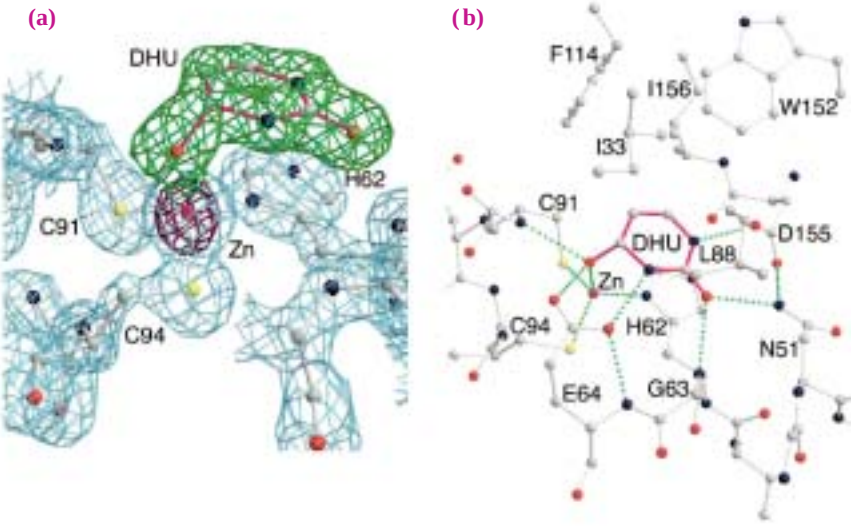

Fig. 3. Active site. **(a)** The $2F_o - F_c$ map at 1.5 σ level in cyan, the difference anomalous map for the zinc ion at 30 σ m level in purple, and the densities for the inhibitor (DHU) in green. **(b)** The interaction networks in the active site. There are six direct hydrogen bonds between the protein and the inhibitor [4].

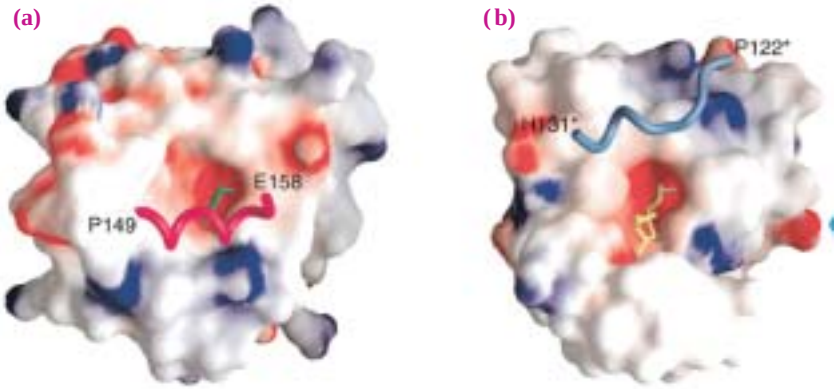

Fig. 4. Molecular surfaces of yeast CD (A) and *B. subtilis* CDA (B) colored for electrostatic potentials from –10 k_BT (red) to 10 k_BT (blue). The C-terminal tail (residues 149-158) of yeast CD is shown explicitly as worms as for the C-terminal residues (residues 122*-131*) from one adjacent subunit in *B. subtilis* CDA. The analogues for cytosine and cytidine are colored green and yellow, respectively. The CDAs have space to accommodate the ribosyl sugar of cytidine, whereas yeast CD does not have space due to the blocking by the C-terminal tail [4].

Shwu-Huey Liaw

Faculty of Life Science, National Yang-Ming University, Taiwan

E-mail: shliaw@ym.edu.tw

References

[1] Y.H. Hsu *et al.*: Acta Cryst. D **59** (2003) 950.
[2] S.H. Liaw *et al.*: J. Biol. Chem. **278** (2003) 4957.
[3] G.C. Ireton *et al.*: J. Mol. Biol. **315** (2002) 687.
[4] T.-P. Ko, J.-J. Lin, C.-Y. Hu, Y.-H. Hsu, A.H.-J. Wang and S.-H. Liaw: J. Biol. Chem. **278** (2003) 19111.

Direct Observation of Photolysis-Induced Structural Changes in Hemoglobin

Hemoglobin (Hb) is a tetrameric protein that consists of two α and two β subunits represented by $\alpha_2\beta_2$ and transports oxygen from lungs to tissues for use in respiration. The α and β subunits are structurally and evolutionarily related to each other, and each subunit has an oxygen binding site which is called heme. Thus, Hb can bind a total of four oxygen molecules. It is well known that Hb is not only a simple oxygen tank, but also functions as a sophisticated oxygen delivery system to provide the proper amount of oxygen to tissues under a wide variety of circumstances. This feature is closely related to a cooperative interaction between oxygen binding sites; that is, the binding of oxygen at one subunit increases the affinity for additional oxygen at another subunit. In this context, Hb has played a central role in exploring the mechanism of the cooperative interaction of proteins in general. It is well established by X-ray crystallographic studies that Hb has two end-structures which are called relaxed (or R) and tense (or T-) states, which correspond to high and low oxygen affinities, respectively [1]. However, intermediate structures between the two end-structures, which must be related to a key structure to understand the cooperative regulation mechanism of Hb, have not been directly observed yet. In particular, the essential part of the mechanism is the structural restraints in the T-state Hb on ligand binding, because the oxygen affinity of the R-state is close to that of the isolated α and β subunits, while the oxygen affinity of the T-state is lower by two orders of magnitude than those of the R-state and isolated subunits. We noted that the structural restrains in the T-state Hb can be elucidated at the atomic level by determining the structure of the photoproduct of T-state HbCO by X-ray crystallography, and here we present an X-ray crystallographic study of CO complexes of the T- and R-states of Hb at cryogenic temperatures in both resting and photolysed states [2].

The experiments were carried out at the RIKEN Structural Biology beamline **BL44B2**. We clearly observed the photodissociation of CO within a single crystal of T- and R-state Hbs, and directly monitored subsequent tertiary structural changes of the α and β subunits in terms of electron density movements. We used iron-nickel hybrid Hb as T-state liganded Hb, in which iron atoms either in the α or β subunit are replaced by nickel atoms. Nickel binds neither oxygen nor CO and mimics deoxy heme, thus the quaternary structure remains in the T-state even two CO molecules bind to either α or β subunit. The 2Fo-Fc map of the α subunit of α-iron β-nickel hemoglobin in the T-state is shown in Fig. 1. A photolyzed CO molecule is clearly observed immediately above the

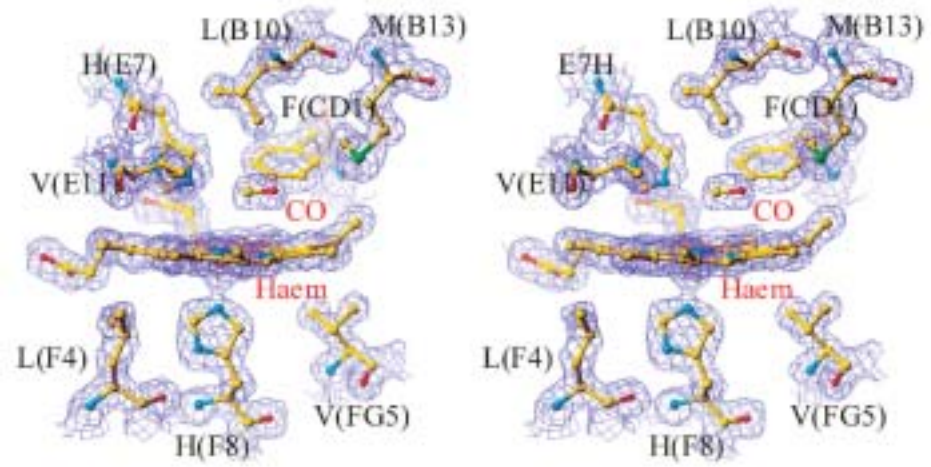

Fig. 1. Stereoview of the electron density map ($2F_o$-F_c map) of the active-site structure of the photolysed CO complex of T-state hybrid Hbs contoured at 1.3 σ. The α_1 heme region in photolysed iron-nickel hybrid HbCO at 25 K is shown [2].

heme iron in the heme pocket. Difference Fourier maps between T-state photoproducts and CO-bound structures gave a clear picture of the dynamic responses of the hemes and protein moieties after photolysis (Fig. 2). We found two important structural differences between the α(Fe) and β(Fe) subunits. First, the downward movement of an F-helix and the bent motion of a pyrrole ring are more marked in the α(Fe) subunit than in the β(Fe) subunit. Secondly, sliding motion of the heme is observed only in the β(Fe) subunit. These results reflect structural restraints retained in each subunit and clearly show that the structural basis of the low affinity of T-state Hb is completely different between the α and β subunits, even though these subunits have similar tertiary structures. This direct observation of photolysis-induced structural changes in Hb suggests that the reduced ligand affinity of T-state Hb is mainly contributed by the structures of relatively local and specific sites close to the heme moiety.

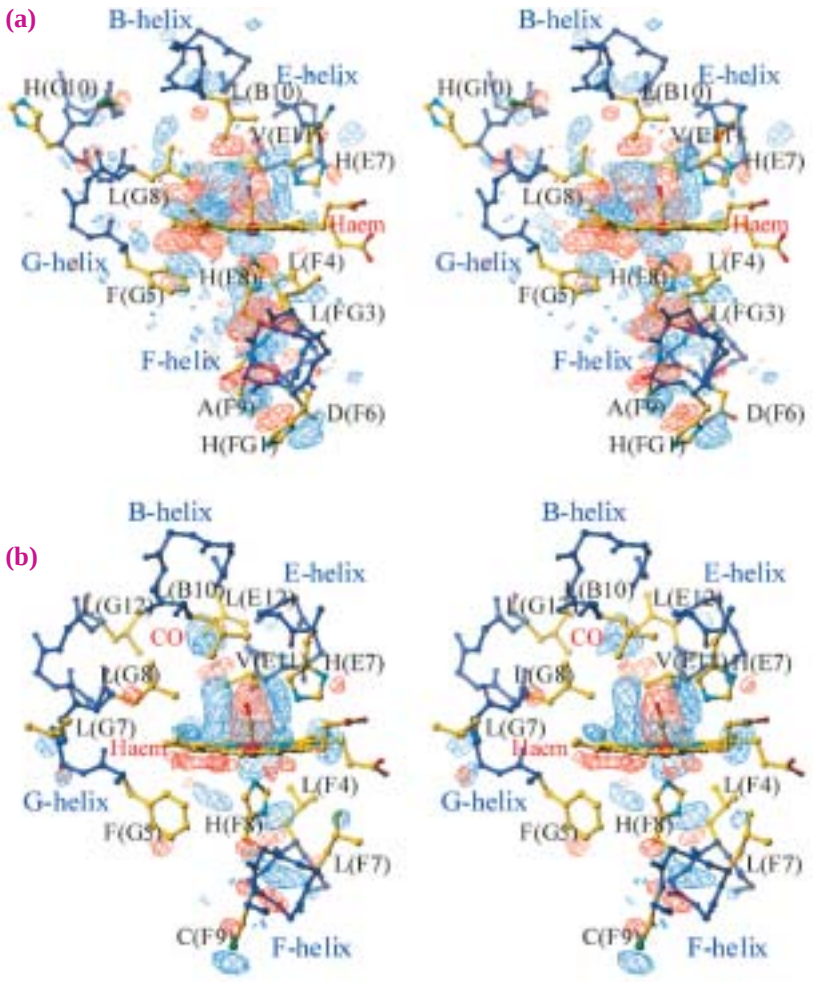

Fig. 2. Stereoview of the difference Fourier map of the active-site structure between the T-state protoproduct and CO-bound forms at ±3σ. **(a)** The α_1 heme region in iron-nickel hybrid HbCO at 25 K. **(b)** The β_2 heme region in iron-nickel hybrid HbCO at 25 K [2].

Shin-ichi Adachi[a,*], Sam-Yong Park[b] and Naoya Shibayama[c]

(a) SPring-8 / RIKEN
(b) Protein Design Laboratory, Yokohama City University
(c) Department of Physiology, Jichi Medical School

* *Present address* : Photon Factory, High Energy Accelerator Research Organization (KEK)

E-mail: shinichi.adachi@kek.jp

References

[1] M. F. Perutz: Nature **228** (1970) 726.
[2] S. Adachi, S.-Y. Park, J.R.H. Tame, Y. Shiro and N. Shibayama: Proc. Natl. Acad. Sci. USA **100** (2003) 7039.

Structure of the L Intermediate of Bacteriorhodopsin

Bacteriorhodopsin (bR), a membrane protein found in the cell membrane of *Halobacterium salinarum*, functions as a light-driven proton transport. Its polypeptide chain is folded into 7 transmembrane helices and retinal is bound to the ε-amino group of Lys216 *via* a protonated Schiff base linkage (Fig. 1). The photoisomerization of the all-*trans* retinal into the 13-*cis*, 15-*anti* configuration initiates a reaction cycle involving several intermediates ($bR_{570} \rightarrow K_{590} \rightarrow L_{550} \rightarrow M_{410} \rightarrow N_{560} \rightarrow O_{630} \rightarrow bR_{570}$). For the elucidation of the proton pumping mechanism, it is important to obtain structural information of the reaction intermediates. Using a 3D crystal belonging to the space group P622, we have previously determined the structures of the ground state (bR_{570}) and the K and the M intermediates at 2.3 - 2.6 Å resolutions [1,2]. Our structural data show that, in the K intermediate, the retinal chromophore has a largely twisted 13-cis, 15-anti configuration. The distortion in the retinal polyene chain is suggested to induce a vertical movement of helix G upon the formation of the M intermediate, which is accompanied by a large rearrangement in the hydrogen-bonding network in the proton release channel.

An increasing number of experimental data has shown that internal water molecules play an important role in regulating the pK_a values of key residues in the pathway of proton transport. The current structural model of the unphotolysed state (bR_{570}) shows that water molecules existing in the active site participate in stabilizing the protonated Schiff base with a very high pK_a (~ 13) and its counter ion (unprotonated Asp85) with a very low pK_a (~ 2.5). Recent FTIR studies of the L intermediate have suggested that, before the primary proton transfer, rearrangements of internal water molecules take place in such a manner that they cause a significant reduction in the pK_a of the Schiff base and a concomitant increase in the pK_a of Asp85. However, the structure of a key intermediate, i.e., the L intermediate, has not yet been determined convincingly, making it difficult to quantitatively analyze the detailed movements of internal water molecules.

For the structural investigation of the L intermediate [3], we carried out a quantitative analysis for X-radiation damage and searched for optimum conditions for X-ray measurements to minimize undesired effects of X-ray-induced structural changes. After a careful structural analysis, we constructed a structural model of the L intermediate at 2.4 Å resolution. Briefly, the P622 crystal was illuminated with green light at 160 K and subsequently with red light at 100K. This yielded a ~1:4 mixture of the L intermediate and the ground state. Diffraction data from such crystals were collected using a low flux of X-rays (~2×10^{15} photons/mm^2 per crystal), and their combined data were compared with those from unphotolyzed crystals. Figure 2 shows a difference electron-density map between the L intermediate and the ground state. These structural data, together with our previous data [1], indicate that the retinal chromophore, which is largely twisted in the K intermediate, takes a more planar 13-cis, 15-anti configuration in the L intermediate. This configurational change, which is accompanied by the reorientation of the Schiff base N-H bond towards the intracellular side, is coupled with a large rotation of the side chain of an amino acid residue (Leu93) making contact with the C13 methyl group of retinal. Following these motions, a water molecule, at first hydrogen-bonded to the Schiff base

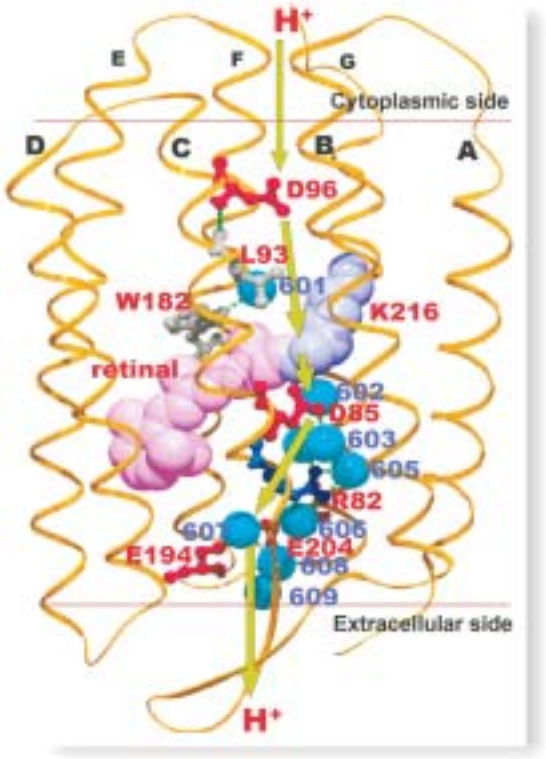

Fig. 1. Crystal structure of the ground-state of bacteriorhodopsin. Internal water molecules (cyan), the retinal-Lys216 chain (pink and light blue) and several key residues (red, blue and gray) are drawn. The green arrows indicate the pathway of proton translocation.

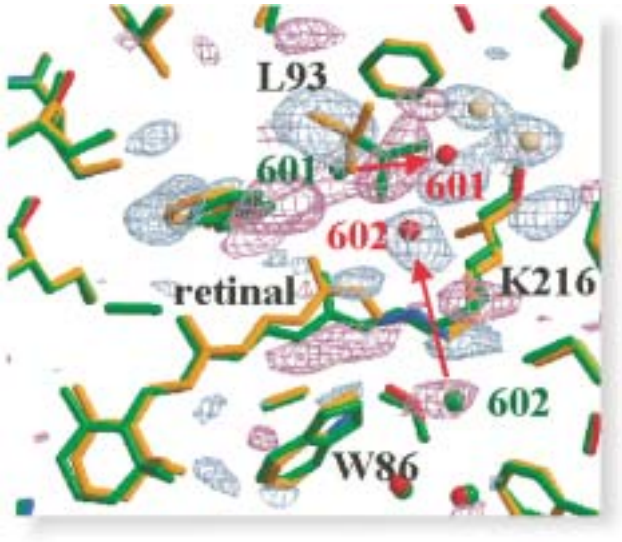

Fig. 2. Difference map between L and bR_{570}, contoured at 3.5σ (cyan, positive density; purple, negative density) and overlaid on the structural models of the ground state (green) and the L intermediate (carbon, oxygen and nitrogen atoms are drawn in orange, red and blue, respectively). Water molecules in L are represented by red (high occupancy) or gray spheres (low occupancy).

and Asp85, is dragged to a space that is originally occupied by Leu93.

In Fig. 3, the movements of water molecules observed in the bR_{570}-to-K and K-to-L transitions are summarized. A small displacement of Wat602 (i.e., towards the C^{δ} of Lys216) is already initiated in the primary photoreaction, which is accompanied by the isomerization of the retinal into a largely twisted 13-*cis*, 15-*anti* configuration. A large jump of Wat602 from the extracellular side of the Schiff base to the opposite side is assisted by the ~ 90° rotation of the N-H bond of the retinal Schiff base.

Now, an interesting question rises as to why the vertical movement of a key water molecule takes place prior to the primary proton transfer (from the Schiff base to Asp85), which takes place in the L-to-M transition. Since the retinal chromophore is accommodated tightly in a hydrophobic pocket, there is no channel for the passive movement of water across a horizontal plane passing through the chromophore. This plane can act as a structural barrier against the movement of water. Probably the backward translocation of Wat602 would not occur unless the cis-to-trans isomerization of the retinal is initiated by the excitation of the L intermediate.

Indeed, diffraction data from a crystal containing the M intermediate showed that this water molecule moves further towards the intracellular side in the L-to-M transition [3]. It is very likely that the detachment of this water molecule from the protonated Schiff base causes a significant decrease in the pK_a of the Schiff base, thereby facilitating the proton transfer to Asp85. On the basis of these observations, we argue that the vertical movement of a water molecule in the K-to-L transition is a key event determining the directionality of proton translocation in the protein.

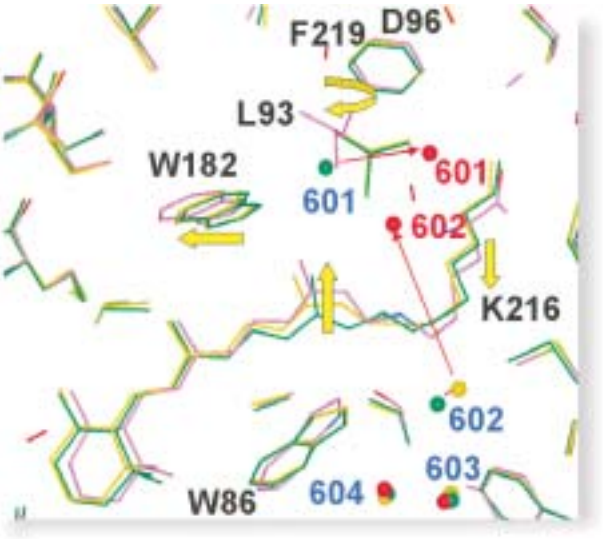

Fig. 3. Movements of key water molecules (indicated by thin arrows) and conformational changes in Leu93, Trp182 and the retinal-Lys216 chain (indicated by thick arrows) during the $bR_{570} \rightarrow K$ and $K \rightarrow L$ transitions. Atoms in bR_{570}, K and L are drawn in different colors.

Tsutomu Kouyama

Department of Physics, Nagoya University

E-mail: kouyama@bio.phys.nagoya-u.ac.jp

References

[1] Y. Matsui *et al.*: J. Mol. Biol. **324** (2002) 469.
[2] K. Takeda, Y. Matsui, N. Kamiya, S. Adachi, H. Okumura and T. Kouyama: submitted to J. Mol. Biol.
[3] T. Kouyama, T. Nishikawa, T. Tokuhisa and H. Okumura: J. Mol. Biol. **335** (2004) 531.

MATERIALS SCIENCE
STRUCTURE

Materials Science researches at SPring-8 have been so far providing crucial information for structure-property relationship of various bulk materials and contributing to rational design of novel materials having specific properties. In addition, the number of research applications for the nanotechnology are now increasing more and more. Although the number of beamlines has not been increasing over the last few years, it does not mean the scientific activities in Materials Science at SPring-8 are saturated. The phase of utilization at each beamline has been shifting to advanced applications. Actually, the most of the planed scientific targets have been achieved successfully and new challenging research activities start at some beamlines. It has to be admitted that the scientific activities at SPring-8 on materials science have more and more varieties and have many important results. A part of the reasons to keep the activities on materials science at relatively high level could be a designation of priority research at SPring-8. For instance, recent increase of nanotechnology relating results may be the case in point. Thus, there are some arguments for the new beamline requirements from materials science and nanotechnology science community.

From structural studies in Materials Science, the following 8 topics are presented in this issue. The first five excellent articles are about the structure-property relationship, nanotechnology, and synthesis of novel materials. Especially, the work of T. Takenobu *et al.* gave the breakthrough for nanotube science. The high pressure work of W. Utsumi is the search of specific condition of GaN crystal synthesis under high pressure. And the imaging techniques are also presented, which are quite unique and promising. These researches may lead to new direction of the synchrotron radiation utilization for materials science.

The plenty of research subjects, for which the SPring-8 can cover and play key role, should be still remained and/or increase in Materials Science. In order to explore and open up the new research field, the corporation with the materials and nanotechnology scientists outside of the SPring-8 cannot be overemphasized.

Makoto Sakata

Direct Observation of Charge Transfer at Jahn-Teller Transition in a Perovskite $RbMn[Fe(CN)_6]$

Transition metal cyanides, $A(I)M(II)[N(III)(CN)_6]$ (A = Na, K, Rb, Cs; M = Mn, Co, Cr; N = Fe, Cr), have been attracting the renewed interest of materials scientists, because they show a novel photoinduced magnetization/demagnetization in addition to the thermally induced spin-state transition. They also have the characteristic structure: the transition metal ions are surrounded by six cyanos (CN^-) and form a three-dimensional —M-NC-N— network analogous to the double-perovskite-type transition metal oxides. In this sense, the study of the transition metal cyanides will contribute to a deeper comprehension of the strongly correlated electron system. Most of the transition metal cyanides, however, contain considerable nonstoichiometric H_2O molecules, which make the structural analysis difficult. Among the transition metal cyanides, $RbMn[Fe(CN)_6]$ [1] does not contain extra H_2O molecules and is suitable for precise structural analysis on the charge density level. Ohkoshi *et al.* [1] observed temperature-induced cubic ($F4\text{-}3m$: Z = 4) tetragonal ($I4\text{-}m2$: Z = 2) transition at around 220 K. The structural transition is ascribed to the charge transfer from the Mn^{2+} site to the Fe^{3+} site, because the resultant Jahn-Teller distortion of Mn^{3+} (d^4) can cause the tetragonal structure [2]. With a further decrease in temperature below 12 K (= T_C), the local spins at the Mn sites are ferromagnetically ordered, as confirmed by neutron powder diffraction experiment [3]. Tokoro *et al.* [4] observed the suppression of magnetization by a visible pulse laser irradiation at 3 K.

To obtain X-ray powder data of good counting statistics with high angular resolution, measurements were carried out at beamline **BL02B2** . The as-grown sample powders were sealed in a 0.3 mmϕ Lindemann capillary, which gave a homogeneous intensity distribution in the Debye-Scherrer powder ring. The wavelength of the incident X-ray was 0.82 Å (slightly longer than the K-edge of Rb), and the exposure times were 26 min at 300 K and 67 min at 92 K.

The electron density distributions at both temperatures were visualized by the maximum entropy method (MEM) combined with the Rietveld refinement. The MEM analysis was carried out with a program ENIGMA using 100×100×100 pixels (72×72×108 pixels) at 300 K (at 92 K). In Fig. 1, the MEM charge density of the (100) section containing Mn, Fe, C, and N atoms is shown at 300 K with schematics of crystal structure. The contour lines are drawn only for the lower density region (4.0 eÅ^{-3}). The MEM charge density clearly exhibits the Mn-N and the Fe-C bonding features. The charge density distribution is isotropic around Mn^{2+} because both the e_g orbitals, that is, dx^2-y^2 and $d3z^2-r^2$, are occupied in the cubic phase. The minimum of the charge density (= 0.80 eÅ^{-3}) in the Fe-C bond is larger than that (= 0.60 eÅ^{-3}) in the Mn-N bond. This bonding electron distribution is consistent with the picture that $RbMn[Fe(CN)_6]$ consists of $Fe(CN)_6$ complexes and cations (Rb^+ and Mn^{2+}). The charge density distribution markedly changes at the cubic-tetragonal transition. Figure 2(a) shows the MEM charge density of $RbMn[Fe(CN)_6]$ for the (110) section at 92 K. One may notice that the charge density distribution around Mn becomes anisotropic: the minimum of the charge density (= 0.65 eÅ^{-3}) in the Mn-N_{xy} bond is higher than that (= 0.28 eÅ^{-3}) in the Mn-N_z bond. Obviously, this anisotropy is attributed to the charge transfer from the Mn^{2+} site to the Fe^{3+} site, which causes a hole on the e_g orbital of the Mn ion.

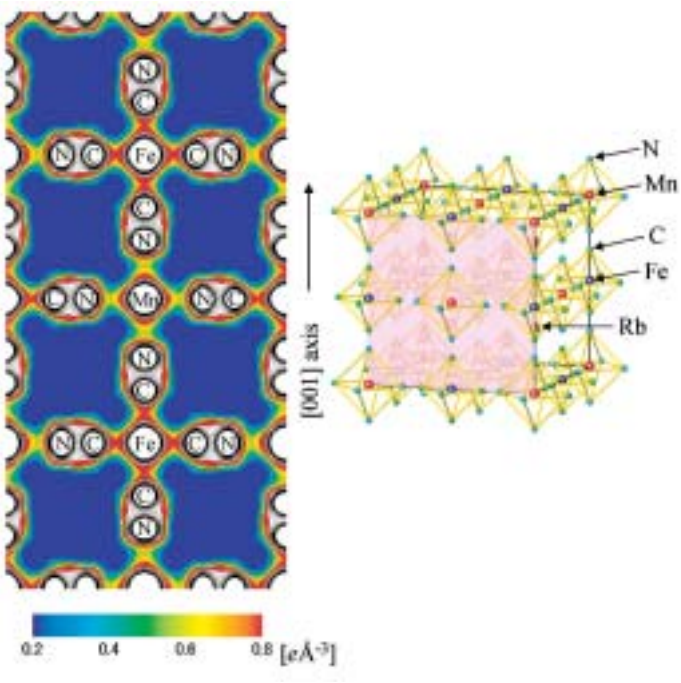

Fig. 1. MEM electron density distribution of $RbMn[Fe(CN)_6]$ for the (100) section at 300 K in the high-temperature cubic phase ($F4\text{-}3m$: Z = 4). Contour lines are drawn from 0.0 to 4.0 eÅ^{-3} at intervals of 0.2 eÅ^{-3}. A schematic shows the crystal structure.

It is interesting to investigate the variation of the charge densities around the Mn ion and the Fe ion at the cubic-tetragonal transition. Figure 3 shows the charge density of $RbMn[Fe(CN)_6]$ along the Mn-NC-Fe bond at 300 and 92 K. The charge density around the Mn ion significantly decreases in the tetragonal phase. We estimated the total charges around the Mn ion by spherical integration up to the midpoint of the Mn-N bond, i.e., 1.09 Å for the cubic phase and 1.06 Å for the tetragonal phase. The total charge decreases from 23.0(2)e to 22 2(2)e at the cubic-tetragonal transition, indicating the valence change from Mn^{2+} to Mn^{3+}.

We have calculated the charge density distribution with the full-potential linearized augmented plane-wave method within the local density approximation (LDA) scheme. The actual tetragonal lattice parameters at 92 K determined by Rietveld analysis were used. The calculated spin moment μ_{Mn} at the Mn site (= 3.2 μ_B) is nearly consistent with the experimental results [μ_{Mn} = 3.2(7) μ_B [3]]. Figure 2(b) shows the calculated charge density of $RbMn[Fe(CN)_6]$ for the (110) section. Heights and interval of the contour lines are the same for both the experimental [Fig. 2(a)] and calculated [Fig. 2(b)] images. The LDA calculation quantitatively reproduces the MEM charge density, including the anisotropic charge density around Mn^{3+}.

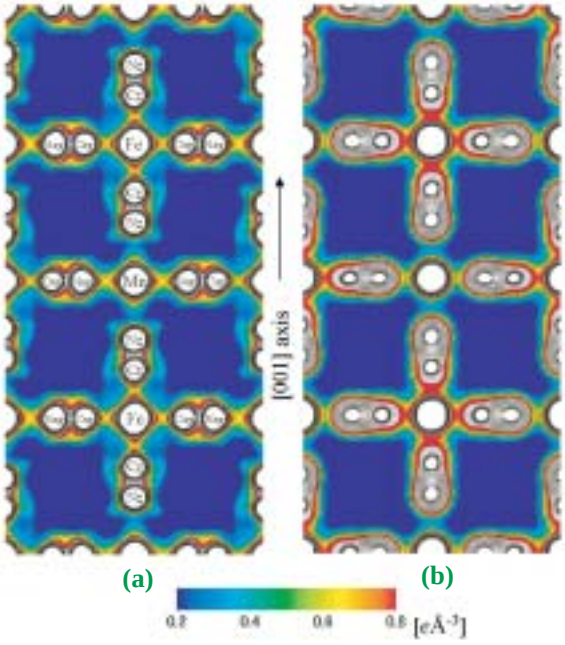

Fig. 2. (**a**) MEM electron density distribution of $RbMn[Fe(CN)_6]$ for the (110) section in the low-temperature tetragonal phase ($I4$-$m2$: Z = 2) at 92 K. (**b**) Electron density distribution of $RbMn[Fe(CN)_6]$ for the (110) section determined by the LDA first-principles calculation based on the actual atomic coordinates. Contour lines are drawn from 0.0 to 4.0 eÅ^{-3} at intervals of 0.2 eÅ^{-3}.

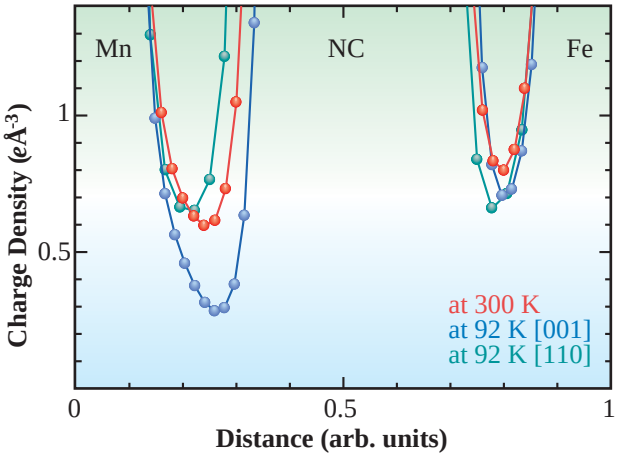

Fig. 3. Charge density of $RbMn[Fe(CN)_6]$ along the Mn-NC-Fe bond at 300 and 92 K, determined by MEM/Rietveld analysis.

Actually, the calculated minima of the charge densities are 0.59 eÅ^{-3} and 0.32 eÅ^{-3} in the Mn-N_{xy} and Mn-N_z bonds, respectively, which are close to the experimentally obtained values (0.65 eÅ^{-3} and 0.28 eÅ^{-3} in the Mn-Nxy and Mn-Nz bonds, respectively).

In summary, we have investigated the variation of charge density at the Jahn-Teller transition of $RbMn[Fe(CN)_6]$ and directly observed the charge transfer from the Mn site to the Fe site at the cubic-tetragonal transition [5]. We further interpreted the anisotropic charge density distribution around Mn^{3+} in terms of the bonding electrons. Thus, the MEM/Rietveld charge density analysis proved to be effective for the deeper comprehension of the transition metal compounds.

Kenichi Kato[a] and Yutaka Moritomo[b]

(a) JASRI / SPring-8
(b) Department of Applied Physics, Nagoya University

E-mail: katok@spring8.or.jp

References

[1] S. Ohkoshi *et al.*: J. Phys. Chem. B **106** (2002) 2423.
[2] Y. Moritomo *et al.*: J. Phys. Soc. Jpn. **71**(2002) 2078.
[3] Y. Moritomo *et al.*: J. Phys. Soc. Jpn. **72** (2003) 456.
[4] H. Tokoro *et al.*: Appl. Phys. Lett. **82** (2003) 1245.
[5] K. Kato, Y. Moritomo, M. Takata, M. Sakata, M. Umekawa, N. Hamada, S. Ohkoshi, H. Tokoro, K. Hashimoto: Phys. Rev. Lett. **91** (2003) 255502.

Charge-Ordered State in Single-Crystalline $CaFeO_3$ Thin Film Studied by X-ray Anomalous Diffraction

Charge ordering (CO) in perovskite-type oxides has been intensively investigated in recent years. $CaFeO_3$ (CFO) shows the CO transition at 290 K [1] with a change of the crystal space group from *Pbnm* in the normal state to $P2_1/n$ in the CO state. The transition accompanies the metal-insulator transition, as seen other mixed valence materials. On the other hand, $SrFeO_3$ (SFO), having the same nominal Fe valence of +4 and nearly the same structure, does not show CO even at 4 K. The CFO crystal has a distorted perovskite-type structure ($GdFeO_3$ structure) shown in Fig. 1, where each FeO_6 octahedron is tilted. Since the Fe^{4+}-O bond has a strong *d*-*p* hybridization, oxygen holes on the antibonding band are considered to be generated initially, and consequently, the system becomes metallic. The Fe-O-Fe bond angle in CFO is 160° which is much reduced from the 180° in SFO. This causes the *d*-*p* band in CFO to be narrower than that in SFO and, as a consequence, the system transforms to the CO state at a relatively high temperature. In the CFO crystal, two major steric configurations of the excess charge have been proposed for the CO state. One is that fully charged Fe^{3+} ($3d^5$) and Fe^{5+} ($3d^3$) are positioned separately with a rocksalt-type structure. This concept was accepted at an early stage and supported by the experiment of the Mössbauer effect. The other, based on XPS measurements, is that holes, as excess charge, are localized around some Fe^{3+} ions, such as $3d^5\ 3d^5\underline{L}^2$($\underline{L}$ denotes a ligand hole). This suggests that the Fe ions of CFO in the CO state split into $Fe^{4+\delta}$ and $Fe^{4-\delta}$ ($0 < \delta \leq 1$) at the CO transition temperature. More recently, neutron and X-ray diffraction analyses of polycrystalline CFO have been performed [2]. These studies revealed that Fe-O bond lengths for each equivalent Fe site are distinct, e.g., at 15 K for Fe(1) and Fe(2) sites, bond lengths are 0.1872(6) and 0.1974(6) nm, respectively [2]. Even with these explicit studies, however, the physical picture appropriate for CO in CFO is still controversial, because of a lack of quantitative information on each electronic state of Fe(1) and Fe(2). We present explicit experimental evidence of the CO state realized in CFO, using an X-ray anomalous diffraction (XAD) technique, and a subsequent electronic band-structure calculation is then compared with the experimental results to obtain the physical picture in terms of the quantitative electronic state difference between Fe(1) and Fe(2) in the CO state of CFO [3].

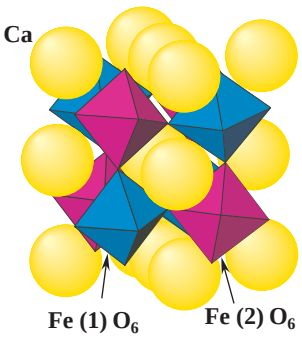

Fig. 1. Crystal structure of $CaFeO_3$. Two types of octahedra contain Fe(1) or Fe(2) alternatively. Spheres symbolize calcium ions.

CFO single-crystalline thin films with [001] orientation parallel to the growth direction were fabricated by pulsed laser deposition with epitaxial growth on the $SrLaAlO_4$ (001) substrate. After the deposition, the films were cooled by blowing partially ozonized oxygen. The size of the films obtained was 10×10 mm^2 in area and 50 nm in thickness. An XAD experiment was carried out near the Fe-*K* absorption edge (E = 7112 eV) with the κ-type six-circle diffractometer installed on beamline **BL14B1**. The X-rays were monochromatized by a Si(111) double-crystal system. The XAD experiment is one of the powerful techniques for studying materials with CO. In the present work, we have focused on a superlattice reflection (0.5, 0.5, 0.5)*p*, where *p* denotes a primitive perovskite structure. Since a structure factor for this reflection is obtained from the reported crystal structure [2] with two Fe atomic sites Fe(1) and Fe(2), we can estimate the Bragg peak intensity with the anomalous scattering factors for the reflection. If we observe the energy dispersion of such a superlattice reflection, there will be a characteristic structure on the dispersion curve, reflecting the difference between both environments of surrounding Fe(1) and Fe(2). Then, in order to study the physical picture of CO in the CFO, we have carried out the XAD measurements of the superlattice reflection, (0.5, 0.5, 0.5)*p*, for CFO thin film. In our experimental geometry, the incident synchrotron beam was polarized perpendicular to the scattering plane (σ) and the diffracted beam was detected without regarding the polarization (i.e., $\sigma' + \pi'$).

Figure 2 shows the energy dependence of the XAD intensity of the (0.5, 0.5, 0.5)*p* reflection with two different azimuthal angles observed at 150 K. The anomalous diffraction intensity has a significant peak at $E \approx 7124$ eV. The antiferromagnetic order (T_N = 115 K) does not appear at that temperature. Thus the structure of the XAD spectra is considered to derive

from the charge order at the Fe ions. The X-ray absorption spectrum (XAS) of the CFO thin film is shown in Fig. 2(b) and the calculated dispersion curves for the two different azimuthal angles are superposed on the observed XAD curve in Fig. 2(a). Generally, the structure factor of reflections with contributions from ions including electrons with a local anisotropy, such as Fe ions in CFO, should be treated as a tensor and show the azimuthal angle dependence. In the present case, however, the dispersion curves are almost identical. This is reasonably supported by the calculation which expects that azimuthal dependence would not appear in the reflection, as shown in the inset of Fig. 2(b), due to the relatively large Thomson scattering term and our optical configuration where the diffracted beam is collected without polarization. The calculated dispersion of the XAD intensity seems well fitted to the experimentally obtained curve. The procedure of the calculation is briefly explained as follows.

The first-principles electronic structure calculation is performed for the antiferromagnetic CFO in the low-temperature phase with the reported crystal structure data [2]. The full-potential linearized augmented-plane-wave method is employed with the LDA-*U* scheme [4]: U_{eff} = 2 eV for the Fe 3*d* orbital. The theoretical curves in the figure were obtained by calculating the (1*s* - 4*p*) dipole-transition amplitude using the Fe 4*p* states. The calculation scheme was established by Takahashi and Igarashi [5]. The CO state is characterized by the hybridization between the Fe 3*d* orbital and the O 2*p* orbital. We show a remarkable feature that is, the total numbers of 3*d* electrons are almost the same for Fe(1) ~ Fe^{+5} and Fe(2) ~ Fe^{+3}, as shown in Table I, where Fe 3*d* electron numbers in the muffin-tin spheres of Fe(1) and Fe(2) are tabulated. Thus, we have a picture for the CO state similar to the oxygen hole scenario in which the 3*d* electron number at the Fe site is fixed at 5, while the change of the electron number is attributed to the oxygen hole. Our picture, however, asserts that the Fe 3*d* electron number is larger than 5 and that the minority-spin 3*d* orbital is also partially occupied; thus, the Fe magnetic moment is significantly reduced from 5 μ_B. This reduction is also observed by the neutron scattering measurement: 2.5 μ_B for Fe(1) and 3.5 μ_B for Fe(2) [2]. The magnetic moments are also consistent with the result of the Mössbauer experiment. Every O atom is a common neighbor on Fe(1) and Fe(2); the charge at the O site is, therefore, unchanged by the CO transition.

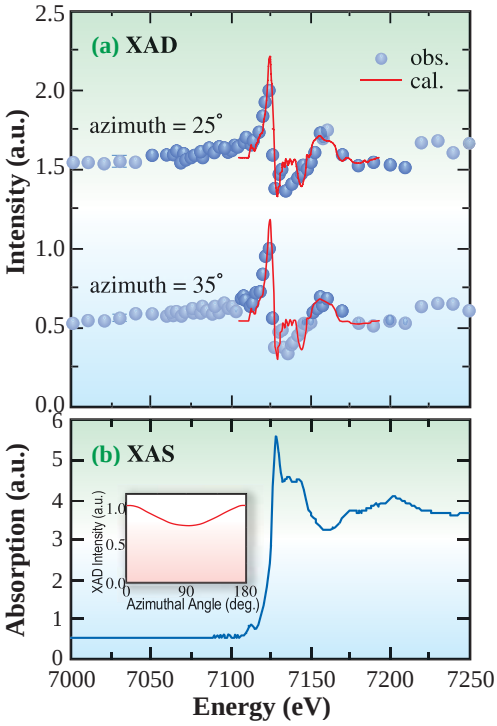

Fig. 2. Energy dependence of **(a)** the intensity of (0.5, 0.5, 0.5)*p* with the filled circles for the azimuthal angles of 25° and 35° at 150 K, and **(b)** the absorption with the solid line at 300 K, near the Fe *K* edge. A typical error of the intensity is represented only for the point of 7030 eV. The solid lines in (a) show the calculated dispersion curve as described in the text. Inset in **(b)** shows a calculated azimuthal angle dependence of the XAD intensity at 7124 eV.

Table I. Numbers of 3*d* electrons and magnetic moments for the two iron sites in $CaFeO_3$.

Site	*Electron number*			*Magnetic moment* / μ_B
	Up	Down	Total	
Fe(1)	4.18	1.41	5.59	2.77
Fe(2)	4.62	0.93	5.55	3.69
Average	4.40	1.17	5.57	3.23

T. Akao[a], J. Mizuki[b] and N. Hamada[c]

(a) Faculty of Engineering, Tottori University
(b) SPring-8 / JAERI
(c) Faculty of Science and Technology, Science University of Tokyo

E-mail: akao@mech.tottori-u.ac.jp

References

[1] M. Takano *et al.*: Mater. Res. Bull. **12** (1977) 923.
[2] P. M. Woodward *et al.*: Phys. Rev. B **62** (2000) 844.
[3] T. Akao, Y. Azuma, M. Usuda, Y. Nishihata, J. Mizuki, N. Hamada, N. Hayashi, T. Terashima and M. Takano: Phys. Rev. Lett. **91** (2003) 156405.
[4] I. Solovyev *et al.*: Phys. Rev. B **53** (1996) 7158.
[5] M. Takahashi and J. Igarashi: Phys. Rev. B **64** (2001) 075110.

Structural Study of Relaxor-like Behavior in the Organic Two-Dimensional Metal λ-$(BETS)_2FeCl_4$

The two-dimensional conductor λ-$(BETS)_2FeCl_4$ has attracted wide interests because it exhibits unique π–d interaction effects[1]. This compound has a layered structure consisting of bis(ethylendithio) tetraselenafulvalene [abbreviated as BETS] organic donor layers and $FeCl_4^-$ acceptor layers as shown in Fig. 1(a). Accordingly, from the simple band calculation disregarding interactions between electrons, the nature of a two-dimensional metal is expected. In fact, its dc conductivity shows a metallic behavior below 100 K to 8 K. However, this compound undergoes a metal-insulator transition at 8 K (T_{MI}) as shown in Fig. 2(a). The ground state below T_{MI} is an antiferromagnetic insulator. It is in contrast with a superconducting state of the isostructural λ-$(BETS)_2GaCl_4$ salt without any metal-insulator transition. This difference indicates the importance of the strong interactions between π electron on BETS and 3*d* electron (S = 5/2) on $FeCl_4^-$. Furthermore, by a microwave response experiment, a peculiar ferroelectric-relaxor-like behavior of the real part of dielectric function ε_1^c was recently found below T_{FM} (= 70 K) above T_{MI} for λ-$(BETS)_2FeCl_4$ despite of the metallic behavior of dc conductivity as shown in Fig. 2(b) [2]. Then, ε_1^c decreases steeply at T_{MI}. These anomalies seem to indicate a possible structural change at low temperature. However, no evidence of such structural change has been observed, partly because of the difficulty of experiments, in particular, high-resolution diffraction at very low temperature. Thus, the possibility of structural change at low temperature has been ignored so far. The aim of this work is to examine the possible structural change of λ-$(BETS)_2FeCl_4$ at low temperature, and to clarify the peculiar behavior of the anomalous metallic phase.

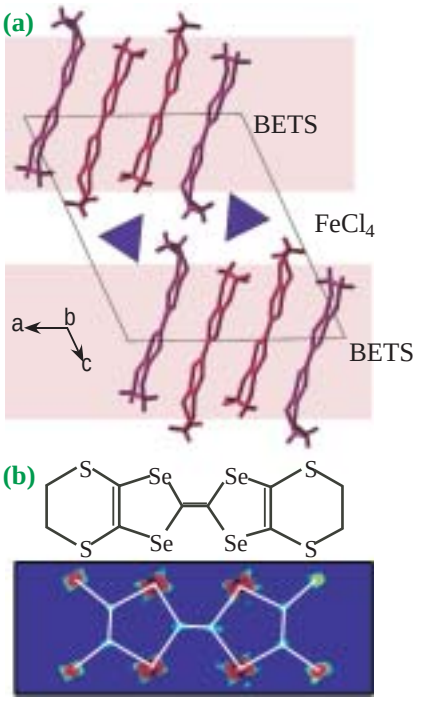

Fig. 1. **(a)** Crystal structure of λ-(BETS)$FeCl_4$. **(b)** Electron density map of the molecular plane of BETS at 20 K. Terminal ethylenes are not on this plane.

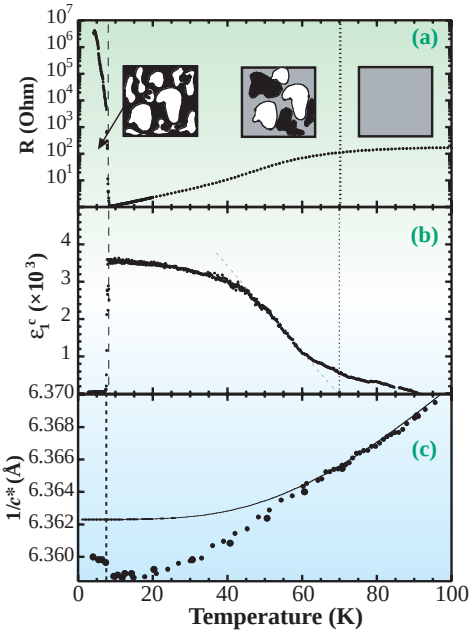

Fig. 2. **(a)** Temperature dependence of resistivity. Inset: Schematic figures of the domain structure. **(b)** Dielectric function ε_1^c[2]. **(c)** Temperature dependence of the lattice parameter 1/*c** measured with an ordinal resolution [3].

All measurements were performed at beamline **BL02B1**. The X-ray beam was tuned to 12.5 keV to avoid the absorption edge of Se atoms in the BETS molecule. First, to perform crystal structure analysis, we obtained oscillation photographs at 20 K (the lowest temperature limit of the instrument) using a vacuum camera with an imaging plate system [3]. At T_{FM} > T = 20 K > T_{MI}, no satellite reflection nor diffuse scattering was found. The reliable factor R = 5%. Compared with the structures at 90 K and 300 K, all atomic positions at 20 K are almost the same. Only small anomalies are found in an electron density map

as shown Fig. 1(b). We can see unique deformations around Se and S atoms in BETS. We shall return to this point later.

Secondly, to detect a small structural change, we investigated the detailed peak profile of the Bragg reflection. A Huber 4-circled diffractometer equipped with a cryostat (Iwatani HE05) down to 4 K was used for this experiment. We focused on the (0 0 7) Bragg reflection, because the large cryostat on the diffractometer limited the χ angle to 30° - 110°. The (0 0 7) is the observable highest angle Bragg reflection in the c^* direction. Figure 2(c) shows the temperature dependence of the $1/c^*$. The $1/c^*$ corresponds to the so-called d-spacing of the c-plane, but is not the same as the c since the unit cell is triclinic. We can see a discontinuous expansion about 0.0008 Å at T_{MI} [3]. This discontinuity indicates the nature of a first-order structural phase transition at T_{MI}. On the other hand, no clear anomaly was found around T_{FM}. What we can only see is the deviation from the fitting curve based on the Debye model shown with the solid line in Fig. 2(c). Thus, to reveal more details, we measured again the peak profiles with much higher resolution [4]. By a 3D map scan for the peak of the (0 0 7) reflection, we found a small peak splitting. The amount of splitting reached $0.017\,a^* - 0.010\,b^* + 0.002\,c^*$. Such small splitting can only be observed with the high resolution. Figure 3 shows the temperature variation of the peak profile along this direction. At 100 K, the peak has a shoulder at the lower angle side. With decreasing temperature, this shoulder developed into a peak, and became sharper as opposed to the higher angle peak that became broader. Below T_{MI}, only a single broad peak was observed. Each of the two peaks has a different d^* value. Therefore, the coexistence of two kinds of crystals was indicated. We conjecture the coexistence of ferroelectric (or antiferroelectric) and paraelectric region sat $T_{FM} > T > T_{MI}$ to interpret the complicated peak profiles mentioned above. This heterogeneous phase is responsible for the anomalous dielectric enhancement similar to a relaxor in the anomalous metallic phase.

We can now consider the anomalous electron density distribution at 20 K. These anomalies may be a circumstantial evidence of the heterogeneous phase, because these anomalies can be considered as an artificial result of averaging the heterogeneous structure. Schematic inset figures in Fig. 2(a) illustrate the temperature variation of the ferroelectric (or antiferroelectric) regions and the paraelectric regions. In the inset figures, both black and white areas denote

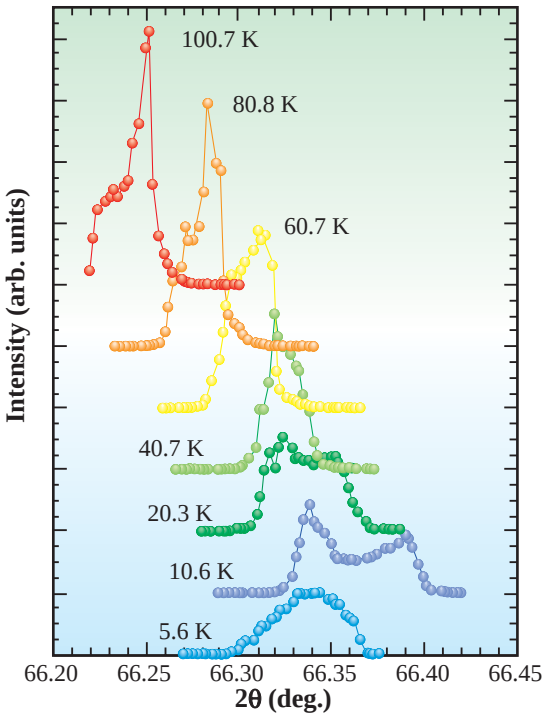

Fig. 3. Peak profiles of the (0 0 7) Bragg reflection measured with high resolution. Scan direction is parallel to $0.017\,a^* - 0.010\,b^* + 0.002\,c^*$ [4].

ferroelectric domains (or antiphase domains in the antiferroelectric region), andthe gray area is a paraelectric region. Above T_{FM}, the crystal is as homogeneous as that in the paraelectric state. In the temperature region of $T_{FM} > T > T_{MI}$, it takes a heterogeneous structure. Below T_{MI}, the crystal is dominated by the ferroelectric (or antiferroelectric) state. However, the detailed crystal structure below T_{MI} is still left unclear, and should be revealed to clarify the origin of spontaneous polarization and relation to the π-d interaction.

Masashi Watanabe, Satoshi Komiyama and Yukio Noda

Institute of Multidisciplinary Research for Advanced Materials (IMRAM), Tohoku University

E-mail: m-wat@tagen.tohoku.ac.jp

References

[1] H. Kobayashi *et al.*: Synth. Met. **70** (1995) 867.
[2] H. Matsui *et al.*: J. Phys. Soc. Jpn. **70** (2001) 2501.
[3] M. Watanabe, S. Komiyama, Y. Noda, E. Negishi and N. Toyota: J. Phys. Soc. Jpn. **72** (2003) 452.
[4] S. Komiyama *et al.*: submitted to J. Phys. Soc. Jpn.

Congruent Melting of GaN at High Pressures

Gallium nitride (GaN) is a very important material in optoelectronic devices for blue light-emitting diodes and lasers [1]. These devices are usually fabricated by epitaxial growth on sapphire (Al_2O_3) substrates because large GaN single crystals are unavailable. There is a large mismatch in the lattice constants of sapphire and GaN, which causes high-density dislocations in the deposited layer and is a major obstacle for improving device quality. Hence, the large single crystals of GaN suitable for substrates are strongly desired. However, such single crystals are difficult to grow because GaN usually decomposes into Ga and N_2 before melting at ambient pressure. Several studies, such as those involving hydride vapor phase epitaxy [2], Na flux method [3], and the absorption of high-pressure N_2 gas to a Ga melt [4], have attempted to alleviate this problem, but have all been unsuccessful in growing large single crystals suitable for the substrates of optoelectronic devices. If high pressure is effective in suppressing the decomposition of GaN at high temperatures, a new method for the single crystal growth of GaN is expected to be developed. In order to clarify the decomposition and melting behaviors of GaN under high pressures and temperatures, *in situ* X-ray diffraction experiments were carried out. The congruent melting of GaN, which occurred above 6.0 GPa and 2215°C, was confirmed for the first time.

The experiments were performed using a multi-anvil high-pressure apparatus installed on beamline **BL14B1**. The pressure was initially increased at room temperature and then the temperature was increased under a constant applied load. The *in situ* powder X-ray diffraction profiles of GaN were obtained for each pressure/temperature condition by the energy-dispersive method using a white synchrotron radiation beam.

Figure 1 shows the variations in the X-ray diffraction profiles as the temperature increased under high pressures [5]. At 2.0 GPa (a), GaN decomposed.

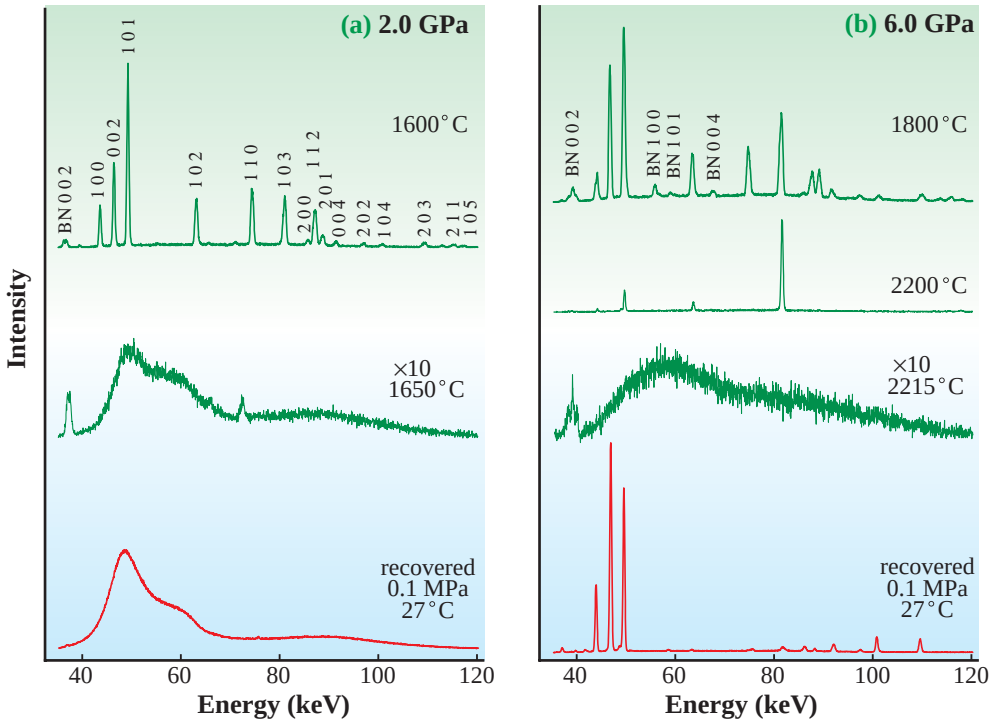

Fig. 1. A series of X-ray diffraction profiles of GaN as the temperature increased at 2.0 GPa **(a)** and 6.0 GPa **(b)**. At 2.0 GPa, GaN decomposed and then Ga was formed at 1650°C. Ga metal was recovered under ambient conditions. In contrast, at 6.0 GPa, the sample melted congruently at 2215°C and it crystallized to the wurtzite GaN as the temperature decreased [5].

The sample maintained its original wurtzite structure up to 1600°C (additional peaks from the BN capsule are also shown). At 1650°C, all sharp peaks from GaN completely disappeared and a continuous broad diffraction profile was observed, which indicates that GaN completely decomposed and a Ga melt formed. On the other hand, GaN melted congruently at 6.0 GPa (b). Although an anomalous variation in the peak intensity occurred and some peaks were unobservable due to the grain growth, the crystal phase of GaN was maintained up to 2200°C. At 2215°C, all the sharp peaks disappeared and a broad diffraction profile appeared. In this profile, the shape and energy of the first sharp diffraction peak were significantly different from those of Ga melt, which suggests that GaN congruently melted at this temperature. After melting was confirmed, turning off the supplied power to the furnace rapidly decreased the temperature and then the pressure was released. The diffraction pattern of the recovered sample was obtained under ambient conditions and showed that the sample was a polycrystal with a wurtzite structure. This indicates that, unlike the case at 2.0 GPa, the melt formed at 6.0 GPa crystallized to the original structure when the temperature was decreased.

The pressure-temperature diagram (Fig. 2) summarizes the decomposition and melting behaviors of GaN. At pressures less than 5.5 GPa, GaN decomposed into Ga and N_2 and the decomposition temperature almost linearly increased with pressure (solid circles). In contrast, at pressures higher than 6.0 GPa, congruent melting occurred at around 2220°C (solid triangles). This phase diagram clearly shows that the decomposition temperature rapidly increases with pressure, while the pressure dependence of the melting temperature is negligible. Consequently, the decomposition temperature exceeds the melting temperature at around 6.0 GPa and congruent melting occurs at higher pressures. Clasius-Clapeyron's equation, $dT/dP=\Delta V/\Delta S$, indicates that the volume change during melting or solidification must be very small because the slope of the melting line is almost negligible.

The present results have great potential in providing high-quality bulk single crystals of GaN by slow cooling of stoichiometric melt of GaN under high pressures. Single crystals of GaN with a diameter of 100 μm have already been obtained successfully by this method using a small high-pressure apparatus at SPring-8. By applying the established high-pressure diamond synthesis technology, the growth of much larger single crystals is expected.

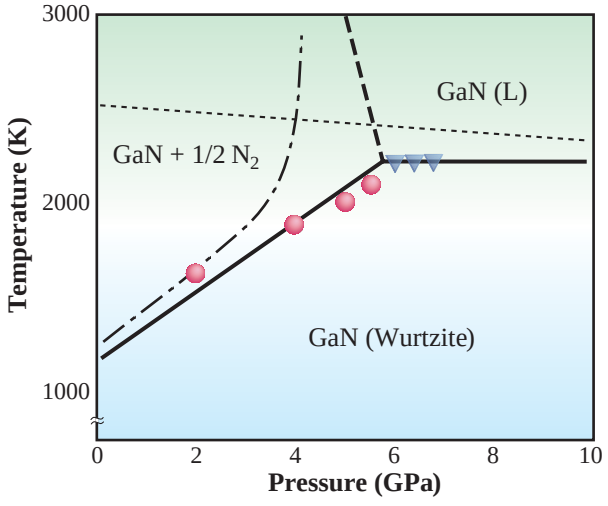

Fig. 2. The phase diagram of GaN under high pressure and temperature. Solid circles and triangles denote the pressure/temperature conditions under which GaN decomposed and congruent melting occurred, respectively. The dash line is a hypothetical phase boundary between Ga+1/2 N_2 and GaN (liquid) [5].

Wataru Utsumi

SPring-8 / JAERI

E-mail: utsumi@spring8.or.jp

References

[1] S. Nakamura *et al.*: J. Appl. Phys. **76** (1994) 8189.
[2] H.P. Maruska and J.J. Tietjen: Appl. Phys. Lett. **15** (1969) 327.
[3]H. Yamane *et al.*: Chem. Mater. **9** (1997) 413.
[4] S. Porowski: J. Cryst. Growth **166** (1996) 583.
[5] W. Utsumi, H. Saitoh, H. Kaneko, T. Watanuki, K. Aoki and O. Shimomura: Nature Materials **2** (2003) 735.

Encapsulation of Molecules in Single-Walled Carbon Nanotube - A Novel Nanodevice Material -

Single-walled carbon nanotube (SWNT) is the most promising material for molecular electronics because of its unique structural and electronic properties. Molecular electronics is an emerging area in which the goal is using molecular materials as core device components. An advantage of molecular electronics is obviously the small size of the core components, surpassing structures attainable by top-down lithography, and could therefore be essential for miniaturization. SWNTs are wires with molecular-scale diameters (~1 nm), and individual semiconducting SWNTs have been actively explored in order to construct nanotube field-effect transistors (FETs). For the further advancement of molecular electronics, the ability to obtain both p- and n-type FETs is important for constructing complementary electronics whose performance is better (for example, low power consumption) than that of devices consisting of unipolar p- or n-type transistors. SWNT-FETs built from as-grown tubes are found to be unipolar p-type. Several doping methods have been developed for nanotubes, although stability in air was not sufficient for the n-type doping.

On the other hand, due to their size and geometry, SWNTs also provide a unique opportunity for nanoscale engineering of novel one-dimensional systems, created by self-assembly of molecules inside the SWNT's hollow core. It has been experimentally shown that fullerenes can be inserted into SWNTs, forming a peapod-like structure [1]. The composite nature of peapod materials raises an exciting possibility of a nanoscale material having a tunable structure that can be tailored to a particular electronic functionality. In this work, we clarify the structure of organics/SWNT compounds, and investigate the charge transfer between SWNT and organic molecules. Since organic molecules predominantly occupy the inner space of SWNTs, the doping state is rather stable in air.

SWNTs were manufactured by laser vaporization of carbon rods doped with Co/Ni in an atmosphere of Ar and subsequently purified with H_2O_2, HCl and NaOH [2]. SWNTs were reacted with vapor of organic molecules, which are shown in Fig. 1, in a manner similar to the case of the C_{60}-peapod [3]. For structural characterization, synchrotron X-ray powder diffraction data were obtained at room temperature at beamline **BL02B2**. Figure 2 shows typical diffraction profiles for pristine, TCNQ-doped and TMTSF-doped SWNT materials. The most obvious difference between doped and undoped SWNTs is the strong reduction of peak intensity at approximately Q ~ 0.4 ($Å^{-1}$), which is indexed as (10) reflection. Such a behavior provides evidence of encapsulation of organic molecules inside SWNTs, as observed in several peapod materials and gas-adsorbed SWNTs [4].

Intensity reduction of the (10) peak allows us to estimate the chemical concentration ratio of encapsulated organic molecules to carbon atoms of SWNT. First, the parameters of pristine SWNTs were determined so as to reproduce the observed diffraction pattern shown in Fig. 2(a), taking the Gaussian distribution of the tube diameter into account. By using the obtained parameters, the intensity distributions of the diffraction pattern for the organic/SWNT compounds were well accounted for by inserting an uniform rod of charge with the diameter of 7 Å inside the tubes. From the density of uniform charge, the carbon number of SWNT per organic

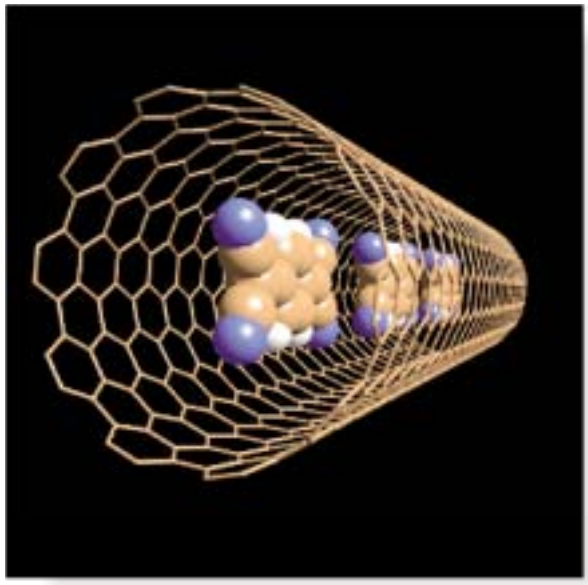

Fig. 1. Single walled carbon nanotube encapsulating TCNQ molecules.

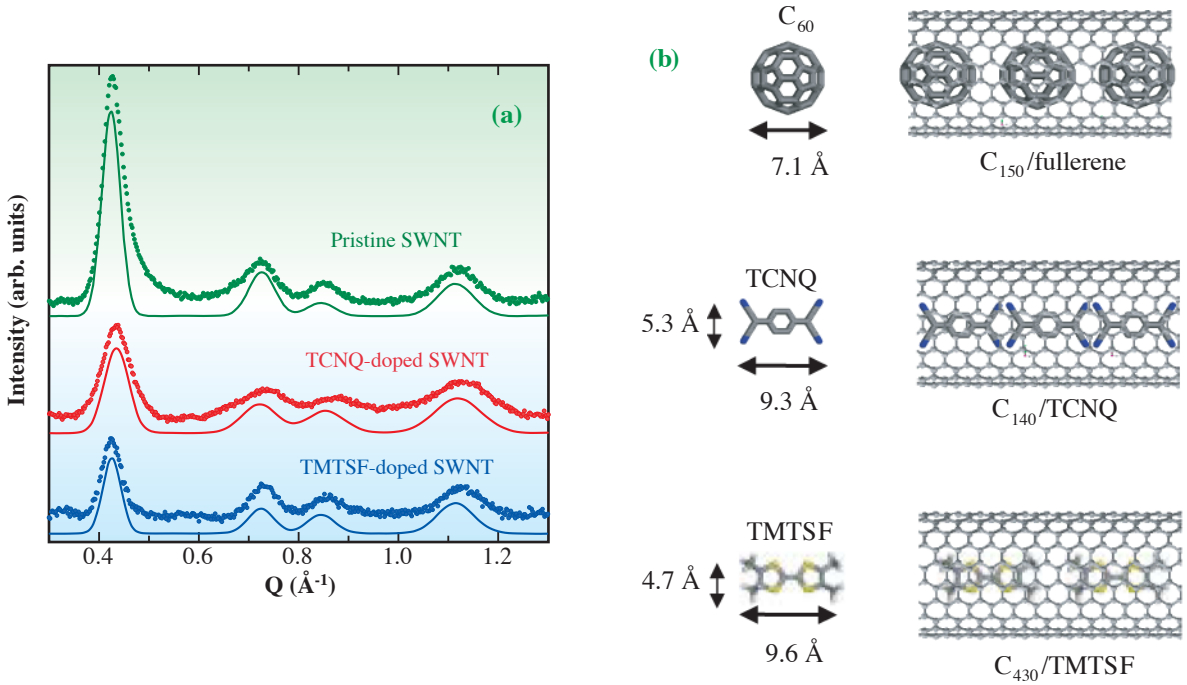

Fig. 2. X-ray diffraction pattern and a schematic structure model of organics/SWNT materials. **(a)** Observed and simulated X-ray diffraction patterns of pristine, TCNQ-reacted and TYMTSF-reacted SWNT. Dotted and solid lines represent observed and simulated patterns, respectively. **(b)** Schematic stacking patterns of C_{60}, TCNQ and TMTSF molecules inside (10, 10) SWNTs.

molecule was derived as $C_{140(10)}$/TCNQ and $C_{430(10)}$/TMTSF. A possible configuration of encapsulated organic molecules inside (10, 10) SWNT is described in Fig. 2(b) and compared with that of C_{60} peapods. The intensity reduction of the (10) peak was observed in all organics/SWNT compounds investigated (Fig. 1). Doping properties have been investigated by Raman and optical absorption spectroscopy. Both measurements clearly provide direct evidence of the charge transfer between SWNTs and organic molecules in SWNTs doped with TCNQ, F4TCNQ, TDAE, TTF, and TMTSF, while no appreciable change was detected in SWNTs doped with C_{60}, anthracene, tetracene, and pentacene [3]. TDAE-, TTF- and TMTSF-doped SWNTs were n-type semiconductors. We have investigated the air stability of organics/SWNT compounds through measurements before and after exposure to air. Spectra were unchanged for one week under ambient conditions, except for TDAE/SWNT compounds, providing evidence of air stability of organics/SWNT materials. Encapsulation of organic molecules in SWNTs is one of the possible reasons for the stability, since the outer wall of SWNTs will protect the molecules from oxygen.

In summary, we have synthesized SWNTs encapsulating organic molecules, and investigated the charge transfer between SWNTs and organic molecules. Since organic molecules predominantly occupy the inner space of SWNTs, the doping state is rather stable in air.

Taishi Takenobu[a,b], Takumi Takano[a] and Yoshihiro Iwasa[a,b]

(a) Institute for Materials Research, Tohoku University
(b) CREST, Japan Science and Technology Agency

E-mail: takenobu@imr.tohoku.ac.jp

References

[1] J. Lee *et al.*: Nature **415** (2002) 1005.
[2] M. Shiraishi *et al.*: Chem. Phys. Lett. **358** (2002) 213.
[3] T. Takenobu, T. Takano, M. Shiraishi, Y. Murakami, M. Ata, H. Kataura, Y. Achiba and Y. Iwasa: Nature Materials **2** (2003) 683.
[4] Y. Maniwa *et al.*: Jpn. J. Appl. Phys. **38** (1999) L668.

Reciprocal-lattice Space Imaging of X-ray Intensities Diffracted from Nanowires

Structural investigation is essential for development of nanotechnological materials such as nanoelectronics and nanophotonics. X-ray diffraction/scattering is one of the most promising non-destructive methods for observing atomic-scale structures and morphology of the nanomaterials. A nanowire structure on a device surface is particularly interesting since this wire could be one of the minimum parts of electrical devices. The conventional approach for determining such a structure maps X-ray diffraction/scattering intensities under Bragg conditions in a reciprocal-lattice space. This provides quantitative information on the strain in the nanowires [1]. One of its disadvantages is its being time-consuming. In order to establish a rapid characterization method, we have developed an "obvious-at-a-glance analysis" technique for nanocrystalline structures [2]. By taking advantage of high-energy and brilliant X-rays of SPring-8, rapid measurements are achieved by mapping many diffracted intensities under Bragg conditions in the reciprocal-lattice space simultaneously. The present method uses many sets of limited diffracted intensities around a Bragg point and coaxes forth specific structural information such as crystallographic domain sizes. In this work, the method was successfully applied to observe sheet-shape diffraction emanating from ultrathin NiO wires and scattering arising from the 20 nm periodicity of stripes of nanowires.

Specimens had the stripes of ultrathin NiO nanowires deposited on an ultrasmooth sapphire (0001) surface with two-atomic-plane step edges at Yoshimoto Res. Group, Tokyo Institute of Technology [3]. We used two samples that were similar except for the nanowires' orientations; in addition, both substrates had a miscut of approximately 0.1°. Sample A had nanowires almost perpendicular to the sapphire [1 0 $\bar{1}$ 0] direction; and sample B had nanowires nearly parallel to the [1 0 $\bar{1}$ 0] direction. The coordination is expressed using a hexagonal symmetry. The samples were grown using a pulsed laser ablation method. The surface morphology of sample A was observed by atomic force microscopy (AFM) in air (Fig. 1). The nanowires were found to be of the order of mm in length, which was surprisingly long, by scrutinizing hundreds of successive AFM images (scan size 10 μm × 10 μm, not shown here). The images indicate that the nanowires were grown along step edges and were approximately 20 nm in width and 0.5 nm (two atomic planes) in height. The density was a nanowire per 50 nm.

Here, the nanowires that we are interested in are very thin, narrow, and long. If the wires are 1D crystalline, the scattering pattern or diffraction domain (the Fourier transform) in the reciprocal-lattice space shows sheets (which are perpendicular to the wires and whose diameters are inversely proportional to the width sof the wires). Let us assume that the sheets elongate along the sample surface normal from bulk-crystal Bragg points due to a surface truncation effect. The Ewald sphere can simultaneously intersect some of the sheets accordingly (Fig. 2). We used possibly high-energy X-rays to excite many diffracted X-rays.

Measurements were performed at the undulator

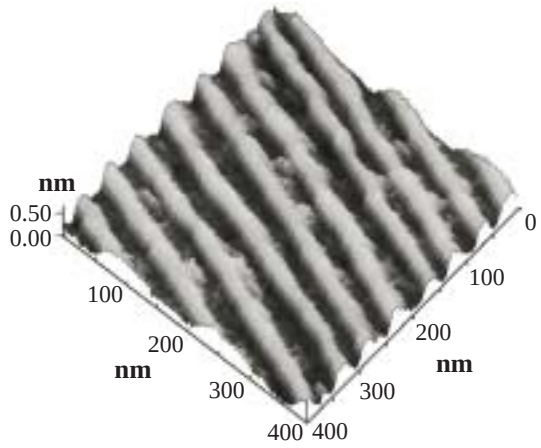

Fig. 1. AFM image (0.4 μm × 0.4 μm) of the nanowires grown on an ultrasmooth sapphire surface of sample A.

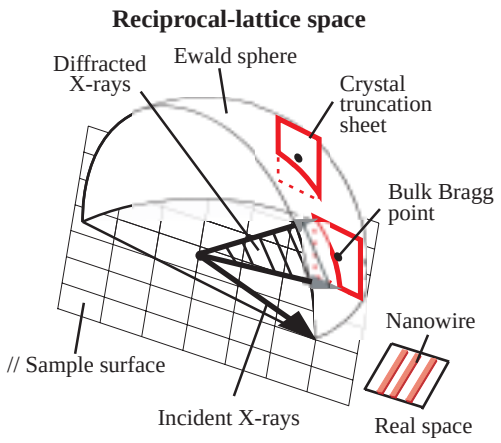

Fig. 2. Geometry of grazing-angle high-energy X-ray scattering.

beamline **BL13XU** for surface and interface structure determination [4]. The experimental setup included a pair of slits for limiting the beam size to 0.1 mm × 0.1 mm and an X-ray imaging plate for recording diffraction. An X-ray beam with a photon energy of 25 keV was incident on the sample at an angle of around 0.1°. The typical exposure time was 10 min. A similar experimental arrangement was used for surface structural observation by Hong *et al.* [5]. They utilized 20 keV X rays and a CCD camera to detect diffracted X-rays; their sample Si was located in ultrahigh vacuum.

Figure 3 shows the diffraction pattern recorded when X rays were incident almost perpendicular to the NiO nanowires. Diffraction images (in rectangles) pointed down at a direct beam position. When X-rays were incident nearly parallel to the nanowires, diffraction images looked like circular arcs round the direct beam position (not shown here). Blunt or dim images were produced by X-ray thermal diffuse scattering of the substrate crystal. We indexed crystal truncation sheets using a conventional notation expressed for crystal truncation rods. Here, the indices h and k are defined by h direction // [1 0 $\bar{1}$ 0] and k direction // [0 1 $\bar{1}$ 0], respectively. Actually, the images extend along the h and l directions; here, the closest integer h values are shown. The diffraction images have intensity profiles (for example, the inset in Fig. 3). From the geometrical consideration in the reciprocal-lattice space, the full-width-at-half-maximum (FWHM) crystallographic domain sizes across the nanowires are 7.5 and 7.2 nm for samples A and B, respectively, obtained using the in-plane FWHM of the intensity profile. The average nanowire-nanowire spacing of 46 nm for sample A was estimated from the peak-to-peak distance. The value is nearly equal to that (~ 50 nm) obtained using the AFM image. By further analysis of the diffraction images, the following structural and morphological information could be obtained: the straightness of the nanowires (in other words, the distribution of the nanowire width), spatial distribution of the nanowires, and atomic-scale roughness of the side surface of the wires.

The method described here will allow us to determine the structures of the nanowires buried in the interfaces between a thin film and a crystalline substrate. Furthermore, it could be applied to structure analysis during growth of nanowires and to rapid observation of a surface phase transition in any atmosphere.

In summary, we demonstrated the feasibility of a new X-ray scattering method for structure analysis of nanowires in air using a combination of grazing-incidence surface scattering and high-energy synchrotron X-rays. The size of X-ray crystalline domains in the nanowires was evaluated. We easily determined whether the nanowires are crystalline or amorphous by grazing-angle high energy X-ray scattering. The method has also been proven feasible for rapid confirmation of the crystallographic orientation and epitaxy of the nanowires.

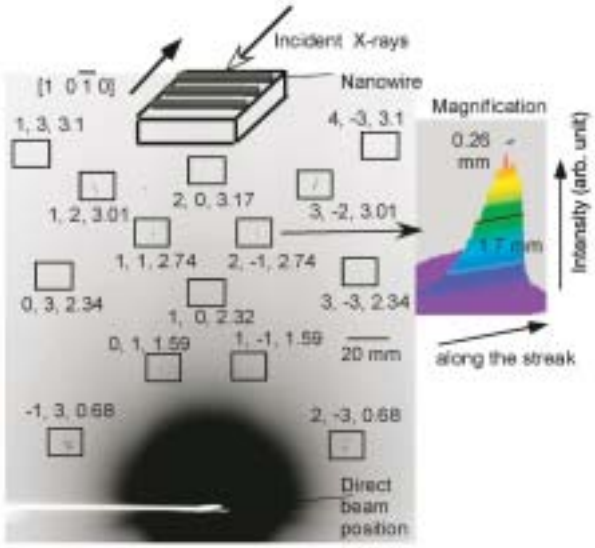

Fig. 3. Pattern diffracted from nanowires nearly perpendicular to the incident X-ray beam. The distance from sample A to the imaging plate (camera length) was 190 mm. A pair of of numbers h, k stands for an index of a crystal truncation sheet. The lengths used for unit vectors **a** (// [1 0 $\bar{1}$ 0]), **b** (// [0 1 $\bar{1}$ 0]), and **c** (// [0 0 0 1] were 0.476, 0.476, and 0.421 nm, respectively.

Osami Sakata

SPring-8 / JASRI

E-mail: o-sakata@spring8.or.jp

References

[1] I.K. Robinson *et al.*: Phys. Rev. Lett. **88** (2002) 096104-1.
[2] O. Sakata, M. Takata, H. Suematsu, A. Matsuda, S. Akiba, A. Sasaki and M. Yoshimoto: Appl. Phys. Lett. **84** (2004) 4239.
[3] M. Yoshimoto *et al.*: Appl. Phys. Lett. **67** (1995) 2615.
[4] O. Sakata *et al.*: Surface Rev. Lett. **10** (2003) 543.
[5] H. Hong *et at.*: Rev. Sci. Instrum. **71** (2000) 3132.

Microanalysis for Polymer Materials by X-ray Microscopes

Polymer fibers have excellent mechanical properties and are light in spite of their flexibility, so they are widely used as clothing, nonwoven fabric, reinforced fiber for advanced composite materials and so on. Generally, polymer fibers are obtained from a polymer solution or a molten polymer by the spinning method at above the melting point of the polymer. This process would form a gradual structure in the radial direction of a polymer fiber, because solidification occurs from the outer region of the polymer fiber during coagulation in poor solvents or during the cooling process. Therefore, a polymer fiber has different microstructures between the outer region and the inner region. The unique microstructure of a polymer fiber is called the skin/core structure.

Recently, with the development of microscopic processing techniques, precise measurement for the structural analysis of very small areas has become increasingly important. The X-ray diffraction method has been widely used for the structural analysis of polymer materials. The transmission electron diffraction method requires a thin sample and a high-vacuum condition. However, no special pretreatment of samples is required for the X-ray diffraction method.

An X-ray microbeam of 10 keV was obtained using a phase zone plate, which was made of tantalum at beamline **BL24XU** [1]. A rhodium-coated plane mirror was introduced in the upstream of the experimental hutch in order to eliminate higher order Bragg reflections properly for different photon energies. The focused beam size at the sample position was evaluated to be 1.1 μm (vertical) × 1.3 μm (horizontal) by the knife-edge method.

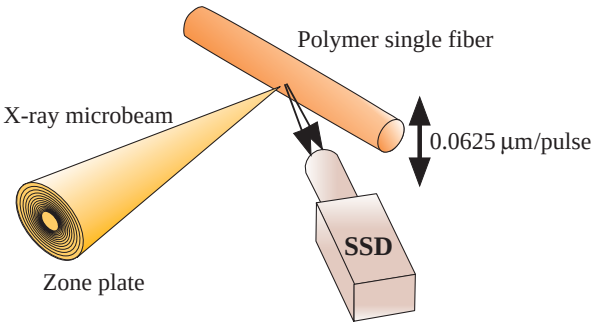

Fig. 1. Schematic representation of the X-ray microdiffraction method for the polymer single fiber. The sample holder was fixed on the high-precision sample stage and the fiber axis was aligned in the horizontal direction.

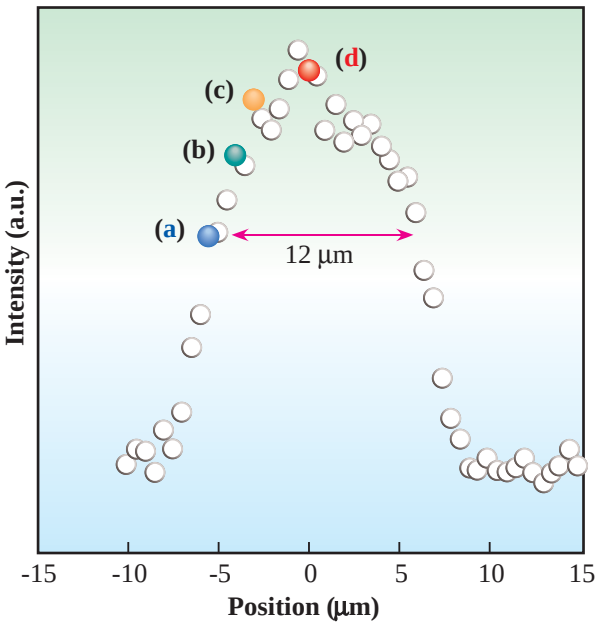

Fig. 2. Intensity profile of Thomson scattering from Kevlar[29] single fiber. Sampling steps of 0.5 μm/point were employed.

As the beam size is small, it is very important to confirm the irradiated area of the X-ray microbeam on samples. An optical microscope, which was set on the X-ray beam path, was used to align the sample position roughly. However, more precise alignment of the X-ray microbeam is very difficult using optical microscope for smaller samples such as a polymer single fiber. In this study, we proposed a novel technique by the Thomson scattering method for the precise alignment of the X-ray microbeam position as shown in Fig. 1.

Figure 2 shows the intensity profile of Thomson scattering from a Kevlar[29] single fiber (fiber diameter *ca.* 12 μm). One-dimensional scans were performed perpendicular to the fiber axis. The intensity of the Thomson scattering is proportional to the number of electrons at the regions where the X-ray penetrated the sample. With changing sample position ((a)-(d)), X-ray diffraction patterns were detected using an imaging plate as shown in Fig. 3. The X-ray exposure time was 600 s per pattern. Judging from the spot-like equatorial reflections (110 and 200 reflections), the degree of the molecular orientation of the skin region (Fig. 3(a)) is higher than that of the core region (Fig. 3(d)).

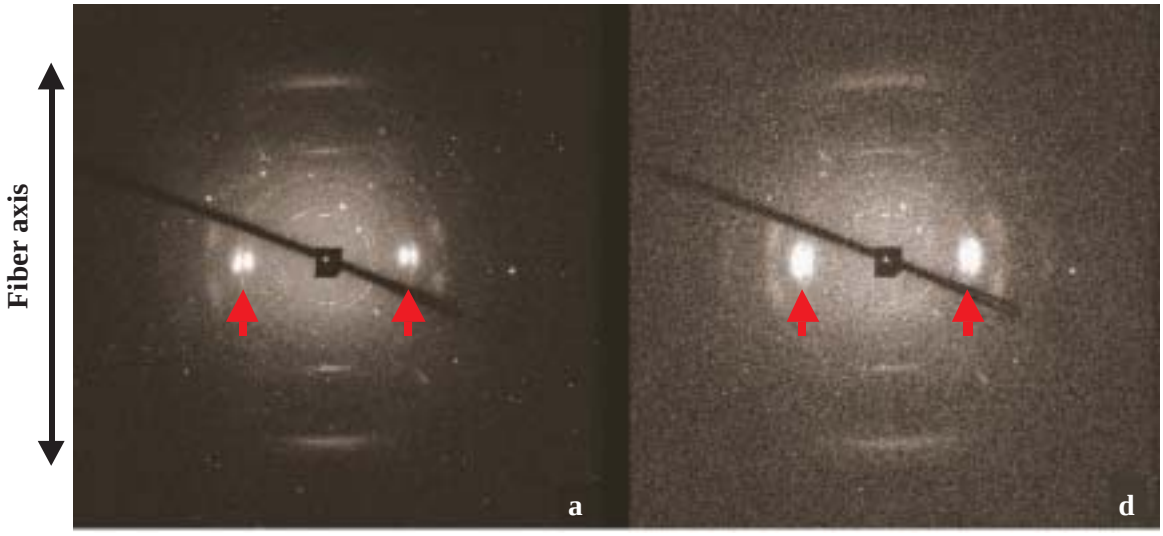

Fig. 3. X-ray fiber pattern of Kevlar[29] single fiber. **(a)** skin region and **(d)** core region.

Figure 4 shows the equatorial diffraction profiles of the Kevlar[29] single fiber at different points ((a)-(d) in Fig. 1) along the fiber axis. In the core region (d) of the single fiber, the peak intensity is $I_{110} < I_{200}$. However, they are reversed when approaching the skin region (a), that is, the peak intensity of 110 reflection gradually increased as the measurement position approached the skin layer. This implies that the b-axis of the Kevlar crystal, which is the direction of a hydrogen bond, is oriented in the radial direction of the fiber [2,3].

According to these results, the X-ray microdiffraction method demonstrated to be a powerful tool for the structural analysis of small areas for polymer materials.

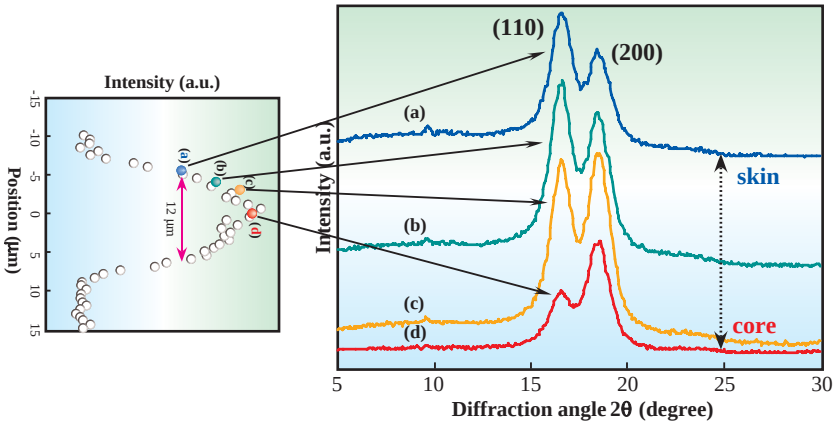

Fig. 4. Equatorial diffraction profiles of Kevlar[29] single fiber at different measurement points along the fiber axis.

Masaru Kotera[a], Takashi Nishino[b] and Yasushi Kagoshima[c]

(a) SPring-8 / JASRI
(b) Kobe University
(c) Himeji Institute of Technology University

E-mail: mkotera@spring8.or.jp

References

[1] Y. Kagoshima *et al.*: Nucl. Instrum. Meth. A **467-468** (2001) 872.
[2] M.G. Dobb *et al.*: J. Polym. Sci., Polym. Phys. Ed. **15** (1977) 2201.
[3] M. Panar *et al.*: J. Polym. Sci., Polym. Phys. Ed. **21** (1983) 4761.

Crystal Structures Studied by Stereo Atomscope

Stereo atomscope, which is realized by the combination of display-type spherical mirror analyzer (DIANA) and circularly polarized X-ray, opens a way to study three-dimensional crystal structures directly [1]. In this paper, the atomic stereo-photograph of Cu (001) single crystal, one of the typical studies of stereo atomscope, will be introduced.

The basic principle of stereo atomscope is circular dichroism in photoelectron angular distribution (PEAD), where forward focusing peak positions rotate in the same direction as that of circularly polarized X-ray electric vector (Fig. 1). The rotation is caused by the angular momentum transfer from circularly polarized X-ray to emitted photoelectrons. The azimuthal shifts of the forward focusing peaks at clockwise (cw) and counterclockwise (ccw) circularly polarized X-rays are utilized as parallax. Here, the cw and ccw circularly polarized lights are defined according to the rotation direction of the electric vector at the sample observed from behind. From the azimuthal shift formula ($\Delta = m/kR\ \sin^2\theta$) [2], the atomic distance (R) or the magnetic quantum number (m) can be obtained.

The schematic image of DIANA is shown in Fig. 2. The emitted photoelectrons of a particular kinetic energy converge to an exact focal point, and the two-dimensional angular distribution of the photoelectrons

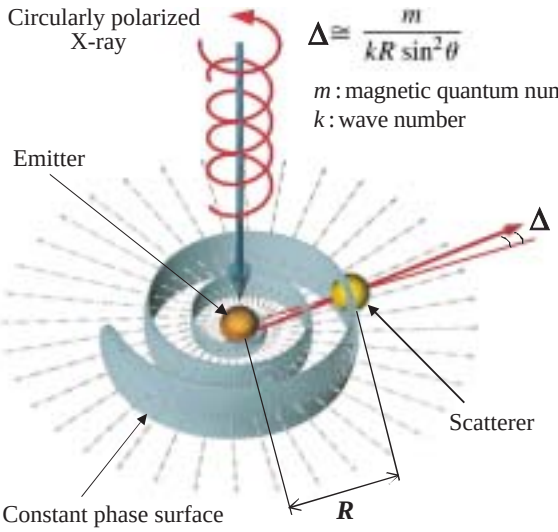

Fig. 1. Image of circularly polarized X-ray and forward focusing peak rotation. The blue strip describes the constant phase surface on which photoelectrons propagate perpendicularly.

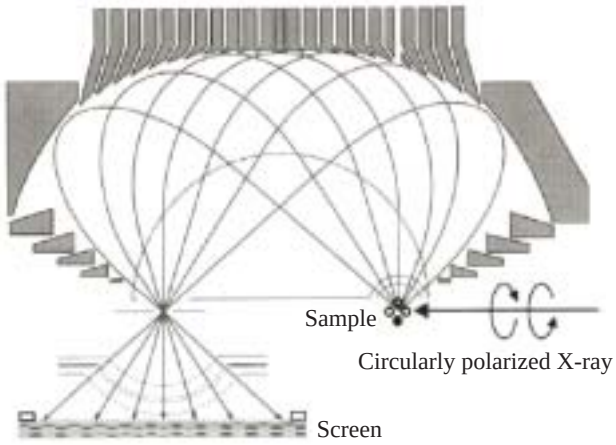

Fig. 2. Schematic image of DIANA. The emitted photoelectrons of a particular kinetic energy converge to an exact focal point.

dimensional angular distribution of the photoelectrons can be measured simultaneously without rotating the sample. The wide acceptance angle (±60°) and the distortion free angular distribution of the photoelectrons make DIANA the best analyzer for taking atomic stereo-photographs. Circularly polarized X-rays are produced at beamline **BL25SU**.

Single crystal Cu(001) was cleaned by repeated cycles of Ar bombardment and annealing. The clean surface was checked by reflective high-energy electron diffraction (RHEED). Experimental results are shown in Fig. 3. The photographs (a) and (b) show the Cu2*p* PEAD patterns taken by DIANA with a pass energy of 500 eV using the cw and ccw circularly polarized X-rays, respectively. The forward focusing peaks distribute regularly. They shift right at cw and left at ccw circularly polarized X-rays. The shift angles become smaller and the peak intensities become weaker for inner peaks, which indicates that the forward focusing peaks are caused by atoms lying in different layers. In order to understand the distribution easily, we marked the forward focusing peaks by circles with different colors. The PEAD patterns show good agreement with the simple projection (d) from the fcc crystal structure model (c) of Cu(001), where the atoms lying in different layers are distinguished by different colors.

The two PEAD patterns form the atomic stereo-photograph viewed from specific atoms. It displays

the three-dimensional atomic arrangements of four nearest layer atoms in single crystal Cu(001) along the [001] direction with a magnification of approximately 1 billion. The distorted peaks in the PEAD patterns are caused by the low transmission and inhomogeneity of retarding grids. The forward focusing peak, which should appear at the right-down position, cannot be observed because of the shadow caused by the electron gun of DIANA. The forward focusing peaks should be sharper under higher kinetic energies; however, the kinetic energies of more than 500 eV are unavailable at present due to the discharge of the analyzer.

Using atomic stereo-photography, not only the atomic stereo-photographs of one-element single crystals, but also those of compounds and intercalation compounds were obtained successfully [3,4]. The direct atomic stereo-photographs obtained by stereo atomscope without any conversion process make it possible to realize real-time observation, which will be used in understanding the dynamics of atoms. The improvements of the stereo atomscope are currently in progress for the construction of an ultimate microscope.

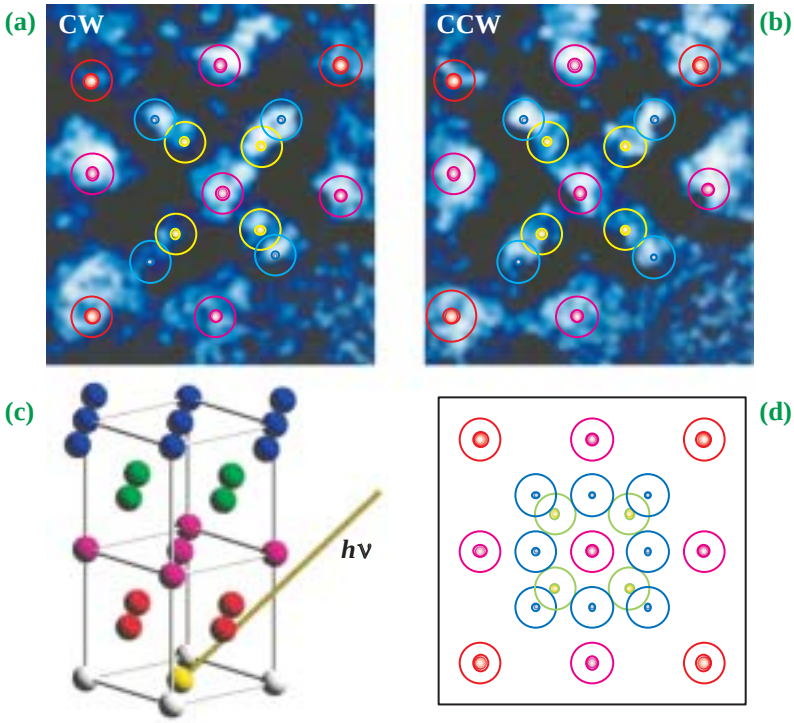

Fig. 3. **(a), (b)** Cu2*p* PEAD patterns taken by DIANA with a pass energy of 500 eV using the cw and ccw circularly polarized X-rays. **(c), (d)** fcc crystal model of Cu(001) and atomic arrangement simple projection.

FangZhun Guo[a], Fumihiko Matsui[b,c] and Hiroshi Daimon[b,c]

(a) JASRI / SPring-8
(b) Graduate School of Materials Science, Nara Institute of Science and Technology
(c) CREST, Japan Science and Technology

E-mail: fz-guo@spring8.or.jp

References

[1] H. Daimon: Phys. Rev. Lett. **86** (2001) 2034.
[2] H. Daimon *et al.*: Jpn. J. Appl. Phys. **32** (1993) L1480.
[3] F.Z. Guo *et al.*: ICESS-9 (Uppsala, June 30 - July 4, 2003).
[4] F.Z. Guo, F. Matsui, T. Matsushita and H. Daimon: Appl. Surf. Sci. (2004) - in press.

Materials Science
Electronics & Magnetism

In the field of Materials Science (Electronics and Magnetism), SPring-8 is a very useful tool from the viewpoints of X-ray diffraction, spectroscopy, Compton and inelastic scattering, imaging and so on. A variety of beamlines cover this field. Research frontiers of materials science are really being produced from SPring-8 owing not only to its high-quality light but also to the new development of experimental techniques. Recently, electronic structures including the magnetic and phonon information of a variety of materials are investigated by bulk sensitive methods. These are great achievements in the use of SPring-8.

As one of the priority research programs, the nanotechnology support program was started in 2003. This program is expected to stress the importance of Materials Science in furthering new achievements and in developing industrial applications. Some interesting projects have been proposed from this program, and new apparatus has been introduced to the beamlines at SPring-8 by the support from this program. Studies using this apparatus are also expected.

Some of the topics that appear in this issue are outstanding studies. These techniques may become more familiar and general to many users worldwide in the near future, which will also support the progress of Materials Science.

Toyohiko Kinoshita

Bulk-sensitive Photoemission on Ti-doped Sr_2RuO_4

Sr_2RuO_4 is the first layered non-cuprate perovskite found to display superconductivity ($T_c \approx 1K$) [1]. As is the case for cuprate high-temperature superconductors, the fundamental issues to be addressed here refer to the pairing mechanism, and in particular, the role of electronic correlations. While the unusual spin-triplet pairing with p-wave symmetry suggests the importance of ferromagnetic fluctuations, in experiments, mainly evidence for antiferromagnetic fluctuations was found. Recently, it was observed that the substitution of the Ru^{4+} ion by the non-magnetic d^0-ion Ti^{4+} induces local-moment magnetism, which statically orders for $Sr_2Ru_{1-x}Ti_xO_4$ with $x \geq 0.03$ [2]. This behavior was confirmed by elastic neutron scattering in which the formation of a static incommensurate spin-density wave (SDW) for $x = 0.09$ below $T_{SDW} = 25K$ [3] is observed. The formation of this static SDW upon slight Ti-doping opens the possibility to study its effects on the electronic structure from a fundamental point of view and might give an important insight into the role of antiferromagnetic fluctuations in the superconducting parent compound as well.

To elucidate these questions we performed photoemission (PE) measurements (see Fig. 1) at high photon energies using **BL25SU** to investigate both a possible change of the Fermi surface (FS) upon doping and possible effects on the low-energy electronic structure along the high-symmetry lines of the Brillouin zone (BZ).

Knowledge of the FS topology is important because it determines the manifold of possible excitations on the FS for a given momentum. If there exist two-dimensional manifolds across the FS, which can be mapped onto each other by one single vector, the respective portions of the FS are said to be nested.

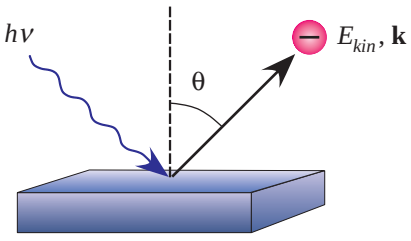

Fig. 1. Schematic of the photoemission process. Monochromatic photons kick out electrons from the surface of a solid. Due to energy and momentum conservation their kinetic energy and emission angle can be traced back to their energy and momentum in the crystal.

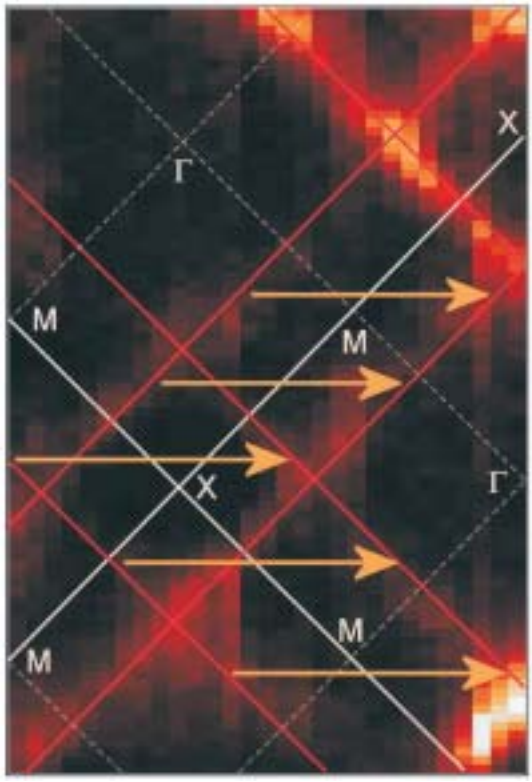

Fig. 2. FS map of $Sr_2Ru_{0.91}Ti_{0.09}O_4$. Indicated are the BZ (white lines), the underlying one-dimensional FS sheets (red lines), and the experimentally observed SDW vectors (arrows). The dashed white lines denote the irreducible parts of the BZ.

At these locations, the FS becomes intrinsically unstable and an SDW with a wavevector corresponding to the nesting vector may develop concomitant with an energy gap. Figure 2 displays an image of the FS of $Sr_2Ru_{0.91}Ti_{0.09}O_4$. Also indicated is the BZ. The arrows mark SDW vectors as experimentally observed by neutron scattering. Their starting and end points lie essentially on two mutually perpendicular pairs of FS sheets and thus give striking evidence that the SDW indeed is driven by FS nesting. They can be viewed as reflecting a hidden one dimensionality in the electronic structure. Note that the thus identified nesting vectors are also in agreement with the findings of band structure calculations. Surprisingly, the FS topology and especially the FS "volume" remain essentially unchanged in comparison with the undoped material [4], indicating that the Ti ions do not much affect the states close to the Fermi energy E_F.

If the electronic structure is not much affected right at E_F, one would nevertheless expect a relatively large

disorder potential to be induced by the Ti ions. This should be reflected by broadened structures and the lack of dispersion particularly of low-lying bands. A typical series of energy distribution curves along the high-symmetry line ΓX is shown in Fig. 3. Intriguingly, one finds sharp dispersing features over the entire valence band region, in particular at E_F, which is again comparable to the findings in the undoped compound.

Yet another important issue has to be addressed, which is a rather fundamental one and always a topic about PE spectroscopy. Since electrons strongly interact with matter, PE in general is a highly surface-sensitive technique. It is important to know this, especially in our case, since it was previously shown [5] that the undoped system, although two-dimensional in nature, exhibits a surface reconstruction which is actually also present in the Ti-doped compound as revealed by low-energy electron diffraction (not shown). This reconstruction imposes a new periodicity on the electron system at the surface, and hence, affects the electronic structure. For example, effects such as band backfolding, the occurrence of replicas of the FS sheets or even an overall change of the electronic structure may result. Indeed, all such effects were found in PE spectroscopy of the undoped system using low-energy photons of approximately 30 eV [5]. High-energy photons of about 700 eV provided by BL25SU transfer much more energy to the electrons and thus give them a significantly higher chance to escape from deeper in the sample into the vacuum. Indeed, we do not see any signs of the above-mentioned effects and thus can conclude that our data truly reflects the intrinsic bulk electronic structure. Looking at the subtle effects of the SDW with a very high resolution (and hence, inevitably low photon energies) our data is urgently needed to disentangle the surface from bulk contributions.

In summary, both the FS image and the band maps recorded by high-energy PE surprisingly indicate that the essential overall electronic structure of Sr_2RuO_4 is preserved upon slight Ti-doping. In particular, we observe sharp dispersing bands despite the large disorder due to the Ti ions. Our results are very important for deconvoluting the surface from bulk contributions if one carries on with studying the subtle effects of the SDW on the electronic structure at low photon energies. Such investigations are currently in progress.

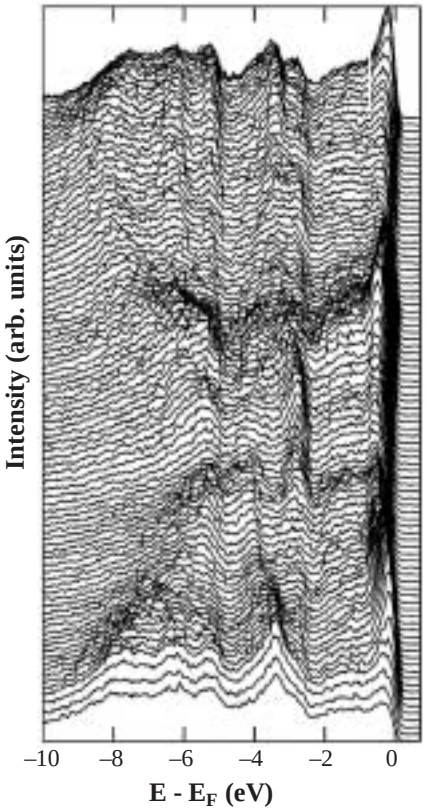

Fig. 3. EDCs along the ΓX high-symmetry line. Note the sharp dispersing features, in particular at the Fermi energy (E_F = 0).

Michael Sing[a,b*], Ralph Claessen[a] and S. Suga[b]

(a) Experimentalphysik II, Universität Augsburg, Germany
(b) Graduate School of Engineering Science, Osaka University

E-mail: sing@physik.uni-augsburg.de

**Present address* : Experimentalphysik II, Universität Augsburg, Germany

References

[1] Y. Maeno *et al.*: Nature **372** (1994) 532.
[2] N. Kikugawa and Y. Maeno: Phys. Rev. Lett. **89** (2002) 117001.
[3] M. Braden *et al.*: Phys. Rev. Lett. **88** (2002) 197002.
[4] A. Sekiyama, S. Kasai, M. Tsunekawa, Y. Ishida, M. Sing, A. Irizawa, S. Imada, T. Muro, Y. Saitoh, Y. Onuki, T. Kimura, Y. Tokura and S. Suga: to be published.
[5] A. Damascelli *et al.*: Phys. Rev. Lett. **85** (2000) 5194.

High-Resolution Hard-X-ray Photoemission Spectroscopy

Photoemission spectroscopy (PES) is a method of measuring the kinetic energy distribution of photoelectrons emitted from materials excited by monochromatic light. It gives information on bound electron states in materials; thus, it has been used extensively to study electronic structures as well as chemical bonding states [1]. Synchrotron radiation (SR) has extended the applicability of PES widely, owing to its high brilliance and energy tunability. However, conventional SR-PES, in which the excitation photon energy is usually less than 1 keV, has a fatal deficiency in detecting bulk electronic structure information. That is, because probing depth is too small, and surface sensitivity is too high due to the short inelastic-mean-free-paths (IMFPs) of the photoelectrons [2]. It is obvious that soft X-ray (SX) PES is still surface sensitive because the IMFPs of the electrons for Au and Si are only 1.3 and 2 nm at a kinetic energy of 1 keV, respectively [2]. As for chemical state analysis, nondestructive measurements of layered materials are becoming more important for the current and future technologies of nanoscience and engineering. The extension of the probing depth up to, for example, 10 nm will greatly widen the applicability to various materials with nanolayered structures and nanoparticles.

Here, we report that core level and valence band (VB)-PES at hard X-ray (HX) excitation of 5.95 keV was realized for the first time with high throughput and resolution. Unprecedentedly, high photon flux density from an undulator compensates for the decrease in cross section, which prevented high resolution measurements in Lindau *et al.*'s preceding trial [3]. Due to the large IMFPs of 5 ~ 15 nm, we do not need to prepare an ideal clean surface.

Experiments were performed at the undulator beamline **BL29XU** [3-5]. A schematic of the experimental setup including optics is shown in Fig. 1. The Si 333 channel cut monochromator reduces photon bandwidth down to 50-70 meV. A Gammadata Scienta SES2002 electron analyzer was modified to measure high-kinetic-energy photoelectrons up to 6 keV.

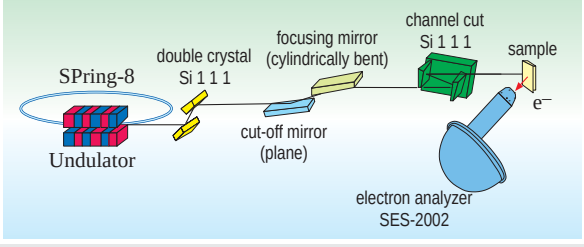

Fig. 1. Schematic of experimental setup including optics. A channel-cut monochromator with Si 333 reflection placed downstream of the mirror made it possible to reduce the energy bandwidth down to 70 meV. At the sample position, photon flux in a focal spot of 0.12 mm (vertical) × 0.7 mm (horizontal) was measured to be 2×10^{11} counts/sec.

The performance of the detection system was tested [4,5] by measuring Au 4*f* spectra with an analyzer pass energy (E_p) of 200 eV. To confirm surface insensitivity, no surface treatment was made on the Au sample plate before or after introducing it into the analyzer chamber. Figure 2 shows the observed spectra with accumulation times of 10 min at 80 mA ring current. The full width at half maximum (FWHM) of the Au $4f_{7/2}$ peak is 470 meV. The VB spectrum was obtained with an accumulation time of 30 min and the Fermi-edge of Au is clearly observed at 20 K as shown in the inset of Fig. 2. The instrumental energy resolution including the X-ray bandwidth is determined to be 240 meV from the Fermi-edge profile.

To confirm the capability of the present method to probe the bulk states of reactive surfaces, the VB spectrum of a thin SiO_2 layer (0.58 nm) on Si(100) was measured. Figure 3 shows the spectrum obtained at 5.95 keV with an accumulation period of 30 min at room temperature. The spectrum measured with SX excitation at 0.85 keV using SR is also shown as a reference. The reference SX spectrum is evidently

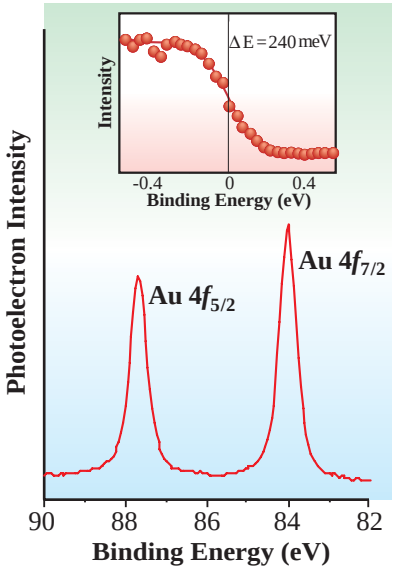

Fig. 2. Au 4*f* core level spectra of a Au plate measured at 5950 eV excitation with E_p = 200 eV. The inset shows the Fermi-edge spectrum at 20 K with E_p = 200 eV. The total energy resolution was estimated to be 240 meV for E_p = 200 eV from the Fermi-edge broadening.

dominated by the peaks of structures originated from surface SiO_2. These peaks vanish in the hard X-ray spectrum, indicating the negligible contribution of the surface oxide layer of 0.58 nm thickness. From this result, we can expect to obtain "surface insensitive" spectra for most materials without resorting to surface treatment procedures. The total curve (red line) obtained by summing the weighted *s*-like (blue: multiplied by 1) and the *p*-like (green: multiplied by 0.07) partial density of states reproduces the experimental spectra at 5.95 keV.

We also successfully applied this method to detect the chemical reaction in the buried interface of high-k gate dielectrics in Si-LSI. Figure 4 shows the Si 1*s* spectra of this $HfO_2/SiO_2/Si(100)$ structure [5]. The Si 1*s* spectra of a sample with 1.32 nm SiO_2 on Si(100) are shown as a reference. After the deposition of the HfO_2 film, the Si 1*s* peak for the intermediate layer shifts to the lower-binding-energy side by 0.6 eV and is broader than the SiO_2 peak. This is an indication of an interface reaction. Annealing the sample at 1000°C in dry nitrogen gas for 5 sec enhanced the intensity of the Hf silicate peak. This result suggests that silicate formation is related to the diffusion of Si atoms into the deposited layers from the Si substrate. A detectable increase in spectral intensity appearing on the low-binding-energy side of the substrate peak indicates the formation of Hf-Si bonds by the annealing. The present hard X-ray photoemission (HX-PES) is inevitably necessary for the investigation of nanolayers and their buried interfaces in most of real devices, because the thicknesses are far beyond the probe depths of the conventional PES.

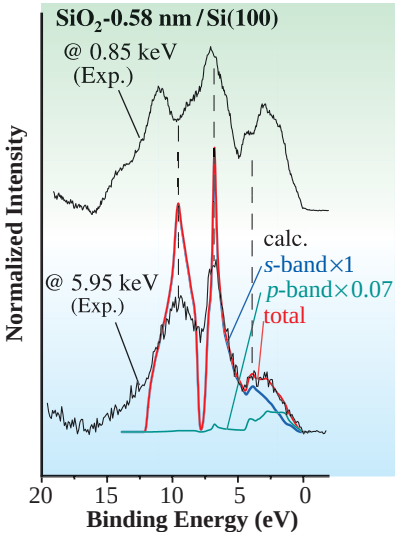

Fig. 3. VB-PES spectra of a thin SiO_2 layer (0.58 nm) on Si(100) measured at 5.95 (lower) and 0.85 keV (upper) with the same E_B – 200 eV. The red curve shows the weighted sum of the *s*-like (blue) and *p*-like (green) partial DOS obtained from first principles calculations.

We have tested the feasibility of this HX-PES to various classes of materials. All the results verify that HX-PES is successfully applied to the investigation of bulk electronic structures and chemical bonding states and can thus contribute to a wide range of basic science and technologies. It should be mentioned that this method has been developed by the collaboration between the X-ray optics group at SPring-8/RIKEN and solid state spectroscopy groups (SPring-8/JASRI, SPring-8/RIKEN, and Hi-SOR).

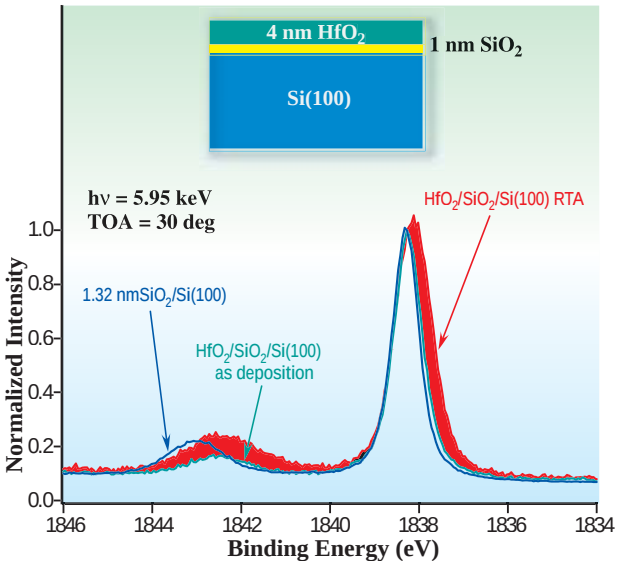

Fig. 4. Si 1*s* spectra measured for as-deposited (green) and treated by (red) rapid thermal annealing (RTA, 5 sec 1000°C) $HfO_2/SiO_2/Si(100)$ are compared with that measured for 1.32 nm $SiO_2/Si(100)$ (blue). The shift of the oxide peak in the as-deposited spectrum from that of the SiO_2 spectrum evidences interface reaction. The RTA spectrum shows a further shift of the oxide peak and an increase in intensity at the lower-binding side of the substrate Si peak. This is attributed to silicide-like Si-Hf bond formation by RTA.

Keisuke Kobayashi[a] and Yasutaka Takata[b]

(a) SPring-8 / JASRI
(b) SPring-8 / RIKEN

E-mail: koba kei@spring8.or.jp

References

[1] S. Hüfner: Photoelectron Spectroscopy (Springer-Verlag, Berlin-Hidelberg, 1995).
[2] NIST Standard Ref. Database 71, "NIST Electron Inelastic-Mean-Free-Path Database: Ver. 1.1", http://www.nist.gov/srd/nist71.htm, and references therein.
[3] P. Lindau *et al.*: Nature **250** (1974) 214.
[4] K. Kobayashi *et al.*: Appl. Phys. Lett. **83** (2003) 1005.
[5] Y. Takata, K. Tamasaku, T. Tokushima, D. Miwa, S. Shin, T. Ishikawa, M. Yabashi, K. Kobayashi, J.J. Kim, T. Yao, T. Yamamoto, M. Arita, H. Namatame and M. Taniguchi: Appl. Phys. Lett. **84** (2004) 4310.

Magnetic Field Induced Phase Transition in Distorted Perovskite $Eu_{0.6}Sr_{0.4}MnO_3$

A distorted perovskite $Eu_{0.6}Sr_{0.4}MnO_3$ shows a magnetic field-induced insulator-to-metal (IM) transition at approximately below 75 K [1,2]. The magnetic field-induced change in resistivity (ρ) exceeds 6 figures (10^6) at 12 K. It also accompanies a transition from a low magnetization phase (σ = 25 emu/g) to a high magnetization phase (85 emu/g). The transition fields are 20 kOe at 5 K and 10 kOe at 20 K. Once it takes places, the induced metallic and ferromagnetic states remain stable even in the absence of a magnetic field. There is no evidence in the $\rho - T$ curve that charge ordering occurs. The electronic state of Eu ions remains unchanged through the transition [3]. The transition also accompanies a magnetostriction of -4×10^{-4} and the application of a pressure also induces the IM transition [4]. This suggests that the transition also accompanies a structural phase transition. Thus, in this investigation, we measured the powder X-ray diffraction in a magnetic field and discuss whether the transition accompanies a structural phase transition. Synchrotron X-ray radiation at beamlines **BL39XU** (λ = 0.8231 Å) and **BL46XU** (λ = 0.56355 Å) was used for the diffraction measurements. The measurements were conducted with magnetic fields up to 20 kOe, perpendicular to the scattering plane [5].

The crystal structure is orthorhombic (*Pnma*) with lattice constants a = 5.4463(3) Å, b = 7.6669(4) Å and c = 5.4329(3) Å at room temperature. Mn-O-Mn angles are about 160°. The lattice constants decrease monotonically with decreasing temperature. No superstructure was detected down to 20 K, which also indicates the absence of charge ordering. At 20 K, the full powder pattern of the insulator phase (H = 0) and that of the metal phase (H = 20 kOe) are both well analyzed to reveal a *Pnma* space group. Therefore, no distinct phase transition is realized through the IM transition.

In Fig. 1, 404 / 080 diffraction peaks at 20 K are shown for various applied magnetic fields (H) after cooled without magnetic field (ZFC). It is seen that with increasing H, both peaks shift toward low 2θ angle and that the peak intensities increase drastically for H > 10 kOe. In Fig. 2, the lattice constant b, determined from the 080 peak position, is plotted against H. It increases with increasing H, showing a jump at approximately 10 kOe where IM transition occurs. The jump $\Delta b/b$ is about 4.3×10^{-4}, whose magnitude is comparable to that observed in a magnetostriction measurement [4]. After the transition, b decreases with decreasing H, showing no jump this time, and reaches a value different

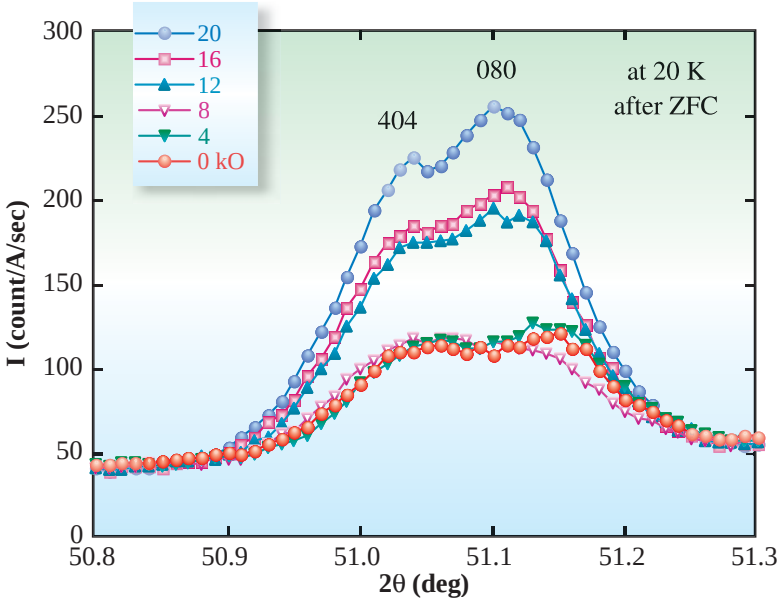

Fig. 1. 404 / 080 peaks at 20 K in various applied magnetic fields after the ZFC process (λ = 0.8231 Å).

from the initial one at H = 0. This is consistent with the H dependences of magnetoresistance and magnetization, and is suggestive of some kind of phase transition.

Here, we consider the change in peak intensity against H. In addition to 404 and 080 peaks, the intensities of 400, 004, 440, and 044 peaks increase through the IM transition. On the other hand those of 511 and 115 peaks decrease. These intensity changes represent the displacement of atoms. Taking the structural factors into account, we can derive information on the displacement of atoms through the IM transition. One simple explanation for all these intensity changes is the displacement of oxygen toward O1 (0.5, 0.25, 0) and O2 (0.25, 0, -0.25). The resultant displacement corresponds to the rotation of MnO_6 octahedrons to increase the Mn-O-Mn angle toward 180°. Such scheme is illustrated in Fig. 3. This structural change leads to a gain of the electron transfer energy in the double exchange mechanism and thus stabilizes the metallic and ferromagnetic states.

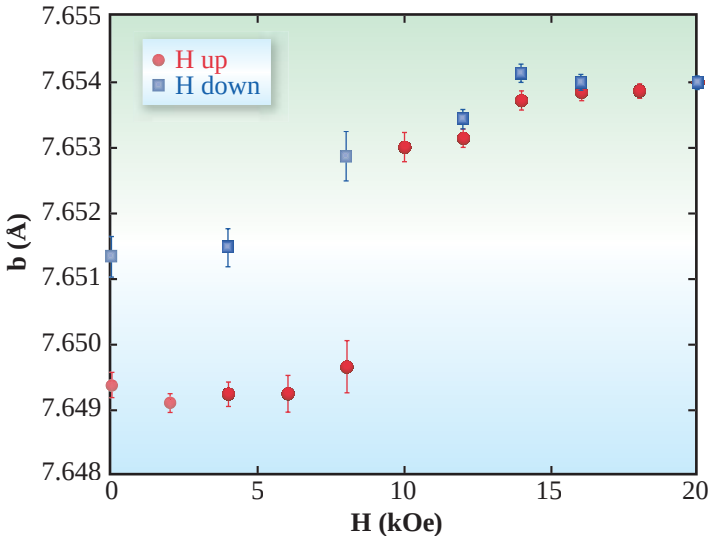

Fig. 2. Dependence of b on H.

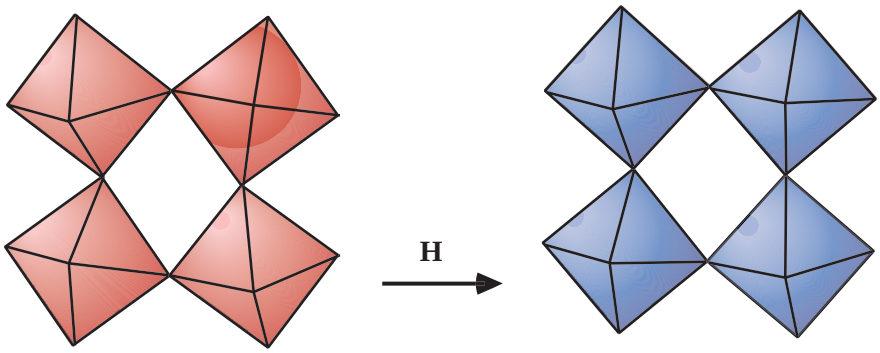

Fig. 3. Rotation of MnO_6 octahedrons through the IM transition.

Shin Nakamura[a], Susumu Shimomura[b] and Naoshi Ikeda[c]

(a) Department of Physics, Teikyo University
(b) Department of Physics, Keio University
(c) SPring-8 / JASRI

E-mail: shin@koala.mse.teikyo-u.ac.jp

References

[1] A. Sundaresan *et al.*: Phys. Rev. B **55** (1997) 5596.
[2] S. Nakamura *et al.*: J. Phys. Soc. Jpn. **68** (1999) 1485.
[3] M. Mizumaki *et al.*: J. Synchrotron Rad. **8** (2001) 440.
[4] I. Kosaka *et al.*: Physica B **281-282** (2000) 500.
[5] S. Nakamura, S. Shimomura, N. Ikeda, M. Mizumaki, H. Ohsumi, S. Nimori, T. Takeuchi and K. Itoh: J. Magn. Magn. Mater. - in press.

High-Frequency Dynamics in Glassy Selenium

The investigation of short wavelength acoustic modes in glasses has stimulated a sizeable number of studies in the last decades. The reason for such interest lies in the close link between these high-frequency excitations and some well-known anomalies, such as the excess of the vibrational density of state (the so-called Boson Peak) or the thermal conductivity plateau observed in the 1<T<10 K region, which mark remarkable differences from the crystalline state. In glassy selenium the competition between two energetically similar local configurations allows for excellent glass-forming ability, a very rare feature in a monatomic system. This explains why g-Se has been intensively investigated in the past, though some crucial aspects related to the features of its microscopic collective dynamics at a wavelength comprising few atomic units are still unknown.

The aim of this experiment is to determine the coherent dynamic structure factor by inelastic X-ray scattering (IXS) in g-Se [1]. The experiment was carried out at the high resolution inelastic scattering beamline **BL35XU** [2]. High resolution was obtained using the (11 11 11) reflection of perfect silicon crystals in an extreme backscattering geometry. The use of four analyzer crystals, placed with 0.78 degree spacing on the 10 m two-theta arm (horizontal scattering plane), and four independent detectors, allowed to collect four momentum transfers simultaneously. Slits in front of the analyzer crystals limited their acceptance to 0.24 nm^{-1} on the scattering plane. The overall resolution of the spectrometer was about 1.5 meV. Elemental Se was prepared in flakes with thicknesses between 50 μm and 100 μm, which are very close to the optimum for matching the absorption length of the X-rays μ^{-1} = 50 μm.

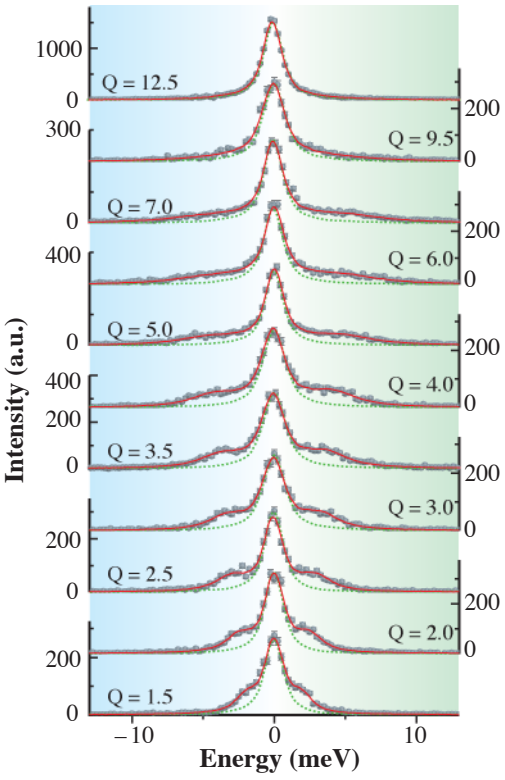

Fig. 1. IXS spectra of g-Se (solid circles) for several momentum transfers, indicated by labels in units of nm^{-1}. The instrument resolution (dotted line) and the best fit lineshape (continuous line) according to the model discussed in the text (corrected for resolution broadening and detailed balance factor) are also indicated.

In Fig. 1, we report the measured spectra for several fixed momentum transfers. Clear evidence of an inelastic mode, at the wings of the elastic peak, can be observed. The behavior of the energy shift of this mode *vs* the momentum transfer strongly resembles a phonon-like propagating mode. The high inelastic/elastic ratio allows for a less ambiguous detailed analysis of this mode than that in previously studied glasses.

Following the prescription of generalized hydrodynamics and modeling the vibrational dynamics as a Markovian process with an instantaneous second order memory function (an appropriate approximation for a glassy system), one ends up with a damped harmonic oscillator line shape to represent the dynamic structure factor:

$$\frac{S(Q,\omega)}{S(Q)} = f(Q)\delta(\omega) + \frac{1-f(Q)}{\pi}\frac{\Omega^2(Q)\Gamma(\omega)}{(\omega^2-\Omega^2(Q))^2-\omega^2\Gamma^2(Q)}$$

The parameters Ω and Γ are the characteristic frequency and attenuation of the mode, respectively, while S(Q) is the static structure factor.

The results of the present IXS experiment are summarized in Fig. 2. Compelling evidence for the existence of an acoustic-like longitudinal branch, which is well defined up to the higher investigated momentum transfer, is shown in Figs. 2(a) and 2(b). No evidence of localization is found at Q = 3 nm^{-1} as it has been suggested in ref. [3]. Moreover, the dispersion curve extends well beyond the boson peak frequency ($E_{BP} \cong 1.7$ meV in g-Se at T = 300 K), confirming earlier observations reported in other glasses [4]. The extrapolated low Q limit of the apparent sound velocity (2000 m/s) falls above the hydrodynamic value (c_0 = 1800 m/s), suggesting the presence of a mild positive dispersion effect. As recently reported for other glassy systems [5], this effect may be due to a residual relaxation process related to the positional disorder intrinsic of the glassy phase.

The sound attenuation parameter $\Gamma(Q)$ (Fig. 2(c)) is found to be compatible with the Q^2 law, up to Q values where the dispersion relation is. This coincidence suggests a simultaneous breakdown of the linear and quadratic laws for $\Omega(Q)$ and $\Gamma(Q)$, respectively, which is expected to be caused by structural effects, i.e., by the Q dependence of the static structure factor. In order to remove this structural dependence we show the value of the sound attenuation parameter plotted against the excitation frequency for all measured Q values in Fig. 2(d). As can be observed, a simple power law relation now extends up to the entire explored momentum region. The best fitted law turns out to be $\Gamma = \Omega^{\alpha}$ with $\alpha = 2.15 \pm 0.10$. The present observation emphasizes another aspect that needs to be encompassed in the explanation of the ubiquitous Q^2 (or Ω^2) dependence which is not yet fully explained.

Finally, the data from the INS experiment [2] are shown in Fig. 3 (full dots), alongside with our IXS data (open dots). As can be observed, the two sets of data are in reasonable agreement. The small differences at the base of the elastic peak are expected, given the difference between the INS and IXS resolution functions: while both have 1.5 meV FWHM, the IXS resolution is approximately Lorentzian, while the INS resolution is Gaussian. The INS measurements, even pushing the limit of the technique at its maximum, span only a limited energy range due to kinematic restrictions.

Summing up, we presented an accurate measurement of the dynamic structure factor in g-Se, exploiting the state of the art capabilities of a new IXS facility. The favorable inelastic/elastic signal, the lack of kinematic constrains and the very good statistics allowed us to perform intensive study in an extended and previously unexplored momentum-energy region. Evidence for a well-defined longitudinal acoustic mode was found, extending all the way beyond the first pseudo-Brillouin zone through the boson peak frequency, thus suggesting a link between this universal feature of glasses and the reported high-frequency acoustic excitation. Moreover, the presence of such a well defined mode allowed us to obtain new insight into the high-frequency sound attenuation issue. Specifically, the quadratic dependence of the sound attenuation on the mode frequency corroborated the Q^2 law holding in a smaller range and observed in other glass formers.

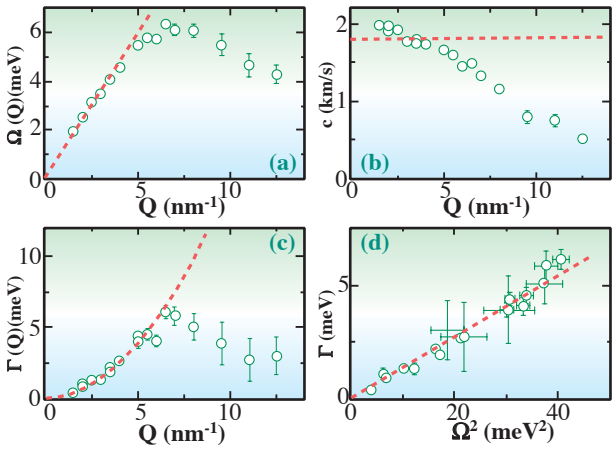

Fig. 2. Dynamical parameters obtained by IXS measurements. **(a)** Excitation frequency (open circles) and hydrodynamic dispersion (dotted line). **(b)** Apparent sound velocity, $\Omega(Q)/Q$ (open circles) and hydrodynamic value (dotted line). **(c)** Sound attenuation (open circles) with the best Q^2 fit $\Gamma(Q) = 0.15Q^2$; Γ and Q expressed in meV and nm^{-1}, respectively (dotted line). **(d)** Sound damping *vs* square of the excitation frequency. The quadratic dependence on the wavevector Q^2 shown in the panel **(c)** turns out to be the low Q limit of the more general dependence shown here.

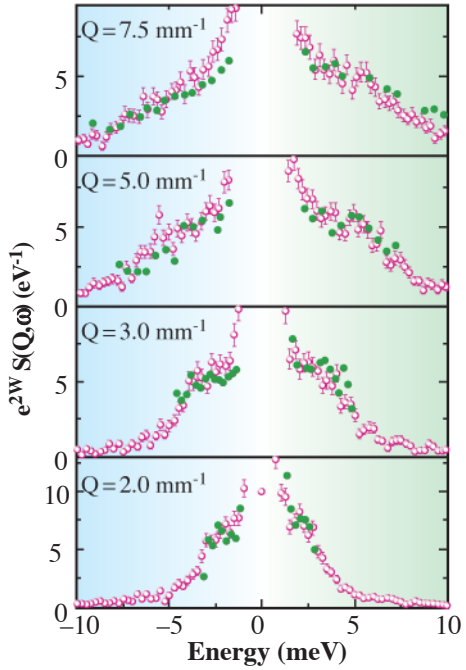

Fig. 3. Comparison between the IXS results (open circles and error bar) and previous INS measurements from ref. [3] (solid circles).

T. Scopigno[a], A.Q.R. Baron[b] and R. Di Leonardo[a]

(a) Dipartimento di Fisica and INFM, Universitá di Roma "La Sapienza," Italy
(b) SPring-8 / JASRI

E-mail: tullio.scopigno@phys.uniroma1.it

References

[1] T. Scopigno, R. Di Leonardo, G. Ruocco, A.Q.R. Baron, S. Tsutsui, F. Bossard and S.N. Yannopoluos: Phys. Rev. Lett. **92** (2004) 025503.
[2] A.Q.R. Baron *et al.*: J. Phys. Chem. Solids **61** (2000) 461.
[3] M. Foret *et al.*: Phys. Rev. Lett. **81**(1998) 2100.
[4] F. Sette *et al.*: Science **280** (1998) 1550.
[5] G. Ruocco *et al.*: Phys. Rev. Lett. **84** (2000) 5788.

Kohn Anomaly in MgB_2 and Related Compounds by Inelastic X-ray Scattering

MgB_2 has generated an immense amount of interest since its high T_c, ~ 39 K, was first demonstrated a few years ago [1]. This is the highest known critical temperature for a simple metallic material and rather outside the range for T_c using standard estimates. One of the especially interesting properties of MgB_2 is that the electron-phonon coupling (EPC) that causes this high T_c is predominantly to a *particular* phonon mode (with E_{2g} symmetry at Γ), which makes investigating the behavior of this mode very important. Furthermore, the relevant sections of the Fermi surface ("sigma" sheets) are nearly simple cylinders along the c* axis, thus the effects of the electron-phonon coupling should be clear and easy to see in phonon spectra.

A difficulty with MgB_2, however, is that available single crystals are small, ~ 0.01 mm^3, so that the conventional method of investigating phonon dispersion, inelastic neutron scattering, cannot be applied. However, the high brilliance of SPring-8 means that, in principle, such investigations can be carried out with X-rays, assuming a suitable, highly efficient, spectrometer is available. We used the **BL35XU** spectrometer [2], which provides ~ 3×10^{10} photons/s in a 4 meV bandwidth and a small (~100 micron diameter) spot on the sample. Good quality inelastic X-ray scattering (IXS) spectra could be measured from samples of size ~ $0.5 \times 0.2 \times 0.05 = 0.005$ mm^3 in about 12 h, using a 6 meV resolution setup at 15.8 keV (corresponding to the (888) back reflection in silicon).

The EPC of the E_{2g} mode to the sigma surfaces is expected to cause strong softening and a huge increase in the linewidth of the phonon mode as one reduces the in-plane component of the probed momentum transfer from values larger than the diameter of the sigma Fermi surfaces to smaller values. The softening is an extreme example of a Kohn anomaly, while the broadening corresponds to the reduction in phonon lifetime that occurs as the additional decay channel (excitation of the electronic system) turns on at smaller momentum transfers. The momentum transfer dependence is easily understood qualitatively based on the shape of the sigma Fermi surfaces: since phonon energies are negligible on the

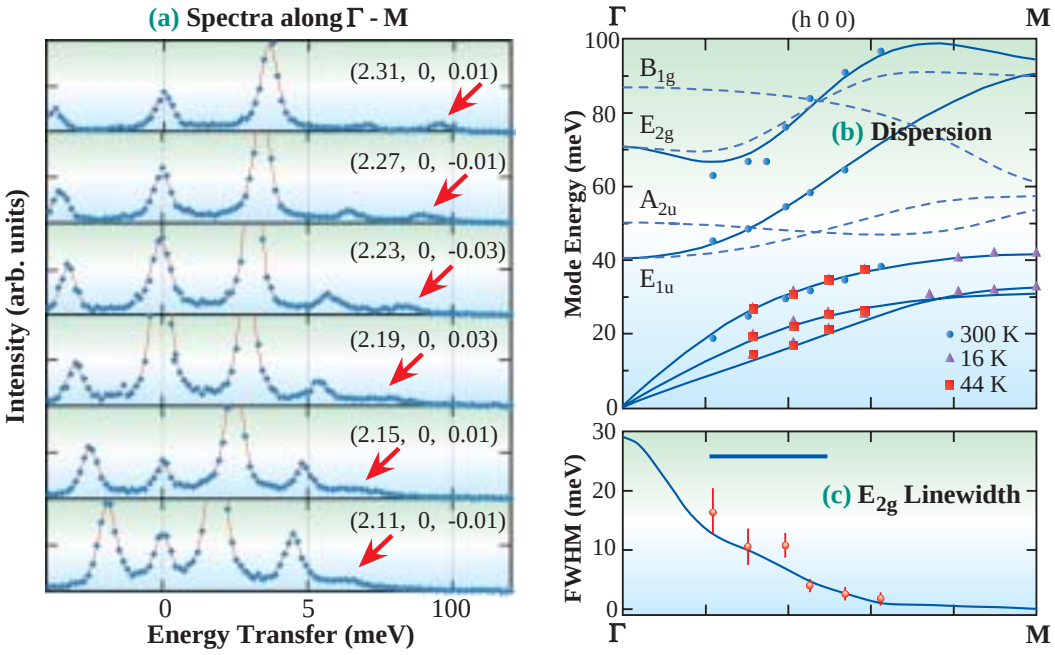

Fig. 1. Phonon dispersion in pure MgB_2 (see [3]).
(1a) Selected IXS spectra (room temperature) with fits (solid lines). The softening and broadening of the E_{2g} mode (indicated by red arrows) are readily apparent. **(1b)** Phonon dispersion determined by fits to the data (points) and the results of *ab initio* calculations (lines - Bohnen *et al.*, Phys. Rev. Lett. **86** (2001) 5771; dashed lines are modes not expected to be observed from phonon polarization considerations). **(1c)** Measured linewidth after correction for resolution, and the theoretical calculation (see text). In general, there is excellent agreement with the theoretical calculation. The solid horizontal bar shows the diameter of the sigma Fermi surfaces projected into the basal plane which is the expected position for the Kohn anomaly.

scale of most electron states, EPC is only possible for phonons with momenta appropriate to move electrons within the neighborhood of a Fermi surface. Given the nearly circular projection of the sigma surfaces into the basal plane, small phonon momenta can move electrons from one location to another across the Fermi surface. However, for larger momenta ($Q > 2\,k_F$), all appropriate states are filled, thus the coupling is reduced. Figure 1 shows the results from a pure MgB_2 sample along the ΓM line [3] of the basal plane – the softening and broadening as one moves inside the sigma surfaces are immediately clear. Furthermore, the agreement with theoretical calculations is excellent, both in dispersion and linewidth, even for this very extreme case of strong coupling of single mode. This provides crucial confirmation that MgB_2 is an extreme case of a conventional BCS / Eliashberg-type superconductor.

Having demonstrated the effects of the EPC on the E_{2g} mode and their good agreement with theoretical results, we tried to modify the sample a bit; the recent growth of single crystalline carbon-doped $Mg(B_{1-x}C_x)_2$ [4] provides an excellent opportunity. In particular, the sigma sheets of the Fermi surfaces are hole surfaces, so that electron doping with C can be expected to close them and remove the electron phonon coupling. Thus, we investigated the behavior of the E_{2g} mode in samples with 2%, 5% and 12.5% carbon doping, corresponding to transition temperatures of 35.5, 30 and 2.5 K, respectively. The softening remains clear in the 2% and 5% samples; however, as evident in Fig. 2, in the 12.5% sample, the softening goes away, and the E_{2g} mode "pops up", showing the removal of the EPC from these surfaces. This is in good agreement both with expectations regarding the changes in T_c and with one calculation suggesting that about 9% carbon doping should be sufficient to fill the sigma bands.

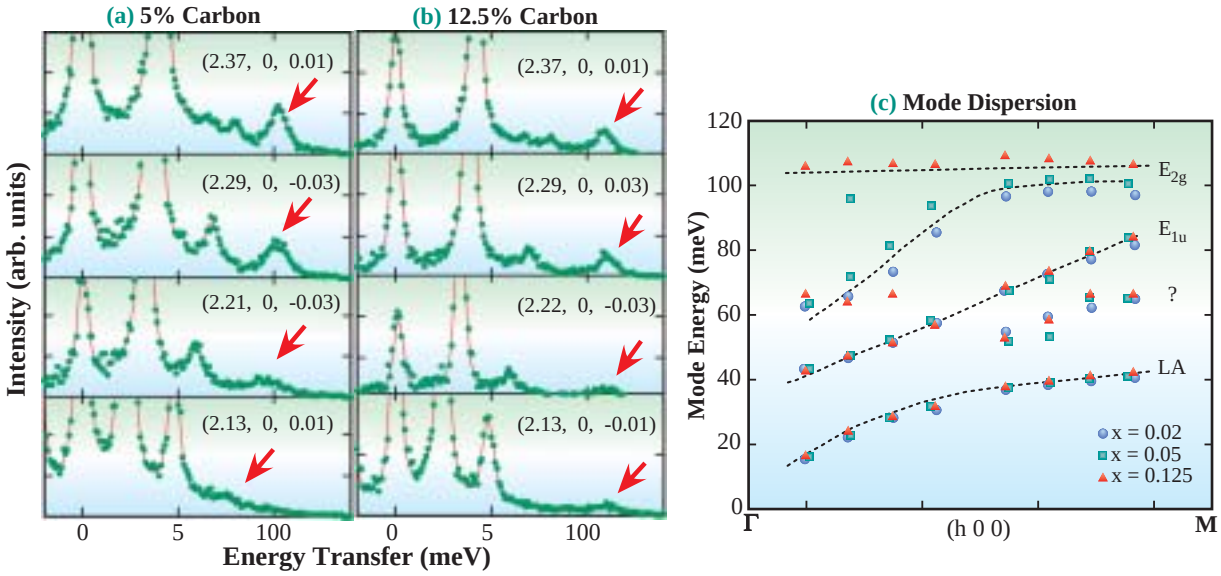

Fig. 2. Phonon dispersion in carbon-doped material, $Mg(B_{1-x}C_x)_2$ [5]. Selected IXS spectra (room temperature) with fits (solid lines) from **(a)** x = 0.05 sample and **(b)** x = 0.125 sample. **(c)** shows the phonon dispersion determined from the fits and a guide to the eye (dashed lines). The E_{2g} mode "pops up" when the carbon content is increased to 12.5%, as expected from filling the sigma surfaces. The presence of the extra mode evident at higher momentum transfers and other details are being analyzed

Alfred Q.R. Baron[a] and Hiroshi Uchiyama[b]

(a) SPring-8 / JASRI
(b) Superconductivity Research Laboratory, ISTEC

E-mail: Baron@spring8.or.jp

References

[1] J. Nagamatsu *et al.*: Nature **410** (2001) 63.
[2] A.Q.R. Baron *et al.*: J. Phys. & Chem. Solids **61** (2000) 461.
[3] A.Q.R. Baron, H. Uchiyama, Y. Tanaka, S. Tsutsui, D. Ishikawa, S. Lee, R. Heid, K.-P. Bohnen, S. Tajima and T. Ishikawa: Phys. Rev. Lett. **92** (2004) 197004.
[4] S. Lee *et al.*: Physica C **397** (2003) 7.
[5] A.Q.R. Baron, H. Uchiyama, S. Tsutsui, S. Lee and S. Tajima: in preparation.

Site-Specific Phonon Density of States Measured using Nuclear Resonant Scattering

It is well known that all atoms oscillate in a solid material even at low temperature, and their quantized vibrations are known as phonons. Except for simple materials, different kinds of atoms are usually contained in a material, and the properties of their oscillations are generally not the same. The atomic motion of a certain atom sometimes plays an important role in the characteristics of the material such as the vibration of the impurity or doped atoms in metals or semiconductors, the carrier ion's motions in ionic conductors, and the oscillations of rare-earth atoms in filled skutterudite antimonides. Therefore, each atomic motion provides important information. The nuclear resonant inelastic scattering of synchrotron radiation offers element-(isotope)-specific phonon energy spectra [1]. In this method, the nuclear resonant excitation is attained with synchrotron radiation, the bandwidth of which is reduced to the order of meV, and the energy dependence of the delayed emission from the relatively long-lived excited state yields the inelastic excitation spectrum, i.e., the phonon energy spectrum. Usually, the excitation energy level is inherent to each nucleus and simultaneous excitation of more than two nuclei can be ignored. Therefore, if we tune the incident photon energy around the excitation energy of a certain nuclide, we can obtain the element-specific phonon energy spectrum. However, in the case of compounds with two or more different states of atoms of the same element, such as magnetite, which is a mixed valent Fe compound [2], the observed phonon energy spectrum is the superposition of the partial phonon spectra of individual atoms. Therefore, even this method seems unable to distinguish the "site-specific" phonon energy spectrum. Although the phonon is one of the most fundamental concepts in solids, it was impossible to discern the site-specific atomic motions by previous methods. However, we could use a new method, which is an extension of the nuclear resonant scattering method, and it led to the observation of the site-specific phonons [3]. In general, nuclear energy levels are split and/or shifted owing to the surrounding electronic states; these interactions are small compared to the nuclear excitation energy and known as hyperfine interactions. Because the information of the individual site through hyperfine interactions is obtained from the incoherent inelastic scattering, we can identify each phonon component of every site by measuring the hyperfine interactions. The effect of hyperfine interactions can be observed in the time evolution of the delayed scattering. Therefore, the measurements of time evolution of the incoherent inelastic scattering at different phonon energies permit us to observe the site-specific phonon energy spectra.

We have performed the measurement of site-specific phonons in magnetite (Fe_3O_4). In magnetite, the iron atoms are located in two nonequivalent positions in the unit cell at room temperature; one-third of the Fe ions (Fe^{3+}) occupy the A sites tetrahedrally coordinated by four oxygen ions and two-thirds of the Fe ions ($Fe^{2.5+}$) occupy the B sites octahedrally surrounded by six oxygen ions. A polycrystalline sample pressed into the pellet form was used. The measurements were performed at the nuclear resonant scattering beamline **BL09XU** and the JAERI beamline **BL11XU**. The incident radiation was monochromatized to the bandwidth of 3.2 meV (FWHM), and the energy of the radiation was varied around the first nuclear resonant excitation energy of ^{57}Fe (14.413 keV). The scattered 14.413 keV γ rays

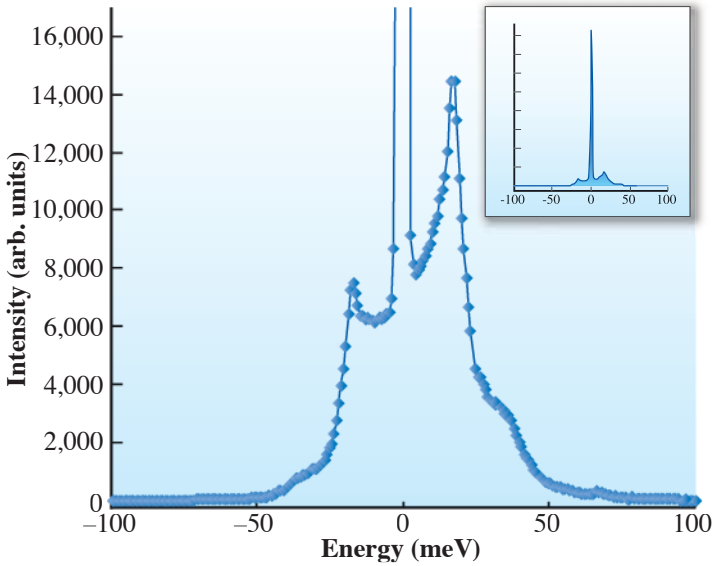

Fig. 1. Energy spectrum of nuclear resonant scattering of all ^{57}Fe atoms in Fe_3O_4.

at the deexcitation from a resonantly excited nucleus were measured using a multielement Si-avalanche photodiode (APD) detector.

Nuclear resonant inelastic scattering spectrum of ^{57}Fe in Fe_3O_4 is shown in Fig. 1, which is the superposition of the inelastic scattering from both A and B sites. Typical time spectra measured at different incident photon energies are shown in Fig. 2, and the component ratios of A site to B site were obtained at each phonon energy. From a measured nuclear resonant inelastic scattering spectrum (Fig. 1), phonon density of states (PDOS) of all Fe atoms in Fe_3O_4 was reduced and is shown in Fig. 3 as closed circles. Site-specific partial PDOS of A and B sites obtained using the total Fe PDOS and the component ratios in time spectra are shown in Fig. 3 as downward and upward triangles, respectively, and the differences are clearly seen. Around the first peak of 17 meV, the intensity of the B site is larger than that of the A site while their intensities are almost the same at around 35 meV. The observed characteristics indicate their couplings to surrounding atoms, and the phonons at around 17 meV and at around 35 meV are considered to be mainly due to the iron atom's motions and the coupled motions of iron and oxygen atoms, respectively.

We could observe for the first time the partial PDOS identified using the electronic states. This method is applicable not only to solids but also to soft materials and liquids if only their electronic states can be identified in the time spectra. The method allows us to study site-specific phonons in various systems, which we could not access, and will enable the extensive study of the relationships of the electronic states to the local phonon states.

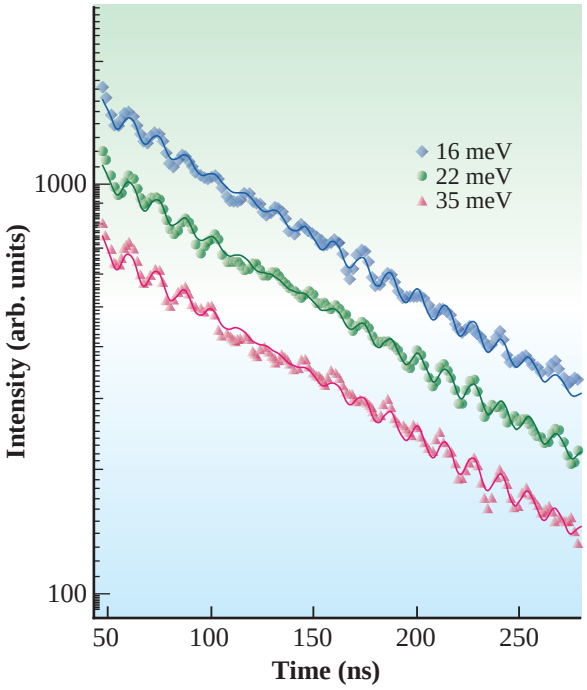

Fig. 2. Time spectra measured at different incident photon energies (deviations from nuclear resonant energy; diamonds: 16 meV, circles: 22 meV, triangles: 35 meV). Lines are least-square fitted spectra with two exponential functions accompanied by sinusoidal quantum beats.

Makoto Seto

Research Reactor Institute, Kyoto University

E-mail: seto@rri.kyoto-u.ac.jp

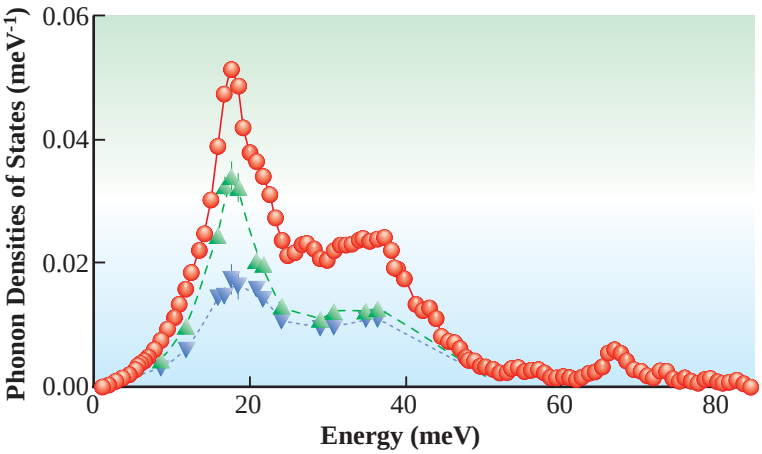

Fig. 3. Phonon densities of states of ^{57}Fe in the Fe_3O_4 sample. The phonon density of states of all Fe is shown in solid circles. The partial phonon densities of states of the A and B sites obtained experimentally are shown as downward and upward triangles, respectively. Lines are guides for the eye.

References

[1] M. Seto *et al.*: Phys. Rev. Lett. **74** (1995) 3828.

[2] For a review, see N. Tsuda *et al.*: Electronic Conduction in Oxides, 2nd ed. (Springer-Verlag, Berlin, 2000).

[3] M. Seto, S. Kitao, Y. Kobayashi, R. Haruki, Y. Yoda, T. Mitsui and T. Ishikawa: Phys. Rev. Lett. **91** (2003) 185505; P. Schewe *et al.*: Physics News Update **661** (2003), (http://www.aip.org/enews/physnews/2003/661.html)

Nuclear Resonant Reflectometry of Thin Films by Stroboscopic Detection of Synchrotron Radiation

Here we report on the first grazing incidence synchrotron Mössbauer study in energy domain [1]. The experiments were performed on ^{57}Fe-containing thin films using the recently developed stroboscopic detection scheme [2,3].

Nuclear resonant scattering (NRS) of synchrotron radiation (SR) became an established nuclear hyperfine method in the last two decades [4]. NRS of SR in the forward direction is conventionally recorded as a beating time response of the nuclear ensemble following a short resonant synchrotron pulse. The beat frequencies are characteristic of the hyperfine fields.

In grazing incidence, the interferences of the SR plane waves reflected from different surfaces or interfaces of a stratified sample result in an angle-dependent reflectivity and strong depth selectivity. By recording the prompt electronic and the delayed nuclear resonant reflectivity curves, both the chemical and the hyperfine depth profile can be probed with nanometer-scale resolution. Grazing-incident NRS of SR is commonly called Synchrotron Mössbauer Reflectometry (SMR) [4,5].

The feasibility of the stroboscopic detection (SD) scheme for NRS of SR was first demonstrated in the forward direction [2]. In an SD experiment, two samples, the investigated one and a vibrating reference absorber coherently scatter the SR. The signal is recorded in a 2D array as a function of both the time elapsed after the SR pulse and the velocity v of the reference absorber. As an advantage, SD of NRS of SR provides a spectrum in the energy domain [2,3] similar to a conventional Mössbauer spectrum.

In the forward scattering geometry, the prompt electronic scattering homogeneously contributes to the stroboscopic spectrum, therefore it does not affect the spectral shape. However, in grazing-incidence, the stroboscopically detected SMR (⇒ SDSMR) line shape considerably differs from the shape of lines in a SD of NRS line in the forward direction due to the coherency of the electronic and nuclear scattering. The description of the time-domain SMR [4] was recently extended to evaluate stroboscopic spectra [1]. The code was merged into the EFFINO program [4] and used in the data evaluation below.

In the experiments performed at beamline **BL09XU**, SDSMR was applied for the first time. The experiments were performed in 203-bunch mode, which corresponds to a ~24 ns bunch separation time. ^{57}Fe-containing isotopic and magnetic multilayer samples were investigated using the 14.4 keV Mössbauer transition of ^{57}Fe nuclei. The experimental setup is shown in Fig. 1. Prompt X-ray and delayed nuclear reflectivity curves, as well as SDSMR spectra were recorded using three 2-ns dead-time Hamamatsu avalanche photodiodes (APD) in series. The velocity range of the reference absorber on the Mössbauer drive was v_{max} = ±20 mm/s. The 1024×1024 channel SDSMR data were time-integrated using appropriate time windows of 8 ns period and 4 ns length [2,3].

In Fig. 2, prompt electronic (a) and delayed nuclear (b) reflectivity curves as well as SDSMR spectra (c) to (e) are shown for a glass/$[^{56}Fe / ^{57}Fe]_{10}$ isotopic multilayer saturated in a transversal magnetic field. The peak in the delayed reflectivity at the total reflection angle in panel b) is a special feature of SMR (e.g. [4], p. 427). In panels (c) to (e), the four resonance lines of the +1 and –1 stroboscopic orders (right and left side, respectively), partially overlap with the 0th order in the middle. The delicate interplay between electronic and nuclear scattering is demonstrated by considerably different SDSMR spectra (c) to (e) at only slightly different angles near the total reflection angle. The full lines are simultaneous least-squares fit.

Figure 3 shows a similar set of spectra of ^{57}Fe/Cr

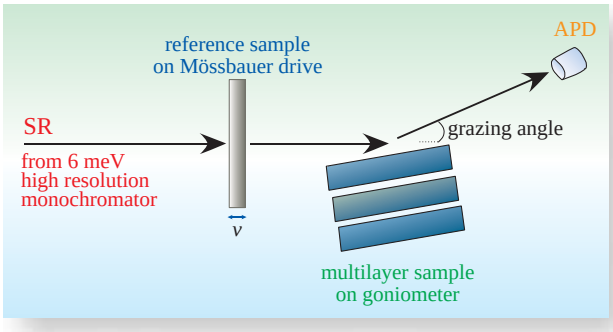

Fig. 1. Experimental setup for stroboscopically detected synchrotron Mössbauer reflectometry.

antiferromagnetically coupled epitaxial multilayer prepared on a MgO(001) substrate. Stroboscopic spectra are shown at the angles of total reflection, the antiferromagnetic (AF) and the structural Bragg peaks, (c) to (e), respectively. Continuous lines are simultaneous fits to a model structure of $[^{57}Fe(2.6\ nm)/Cr(1.3\ nm)]_{20}$ with Fe magnetizations parallel/antiparallel to the wave vector along the in-plane Fe (100) easy axis. This alternating longitudinal hyperfine field in consecutive Fe layers is justified by the fit.

In conclusion, we have demonstrated that, synchrotron Mössbauer reflectometry of ^{57}Fe-containing thin films is feasible in the energy domain by using the stroboscopic detection scheme.

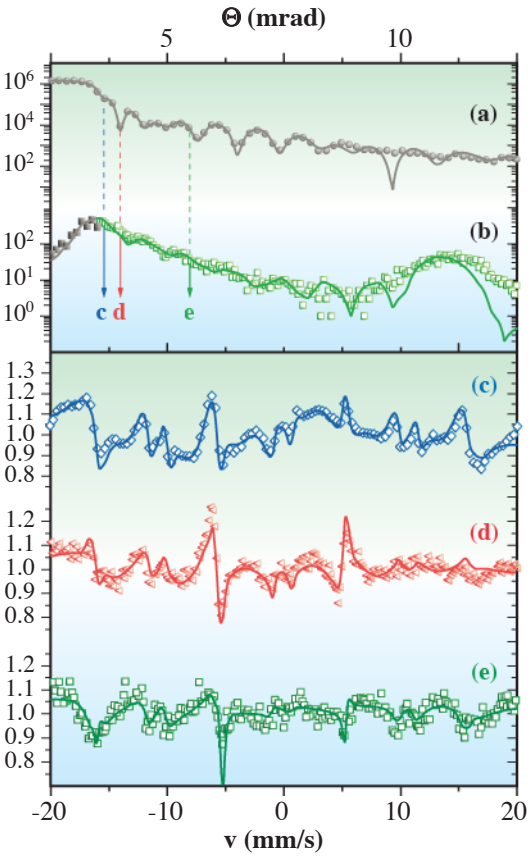

Fig. 2. Prompt electronic **(a)** and delayed nuclear **(b)** reflectivity curves and SDSMR spectra **(c)** to **(e)** of a $[^{56}Fe/^{57}Fe]_{10}$ isotopic multilayer at grazing angles indicated by the arrows.

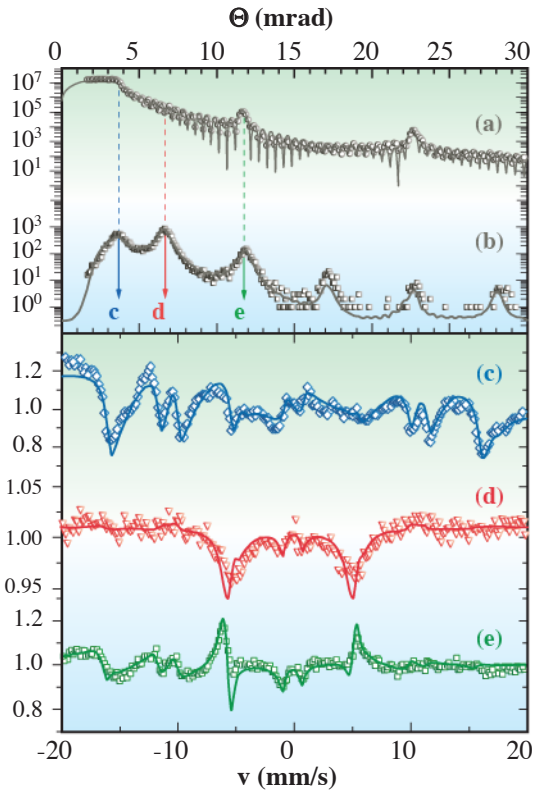

Fig. 3. Prompt electronic **(a)** and delayed nuclear **(b)** reflectivity curves and SDSMR spectra **(c)** to **(e)** of $[^{57}Fe\ (2.6\ nm)/Cr\ (1.3\ nm)]_{20}$ at various angles indicated by arrows.

László Bottyán[a], László Deák[a] and Romain Coussement[b]

(a) KFKI Research Institute for Particle and Nuclear Physics, Budapest, Hungary
(b) Instituut voor Kern- en Stralingsfysica, Katholieke Universiteit Leuven, Belgium

E-mail: deak@rmki.kfki.hu

References

[1] L. Deák, L. Bottyán, R. Callens, R Coussement, M. Major, S. Nasu and Y. Yoda: to be published in Phys. Rev. B.
[2] R. Callens *et al.*: Phys. Rev. B **65** (2002) 160404(R).
[3] R. Callens *et al.*: Phys. Rev. B **67** (2003) 104423.
[4] E. Gerdau and H. de Waard: Hyperfine Interact. **123-125** (2000) reviews and references therein.
[5] L. Deák *et al.*: Physica B **297** (2001) 113.

CHEMICAL SCIENCE

In Chemical Science, the subjects are distributed into a vast area of science. In particular, it is closely related to Materials Science. Chemical Science covers the most of the types of experiments having been carried out at SPring-8. One can easily surmise by glancing at the titles of the articles appearing in the contents page of Chemical Science. The first distinguishing feature of Chemical Science compared with Materials Science and the other categories is that its interest is focused on the observation and study of the change in the state of substances and the variation of substances. This is directly related to witnessing chemical reactions and *in situ* state analysis of materials. The second is the development of spectroscopic technique which enables time-resolved and/or space-resolved measurements. On these bases, eleven studies are highlighted as subjects in the Chemical Science category from among the experiments performed during the period of 2002B and 2003A at almost all of the beamlines installed at SPring-8.

In situ observation of dynamic change of materials is reported in the 1st, 2nd and 3rd, and 4th articles employing X-ray absorption, X-ray diffraction, and photoemission phenomena, respectively. The 5th and 6th articles focus on the techniques used for studying the static change of materials by nuclear resonant vibrational spectroscopy (NRVS) and total-reflection XAFS, elucidating the significant structural difference between the states of the substance. The 7th article introduces the first successful data acquisition of soft X-ray CD spectra of L- and D- racemic amino acids. Detailed analyses with theoretical interpretation of the X-ray absorption edge and Auger process are reported in articles no. 8 and 9, and 10 and 11, respectively.

There is an increase in the number of articles in this section this year, suggesting the diversification of studies due to the incessant search for new knowledge based on the stable supply of abundant photons with high resolution in energy and space achieved at SPring-8.

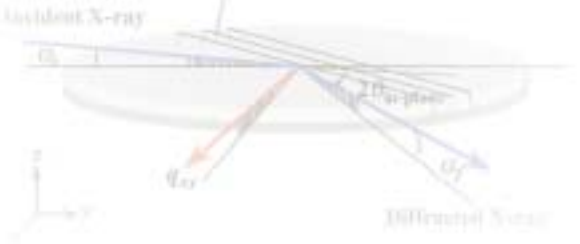

Tsunehiro Tanaka

DXAFS Studies on the Spontaneous Dispersion of PdO Interacted with Zeolites

Metal-support interaction in supported metal catalysts is important in understanding the structure and catalysis of supported metal. Previous studies concerning palladium catalysis, such as selective reduction of NO and total oxidation of methane, revealed that the catalysis of the Pd center was significantly affected by the acid property of the support. One of the reasons for these effects could be attributed to the strong interaction between PdO and acid sites of supports. Indeed, we have observed spontaneous migration of agglomerated metal Pd into the highly dispersed PdO on acid sites under O_2 atmosphere at elevated temperature. In addition it was found that the spontaneous dispersion of PdO upon repetition of reduction and oxidation treatment was reversible. The phenomena implied that the interaction between PdO and acid sites of zeolites plays an important role in the determination of dynamic behavior and structure of PdO. In this study, we tried to directly observe the dispersion process of PdO onto acid sites of zeolites. Although previous studies were primarily carried out under static conditions, the dynamic structural change of Pd could be directly observed using *in situ* and quick measurement of Pd structure. For this purpose, energy-dispersive EXAFS (DXAFS) technique newly equipped in SPring-8 was applied for the measurement of the local structure of Pd during Pd oxidation.

Pd *K*-edge DXAFS was measured at beamline **BL28B2**. An Si polychromator crystal was used in a Laue configuration with (422) net plane to obtain an X-ray beam with a dispersed energy region. The schematic configuration of DXAFS measurement is shown in Fig. 1. A waferlike sample was placed in a quartz in situ cell. The sample was heated from room temperature to 773 K with ramping rate of 5 K min^{-1} in an O_2 flow at atmospheric pressure. The spectra measured for 0.3 sec were accumulated 10 times in every 10 K. An example of raw spectra for Pd/H-ZSM-5 (Si/Al_2 = 23.8) is shown in Fig. 2. It was confirmed that data with a high S/N ratio could be obtained despite the low concentration of Pd (0.4 wt%). Fourier transforms of the $k^3\chi(k)$ EXAFS for Pd loaded Na- and H-ZSM-5 were shown in Fig. 3. The coordination numbers of Pd-O, Pd-Pd (metal) and Pd-(O)-Pd (oxide) calculated based on the curve fitting analysis were given in Fig. 4. Initially, the formation of metal Pd was observed from the appearance of an intense nearest-neighboring Pd-Pd peak situated at 0.25 nm on both Pd/H-ZSM-5 and Na-ZSM-5. From the coordination number of the Pd-Pd peak, the Pd particle was supposed to locate on the external surface of zeolites. In the case of Pd/Na-ZSM-5 (Fig. 3(a)), the Pd-Pd (metal) gradually reduced accompanied by increasing the temperature in an oxygen flow. Alternatively, new peaks appeared at 0.15 and 0.32 nm. These peaks could be assigned to the Pd-O and Pd-(O)-Pd characteristic of bulk PdO that is apparent from the comparison with the

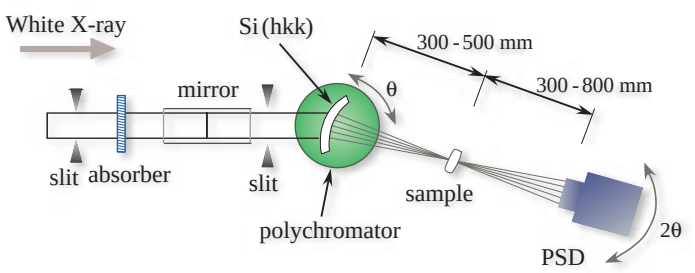

Fig. 1. Schematic view of DXAFS spectrometer with Laue configuration.

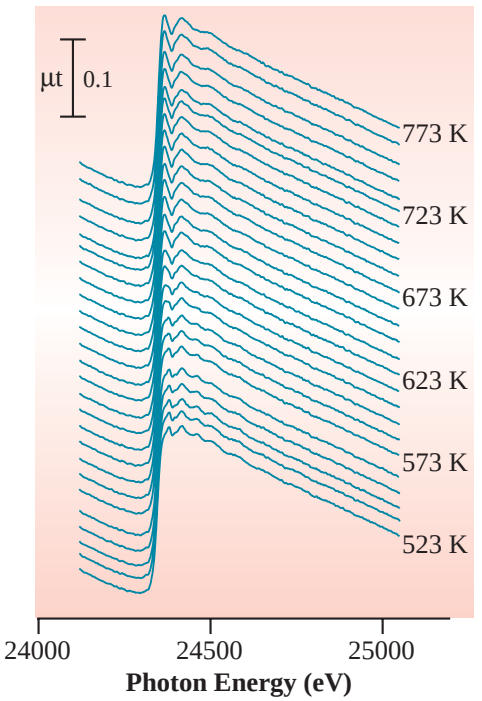

Fig. 2. Pd *K*-edge XAFS spectra for Pd (0.4 wt%) loaded on H-ZSM-5 (Si/Al_2 = 23.8) measured in an O_2 flow.

spectrum of bulk PdO. The generation of the Pd-(O)-Pd indicated that the metal Pd was simply transformed into the agglomerated PdO on the external surface of Na-ZSM-5 at elevated temperature. On the other hand, the metal Pd-Pd peak steeply disappeared at 643 K in the spectra of Pd/H-ZSM-5 (Fig. 3(b)). At the same time, the intensity of the Pd-O peak increased, indicating that the oxidation of metal Pd progressed with increasing the temperature. However, in contrast to the Na form of zeolites, the Pd-(O)-Pd peak due to the agglomerated PdO did not appear. The fact indicated that the agglomerated metal Pd was migrated on the acid sites of zeolites to generate highly dispersed PdO, because the intensity of Pd-(O)-Pd shell reflected the size of PdO. In addition, the data suggested that the migration of Pd occurred immediately after the oxidation of the metal Pd particle since the oxidation and the dispersion of Pd took place at the same time, which was confirmed from the data given in Fig. 4(b). Another dispersion process of PdO was revealed from the comparison with H-ZSM-5 and Na-ZSM-5. That is to say, the transformation of the metal Pd-Pd into Pd-O was steep and occurred at lower temperature over H-ZSM-5 with respect to Na-ZSM-5. Taking this into consideration, it could be assumed that, in addition to spontaneous dispersion of PdO, the oxidation of metal Pd was promoted through the strong metal-support interaction between acid sites of H-ZSM-5 and PdO which possessed basic character.

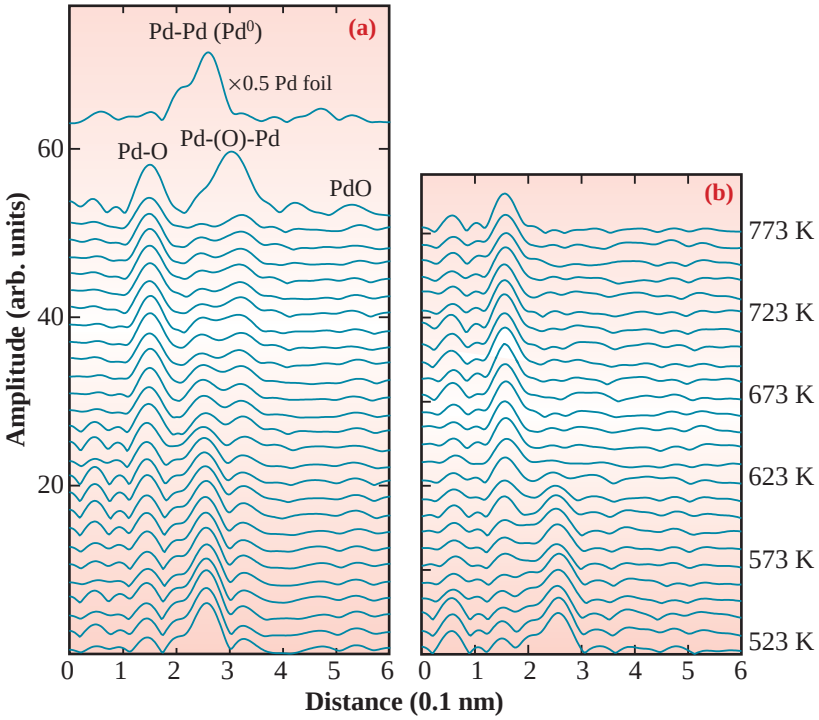

Fig. 3. Pd *K*-edge EXAFS Fourier transforms for Pd loaded on **(a)** Na-ZSM-5 (Si/Al_2 = 23.8) and **(b)** H-ZSM-5 (Si/Al_2 = 23.8) measured in an O_2 flow; Pd loading, 0.4 wt%; temperature ramping rate, 5 K min^{-1}. The spectra of PdO and Pd foil were collected at room temperature.

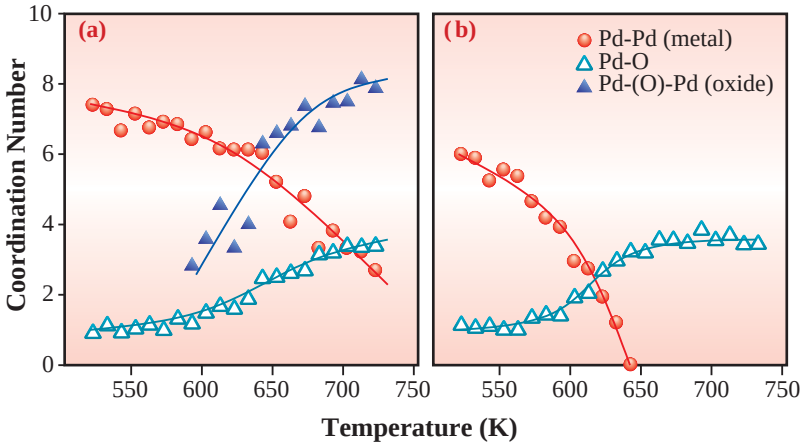

Fig. 4. Relationship between the coordination numbers of Pd loaded on **(a)** Na-ZSM-5 and **(b)** H-ZSM-5 and the temperature measured in an O_2 flow.

Kazu Okumura[a] and Kazuo Kato[b]

(a) Faculty of Engineering, Tottori University
(b) SPring-8 / JASRI

E-mail: okmr@chem.tottori-u.ac.jp

References

[1] K. Okumura, R. Yoshimoto, T. Uruga, H. Tanida, K. Kato, S. Yokota and M. Niwa: J. Phys. Chem. B **108** (2004) 6250.
[2] K. Okumura *et al.*: Phys. Scripta - in press.
[3] K. Okumura *et al.*: Chem. Lett. **32** (2003) 636.
[4] K. Okumura and M. Niwa: Catal. Surv. Jpn. **5** (2002) 121.

Annealing Effect on Surface Crystal Structure of Polyethylene Thin Films

The molecular aggregation structure at the surface of polymeric materials is strongly related to their physical properties such as friction and adhesion. However, the intrinsic features of the molecular aggregation structure at the surface of crystalline polymers have not yet been clarified on the molecular scale. We have been investigating the crystal structure at the solid surface of polyethylene (PE), a typical example of crystalline polymers, by grazing incidence X-ray diffraction (GIXD) measurements. In the case of melt-crystallized PE thin films, it was revealed that the lattice dimension in the in-plane direction was smaller in the near-surface region than in the bulk region. Moreover, we found for the first time that the paracrystalline lattice distortion in the in-plane direction was larger in the near-surface region than in the bulk region but the crystallite size was almost the same between these two regions [1]. On the other hand, Burell and Wehrum *et al.* reported the local alignment of polymer chains at the surface of spin-cast poly(ethylene telepthalate) thin films during annealing [2]. In order to control the surface structural and physical properties of polymeric materials, it is important to clarify the chain packing structure at the surface of crystalline polymers under various conditions. In this study, the annealing effect on crystal structure at the surface was investigated for PE thin films by synchrotron-source GIXD measurements.

High-density polyethylene without additives (HDPE; Hizex 1300J, MI = 14, Mitsui Chemicals, Inc.) was used as a sample. Thin films with a thickness of *ca.* 400 nm were prepared onto silicon substrates from a *p*-xylene solution of HDPE by a dip-coating method. Thus, the obtained films were annealed at various temperatures (T_a) for 24 hours under nitrogen atmosphere. Figure 1 shows the schematic geometry of the in-plane GIXD measurement. In order to measure reflections from crystallographic planes perpendicular to the sample surface, in-plane GIXD measurements were carried out for the films at beamline **BL13XU** [3] using incident X-rays with a wavelength of 0.1280 nm. When the incident angle (α_i) of X-rays to the sample surface is smaller than the critical angle (α_c), the X-rays undergo total external reflection and penetrate into the sample as evanescent waves. Around α_c, the penetration depth changes drastically from several micrometers to several nanometers. Therefore, surface-sensitive and bulk-sensitive profiles were obtained by in-plane GIXD measurements at α_i = 0.11° (< α_c) and 0.20° (> α_c), respectively.

Figure 2 shows the annealing temperature dependence of the lattice constants *a*, *b* and *c* of the orthorhombic unit cell in the near-surface and bulk regions of HDPE thin films calculated on the basis of in-plane GIXD profiles. The *a* and *b* in the near-surface region of the as-prepared films were smaller than those in the bulk region. This tendency was also observed for the films annealed at high T_a which would be released from residual stress induced by dip-coating. Therefore, in-plane GIXD analysis implied that the crystal density in the near-surface region would be essentially higher than that in the bulk region. In the near-surface region, PE chains were considered to be packed closely together to minimize the surface free energy of the films.

Paracrystalline lattice distortion in the in-plane direction was evaluated with the (110) reflection and its higher-order reflections on the basis of the paracrystalline lattice analysis proposed by Hosemann [4]. In the paracrystalline lattice model, the lattice vectors of adjacent unit cells vary in magnitude and direction due to the large displacement of lattice points from their ideal positions, which results in a loss of the long-range crystallographic order. The integral width $\delta\beta$ of a

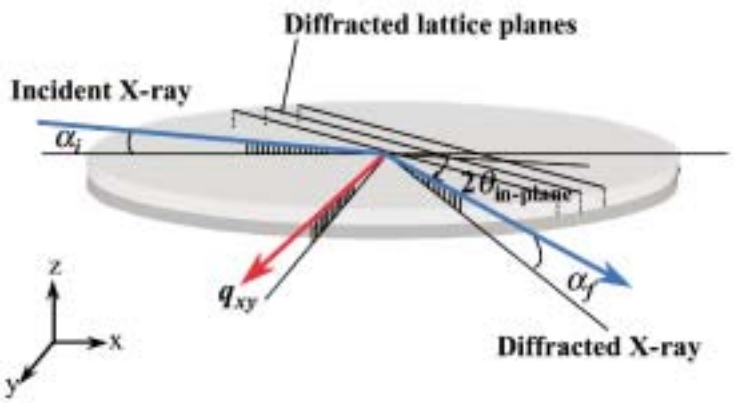

Fig. 1. Schematic geometry of the in-plane GIXD measurement. α_i : incident angle, α_f : take-off angle, q_{xy} : scattering vector.

reflection is expressed by $(\delta\beta)^2 = (1 / \tilde{a}^2)[(1 / N^2) + \pi^4 g^4 h^4]$. Here, g is the standard deviation of the Gaussian distribution divided by the average lattice vector $\tilde{a}$, h is the scattering order and N is the number of scattering units. In other words, g is a parameter used to evaluate the degree of paracrystalline disorder and N corresponds to crystal size. Figures 3(a) and 3(b) show the annealing temperature dependences of $g_{(110)}$ and $N_{(110)}$ in the in-plane [110] direction in the near-surface and bulk regions of the HDPE thin films, respectively. In the case of the as-prepared films, the (220) reflection from the near-surface region was not clearly detected. This indicated extremely large lattice distortion. Also, the $g_{(110)}$ in the near-surface region of the annealed films was larger than that in the bulk region. Therefore, paracrystalline lattice distortion in the in-plane direction would be essentially larger in the near-surface region than in the bulk region. On the other hand, the $N_{(110)}$ in the near-surface region was smaller than or the same as that in the bulk region. The decrease in $g_{(110)}$ and the increase in $N_{(110)}$ from T_a = 343 K to 393 K were large in the near-surface region. These results suggest that structural reorganization accompanying partial-melting and recrystallization drastically occurred in the near-surface region of the films.

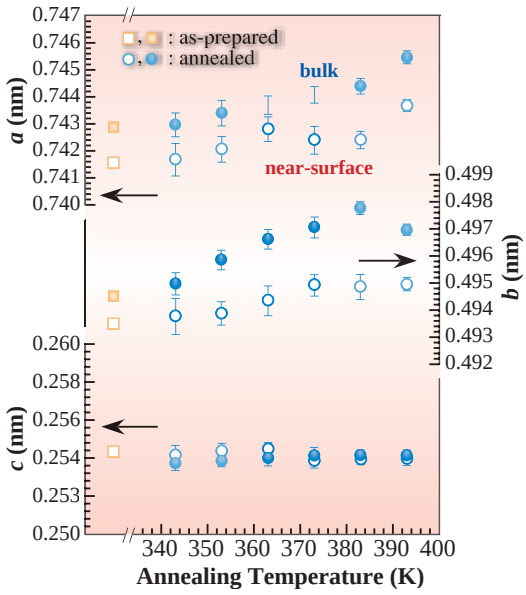

Fig. 2. Annealing temperature dependence of the lattice constants a, b and c of the orthorhombic unit cell in the near-surface and the bulk regions measured for dip-coated HDPE thin films. Open circles: near-surface region, filled circles : bulk region.

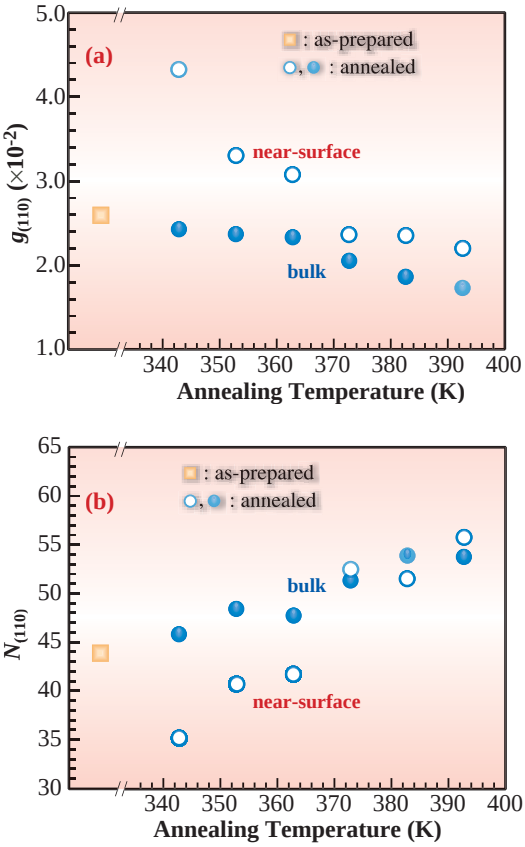

Fig. 3. Annealing temperature dependence of $g_{(110)}$ **(a)** and $N_{(110)}$ **(b)** for dip-coated HDPE thin films. Open circles: near-surface region, filled circles: bulk region.

Sono Sasaki[a,*], Atsushi Takahara[b] and Tisato Kajiyama[c]

(a) Graduate School of Engineering, Kyushu University
(b) Institute for Materials Chemistry and Engineering, Kyushu University
(c) Kyushu University

Present address : SPring-8 / JASRI

E-mail: sono@spring8.or.jp

References

[1] H. Yakabe, S. Sasaki, O. Sakata, A. Takahara and T. Kajiyama: Macromolecules **36** (2003) 5905.
[2] M. Durell *et al.*: Europhys. Lett. **58** (2002) 844.
[3] O. Sakata, *et al.*: Surf. Rev. Lett. **10** (2003) 543.
[4] P.H. Lindenmeyer and R. Hosemann: J. Appl. Phys. **34** (1963) 42.

Analysis of Interfacial Nanostructure of Organic Nanoelectronics Materials

The molecular aggregation structure of organic thin films has received much attention because of their applications to various electronic devices such as light-emitting diodes, field-effect transistors (FET) and photovoltaic cells. A central concern with respect to the performance of organic electronic devices such as FET is that their switching speed is generally too low owing to the low mobility of the charge carriers. One of the factors influencing the magnitude of carrier mobility may be the surface and interfacial molecular aggregation structures of the organic thin films. Grazing incidence X-ray diffraction (GIXD) using evanescent X-rays is an excellent method for characterizing the surface and interfacial molecular aggregation structures of organic polymer thin films [1,2]. In this study, the surface nanostructure of poly (3-hexylthiophene) (P3HT) and pentacene thin films was investigated by means of GIXD.

Pentacene and P3HT were used as samples in this study. GIXD measurements were carried out at beamline **BL13XU**. When the incident angle to the surface of a sample (α_i) is below the critical angle (α_c) in the GIXD measurements, X-rays undergo total external reflection and penetrate into the sample as evanescent waves. Under this condition, diffractions from the ultrathin films are sufficiently strong in intensity to be detected as peaks. The GIXD measurements of pentacene and P3HT thin films were carried out at a α_i smaller than the value of α_c. Bragg diffractions from the crystallographic planes normal to the sample surface were measured in the in-plane direction by a scintillation counter. The scattering vector parallel to the sample surface is defined as q_{xy} (= $2\pi/d = 4\pi \sin\theta/\lambda$) where d, θ, and λ are the d-spacing, the Bragg angle, and the wavelength of incident X-rays, respectively.

In order to develop polymer semiconductors, the crystal structure of polyalkylthiophene has been studied extensively. P3HT thin films prepared on Si substrates by spin-coating and a P3HT powder sample were annealed at 473 K for 30 min. Figure 1 shows the $2\theta/\theta$ symmetric reflection and in-plane GIXD profiles of the annealed P3HT films, and a powder diffraction profile of the annealed P3HT. On each profile for the films and the powder sample, the effect of annealing was apparent due to sharpening of the diffraction peaks, the appearance of higher order peaks and a decrease in intensity of the amorphous scattering. The powder diffraction profile showed the (100) reflection and its higher order reflections corresponding to the side-chain lamellar stacking distance (d_{110} = 1.60 nm) as well as the (010) reflection (d_{010} = 0.38 nm) corresponding to the π–π stacking of the thiophene ring in the main chain. In the symmetric reflection profile, the relative intensity of the (100) reflection and its higher order reflections up to the

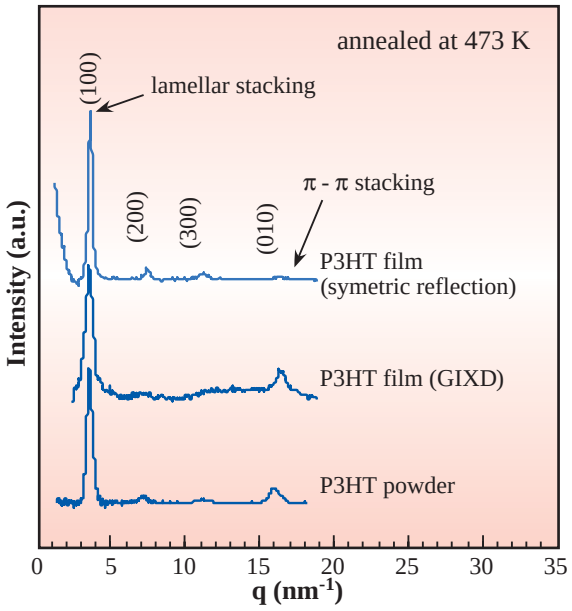

Fig. 1. $2\theta/\theta$ symmetric reflection and in-plane grazing incidence X-ray diffraction (GIXD) profiles of the annealed poly(3-hexylthiophene) (P3HT) films, and a powder diffraction profile of the annealed P3HT.

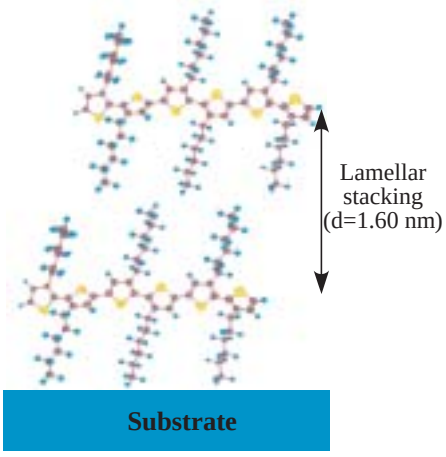

Fig. 2. Schematic representation of the chain orientation in P3HT film.

(010) reflection was very strong. This result indicated that the main chains had a tendency to orient parallel to the film surface (Fig. 2). On the other hand, the in-plane GIXD profile exhibited the (010) reflection corresponding to the π–π stacking of the thiophene ring, as well as the (100) reflection. A comparison between the symmetric reflection and GIXD profiles revealed that the degree of side-chain lamellar orientation was relatively low in the near-surface region. The control of orientation of the conjugated lamellae is expected to control the anisotropic carrier mobility.

Pentacene is a candidate molecule for the semiconducting layer in organic FET. Since pentacene is not soluble in a conventional organic solvent, most thin films of pentacene have been prepared by vapor phase deposition or molecular beam deposition. Breem *et al.* reported that the introduction of the polar group to pentacene by a Diels-Alder reaction (Fig. 3) enhanced the solubility of pentacene in organic solvents [3]. In this study, the thus-prepared pentacene precursor was spin-coated onto Si substrates and annealed at 453 K for 60 min. The powder diffraction profile for the precursor changed under annealing, due to the elimination of N-sulfinylacetamide from the precursor by a retro Diels-Alder reaction. Annealing treatment for the spin-coated films of the precursor also yielded crystalline thin films of pentacene. Figure 4 shows the $2\theta/\theta$ symmetric reflection and GIXD profiles of pentacene thin films, and a powder diffraction profile of pentacene prepared using a soluble pentacene precursor. The (00*l*) reflections were only observed in the symmetric reflection profile. This indicates the possibility of a perpendicular orientation of the c axis to the film surface. Also, the GIXD profile showed a strong diffraction that would relate to regular interchain packing between the aromatic rings in the in-plane direction. These results suggests that the pentacene molecules were oriented almost perpendicular to the film surface.

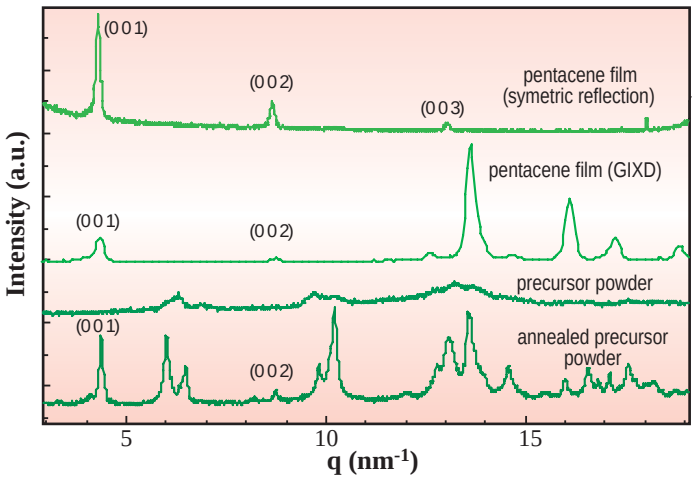

Fig. 4. $2\theta/\theta$ symmetric reflection and in-plane grazing incidence X-ray diffraction (GIXD) profiles of the pentacene films, and powder diffraction profiles of the pentacene precursor and pentacene. Pentacene was prepared from the pentacene precursor through retro Diels-Alder reaction.

In this study, it was revealed that the synchrotron-sourced GIXD measurement is a powerful method for characterizing the state of molecular orientation in organic electronics materials. Further study is now in progress in order to clarify the relationships between semiconductor performance and molecular aggregation states at the surfaces and interfaces.

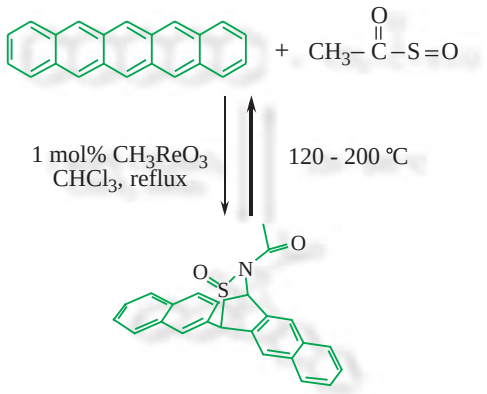

Fig. 3. Diels-Alder and retro Diels-Alder reactions of pentacene. Pentacene was reacted with excess N-sulfinylacetamide in the presence of a catalytic amount of methyltrioxorhenium to give the Diels-Alder adducts (pentacene precursor). The Dielas-Alder adducts then undergoes a retro-Diels Alder reaction starting at 398 K to yield pentacene.

Atsushi Takahara[a], Masamichi Morita[b] and Sono Sasaki[b,c]

(a) Institute for Materials Chemistry and Engineering, Kyushu University
(b) Graduate School of Engineering, Kyushu University
(c) Present address: SPring-8 / JASRI

E-mail: takahara@cstf.kyushu-u.ac.jp

References

[1] T. Koga, M. Morita, H. Ishida, H. Yakabe, S. Sasaki, O. Sakata and A. Takahara: Trans. Mater. Res. Soc. Jpn. **28** (2003) 85.
[2] H. Yakabe *et al.*: Macromolecules **36** (2003) 5905.
[3] A. Afzail *et al.*: J. Am. Chem. Soc. **124** (2002) 8812.

Real-time *in situ* photoemission spectroscopy for the analysis of Si(001) oxidation induced by supersonic O_2 molecular beams

The analysis of chemical phenomena occurring at the gas-solid interface is a fundamental step in research to understand and control surface chemical reactions. In particular, it is considerably essential to realize and control surface chemical reactions with respect to the recent development of nanotechnologies which require the atomicscale manipulation in terms of device sizes and chemical compositions. Photoemission spectroscopy combined with soft X-ray synchrotron radiation, which offers the advantages of energy resolution, intensity, beam size and wide energy regions, is a powerful experimental technique for observing the chemical composition and chemical bonds on solid surfaces. Furthermore, we can *in situ* monitor the time-evolution of chemical species on the solid surface in the core-level photoemission spectra during chemical reactions.

Here, we demonstrate the advantages of real-time *in situ* photoemission spectroscopy combined with a high-performance soft X-ray synchrotron radiation source for the monitoring of chemical reactions on solid surfaces. The real-time monitoring of oxidation on the Si(001) surface induced by translational kinetic energy of O_2 at room temperature is reported. This reaction system is an important subject, not only for the semiconductor industry, but also in terms of the reaction dynamics in surface science [1-4].

The SUREAC2000 [5], especially designed for the analysis of surface chemical reactions at beamline **BL23SU**, was used for all experiments. An important advantage of the SUREAC2000 is that *in situ* photoemission measurements with synchrotron radiation can be carried out under supersonic molecular beam (SSMB) irradiation on solid surfaces. The photon energy resolution was better than 100 meV and the photon flux was on the order of 10^{11} photons•s^{-1}. Photoelectrons were collected with a 125 mm hemispherical electron energy analyzer (Omicron Nano Technology, GmbH) with five channeltrons. The excitation energies for the O-1*s* and Si-2*p* core levels were 830 eV and 409 eV, respectively. The analysis depth from the surface was roughly estimated to be 0.7 nm.

The O_2 beam with the kinetic energy of 2.2 eV was exposed to the n-type Si(001) substrate at 9 degrees from the surface normal at room temperature.

Figure 1 shows representative high-energy-resolution Si-2*p* photoemission spectra obtained by real-time *in situ* measurements taken during irradiation of the O_2 SSMB. The O_2 dose is indicated in Langmuir units (1L = 1.3 × 10^4 Pa•s). It took approximately 40 s to obtain an Si-2*p* and an O-1*s* photoemission spectrum. Peak deconvolution was performed to obtain the components related to Si oxidation by the curve fitting procedure. The spin-orbit splitting between Si2$p_{1/2}$ and Si2$p_{3/2}$ was set to be 0.6 eV. Prior to the curve fitting, the backgrounds

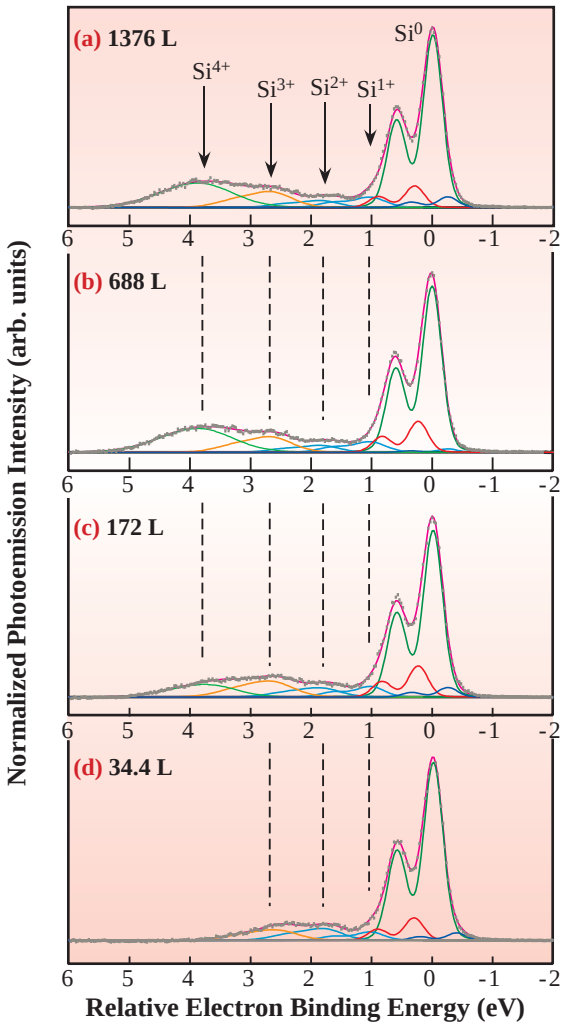

Fig. 1. Representative high-resolution Si-2*p* photoemission spectra for the real-time *in situ* observation of oxidation on a Si(001)- 2×1 surface induced by O_2 molecular beams at room temperature.

in the photoemission spectrum were numerically eliminated using the Tougaard method. The photoemission intensity ratio (Si2$p_{1/2}$/Si2$p_{3/2}$) was assumed to be 0.5 according to their statistical weights. Core level shifts related to the Si oxidation were estimated to be 1.00 (Si^{1+}), 1.82 (Si^{2+}), 2.62 (S^{3+}) and 3.67 (Si^{4+}) eV, with respect to the binding energy of the bulk Si-2$p_{3/2}$ peak position. Furthermore, α (0.23eV) and β (-0.26eV) were due to the slight distortion in the bond angles at the interface Si atoms. With increasing molecular beam exposure, the oxide components gradually increased without shifts of their peak positions.

Figure 2 shows the time evolution of (a) the oxide thickness, (b) the oxygen amount and (c)-(f) the intensities of each oxide component (Si^{4+}, Si^{3+}, Si^{2+} and Si^{1+}) normalized by the oxide thickness. As shown in Figs. 2 (a) and (b), the oxide thickness and the O-1*s* photoemission intensity drastically increased with irradiation doses less than 50L and then gradually increased. The saturated thickness of the oxide layers was estimated to be approximately 0.57 nm from the backbond oxidation of the subsurface Si layers. Time evolutions of the suboxide components are illustrated as a function of the O_2 dose in Figs. 2 (c) to (f). Since the Si^{4+} species is not observed at the early stage of molecular beam irradiation, up to 34.4L, the topmost Si dimer atoms are hardly surrounded by four oxygen atoms in the initial oxidation stage. As shown in Fig. 2 (d) and (f), the Si^{1+} and the Si^{3+} components gradually decrease with increasing the oxide thickness. This result indicates that the number of Si^{1+} and Si^{3+} atoms per unit oxide thickness is nearly constant, regardless of the oxide growth. The Si^{1+} species remain at the interface between the oxide layers and Si(001) substrate, whereas the Si^{3+} species are distributed over all oxide layers. As shown in Fig. 2(e), the amount of Si^{2+} species decreased with increasing amounts of Si^{4+}, whereas the amounts of Si^{1+} and Si^{3+} were virtually unchanged. This result indicates that the Si^{4+} species was directly converted from the Si^{2+} species.

Using real-time photoemission spectroscopy, we clarified the reaction mechanisms of oxidation on a Si(001) surface induced by the incident energy of O_2 at room temperature. In conclusion, we succeeded in showing that real-time photoemission spectroscopy using synchrotron radiation is a powerful method for investigating the surface chemical reactions from the viewpoints of kinetics and dynamics.

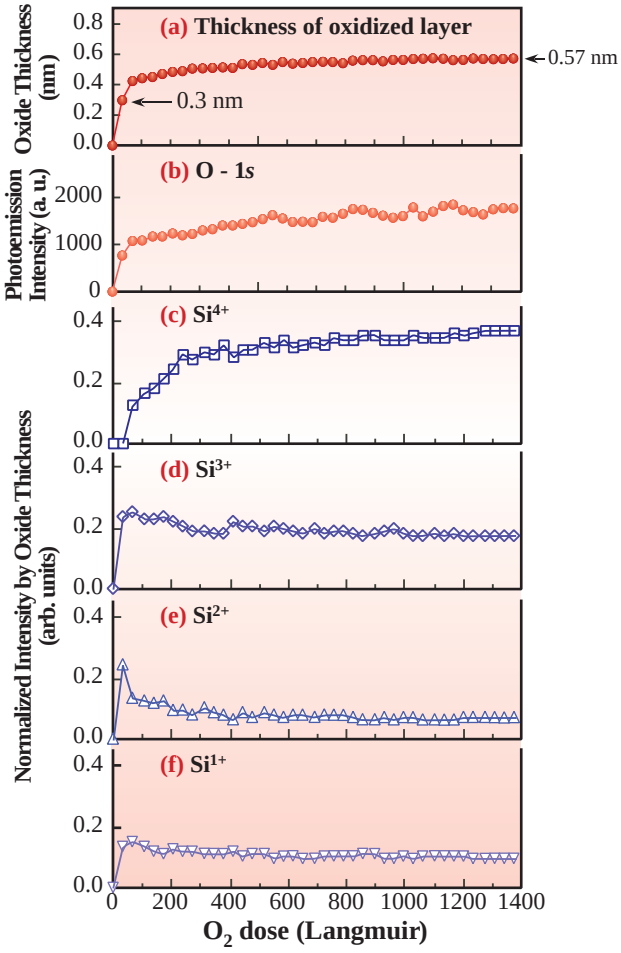

Fig. 2. Variation of **(a)** oxide thickness, **(b)** the O-1*s* photoemission intensity and **(c)-(f)** each Si-2*p* oxide component area intensity as a function of O_2 irradiation dose. Intensities for the Si-2*p* oxide components were normalized by the oxide thickness.

Akitaka Yoshigoe and Yuden Teraoka

SPring-8 / JAERI

E-mail: yoshigoe@spring8.or.jp

References

[1] A. Yoshigoe and Y. Teraoka: Appl. Surf. Sci. **190** (2002) 60.
[2] A. Yoshigoe and Y. Teraoka: Surf. Sci. **532-535** (2003) 690.
[3] A. Yoshigoe and Y. Teraoka: Surf. Interface Anal. **34** (2002) 432.
[4] A. Yoshigoe, K. Moritani and Y. Teraoka: Jpn. J. App. Phys. **42** (2003) 4676.
[5] Y. Teraoka *et al.*: Jpn. J. Appl. Phys. **38** Suppl. 38-1 (1999) 642; Appl. Surf. Sci. **169-170** (2001) 738.

Nuclear Resonance Vibrational Spectroscopy (NRVS) of Hydrogen and Oxygen Activation by Biological Systems

The enzymes nitrogenase (N_2ase), hydrogenase (H_2ase), methane monooxygenase (MMO), and cytochrome P-450 catalyze environmentally or medically critical reactions [1]. These proteins all contain Fe in their active sites. Although crystal structures are available for resting forms (Fig. 1), many key intermediates can only be observed by spectroscopy. The goal of our program is to use nuclear resonant vibrational spectroscopy (NRVS) to characterize the structures of these intermediates. This information will help to better define catalytic mechanisms, and it may eventually prove useful for the development of synthetic small molecule 'mimics' that can catalyze the same reactions.

NRVS is a relatively new technique that involves scanning an extremely monochromatic X-ray beam through a nuclear resonance [4-6]. Apart from the familiar 'zero phonon' Mössbauer resonance, there are additional transitions that correspond to nuclear excitation in combination with the excitation (Stokes) or de-excitation (anti-Stokes) of vibrational modes. For ^{57}Fe, the nuclear resonance is at 14.412 keV, and vibrational linewidths are less than 1 meV. The experiments therefore require a strong, tunable source with a resolution on the order of 10^{-7}. Only a third-generation synchrotron radiation source such as SPring-8 can provide sufficient spectral brightness to make such measurements feasible. Experiments were carried out at beamline **BL09XU**.

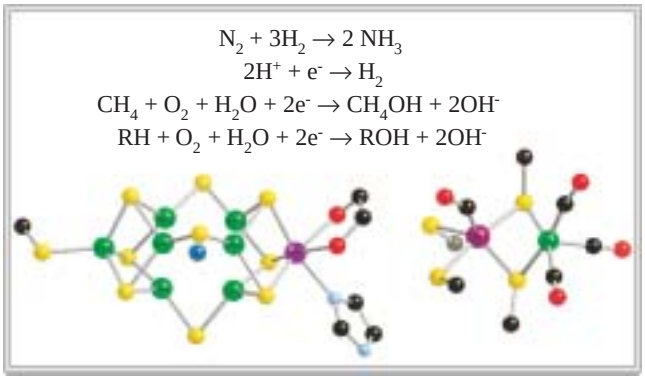

Fig. 1. Active site crystal structures for two key enzymes in this project. Left: high-resolution crystal structure of *Azotobacter vinelandii* N_2ase M center (PDB 1M1N) [2]. Sulfur atoms are drawn in yellow, oxygen in red, and carbon in black. Right: high-resolution crystal structure for a CO-inhibited form of *Desulfovibrio vulgaris* Miyazaki F H_2ase [NiFe] center (PDB 1UBJ) [3]. One or two of the CO ligands to Fe may well be CN^- instead. In the active forms of the enzyme, CO is not bound to Ni, and there are proposals that a hydride ion bridges the Ni and Fe ions.

Since metalloprotein samples are dilute, only a small fraction of the incident beam is absorbed in the NRVS process. The measurement technique exploits the relatively long lifetime of the nuclear excitation, along with the pulsed nature of the synchrotron source, by electronically gating the Fe Kα emission that occurs following internal conversion in between synchrotron pulses (Fig. 2).

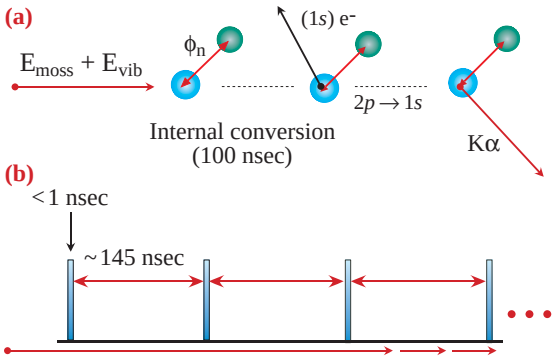

Fig. 2. **(a)** Chemist's view of the NRVS process. A photon excites a nucleus in the system to an excited state (E_{moss}), along with promoting the system to a higher vibrational level (E_{vib}). The nucleus relaxes (primarily) by internal conversion (emission of a core electron) followed by Kα fluorescence. **(b)** The NRVS detection scheme relies on gating the detector only during an interval between prompt synchrotron pulses.

In principle, clusters such as the FeMo-cofactor and the [NiFe] cluster have dozens of discrete normal modes that require hundreds of parameters for the definition of vibrational frequencies. One approach to simplifying the problem depends on model compounds and Urey-Bradley force fields to derive a set of transferable parameters for the Fe-S clusters. In this 'aufbau' approach, one starts with mononuclear tetrahedral compounds, and then builds up to binuclear, trinuclear, and more complex structures. As seen in Fig. 3, the spectra of Fe-S clusters divide approximately into high-frequency modes with a strong Fe-S stretching motion, and a wide range of lower frequency bands. Low-frequency modes can be further subdivided into simple three-atom bends, more complex ruffling and twisting motions of the entire cluster, and lattice modes.

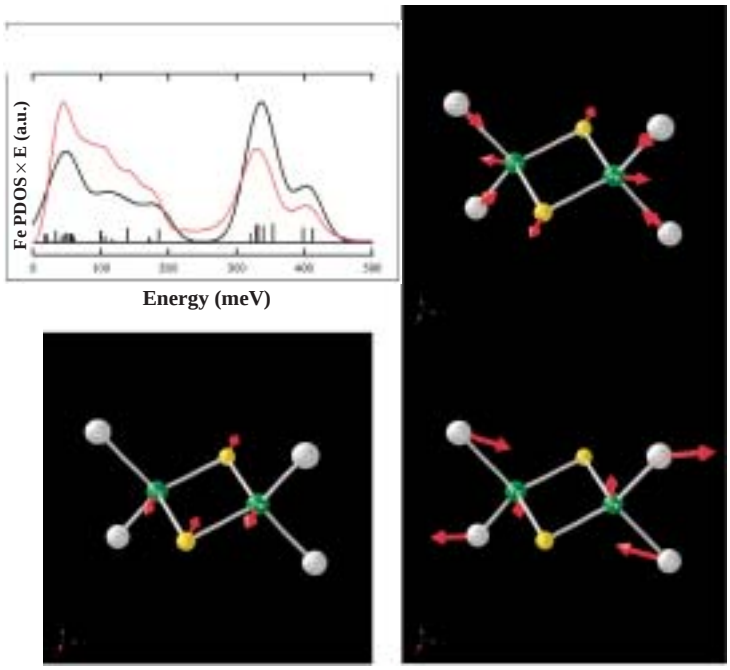

Fig. 3. Top left: spectrum (—) and simulation (— and sticks) for $(NEt_4)[Fe_2S_2Cl_4]$. Top right: the totally symmetric A_{1g} mode. Bottom left: the highest frequency B_{3u} mode, which combines with the A_{1g} mode to produce the > 400 cm^{-1} peak. Bottom right: the B_{3g} mode that contributes to the low frequency intensity near 100 cm^{-1}. The cluster of features around 50 cm^{-1} has been assigned to the lattice vibrations of the entire cluster. The normal modes in all figures were calculated using the 'VIBRATZ' analysis program from Shape Software (http://www. shapesoftware.com/).

The N_2 ase spectrum is significantly more structured than the $[Fe_2S_2Cl4]^{2-}$ spectrum (Fig. 4), partly because of the large number of Fe in the FeMo-cofactor, but also because of the presence of another eight Fe in the so-called 'P cluster' (not shown). Despite this complexity, the normal modes of FeMo-co are gradually becoming untangled (Fig. 4). The richness of these spectra, combined with relatively straightforward analysis procedures and the potential for isotopic substitution, suggest that NRVS will become a powerful tool for the characterization of metals in enzymes.

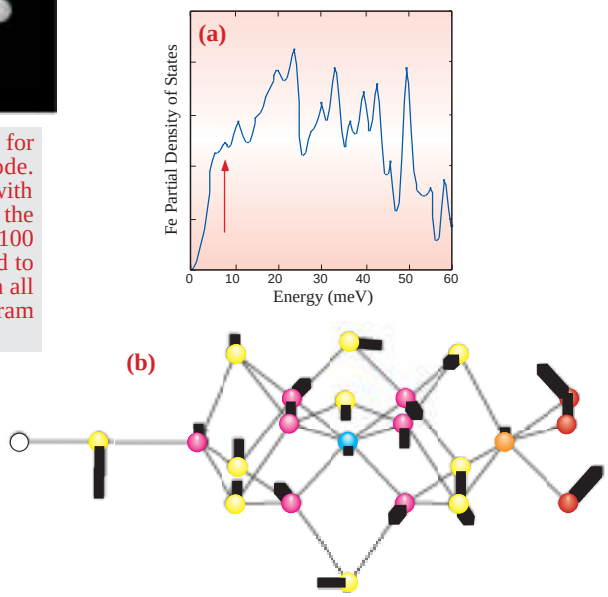

Fig. 4. **(a)** NRVS spectrum for the nitrogenase enzyme. **(b)** the twisting normal mode for the FeMo-cofactor cluster, predicted to occur around 10 meV in the NRVS spectrum. The cluster was simplified by making all Mo (orange) ligands oxygen atoms (red). Fe atoms are purple and Sulfurs are yellow.

References

[1] D. C. Rees, J. B. Howard: Science **300** (2003) 929.
[2] O. Einsle *et al.*: Science **297** (2002) 1696.
[3] H. Ogata *et al.*: J. Am. Chem. Soc. **124** (2002) 11628.
[4] U. Bergmann, W. Sturhahn, D.E. Linn, F.E. Jenney Jr., M.W.W. Adams, K. Rupnik, B.J. Hales, E.E. Alp, A. Mayse, S.P. Cramer: J. Am. Chem. Soc. **125** (2003) 4016.
[5] W. Sturhahn *et al.*: Phys. Rev. Lett. **74** (1995) 3832-3835.
[6] Y. Yoda *et al.*: Nucl. Instrum. Meth. A **467** (2001) 715.
[7] Y. Xiao, Y. Yoda, S.P. Cramer, S. George, D. Coucouvanis, M. Koutmos, K. Fisher - in preparation

Yuming Xiao[a,b], Yoshitaka Yoda[c] and Stephen P. Cramer[a,b]

(a) Department of Applied Science, University of California, USA
(b) Lawrence Berkeley National Laboratory, USA
(c) SPring-8 / JASRI

E-mail: spcramer@ucdavis.edu

Metal Complex Spread on Liquid Surface Studied by Polarization-dependent X-ray Absorption Spectroscopy

Recent advances in a total-reflection X-ray absorption fine structure (TR-XAFS) method allow us to investigate the solvation structure of ions at the air-water interface [1-3]. There is very little information on this phenomenon due to the lack of a suitable experimental technique; however, such information is important for colloid and solution chemistry. Further progress in the TR-XAFS method with linearly polarized X-rays described here has been achieved by introducing an X-ray phase retarder to the undulator beamline [4].

Experiments were carried out at the undulator beamlines **BL39XU** and **BL37XU**. The linearly polarized X-ray on the horizontal plane from the undulator was converted to a vertically polarized one using a diamond crystal phase retarder. The degree of linear polarization, P_L, is defined by the following equation: $P_L = (I_h - I_v) / (I_h + I_v)$, where I_h and I_v are the intensities of the polarized X-rays. P_L = -1 corresponds to a perfect linear polarization on the vertical plane. In the present setup, the P_L value was estimated to be approximately – 0.9 for the vertically polarized X-ray.

Various metalloporphyrins have been applied to photoenergy conversion systems as well as to supramolecular structures involving self-assembly features that could further improve the functionality of porphyrin-containing thin films organized by interfacial processes. In this work, we applied the polarized TR-XAFS method to a monolayer of planar zinc(II) porphyrin, *meso*-tetrakis(4-carboxyphenyl) porphyrinato zinc(II) (ZnTPPC), at the air-water interface in order to determine the coordination structure around zinc and the molecular orientation. Under the present acidic condition, four carboxyl groups of ZnTPPC are not dissociated, and consequently, the neutral form of ZnTPPC does not dissolve into the aqueous subphase.

The X-ray absorption near-edge structure (XANES) spectra at the Zn *K*-edge for ZnTPPC are displayed in Fig. 1. A XANES spectrum with a horizontally polarized X-ray (a) is different from that with a vertically polarized one (b); the most striking difference is the appearance of a very strong first peak at 9662 eV in Fig. 1(b), which must correspond to the shoulder structure of the powder sample (d) at the same energy, but is absent in the horizontal spectrum (a). The strong pre-edge or shoulder peak in the XANES spectrum at the Zn *K*-edge must be associated with the 1*s* - 4p_z transition in the absence of the axial coordination for zinc atoms, since the assignment of such a peak has been well established for square planar complexes [5]. The polarization dependence of the XANES spectrum indicates that the plane of the ZnTPPC molecule is unambiguously oriented parallel to the air-water interface and there is no coordination to the axial sites of the zinc atoms. On the other hand, the absence of any pre-edge peak in the spectrum for ethyl acetate solution in Fig. 1(c) suggests that the solvent molecules are coordinated to the axial sites of a zinc atom in ethyl acetate (Fig. 2).

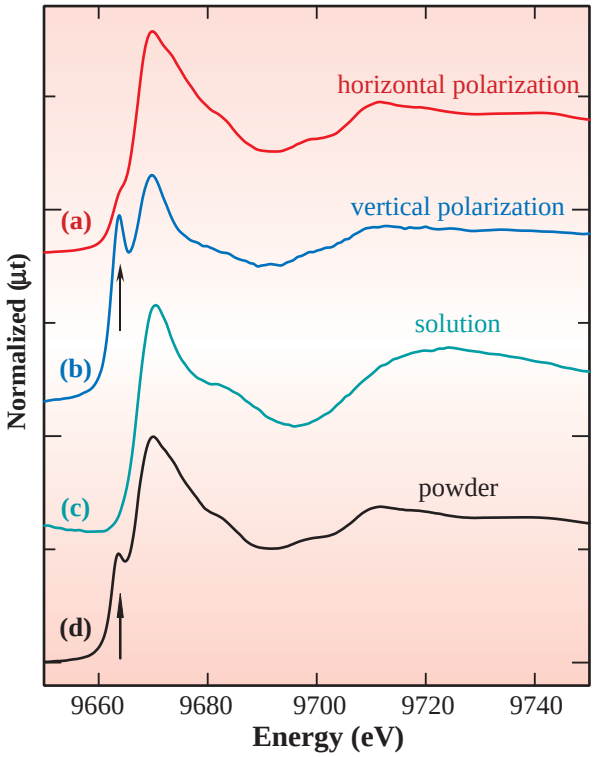

Fig. 1. XANES spectra at the Zn *K*-edge for ZnTPPC spread as a monolayer in the acidic aqueous solution taken with **(a)** horizontal and **(b)** vertical polarization by the TR-XAFS method, **(c)** in the ethyl acetate solution by the fluorescence mode, and **(d)** in the solid powder by the transmission mode.

XAFS is a powerful technique for clarifying the coordination structure in a complex around a metal center. The present results clearly demonstrate that the TR-XAFS method enable the determination of the orientation of a planar complex at the air-water interface in a very simple manner by introducing polarized X-rays. Furthermore, EXAFS analysis would allow us to characterize the molecular structure of metal complex at the interface within the horizontal or the vertical plane separately, e.g., solvation and coordination distances between metal and ligands involved in the self-assembled monolayer, or the Langmuir-Blodgett film formed or in process.

XAFS is a powerful technique for clarifying the coordination structure in a complex around a metal center. The present results clearly demonstrate that the TR-XAFS method enable the determination of the orientation of a planar complex at the air-water interface in a very simple manner by introducing polarized X-rays. Furthermore, EXAFS analysis would allow us to characterize the molecular structure of metal complex at the interface within the horizontal or the vertical plane separately, e.g., solvation and coordination distances between metal and ligands involved in the self-assembled monolayer, or the Langmuir-Blodgett film formed or in process.

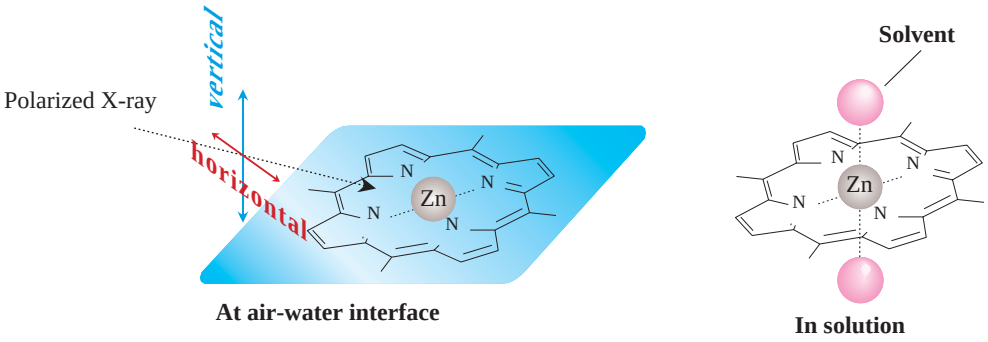

Fig. 2. Schematic drawing of the predicted molecular orientation of ZnTPPC at the air-water interface and the solvation structure in the solution.

Hirohisa Nagatani[a], Hajime Tanida[b] and Iwao Watanabe[c]

(a) Department of Natural Sciences, Hyogo University of Teacher Education
(b) SPring-8/JASRI
(c) Faculty of Science, Osaka Women's University

E-mail: nagatani@sci.hyogo-u.ac.jp

References

[1] I. Watanabe: SPring-8 Research Frontiers 1999/2000, p. 55.
[2] I. Watanabe *et al.*: Rev. Sci. Instrum. **68** (1997) 3307.
[3] I. Watanabe *et al.*: J. Am. Chem. Soc **119** (1997) 12018.
[4] H. Tanida, H. Nagatani and I. Watanabe: J. Chem. Phys. **118** (2003) 10369.
[5] A.I. Frenkel *et al.*: J. Chem. Phys. **116** (2002) 9449.

First Observation of Natural Circular Dichroism for Biomolecules in Soft X-ray Region using a Polarizing Undulator

Amino acids are well known chiral molecules, which have handedness or chirality. Right- and left-handed amino acids are called D- and L-amino acid. Life forms on the earth use only L-type amino acids to make proteins. This is known as the homochirality of amino acids (or proteins) in the body of life forms. Although almost all amino acids found in meteorites were a mixture of 50% D-amino and 50% L-amino acid (i.e., racemic), some meteorites such as the Merchison meteorite were found recently to have enrichment of L-amino acids [1]. Among various hypotheses for this enrichment, photochemical enrichment is studied extensively by several groups with the circularly polarized light from the ultraviolet-to-vacuum ultraviolet region using the abundant data of circular dichroism (CD), which is the difference in absorption coefficient μ between left and right circularly polarized lights; CD = $\mu_L - \mu_R$. However, no CD data was available in the soft X-ray region, at which the energy region interaction of electromagnetic waves and matter is violently stronger than the ultraviolet region. In this work, we attemped at the first time to detect the CD of biomolecules in the soft X-ray region [2]. The basic idea of this work is that the L- and D-amino acids should show CD spectra with the same magnitude but opposite signs and the racemic amino acid should show no CD just like the abundant data obtained in the ultraviolet region and the pioneering soft X-ray work of a metal complex by Goulon *et al.* [3].

The experiment was carried out at beamline **BL23SU** by mechanical switching the left and right polarized light with 0.1 Hz using a polarizing undulator. The values of μ_L and μ_R were determined from the sample photocurrent ***i*** divided by the incident photonumber I_0 estimated from the photocurrent of the focusing mirror M_3 for the left and right polarized light, respectively. Amino acid film samples were prepared on Cu-Be substrates by the vacuum sublimation technique. Film thickness was monitored during sublimation using a quartz oscillator thickness monitor and confirmed after sublimation by HPLC analysis. HPLC analysis also confirmed that no thermal decomposition occurred during vacuum sublimation. Figure 1 shows the molecular structures of L- and D-serine, and L- and D-phenylalanine used in this experiment.

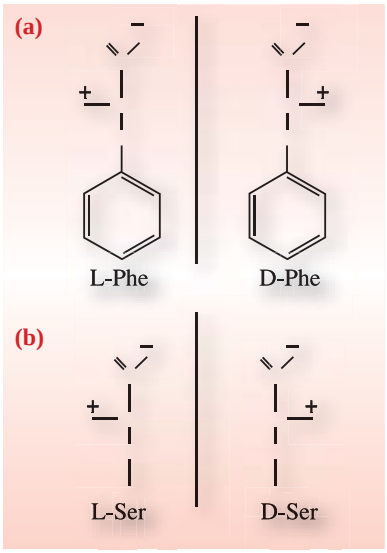

Fig. 1. Molecular structures of amino acids. **(a)** L- and D-phenylalanine, **(b)** L- and D-serine.

Figure 2 shows the absorption spectrum of a phenylalanine film (Fig. 2(a)) measured by us in the *K*-edge region of nitrogen atom, CD measured in this work (Fig. 2(b)), and result of the theoretical calculation (Fig. 2(c)) by Li Yang *et al.* [4]. As seen in the figure, the sign of CD spectrum of L-phenylalanine is opposite that of D-phenylalanine and the absolute magnitude of the CD spectrum of L-phenylalanine seems to be the same as that of D-phenylalanine. Although somewhat noisy, racemic phenylalanine seems to show no CD. Figure 3 shows, in the similar manner, the absorption spectra of serine film (Fig. 3(a)) in the *K*-edge region of oxygen atom, CD measured in this work (Fig. 3(b)), and result of the theoretical calculation (Fig. 3(c)) by Plashkevych *et al.* [5]. As seen in the figure, the sign of CD spectrum of L- serine is opposite that of D- serine and the absolute magnitude of the CD spectrum of L- serine seems to be the same as that of D- serine.

It should be noted that theoretical calculations by Yang *et al.* [4] and Plashkevych *et al.* [5] seem to reproduce our experimental result. However, the mechanism of CD is not yet clear. Both theoretical

calculations were carried out on the basis of the interference between the electric dipole (E1) and the magnetic dipole (M1) transitions. On the other hand, the ESRF group headed by Goulon ascribed many CD transitions in the hard X-ray region to be the E1-E2 interference mechanism. Moreover, in the UV-to-VUV region, the mechanism of CD is believed to be the E1-M1 mechanism. Because the soft X-ray region is the bridge energy region between UV and hard X-ray, the mechanism from which CD arises is a challenging subject for experimental and theoretical physicists and chemists.

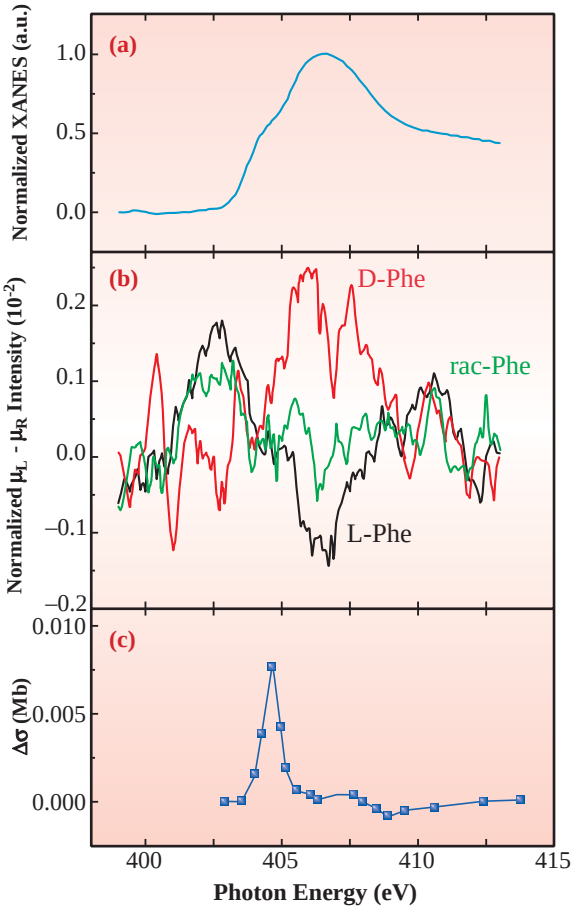

Fig. 2. **(a)** Absorption spectrum of a phenylalanine film. **(b)** CD spectra measured in this work. **(c)** Result of the theoretical calculation by Yang *et al.* [4].

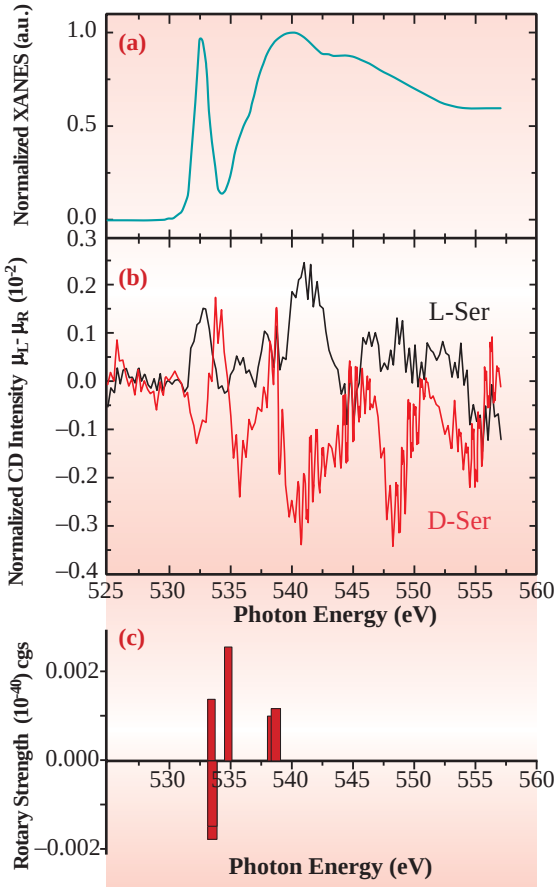

Fig. 3. **(a)** Absorption spectrum of a serine film. **(b)** CD spectra measured in this work. **(c)** Result of the theoretical calculation by Plashkevych *et al.* [5].

Kazumichi Nakagawa

Faculty of Human Development, Kobe University

E-mail: nakagawa@kobe-u.ac.jp

References

[1] J.R. Cronin and S. Pizzarello: Science **275** (1997) 951.
[2] M. Tanaka, K. Nakagawa, A. Agui, K. Fujii and A. Yokoya: Physica Scripta (2004) - in press.
[3] J. Goulon *et al.*: Jpn. J. Appl. Phys. **32** Suppl. (1993) 284.
[4] L. Yang *et al.*: J. Synchrotron Rad. **6** (1999) 708.
[5] O. Plashkevych *et al.*: Chem. Phys. **232** (1998) 49.

Developments of Lifetime-broadening-removed XANES Spectroscopy

X-ray absorption near-edge structure (XANES) is a powerful technique for studying electronic states around selected atomic species. XANES features are, however, often smeared out because of the natural lifetime width of the core holes. Intense monochromatic X-rays available at SPring-8 have made it possible to experimentally substantiate the observation of lifetime-broadening-removed (LBR) XANES from resonant inelastic X-ray scattering (RIXS) spectra [1]. In this article using CuO data it is demonstrated that 1*s*-LBR-XANES and 1*s* as well as 2*p*-LBR or lifetime-broadening-free (LBF) XANES can be deduced from experimental RIXS spectra.

The experiments were carried out at beamline **BL47XU**. The RIXS from powder CuO was analyzed with a spherically bent ϕ75 mm Si(444) crystal having an 820 mm radius of curvature, and detected by a scintillation counter. The overall resolution was 1.1 eV.

Figure 1 shows the excitation energy dependence of 1*s* 2*p* RIXS spectra of CuO [1]. Spectral shape and intensity change with excitation energy significantly. Excitation with X-ray energies well above the *K*-absorption edge energy yields a single band, which is the well-known Cu $K\alpha_1$. As the excitation energy is decreased, the main feature corresponding to the $K\alpha_1$ (A) is shifted down with its width broadened. By decreasing the excitation energy to ~ 8983 eV, a new branch (B) appears. Another feature labeled C is prominent at the excitation energy below 8983 eV, and is the strongest at the $1s \rightarrow 3d$ transition energy, ~ 8980 eV [2].

The differential cross section of 1*s* 2*p* RIXS process can be deduced from the well-known Kramers-Heisenberg equation [1,3]:

$$\frac{d\sigma(\omega_1)}{d\omega_2} \propto \int \frac{(\omega_2/\omega_1)(\Omega_{1s}+\omega)(dg_{1s}/d\omega)}{((\Omega_{1s}+\omega-\omega_1)^2+\Gamma_{1s}^2/4\hbar^2)((\Omega_{2p}+\omega_2+\omega-\omega_1)^2+\Gamma_{2p}^2/4\hbar^2)} d\omega \quad (1)$$

Here, $\hbar\omega_1$ and $\hbar\omega_2$ are incident and scattered photon energies, $\hbar\omega$ is the energy of the excited electron, and Γ_{1s} and Γ_{2p} are the widths of the 1*s* and 2*p* levels, the energies of which are represented by $\hbar\Omega_{1s}$ and $\hbar\Omega_{2p}$, respectively. The $dg_{1s}/d\omega$ corresponds to LBF-XANES profile.

Under the approximation that $\Gamma_{2p}/\hbar << 1$, Eq. (1) can be transformed in to Eq. (2) [1,3]:

$$\frac{d\sigma(\omega_1)}{d\omega_2} \propto \frac{(\omega_2/\omega_1)\,\omega_{abs}(dg_{1s}/d\omega_{abs})}{(\Omega_{1s}-\Omega_{2p}-\omega_2)^2+\Gamma_{1s}^2/4\hbar^2}, \quad (2)$$

where $\omega_{abs} = \Omega_{1s}+\omega$. Equation (2) allows us to calculate $dg_{1s}/d\omega$ analytically from the experimental RIXS spectra directly. The $dg_{1s}/d\omega$ derived (LBR-XANES) is free from the Γ_{1s} broadening and the width is determined only by Γ_{2p}.

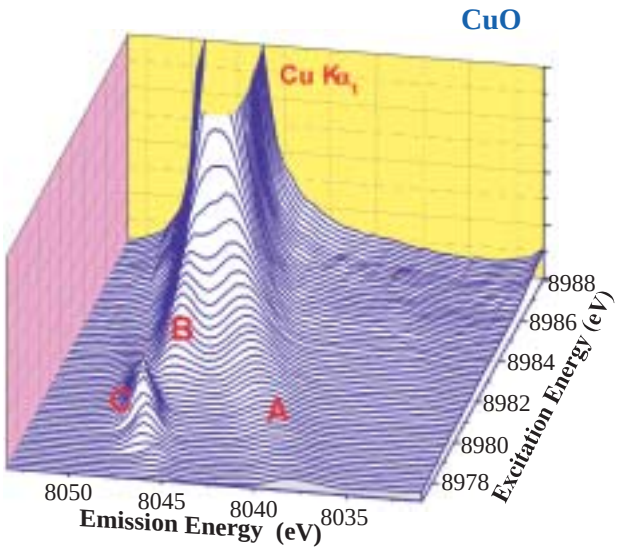

Fig. 1. Excitation energy dependence of RIXS spectra of CuO as a function of excitation energy and emission energy.

In the upper panel of Fig. 2, the RIXS spectra of CuO excited at several energies ('Exp.') are shown. The LBR-XANES profiles analytically derived from them are plotted in the lower panel. The inset shows $1s \rightarrow 3d$ transition region in an expanded scale. It is notable that, despite of significant differences in RIXS

spectra, the LBR-XANES derived almost overlaps with each other. Thus, complicated RIXS behavior can be fully explained as the reflection of the LBR-XANES: the RIXS features, A, B, and C, are determined by the XANES features, a, b, and c, respectively [1]. The LBR-XANES is much more distinct than conventional XANES, which suggests that Γ_{1s} broadening is removed.

Since the quality of the present RIXS data allows us to examine the profiles in detail numerically, deriving $dg_{1s}/d\omega$ on the basis of Eq. (1) without assuming $\Gamma_{2p}/\hbar << 1$ was attempted next. The $dg_{1s}/d\omega$ thus obtained corresponds to LBF-XANES. The $dg_{1s}/d\omega$ that reproduces the observed RIXS spectra best and the calculated RIXS profiles ('Best-fit LBF-XANES') are shown in the lower and the upper panels of Fig. 2, respectively. In the upper panel, it is found that the observed RIXS spectra almost exactly coincide with the calculations by the best-fit $dg_{1s}/d\omega$. In the lower panel, it is evident that the best-fit $dg_{1s}/d\omega$ shows much more distinct features than those analytically obtained, demonstrating that the lifetimes of 2p as well as 1s are removed.

Many exciting applications of the LBR- or LBF-XANES spectroscopy, e.g., for high-Tc materials [4], can be envisaged.

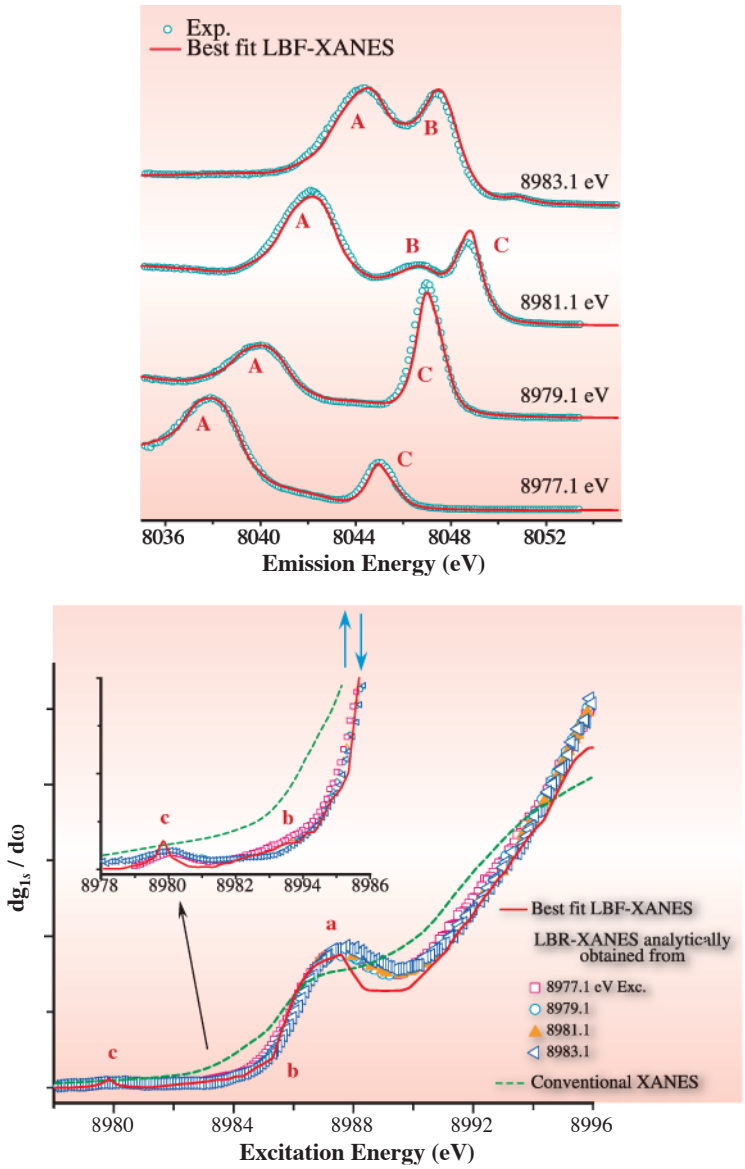

Fig. 2. Upper panel: comparisons of the observed RIXS spectra (circles) and calculated ones (solid line) using the best-fit $dg_{1s}/d\omega$ model. Lower panel: the best-fit LBF-XANES ($dg_{1s}/d\omega$) numerically obtained as well as LBR-XANES spectra analytically obtained from RIXS spectra of the upper panel. Conventional XANES is also shown for comparison.

Hisashi Hayashi

IMRAM, Tohoku University

E-mail: hayashi@tagen.tohoku.ac.jp

References

[1] H. Hayashi *et al.*: Phys. Rev. B **68** (2003) 45122.
[2] N. Kosugi *et al.*: Chem. Phys. **135** (1989) 149.
[3] J. Tulkki *et al.*: J.Phys. B **15** (1982) L435.
[4] H. Hayashi, R. Takeda, M. Kawata, Y. Udagawa, Y. Watanabe, T. Takano, S. Nanao, N. Kawamura, T. Uefuji and K. Yamada: J. Electron Spectrosc. Relat. Phenom. **136** (2004)199.

Identification of Ultra-Dilute Dopants in Ceramics

The properties of ceramic materials are strongly influenced by the presence of ultra-dilute impurities or dopants. The near-edge X-ray absorption fine structure (NEXAFS) method by the third-generation synchrotron can be a powerful tool for identifying impurities if a good theoretical tool for interpreting the spectra is provided. We have adopted a novel method to break the bottleneck for its wide application [1]. Local environments of a few 10 ppm levels of Ga in otherwise high-purity MgO ceramic samples were quantitatively examined by NEXAFS and the first-principles supercell calculation. Formation of Mg vacancy to compensate the extra charge of substitutional Ga at the Mg site is suggested by the analysis. It is then unambiguously confirmed by the combined study of positron lifetime measurements and plane-wave pseudopotentials calculations. The powerful combination of techniques with NEXAFS to identify the ultra-dilute dopant is fully demonstrated.

The experiments were carried out at beamline **BL01B1** with a bending magnet system with two mirrors and a fixed-exit double crystal monochromator utilizing Si (311) planes. X-ray fluorescence from the sample was detected by a 19-element Ge solid-state detector. Most of previous studies on ultra dilute samples in the literature used Si(111) planes in order to maximize photon flux. In the present study, we adopted Si(311) in order to achieve high energy resolution at the expense of reducing the photon flux. All measurements were carried out in air at room temperature.

In order to interpret NEXAFS and analyze the local environment of dilute dopants, reliable theoretical calculations of NEXAFS are necessary. It is true that a number of theoretical methods have been utilized to simulate the NEXAFS. However, there has been very little success in systematic and quantitative reproduction of NEXAFS for dilute dopants. We have adopted a novel method to break the bottleneck. In Fig. 1, experimental Ga-*K*-edge NEXAFS of β-Ga_2O_3 is compared with the theoretical spectrum obtained by an orthogonalized linear combination of atomic orbital (OLCAO) method [2] that is a first-principles band structure method. A large supercell composed of 120 atoms was used in order to minimize interactions among core holes. Since two kinds of different sites of equal numbers are present in the β-Ga_2O_3 crystal, two sets of initial and final states calculations for different

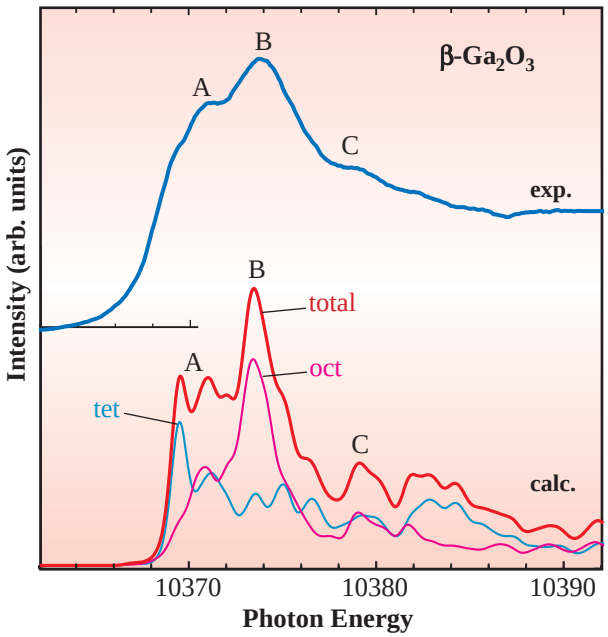

Fig. 1. Comparison of experimental and theoretical Ga-*K*-edge NEXAFS of β-Ga_2O_3. Theoretical spectra denoted by tet and oct correspond to spectra for Ga atoms at tetrahedral and octahedral sites, respectively. The sum of the two spectra is shown as total.

Ga sites were performed. The combined spectrum from the two sites shows excellent agreement with the measured one.

Local environments of 30 ppm Ga in otherwise high-purity MgO ceramic samples were identified by the combination of NEXAFS and the first-principles calculations. Three kinds of models as shown in Fig. 2 were constructed for Ga in MgO. Among them, Model 3 in which Mg vacancy is formed to compensate the extra charge of substitutional Ga at the 2nd nearest-neighbor Mg site shows best agreement with the experimental NEXAFS. The validity of the model is then confirmed by the combined study of positron lifetime measurements and plane-wave pseudopotentials (PWPP) calculations [3]. The formation energy obtained by PWPP calculation is found to be 0.05 eV per Ga atom smaller for Model 3 than that for Model 2. Model 1 shows a prohibitively high formation energy. All theoretical and experimental results show good consistency.

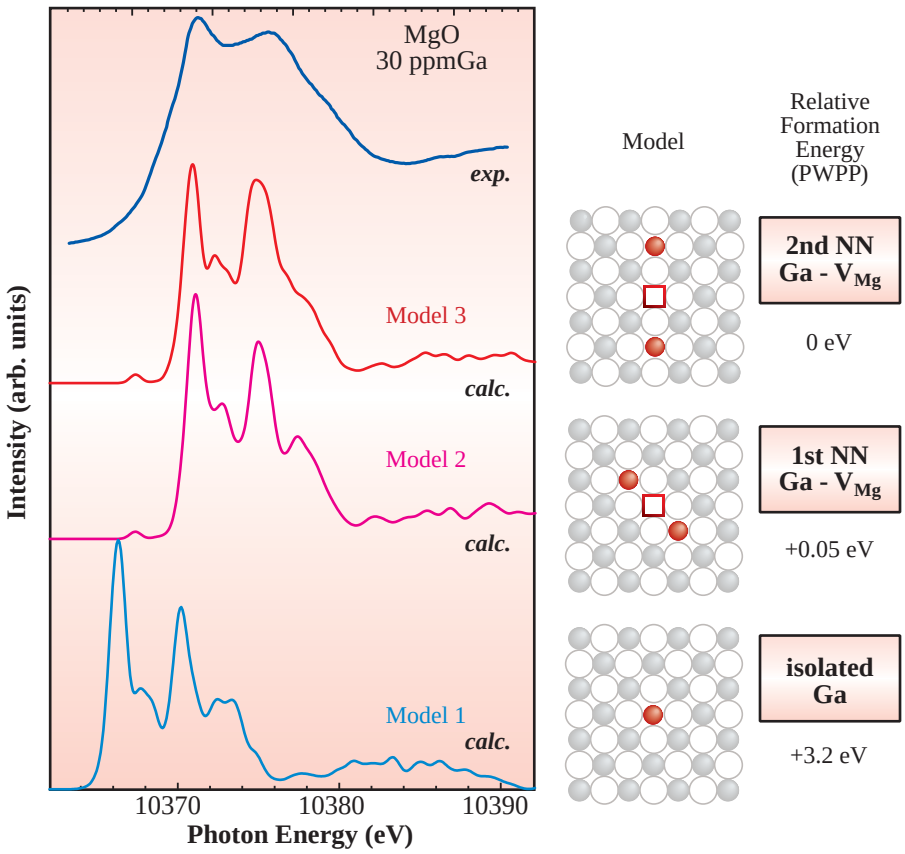

Fig. 2. Comparison of experimental and theoretical Ga-*K*-edge NEXAFS of Ga in MgO. Theoretical formation energies per Ga atom in MgO obtained by the PWPP calculations for the three models are shown together.

Isao Tanaka

Department of Materials Science and Engineering, Kyoto University

E-mail: itanaka@MTL.kyoto-u.ac.jp

References

[1] I. Tanaka, T. Mizoguchi, M. Matsui, S. Yoshioka, H. Adachi, T. Yamamoto, T. Okajima, M. Umesaki, W.Y. Ching, Y. Inoue, M. Mizuno, H. Araki and Y. Shirai: Nature Materials **2** (2003) 541.
[2] S.-D. Mo and W.Y. Ching: Phys. Rev. B **62** (2000) 7901.
[3] M.D. Segall *et al.*: J. Phys. Cond. Matter. **14** (2002) 2717.

Ultrafast Dissociation of Molecular Core-excited States by High-Resolution Auger Electron Spectroscopy

Soft X-ray absorption spectra of many kinds of molecules show rich structure in the pre-edge region, due to excitation of core electrons to unoccupied molecular orbitals. The core hole decays predominantly with Auger emission. Recent studies of high-resolution resonant Auger electron spectroscopy have shown that the nuclear motion of the molecular core-excited states is promoted in competition with the Auger decay [1]. The typical time scale of this competition is < 10^{-14} s. Gel'mukhanov and coworkers predicted that the Doppler effect in resonant photoemission may occur, when the resonant Auger spectrum from the decay of repulsive core-excited states reflects both the molecular decay and that from excited dissociation fragments [2]. Doppler-type line shift is the energy-split atomic fragment emission lines arising from dissociation on a time scale comparable to the core-hole lifetime, which is of the order of 3 fs, i.e., ultrafast dissociation. The existence of Doppler-type line shift due to the ultrafast dissociation of core-excited molecules has been reported for small molecules such as DF, O_2, O_3, and CF_4 [3]. Here, we report on an extensive study of the Doppler-type line shift observed in the F 1*s* resonant Auger spectra from SF_6 molecules [4].

Figure 1 shows a schematic diagram of the Doppler effect observed in the resonant Auger emission. If the dissociation is highly anisotropic and occurs along the polarization vector of the light, and if the electron emission is observed along this direction, then the Auger line of the departing atomic fragment can Doppler split. The Doppler splitting disappears when the electron emission is observed in the direction perpendicular to the polarization vector. Precise analysis of Doppler-type line shift can provide information on anisotropy of the dissociation (β), dissociation energy (DE), Auger electron energy (KE), and anisotropy of the atomic-like Auger emission in the molecular frame (ζ).

Measurements have been carried out on the c-branch of beamline **BL27SU**. The figure-8 undulator at BL27SU provides linearly polarized radiation either in the plane of the storage ring or in the plane perpendicular to it. Angle-resolved electron emission measurements are performed by changing the undulator gap, without rotating the electron analyzer. The electron spectroscopy apparatus consists of a hemispherical electron analyzer (Gammadata Scienta SES-2002), a gas cell, and a differentially pumped chamber. The overall resolution used in the present measurements is 150 meV.

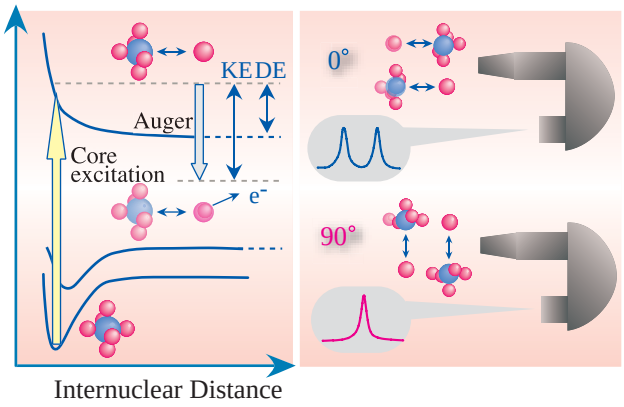

Fig. 1. Schematic representation of the formation of "atomic" contributions to the Auger spectrum and Doppler-type line shift of the "atomic" Auger lines following the dissociation of core-excited molecules. Doppler-type line shift results in a splitting of the peak when the electron emission is observed in the direction perpendicular to the dissociation, i.e. θ = 0°. The Doppler splitting disappears when the electron emission is observed in the direction perpendicular to the dissociation, i.e. θ = 90°.

Figure 2 shows electron-emission spectra of SF_6 at 14 different photon energies across the F 1*s* → a_{1g} resonance at ≈688 eV and F 1*s* → t_{1u} resonance at ≈ 694 eV, as indicated by arrows in the right panel, where the total ion yield spectrum is displayed. The spectra are recorded for electron emission in the direction parallel and perpendicular to the polarization vector of the incident light. The kinetic energy of the valence photoelectron bands, labeled by X, A, B, C to F, increases with an increase in the photon energy. The non-dispersive spectral feature indicated by the dotted circle, on the other hand, exhibits a splitting, characteristic of the Doppler effect, in the 0° spectrum. The kinetic energy of this band, 656.3 eV, is very close to the energy of the Auger line, 656.5 eV, of the atomic fluorine fragment. This shows the existence of ultrafast dissociation of the F 1*s* → a_{1g} core-excited state of SF_6.

In order to analyze Doppler-type line shift, a fitting based on the model of Gel'mukhanov *et al.* [2] has been employed. The results of the fit are shown in Fig. 3 by solid curves together with the experimental results. Parameters extracted from the fit are the energy for the center of the atomic-like Auger line, KE,

dissociation energy, DE, the anisotropy parameter β of the F fragment relative to the polarization vector, and the anisotropy parameter ζ for the Auger emission in the molecular frame. Fitting results show that dissociation energy of the core-excited F fragment (DE) increases with increasing the excitation photon energy ($h\nu$). However, the increase in DE is only about half of that of $h\nu$. Therefore, dissociation counterpart, SF_5, is considered to be highly vibrational excited after the ultrafast dissociation. The most interesting finding is that Auger anisotropy ζ decreases with increasing photon energy. The displacement of the F*, $\Delta R \cong v/\Gamma$, with v and Γ being the velocity of the F* and the decay width of the F*, increases with increasing in $h\nu$. Thus ζ decreases with increasing in ΔR. This shows that the anisotropic effect is a purely molecular effect due to the anisotropic molecular field.

We have shown that ultra-high-resolution measurement of the resonant Auger spectra provides a unique possibility for studying details of the nuclear dynamics as well as Auger dynamics. Further systematic studies are now in progress.

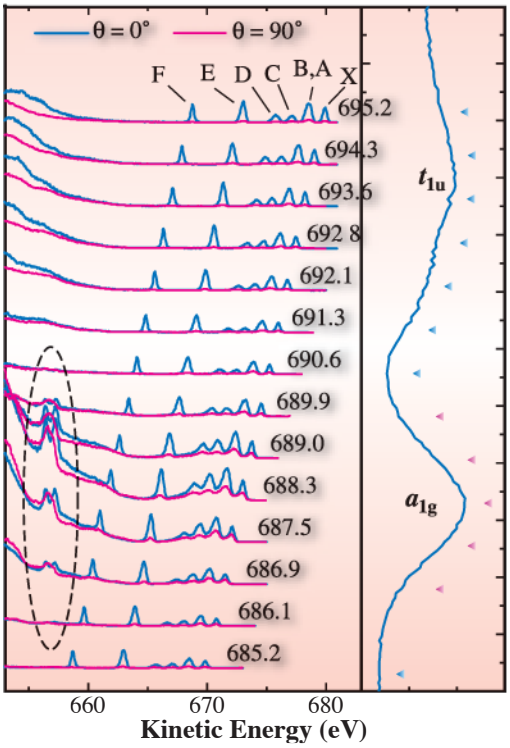

Fig. 2. Electron spectra of SF_6 recorded for parallel and perpendicular polarizations. The measurements are carried out at 14 different photon energies across the F $1s \rightarrow a_{1g}$ and F $1s \rightarrow t_{1u}$ resonances, as indicated by the arrows in the right panel, where the total ion yield spectrum is displayed.

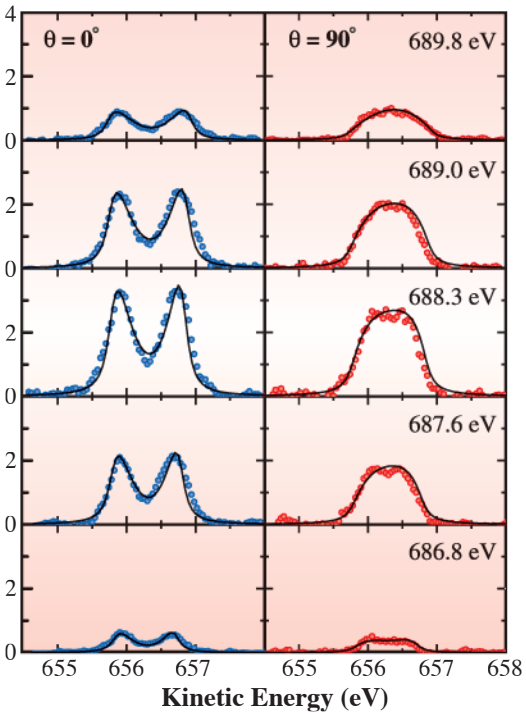

Fig. 3. Experimental and fitted curves for Doppler split peak observed in the Auger spectra obtained at $SF_6 \rightarrow F\ 1s^{-1}\ a_{1g}$ resonance. Baselines are subtracted.

Masashi Kitajima[a], Hiroshi Tanaka[a] and Kiyoshi Ueda[b]

(a) Sophia University, Department of Physics
(b) Institute of Multidisciplinary Research for Advanced Materials, Tohoku University

E-mail: kitaji-m@sophia.ac.jp

References

[1] K. Ueda: J. Phys. B **36** (2003) R1, and references cited therein.
[2] F. Gel'mukhanov *et al.*: Phys. Rev. A **57** (1998) 2511.
[3] O. Björneholm *et al.*: Phys. Rev. Lett. **84** (2000) 2826; L. Rosenqvist *et al.*: J. Chem. Phys. **115** (2001) 3614; K. Wiesner *et al.*: Chem. Phys. Lett. **354** (2002) 382; K. Ueda *et al.*: Phys. Rev. Lett. **90** (2003) 233006.
[4] M. Kitajima *et al.*: Phys. Rev. Lett. **91** (2003) 213003.

Resonant Auger Decay of Above-threshold Core-excited H_2O

The study of decay processes of core-excited molecules provides a wealth of information on the nature of the intermediate state and on the dynamics of photoexcitation, photoemission and photofragmentation processes. The typical experimental procedure is to identify resonant processes in photoabsorption measurements, and then to tune the photon energy to the position of a particular resonant feature and to investigate the corresponding valence electron emission. The resonant Auger spectrum thus obtained includes features related to final states with one electron vacancy ("participator" decay) or two electron vacancies and one excited electron ("spectator" decay). It is also possible to identify features related to fragments in the case of dissociation events occuring on the same time scale of electron decay (the so-called "ultrafast" dissociation).

In water, the photoabsorption spectrum around the O *K*-edge has been measured several times, recently with state-of-the-art resolution [1]. In the above-threshold region, the photoabsorption curve is rather flat, without pronounced resonant features. However, in one particular experiment, namely negative ion yield spectroscopy, it has been possible to identify a resonant feature approximately 10 eV above the ionization threshold [2]. This feature has to be related to doubly excited states, since it is well known that there are no shape resonances in water.

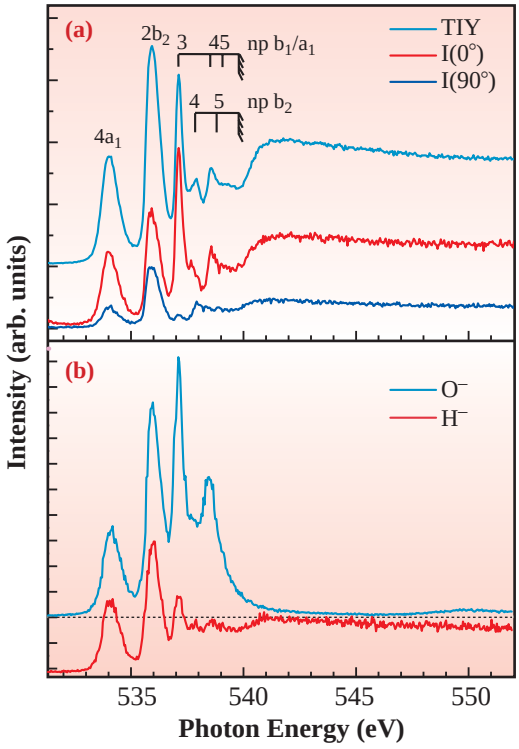

Fig. 1. **(a)** Total ion yield spectrum of H_2O in the O 1*s* excitation region measured with ~ 50 meV photon bandwidth. **(b)** Negative ion yields for the H^- and O^- fragments (curves from Ref. [2]).

In Fig. 1(a), we show the total ion yield spectrum and the angle-resolved ion yield spectra recorded at 0° and 90° with respect to the polarization vector. All spectra appear rather flat in the photon energy region just above the ionization threshold (539.79 eV). At variance with this finding, in Fig. 1(b) from Ref. [2], we show partial ion yield spectra of negative fragments O^- and H^-. It is evident that above threshold the total ion yield spectrum (which we can consider equivalent to photoabsorption) is featureless, while a broad resonance at approximately 10 eV above the threshold is clearly evident in the O^- negative ion yields.

We recorded resonant Auger spectra at several photon energies within the width of the resonance, locating its position with the aid of negative ion yield spectra [3]. The aim was to characterize the possible increase in relative intensity of spectral features related to single-hole final states, and/or to verify the presence of features which could be connected to ultrafast dissociation, i.e. lines derived from resonant Auger decay of the OH fragment rather than from decay of the intact molecule. In a previous work, ultrafast dissociation was investigated in water excited below the O *K*-edge, and the decay spectrum of the OH fragment was well characterized [4].

In Fig. 2 we show resonant Auger spectra recorded at 0° and 90°, I(0) and I(90), respectively, with respect to the polarization vector and the angle-integrated spectrum as given by I(0)+2I(90). The photon energy corresponds to the maximum of the resonance identified in the negative ion yield curves. The decay spectra exhibit a broad feature at a binding energy of 32.2 eV, which is related to an inner-valence molecular state, and superimposed to it some sharp structures with vibrational substructure. The relative position of such features and their vibrational spacing are consistent with the resonant Auger spectrum of the OH fragment [4]. As a further test, we measured the decay spectrum at several different photon energy values within the resonant structure in the absorption. We can confirm the assignment of such peaks as due

to the decay of the OH radical, as indicated in Fig. 2, on the grounds of their dispersion law. Namely, while the molecular structure disperses linearly in kinetic energy as a function of photon energy, thus remaining at constant binding energy, the sharp structures show apparently constant kinetic energy. Such behaviour is typical of spectral features related to fragments [4]. We can conclude that the resonant state evident only in the negative ion yield spectra is dissociative, as proven by the appearance of fragment-related spectral structures. The very high spectral intensity and resolution available at SPring-8 have enabled us to detect such a "hidden" resonant process.

The experiment has been carried out on the c branch of the soft-X-ray photochemistry **BL27SU** [5]. The radiation source is a figure-of-eight undulator that provides linearly polarized light: the polarization vector *E* is horizontal for the first-order harmonic light and vertical for the 0.5-order harmonic light. The monochromator installed on this branch is of Hettrick type and provides monochromatic soft X-rays with the bandwidth ≈ 50 meV in the O 1*s* excitation region.

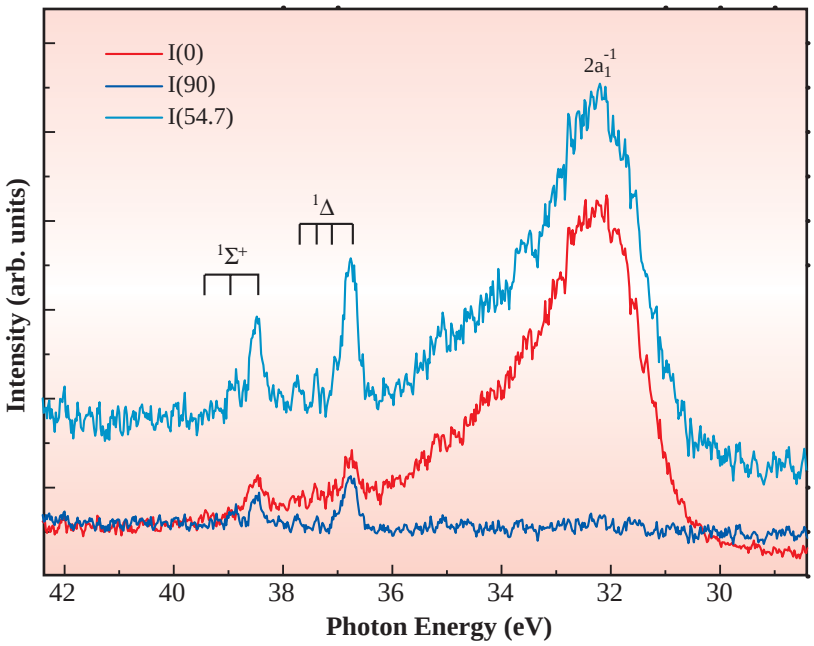

Fig. 2. Resonant Auger spectrum recorded on top of the resonance at ~ 550 eV photon energy [see Fig. 1(b)].

M. N. Piancastelli[a], R. Sankari[b] and K. Ueda[c]

(a) Dept. of Chemical Sciences and Technologies, University "Tor Vergata", Italy
(b) Dept. of Physical Sciences, University of Oulu, Finland
(c) Institute of Multidisciplinary Research for Advanced Materials, Tohoku University

E-mail: pianca@roma2.infn.it

References

[1] A. Hiraya *et al.*: Phys. Rev. A **63** (2001) 042705.
[2] W.C. Stolte *et al.*: Phys. Rev. A **68** (2003) 022701.
[3] M.N. Piancastelli, R. Sankari, S. Sorensen, A. De Fanis, H. Yoshida, M. Kitajima, H. Tanaka and K. Ueda: to be published.
[4] I. Hjelte *et al.*: Chem. Phys. Lett. **334** (2001) 151.
[5] H. Ohashi *et al.*: Nucl. Instrum. Meth. A **467** (2001) 533.

EARTH & PLANETARY SCIENCE

Some technically important progress has been made in beamlines related to high-pressure Earth sciences. A combination of a laser-heated diamond anvil cell (LHDAC) and monochromatic X-rays at BL10XU has made it possible to conduct *in situ* diffraction measurements under P/T conditions equivalent to the mantle-core boundary (a depth of ~3000 km) of Earth. On the other hand, a newly installed large-volume multianvil apparatus press (LVMAP or Kawai-type apparatus), referred to as "SPEED-MkII," at BL04B1 has been used for the precise determination of phase boundaries and higher pressure generation with sintered diamond anvils utilizing its improved guide block and new oscillation systems.

Isshiki *et al.* first made an *in situ* X-ray diffraction measurement of $MgCO_3$ magnesite, the major carbonate in the deep mantle, under entire mantle conditions using the LHDAC at BL10XU to address long-term carbon recycling in the solid Earth-ocean-atmosphere system. They found that magnesite is stable at depths down to ~ 2600 km in the mantle, where it is transformed into a new structure, which is unquenchable under ambient conditions. Parts of this study have been published in *Nature*, and have drown the attention of researchers from a wide range of specialties.

Using a DAC with an external heating system at BL04B2, Kawamoto *et al.* suggested the occurrence of a drastic compositional change in an aqueous fluid at approximately 3 GPa, based on *in situ* X-ray observations for the coexisting solid phases under precisely controlled pressure and temperature. They concluded that the aqueous fluid and the hydrous partial melt may unite to form a single phase under a certain P/T condition in the upper mantle, as these phases should have similar compositions possessing high Mg/Si ratios.

The determination of this "second critical endpoint" has been challenged with a different approach by Mibe *et al.* using the LVMAP (SPEED-1500) at BL04B1. They directly observed morphological changes in the coexisting phases in a synthetic hydrous sample using an X-ray radiographic imaging technique at high pressure and high temperature. They claim that the second critical endpoint exists at a pressure in the range of 4 - 4.3 GPa for the specific composition they used, on the basis of the observed changes in the sample under pressure and those in the quenched sample.

Katsura *et al.* reported detailed specifications and characteristics of the newly designed LVMAP installed at BL04B1 in 2002. This system uses a new guide block, which equally pressurizes the second-stage anvil assemblage for the safer operation of second-stage anvils made of expensive polycrystalline diamond sintered material. The other major improvement in SPEED-MkII is the adoption of a mechanism to oscillate the entire press system while *in situ* X-ray diffraction data are being acquired, so that the effect of crystal growth on diffraction profiles can be minimized during high-pressure and high-temperature runs. Initial tests on these improved points in SPEED-MkII are reported to be quite satisfactory.

Nishiyama *et al.* then used SPEED-MkII for the determination of the B1-B2 transition in NaCl by an *in situ* X-ray diffraction method at pressures up to ~ 25 GPa and temperatures up to 2100 K. They found that the new oscillation system of SPEED-MkII works remarkably well, and were able to define the boundary very precisely under these conditions despite of the observed significant crystal growth of NaCl. They concluded that NaCl cannot be used as the pressure scale for the P/T conditions equivalent to the base of the mantle transition region (~ 600 km in depth) due to the transition to the B2 phase.

Developments in the new technology in both the LHDAC and LVMAP combined with the bright light source at SPring-8 thus provide opportunities for observing the detailed structures, physical properties, and dynamic processes in deeper parts of Earth's and planetary interiors with much improved accuracy.

Tetsuo Irifune

In Situ X-ray Observation of the Stability of $MgCO_3$ Magnesite throughout Earth's Lower Mantle

Carbonates, such as $CaCO_3$ calcite and aragonite, $MgCO_3$ magnesite, and $CaMg(CO_3)_2$ dolomite, are important constituents of marine sediments and play a fundamental role in the long-term recycling of carbon into Earth's deep interior via oceanic plates subduction. It has been demonstrated that these subducted carbonates react with surrounding silicates and/or decompose to CO_2-bearing assemblages at certain depths in the upper mantle (a region of 30-660 km depths), and therefore, $MgCO_3$ magnesite is believed to be the major carbonate in the deeper part of the upper mantle near 660 km [1].

A study of the stability of magnesite under the pressure and temperature corresponding to those of entire mantle conditions down to 2900 Km depth (P = ~ 136 GPa and T = ~ 4000 K) is thus crucial in modelling the carbon circulation in the entire Earth system. However, such experiments have been limited to upper mantle conditions (P < 24 GPa) with few exceptions [2]. Moreover, most of these studies adopted a quench method, and no *in situ* X-ray diffraction measurements have been made under simultaneous high pressure and high temperature conditions of the lower mantle.

We firstly made an *in situ* X-ray diffraction study of the stability of magnesite under P-T conditions approaching the mantle-core boundary using a laser heated diamond anvil cell (LHDAC) at beamline **BL10XU** (Fig. 1) [3], the details of which have been reported by Isshiki *et al.* [4]. We found the magnesite persists at pressures up to about 100 GPa at temperatures up to 3000 K, without dissociation into a CO_2-bearing assemblage (Figs. 2(a-c)). However, we noted that several new peaks appeared at the expense of those of magnesite when the temperature and the pressure were increased to 2200 K and ~115 GPa, respectively (Fig. 2(d)). These new peaks were present at room temperature after quenching under pressure (Fig. 2(e)), but completely disappeared when pressure was released (Fig. 2(f)), and only the diffraction peaks of magnesite were observed in the recovered sample. These new peaks did not correspond to any possible dissociation products of magnesite, and the presence of only the diffraction peaks of magnesite in the recovered sample also precludes its dissociation and/or reaction with the surrounding Al_2O_3 pressure medium.

Thus we conclude that magnesite transforms to a new high-pressure form (magnesite II) at pressures above ~ 115 GPa at temperatures of 2100 – 2200 K (equivalent to a depth of ~ 2600 km in the lower mantle), although we were unable to refine its crystal

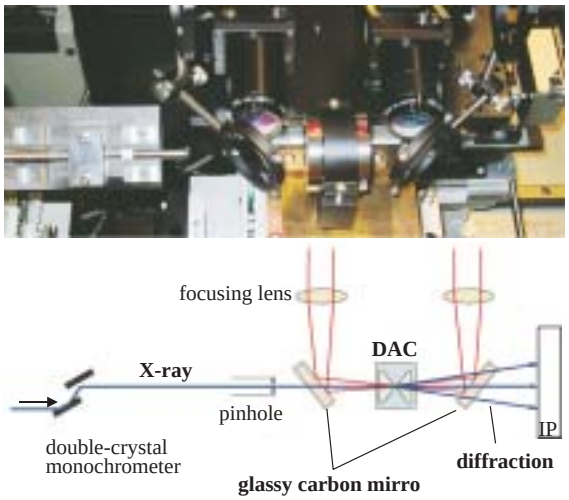

Fig. 1. LHDAC system at BL10XU used in the present study.

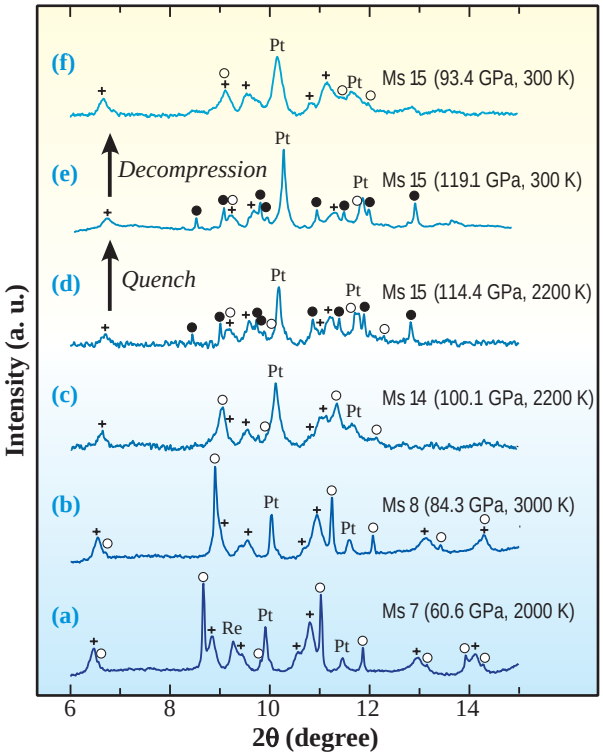

Fig. 2. X-ray diffraction profiles with increasing pressure at maximum temperatures in selected experiments. ○, Magnesite; ●, Magnesite II; Pt, Platinum; Re, Rhenium; +, Al_2O_3 [4].

structure, partly because of the possible overlap of the diffraction peaks with those of corundum, platinum, magnesite and rhenium. The unquenchability of magnesite II also made it difficult to determine its crystal structure from the observed diffraction profile. Nevertheless, we found that the X-ray diffraction peaks of magnesite II can be reasonably indexed on the basis of an orthorhombic symmetry, yielding a density of 5.20 g/cm^3 at ~ 120 GPa, which is about 17% denser than that of magnesite (4.46 g/cm^3) under the same P/T conditions.

Figure 3 shows the present experimental conditions and the results, and depicts a typical geotherm in the mantle and the predicted boundary for the dissociation of $MgCO_3$. It is seen that the dissociation of magnesite into MgO and CO_2 is unlikely to occur throughout the mantle. Subducted oceanic plates are significantly colder than the surrounding mantle into the uppermost part of the lower mantle, and accordingly, magnesite should survive and be transported down to the upper mantle-lower mantle boundary at ~ 660 km depth without dissociation into a CO_2-bearing assemblage. Moreover, parts of the stagnant plates at these depths may ultimately sink into the lower mantle after they are accumulated to a critical size to form a megalith structure [5]. Thus, magnesite is likely to be transported further into the lower mantle, where it is transformed into magnesite II at 110 - 120 GPa, as illustrated in Fig. 4.

The present results suggest that magnesite II is the major host for oxidized carbon in the D" layer, and some of the "missing carbon" may be stored in this phase at the base of the mantle. It is also possible that a certain amount of carbon is incorporated into the iron core and/or reduced to form diamond in the D" layer if it is in sufficiently low oxygen fugacity. On the other hand, magnesite II may dissociate to MgO + CO_2 in the D" layer, as a result of the predicted dramatic temperature increase with depth in this region (Fig. 3). Release of CO_2 from magnesite II may trigger partial melting of materials present in the D" layer, which should contribute to initiate rising plumes from this region.

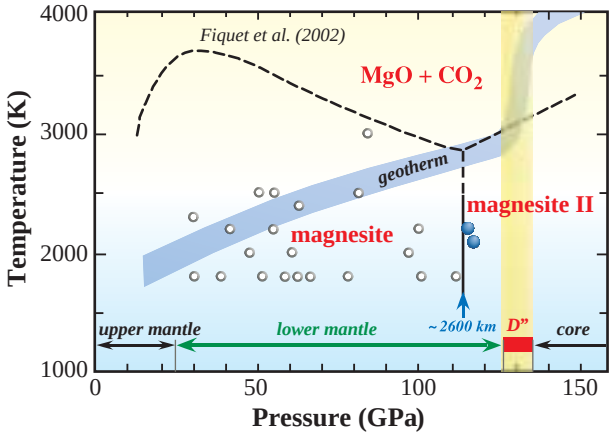

Fig. 3. Possible phase relations of $MgCO_3$ and a typical geotherm in the deep mantle [4].

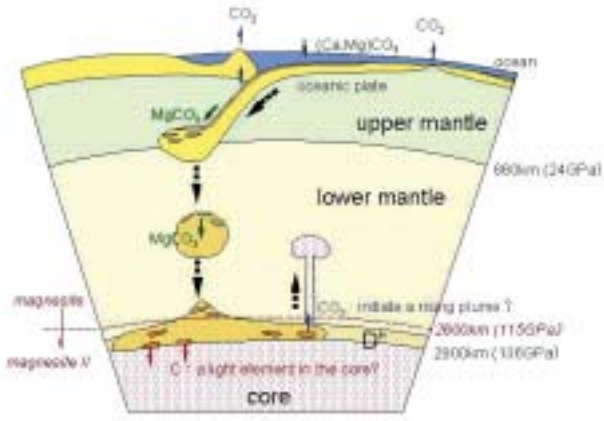

Fig. 4. Schematic illustration of possible carbon circulation in the deep mantle.

Maiko Isshiki and Tetsuo Irifune

Geodynamics Research Center, Ehime University

E-mail: isshiki@sci.ehime-u.ac.jp

References

[1] C. Biellmann *et al.*: Earth Planet. Sci. Lett. **118** (1993) 31.
[2] T. Katsura *et al.*: Proc. Jpn. Acad. **67**, Ser. B (1991) 57.
[3] T. Watanuki *et al.*: Rev. Sci. Instrum. **72** (2001) 1289.
[4] M. Isshiki, T. Irifune, K. Hirose, S. Ono, Y. Ohishi, T. Watanuki, E. Nishibori, M. Takata and M. Sakata: Nature **427** (2004) 60.
[5] A.E. Ringwood and T. Irifune: Nature **331** (1988) 131.

Mg/Si Ratios of Aqueous Fluids in Earth's Upper Mantle

Water influences most physicochemical characteristics of earth-forming materials: melting temperature, partial melt chemistry, density and viscosity, electric conductivity, melt extraction, phase transition boundaries and element distribution. Aqueous fluids can dissolve significant amounts of silicate components under high pressure and high temperature conditions. Such fluids can act, therefore, as transfer agents during metamorphism, magmatism, and volcanism. Therefore, knowledge of the chemical compositions of silicates dissolved in aqueous fluids is essential to the understanding of the effects of H_2O on the physicochemical properties of rocks.

A direct observation of aqueous fluids coexisting with $MgSiO_3$ enstatite and/or Mg_2SiO_4 forsterite is performed at 0.5 - 5.8 GPa and 800 - 1000°C with a Bassett-modified externally heated diamond anvil cell [1] and synchrotron X-rays at beamline **BL04B2** [2]. Rigorous temperature control maintains the temperature of each diamond to be within a few °C. Pressure was determined from the measured unit-cell volume of gold foils using the P-V-T equation of state for gold. Use of this synchrotron X-ray system enables the mineral coexisting with aqueous fluids under high pressure and high temperature conditions to be identified and the Mg/Si ratios of aqueous fluids coexisting with $MgSiO_3$ enstatite and Mg_2SiO_4 forsterite, which are the main mineral constituents of Earth's upper mantle, to be estimated.

Possible Mg/Si ratios of aqueous fluids coexisting with $MgSiO_3$ enstatite and Mg_2SiO_4 forsterite are shown in Fig. 1(a) [3]. In the pressure range of 0.5 - 2.8 GPa, Mg_2SiO_4 forsterite crystallizes at 1000°C in the $MgSiO_3$-H_2O system. This indicates that the aqueous fluids can dissolve more SiO_2-rich components than MgO-rich components, resulting in Mg/Si atomic ratio of less than unity (Fig. 1 (b)). In contrast, at pressures greater than 3.9 GPa, $MgSiO_3$ enstatite dissolves congruently at 1000°C, whereas Mg_2SiO_4 forsterite dissolves congruently up to 5.0 GPa. These data suggest that the aqueous fluids coexisting with Mg_2SiO_4 enstatite and Mg_2SiO_4 forsterite can have Mg/Si ratios in the range $1 < Mg/Si < 2$ under these conditions (Fig. 1(c)). In the present experimental

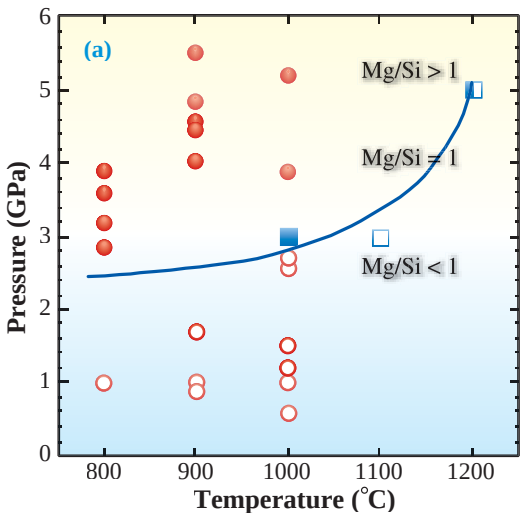

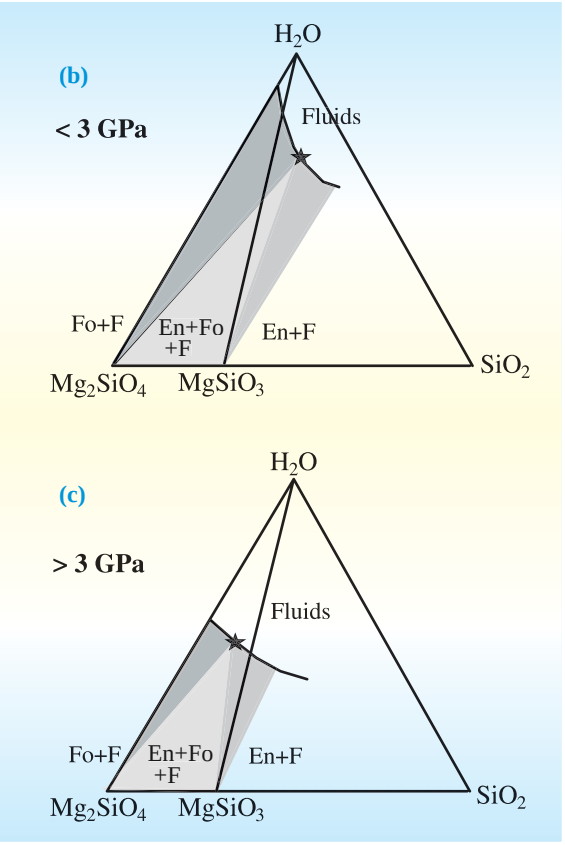

Fig. 1. **(a)** Experimental results showing Mg/Si ratios of silicate components in aqueous fluids coexisting with enstatite (En) and forsterite (Fo). The values of 1200°C at 5 GPa and 1000°C and 1100°C at 3 GPa are obtained from previous studies [4,5]. **(b, c)** Schematic isothermal sections of Mg_2SiO_4-SiO_2-H_2O system at 1000°C. Stars represent possible H_2O fluids coexisting with Fo and En. At pressures lower than 3 GPa, the aqueous fluids (F) coexisting with En and Fo have $Mg/Si < 1$, and at pressures higher than 3 GPa, they have $1 < Mg/Si < 2$.

configurations, the Mg/Si ratios of aqueous fluids are fixed by the starting material. As we see in Fig. 1(b,c), the fluid compositions can change along the univariant curve. Therefore, in the present experiments, we cannot determine the Mg/Si ratios but can only suggest the chemical ranges of the aqueous fluids coexisting with enstatite and forsterite: Mg/Si < 1 or 1 < Mg/Si < 2.

The present experimental data and the data from previous quench experiments [4] suggest that the Mg/Si ratios of aqueous fluids can change drastically from SiO_2-rich to MgO-rich regime at around 3 GPa (Fig. 2(a)). The origin of such a drastic change remains to be investigated in the future. Liquid H_2O may change its structure under these conditions and cause the change in solution chemistry [6]. This speculation is based on the discontinuity in the pressure dependence of the Raman OH stretching frequency of water at 0.4 ±0.1 GPa at 25°C, 1.0 ±0.1 GPa at 100°C and 1.3 ± 0.1 GPa at 300°C.

The chemical compositions of partial melts of H_2O-saturated mantle peridotite were also characterized by high Mg/Si ratios [7]. The aqueous fluids that coexist with mantle minerals have Mg/Si ratios similar to those found in the partial melts of hydrous peridotite (Fig. 2(b)). Somewhere within the upper mantle these two fluids unite to form a single regime and a continuous change between these two fluids occurs. Therefore, the traditional H_2O-saturated solidus temperature may represent a temperature where the concentrations of silicate components dissolved into aqueous fluids increase drastically and may therefore justify its description as a "practical solidus."

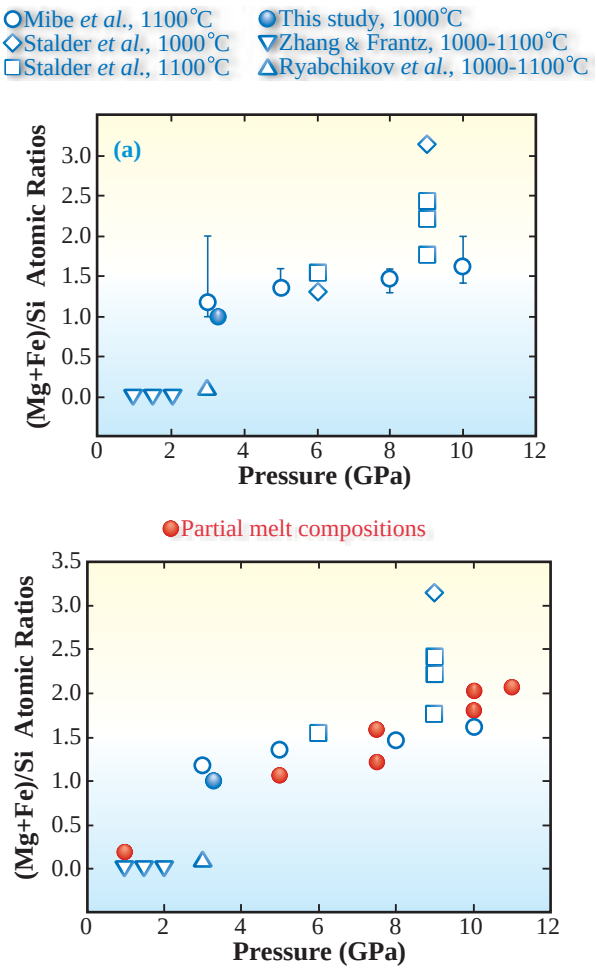

Fig. 2. **(a)** Pressure and Mg/Si ratios of aqueous fluids coexisting with forsterite and enstatite at a temperature range from 1000 to 1100 °C [4]. **(b)** Comparison of aqueous fluid chemistry with partial melt chemistry at 1050 - 1100 °C in a mantle peridotite model of 13.7 weight % H_2O [7].

Tatsuhiko Kawamoto

Graduate School of Science, Kyoto University

Email: kawamoto@bep.vgs.kyoto-u.ac.jp

References

[1] W.A. Bassett *et al.*: Rev. Sci. Instrum. **64** (1993) 2340.
[2] M. Isshiki *et al.*: Nucl. Instrum. Meth. Phys. Res. A **467-468** (2001) 663.
[3] T. Kawamoto, K.N. Matsukage, K. Mibe, K. Nishimura, M. Isshiki, N. Ishimatsu, and S. Ono: to be published in Am. Mineral (October, 2004).
[4] K. Mibe *et al.*: Geochim. Cosmochim. Acta **66** (2002) 2273, and references cited herein.
[5] I. Kushiro *et al.*: Geol. Soc. Am. Bull. **79** (1968) 1685 .
[6] T. Kawamoto *et al.*: J. Chem. Phys. **120** (2004) 5867.
[7] T. Kawamoto and J.R. Holloway: Science **276** (1997) 240.

Determination of the Second Critical Endpoint in Silicate-H_2O Systems

H_2O plays an important role in magmatism and chemical evolution in Earth's interior. Two types of hydrous mobile phase, aqueous fluid and hydrous silicate melt, could exist in Earth's crust and mantle. In general, both the solubility of water in silicate melt and the solubility of silicate materials in aqueous fluid increase with increasing pressure. This could suggest that, above a certain critical pressure and temperature, silicate melt and aqueous fluid become indistinguishable from each other [1]. This critical condition is called the second critical endpoint.

Previous studies for direct observations of coexisting aqueous fluid and silicate melt, which have relatively low melting temperature [2], were conducted using a hydrothermal diamond anvil cell (HDAC). However, it is difficult to obtain the temperature optimal for observing fluid and melt with high melting temperature, such as basalt and mantle peridotite, using the HDAC. Our main purpose is to develop a new method for the determination of the second critical endpoint in basalt-H_2O and peridotite-H_2O systems at high pressure and temperature.

Experiments were conducted using an X-ray radiography technique [3] together with a Kawai-type multi-anvil high pressure apparatus (SPEED-1500) installed at beamline **BL04B1** [4]. The direct X-ray beam, which passes through the anvil gaps of SPEED-1500 and the sample under high pressure, is observed with an X-ray camera (Fig. 1). A hydrous strontium-plagioclase (mixtures of oxides and hydroxides) system is used as a starting material to obtain a better contrast in radiographic images. In addition to water in hydroxides, deionized water is added to the sample. The sample container should not react with hydrous samples, but should be X-ray transparent. We, therefore, developed a new sample container [5], which is composed of a metal (Pt or AuPd) tube and a pair of single crystal diamond lids placed on both ends of the metal tube (Fig. 1). The sample, which is placed inside the container, can directly be observed through the diamond lids and the aperture of the metal tube.

The experimental conditions are pressures from 3 to 4.3 GPa and temperatures up to approximately 1500°C. Pressure is applied first, and then temperature is increased. After the observation with the X-ray camera, the samples were quenched at the desired P-T conditions so that the X-ray radiographic images might be compared with the quenched textures.

At around 900 to 1000°C and 3 GPa, some light-gray spherical bubbles (100-500 microns diameter) moving upward in the dark-gray matrix were observed. The light-gray spherules that absorbed less X-ray are considered to be the aqueous fluid phase, whereas the dark-gray matrix is a silicate melt. With a further increase in temperature, small bubbles were coalescing to form large bubbles. Then, these large bubbles became hemispheres wetted on the upper wall of the metal tube (Fig. 2). In experiments up to 4 GPa, two phases (i.e., aqueous fluid and silicate melt) were observed, whereas at 4.3 GPa, no bubbles were observed during heating up to about 1500°C.

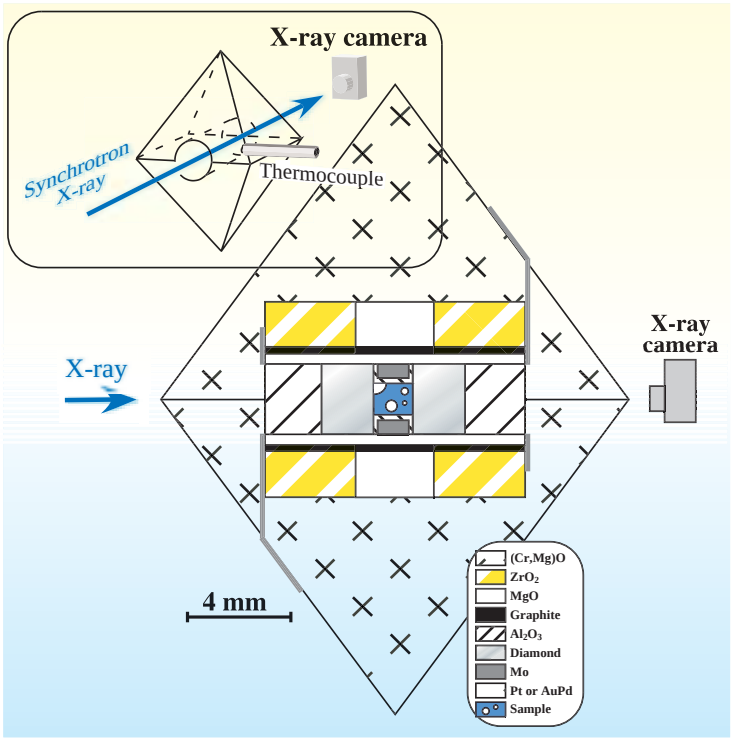

Fig. 1. Experimental configurations and the furnace assembly used in high-pressure and high-temperature experiments. Images are recorded with a digital video camera.

The image of the recovered sample quenched at 3 GPa and 1300˚C is shown in Fig. 3. A large and hemispherical bubble, which is considered to be the aqueous fluid phase at high pressure and temperature, can be seen in the glass matrix, which on the other hand is considered to be the silicate melt phase during the run. This image (Fig. 3) is consistent with the X-ray radiographic image (Fig. 2) that showed two phases at this pressure and temperature. In the recovered sample quenched at 4.3 GPa and 1300˚C, no bubbles were found. Instead, quenched crystals were homogeneously distributed in the entire sample capsule.

Both radiographic observations and inspection of quenched samples indicate that aqueous fluid and melt can coexist at pressures up to 4 GPa and there is no difference between these two phases above 4.3 GPa in a Sr-plagioclase-H_2O system. Therefore, it is concluded that the second critical endpoint in the Sr-plagioclase-H_2O system exists at pressure between 4 and 4.3 GPa. Our new technique could be applied to direct observations of various kinds of 2-fluid coexisting under deep mantle conditions that could not be achieved by the HDAC. Detailed studies for the determination of the second critical endpoint in the basalt-H_2O and peridotite-H_2O systems are now being undertaken for the better understanding of the properties of fluid and melt in Earth's deep interior.

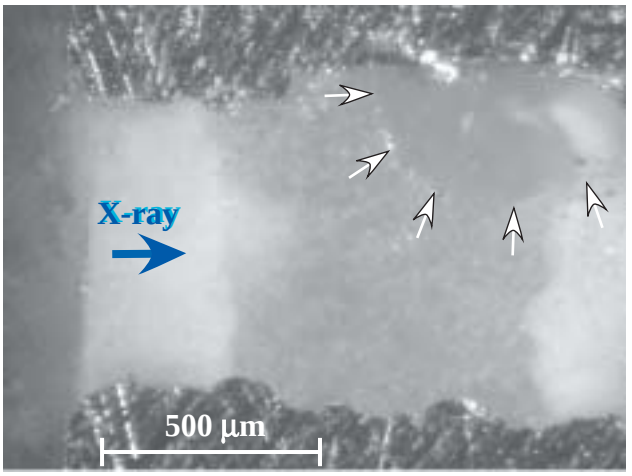

Fig. 3. Image of the recovered sample quenched at 3 GPa and 1300 ˚C.

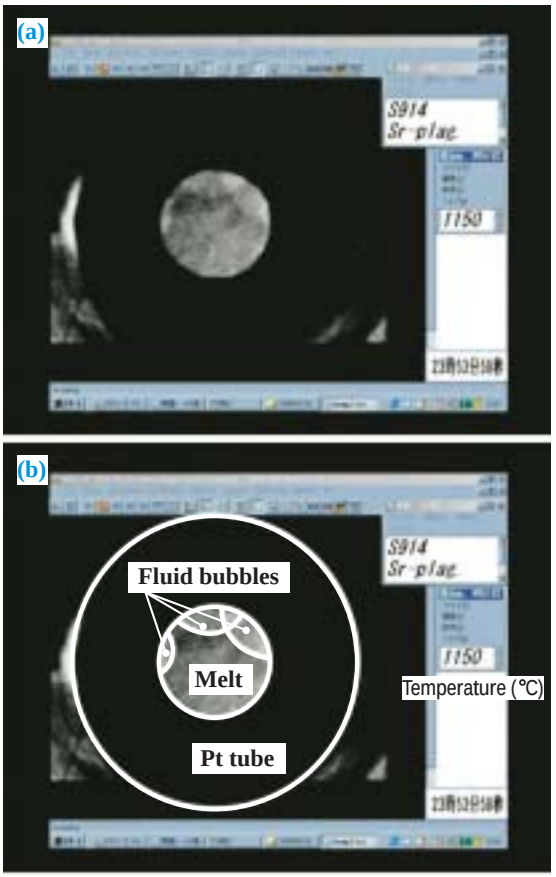

Fig. 2. X-ray radiographic images taken at 3 GPa and 1150 ˚C. **(a)** Image. **(b)** Explanatory notes along with **(a)**.

Kenji Mibe[a,b] and Masami Kanzaki[c]

(a) Carnegie Institution of Washington, Geophysical Laboratory, USA
(b) Earthquake Research Institute, The University of Tokyo
(c) Institute for Study of the Earth's Interior, Okayama University

E-mail: mibe@eri.u-tokyo.ac.jp

References

[1] O. Paillat *et al.*: Contrib. Mineral. Petrol. **112** (1992) 490.
[2] A. Shen and H. Keppler: Nature **385** (1997) 710.
[3] M. Kanzaki *et al.*: High Pressure Res. Mineral Phys. (1987) 195.
[4] W. Utsumi *et al.*: Rev. High Pressure Sci. Tech. **7** (1998) 1484.
[5] K. Mibe, M. Kanzaki, T. Kawamoto, K.N. Matsukage, Y. Fei and S. Ono: J. Geography **112** (2003) 970.

New Large-volume High P-T *In Situ* X-ray Diffraction System at BL04B1

Earth's interior is under extremely high pressure and high temperature conditions. Therefore, knowledge of the physical and chemical properties of Earth's materials at high pressures and temperatures are indispensable for studying the structure, dynamics and evolution of Earth. *In situ* X-ray diffraction is a useful and powerful method for studying crystal structures, phase relations, equations of state, viscoelastic properties of minerals and melts at high *P-T* conditions. The KAWAI-type apparatus, together with a diamond anvil cell, is one of the most widely used high-pressure apparatuses, particularly in geosciences. The reason is that high pressures up to 30 GPa can be generated in relatively large volumes, rendering it possible to conduct sophisticated experiments with a complex sample assembly in fairly homogeneous high P-T conditions. In SPring-8, a KAWAI-type apparatus for *in situ* X-ray observation, named SPEED-1500, was installed at the bending magnet beamline **BL04B1** in 1997 [1], and a number of important experimental results have been obtained.

Despite the great success of SPEED-1500, further developments of high P-T *in situ* X-ray observation in a KAWAI-type apparatus are necessary to extend the pressure and temperature ranges. SPEED-1500 was originally designed for experiments using tungsten carbide (WC) anvils, which limit the generated pressures to *ca*. 30 GPa. In order to extend the pressure range, the use of sintered diamond (SD) is necessary. Because SD is very brittle, however, we need much more precise dimensions of the guide block system and control of press load than those of SPEED-1500. At high temperatures, grain growth of the sample materials is very rapid in a Kawai-type apparatus. As a result, we often miss many lines in diffraction patterns taken by SPEED-1500 at high temperatures. In such cases, we had very low precision in determining pressures and unit cell volumes of samples, and sometimes failed to identify the phases present. Hence, we need an oscillation system to obtain high-quality diffraction patterns against grain growth. Mainly because of these two reasons, we have designed and installed the second KAWAI-type high P-T apparatus, SPEED-Mk II, at the same beamline BL04B1 (Fig. 1) [2].

Fig. 1. Photograph of the press part of SPEED-Mk II.

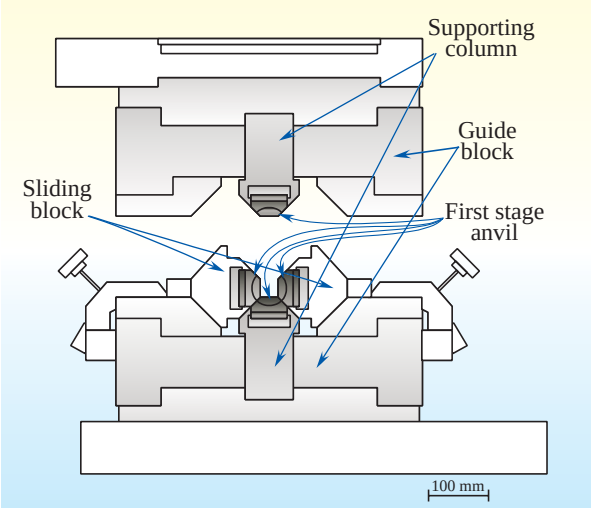

Fig. 2. Schematic drawing of the high-pressure vessel. The columns that support the upper and lower first-stage anvils (supporting columns) are separated from the main parts of the guide blocks so that the change in the relative dimension of the cubic compression space with press load can be minimized through adjustment.

The basic design of SPEED-Mk II has followed that of SPEED-1500. Namely, it is equipped with a DIA-type guide block system, a hydraulic system for maximum press load of 15 MN, a heating system, and a horizontal goniometer with a Ge-SSD for energy-dispersive X-ray diffraction.

Six first-stage anvils on the DIA-type guide block system compress a cubic space for a KAWAI-type assembly composed of eight second-stage cubic anvils, each with a truncated corner. One of the serious problems for pressure generation in such a system is that the compression space deforms with

increasing press load, which may cause blow-out or breaking of SD anvils. In fact, the horizontal dimension of the compression space increases relatively to the vertical one with increasing press load at a rate of 13 μm/MN in SPEED-1500. In order to fix this problem, the columns supporting the top and bottom first-stage anvils are separated from the main part of the guide blocks so that the strength supporting these anvils can be adjusted while examining the relative deformation of the compression space (Fig. 2). By repeating adjustments, the rate of the relative deformation has been suppressed to 4 μm/MN.

In addition to the dimensions of the compression space, the press load is also controlled precisely in SPEED-Mk II. The press load is controlled with divisions of 20 ~ 30 kN in SPEED-1500, whereas it is controlled with 3 kN divisions in SPEED-Mk II. Furthermore, the hydraulic system is equipped with two inverter pumps, which rotate in proportion to the difference between the set and real loads so as to allow smooth compression and decompression.

Because of these improvements, we have succeeded in extending the pressure range generated by a Kawai-type apparatus. The highest pressure generated by SPEED-1500 is 40 GPa, whereas pressure of 63 GPa has been achieved by SPEED-Mk II (in Feb. 2004, by E. Ito, ISEI, Okayama University).

SPEED-Mk II is placed on a stage system mainly for positioning the samples to the diffraction area. The stage system has one rotation axis around the vertical direction (κ-axis) from -7° to 13°. This κ-axis is used for controlling the sample oscillation. Figure 3 shows diffraction patterns of MgO at 3 GPa and 2070 K collected with and without operating the oscillation system. Many of the MgO peaks are not observed in the diffraction pattern taken without oscillation (Fig. 3(a)). On the contrary, most of them are observed if the oscillation is operated (Fig. 3(b)). The press stage could be bent during oscillation because the press is very heavy (20 ton). Special attention was paid to designing the stage such that shifts of the sample with oscillation can be suppressed to 50 μm.

Thus, we have improved a Kawai-type apparatus for *in situ* X-ray diffraction to obtain high-quality diffraction patterns at higher temperatures and pressures. We expect that a number of important experimental results will be obtained using this apparatus.

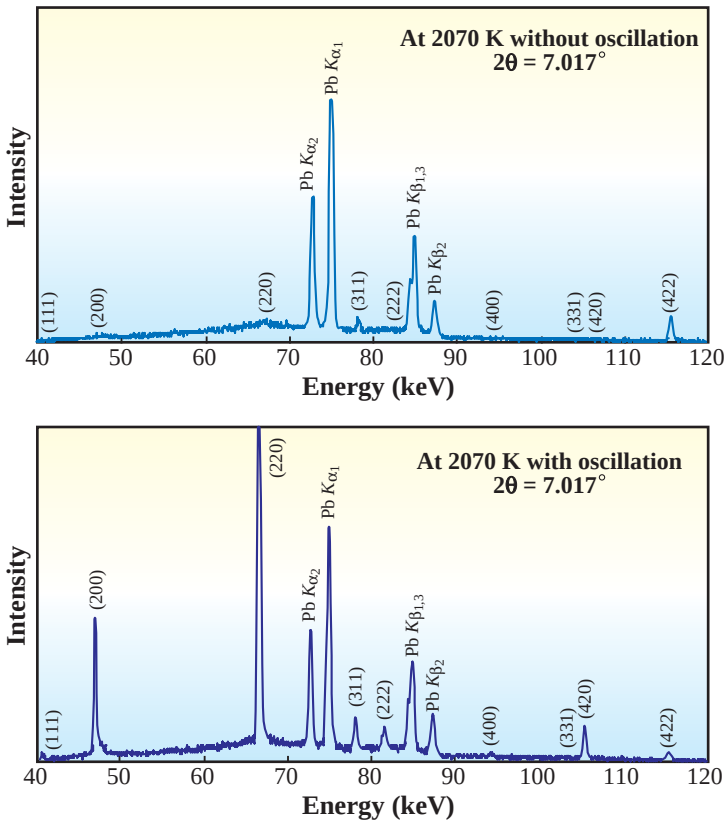

Fig. 3. Diffraction patterns of MgO with and without oscillation at 3 GPa and 2070 K: **(a)** diffraction pattern taken without oscillation, and **(b)** with oscillation. The MgO peaks are labeled by the lattice index. The peaks by Pb fluorescence are labeled as PbKα_1 and so on.

Tomoo Katsura[a] and Ken-ichi Funakoshi[b]

(a) Institute for Study of the Earth's Interior, Okayama University
(b) SPring-8 / JASRI

E-mail: tkatsura@misasa.okayama-u.ac.jp

References

[1] W. Utsumi *et al.*: High Press. Sci. Technol. **7** (1998) 1484.
[2] T. Katsura, K. Funakoshi, A. Kubo, N. Nishiyama, Y. Tange, Y. Sueda, T. Kubo and W. Utsumi: Phys. Earth Planet. Int. **143-144** (2004) 497.

Determination of the Phase Boundary Between the B1 and B2 Phases in NaCl by *In Situ* X-ray Diffraction using a New High Pressure Apparatus, SPEED-Mk II, with an Oscillation System

NaCl is one of the simplest and most thoroughly studied ionic crystals. Thus, the physical properties of NaCl such as its phase transformation, compressibility, and thermal expansivity can provide a basic model for understanding the physical properties of more complex ionic crystals. It has been well established that NaCl with a rock salt structure (the B1 phase) transforms into a CsCl structure (the B2 phase) at about 30 GPa and room temperature [1]. However, transition pressures at high temperatures have neither been well established nor well studied experimentally. The accurate location of this phase boundary in P-T space is useful for high-pressure earth science because the B1 phase of NaCl is frequently used as a pressure gauge in *in situ* X-ray diffraction experiments because it is very compressible and its P-V-T equation of state has been well established [2]. Pressure corresponds to depth, which is the most essential variable when physical properties of mantle minerals are studied. However, under P-T conditions above the B1-B2 phase boundary, NaCl is unusable as a pressure gauge because of its transformation to the B2 phase. Thus, this phase boundary sets a limit to the P-T conditions where the B1 phase can be used as a pressure gauge.

To elucidate the phase boundary between B1 and B2 phases of NaCl at high temperatures, we carried out a series of *in situ* X-ray diffraction experiments using a new Kawai-type apparatus, SPEED-Mk II, installed in **BL04B1** . To our knowledge, this is the first Kawai-type apparatus with an oscillation system [3]. It has been reported that grains of the B2 phase grow very fast even at temperatures below 673 K [4]. Thus it has been difficult to obtain a powder X-ray diffraction pattern of the B2 phase particularly at high temperature because of a shortage in the number of grains contributing to the X-ray diffraction pattern. Since the new apparatus, SPEED-Mk II, has a press-oscillation system, the sample under high pressure and temperature conditions can be oscillated during data collection, which increases the number of grains contributing to the diffraction pattern and reduces the effect of grain growth of the sample on the diffraction pattern. Figure 1 shows a schematic illustration of the cell assembly used in the present study. At temperatures above 1100 K, the press was oscillated within the angular range from –4° to 7° during data collection.

Figure 2 shows a comparison between a diffraction pattern collected without press oscillation and that collected with press oscillation. These diffraction patterns were collected under the same P-T conditions of 24.7 GPa and 1150 K. In the pattern obtained without press oscillation, only two peaks of the B2 phase, indexed as (111) and (222), were observed; these are minor peaks in the X-ray diffraction patterns obtained in a previous study. In the X-ray diffraction pattern obtained with press-oscillation, we observed an intense peak of B2 phase indexed as (110), which is the most intense peak of B2 phase. Two other diffraction peaks of the B2 phase [those indexed as (111) and (220)] were also observed in this profile. The relative intensities of these peaks are reasonably consistent with those observed in the previous study. According to these results, it is obvious that the press-oscillation system helped us to identify the B2 phase under these P-T conditions, because the most intense peak of this phase was clearly observed in the diffraction pattern obtained with press oscillation, whereas this peak was not observed in the diffraction pattern obtained without press oscillation.

A summary of the experimental results is shown in Fig. 3. At temperatures below 1500 K, the B1 to B2 (forward) and B2 to B1 (backward) transitions were observed; above this temperature, we observed complete transitions from one phase to the other, which

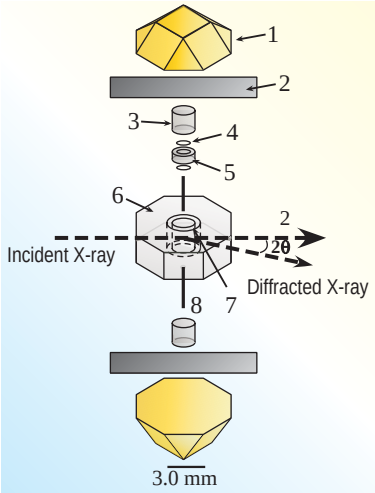

Fig. 1. A schematic illustration of the cell assembly for TEL = 3.0 mm used in the present study:
1: pressure medium (MgO),
2: electrode (Mo),
3: ZrO_2 rod,
4: rhenium disk,
5: sample container (graphite),
6: pressure medium (ZrO_2),
7: heater ($LaCrO_3$), and
8: thermocouple ($W_{97}Re_3$-$W_{75}Re_{25}$).

placed some restrictions on the phase boundary. The equilibrium phase boundary determined in the present study is represented by a dashed line, and is given by P(GPa) – 30.6 –0.0053 T (K). At the highest temperature of 2100 K and at apressure of about 20 GPa, no diffraction peaks of either the B1 or the B2 phase were observed. Thus, we concluded that NaCl melted under these P-T conditions. Taking all the experimental data obtained in the present study into consideration, the triple point between B1, B2, and liquid NaCl would be located at a pressure of about 19.7 ±0.5 GPa and a temperature of about 2050 ±50 K.

According to the results of the present study, the B1 phase of NaCl cannot be used as a pressure gauge under P-T conditions corresponding to those at the bottom of the mantle transition zone and the lower mantle. Thus, we have to use other pressure gauges for *in situ* X-ray diffraction experiments to study properties of lower mantle minerals. MgO can be the best pressure gauge under lower mantle conditions because of its wide stability field. Many studies including those using MD simulations have been performed to establish the P-V-T equation of state of MgO [5].

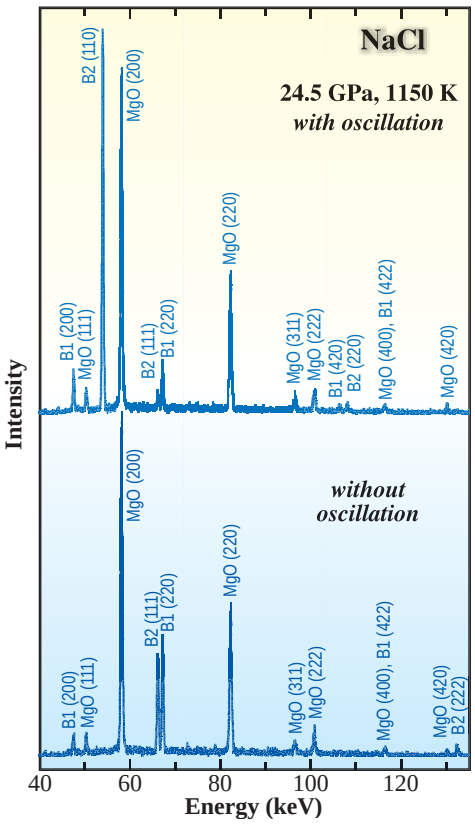

Fig. 2. Comparison between a diffraction pattern collected without press oscillation and that collected with press oscillation. These diffraction patterns were collected under the same P-T conditions of 24.7 GPa and 1150 K using the energy dispersive method with a fixed angle of approximately 6 degrees. The most intense peak of the B2 phase indexed as (110) was observed in the diffraction pattern obtained with press oscillation, whereas this peak was not observed in that obtained without press oscillation. The press oscillation dramatically reduces the effect of NaCl grain growth at high temperature on diffraction patterns obtained using the energy-dispersive method.

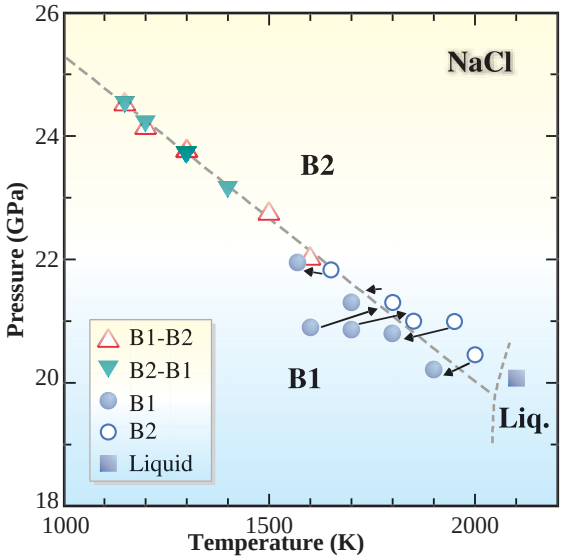

Fig. 3. The equilibrium phase boundary between the B1 and B2 phases in NaCl determined in the present study (dashed line between the B1 and B2 phases). Open and closed triangles represent P-T conditions where the B1 to B2 (forward) and B2 to B1 (backward) transitions were observed, respectively. Open and closed circles represent P-T conditions where single phases of B1 and B2 were observed, respectively. Under P-T conditions of 20.1 GPa and 2100 K, liquid NaCl was observed (a solid square). Upward and downward arrows represent complete transitions from B1 to B2 and those from B2 to B1, respectively. According to the present experimental results, the triple point between B1, B2, and liquid NaCl would be located at a pressure of 19.7 ± 0.5 GPa and at a temperature of 2050 ± 50 K.

Norimasa Nishiyama[a,*], Tomoo Katsura[b] and Ken-ichi Funakoshi[c]

(a) Geodynamics Research Center, Ehime University
(b) Institute of Study of the Earth's Interior, Okayama University
(c) SPring-8 / JASRI

Present address : GeoSoilEnviroCARS, University of Chicago, U.S.A.

E-mail: Nishiyama@cars.uchicago.edu

References

[1] W. A. Bassett *et al.*: J. Appl. Phys. **39** (1968) 319.
[2] D. L. Decker: J. Appl. Phys. **42** (1971) 3239.
[3] T. Katsura *et al.*: to be published in Phys. Earth Planet. Inter. (2004).
[4] X. Li and R. Jeanloz: Phys. Rev. B **36** (1987) 474.
[5] M. Matsui *et al.*: Am. Mineral. **85** (2000) 312.

Environmental Science

X-ray, which is a useful analytical tool for Environmental Science, makes it possible to analyze environmental objects directly, nondestructively and without pretreatment. These features allow the analyzed samples to be preserved for further investigation or as evidence, because the chemical states of elements of interest do not change during experiments and the obtained data are reproducible and objective.

The above-mentioned items are related to general analytical methods using X-ray, including those involving laboratory experiments with conventional equipment. Additionally, a powerful X-ray beam from the SPring-8 synchrotron radiation source has enabled microanalysis, microarea analysis, and chemical state analysis for almost all elements.

The three topics described below are XAFS applications for toxic heavy elements in environmental samples. The characterization by XAFS of heavy elements is important because the toxicity of elements often depends on the oxidation state and the local structure around an atom.

The first topic, which has been investigated by Takahashi *et al.*, concerns organotin compounds used in marine anti-fouling paints and fishing nets. They have determined “the organic extent” of organotin compounds.

The second topic, which has been investigated by Fujiwara *et al.*, concerns environmental restoration technologies using microorganisms. Reduction steps of Se (VI) by anaerobic bacteria have been clarified by XANES of the Se *K*-edge.

The third topic, which has been investigated by Izumi *et al.*, concerns the removal of trace heavy metals in water. For this topic, a high-resolution detector with a crystal analyzer was employed to measure X-ray fluorescence from Pb and As, although a 19-element solid-state detector was employed for the other two topics discussed in this paper. The chemical states of adsorbed metals have been clarified by XANES analysis, and surface reactions on the adsorbent are discussed.

Momoko Takemura

Speciation of Tin Compounds in Environmental Samples Using Sn *K*-edge XANES

Speciation, identification of the chemical states of elements in the environment, is indispensable in determining the environmental behavior, bioavailability, and the influence of elements on the quality of the environment. For speciation, X-ray absorption fine structure (XAFS) is a powerful tool, because it is a direct method by which we can avoid the change of the chemical state of target elements in environmental samples. XAFS is reasonably sensitive especially when conducted in the fluorescence mode using sensitive detection techniques such as the use of a multi-element semiconductor detector. The water solubility, bioavailability, and toxicity of an element depend on the oxidation state and the ligand coordinated to the element. We have studied the environmental behavior of arsenic, lead, iodine, and other elements [1-3] in terms of the redox reaction and the determination of tin species particularly organotin species [4,5].

Organotin compounds such as tributyltin (TBT) and triphenyltin (TPT) have been widely used as biocides in anti-fouling paints and fishing nets. However, it has been found that these compounds cause damage to marine organisms, such as imposex and deformity in mollusks. The speciation of organotin compounds has been of great interest due to the species-dependent toxicity and the widespread application of organotin compounds as biocides. In recent years, chromatographic techniques such as gas chromatography or liquid chromatography coupled with appropriate detectors have been widely used for the analysis of organotin compounds. These analytical methods essentially require many pretreatment procedures, such as decomposition, extraction, enrichment, and derivatization. In this study, we have tested the possibility of using an X-ray absorption near-edge structure (XANES) as a nondestructive method for identifying inorganic and organic tin species in solid environmental samples. A high-energy XANES for the Sn *K*-edge (29.19 keV) was applied in this study to determine Sn speciation [4]. It is better to employ the *K*-edge rather than the *L*-edge (3.9 – 4.5 keV) for Sn, as this enables us to measure the XANES for environmental samples containing water, whereas the sensitivity would be lower using the *L*-edge, which is close to the soft X-ray region, as a result of X-ray scatterings. It is also expected that there would be no interference in the *K*-edge region from major elements such as Ca and K, which can interfere with the *L*-edge XANES for Sn.

Tin *K*-edge XANES spectra of all reference materials of inorganic and organic tin compounds, an anti-fouling paint sample, and a sediment reference material (NIES CRM No. 12) were obtained at beamline **BL01B1**. In order to obtain the fluorescence XANES spectra, a 19-element solid-state detector (SSD) was employed to collect fluorescence X-rays from Sn in the samples.

Figure 1 shows normalized XANES spectra at the Sn *K*-edge for the standard samples such as tetrabutyltin (TeBT), tributyltin chloride (TBTCl), dibutyltin chloride (DBTCl), monobutyltin chloride (MBTCl), and $SnCl_4$. It is obvious that the first peak

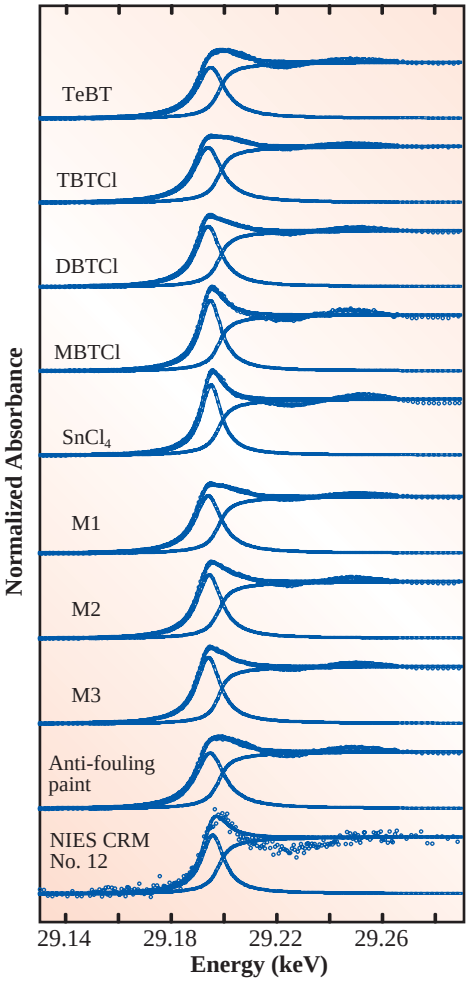

Fig. 1. Tin *K*-edge XANES spectra of standard materials (TeBT, TBTCl, DBTCl, MBTCl, and $SnCl_4$), mixtures of the standard materials (M1, M2, and M3), an anti-fouling paint sample and NIES CRM No. 12 (reference sediment sample) with simulation results by arctangent and Lorentzian functions. M1 = 1:1 mixture of TBTCl and DBTCl by mole ratio; M2 = 1:1 mixture of TBTCl and MBTCl; M3 = 1:1 mixture of DBTCl and MBTCl.

exhibits systematic broadening upon increasing the number of butyl groups bound to Sn, which is presumably due to multiple scatterings by the butyl groups bound to Sn. We found a similar broadening for butyltin compounds with different counter anions (hydroxide, oxide, acetate, and hydride) and phenyltin and methyltin compounds, which confirms that the variation is due to the coordination of the organic ligands to Sn. These findings suggest that the broadening of the first peak can be employed for the speciation of Sn compounds in environmental samples. To quantitatively analyze the Sn species from the broadening, the XANES spectra were fitted by a combination of a Lorentzian function and an arctangent function (Fig. 1). There is a linear correlation between full width at half maximum (FWHM) of the Lorentzian function and the number of butyl groups (Fig. 2). In environmental samples, Sn species do not consist of one component but include various organic and inorganic species. Therefore, XANES spectra of mixtures of different Sn species (M1, M2, and M3) were also measured (Fig. 1). The FWHM values of the mixtures are plotted in Fig. 2 against the average number of butyl groups bound to Sn in the mixtures, which we name "the organic extent." For example, the organic extent becomes 2.0 for the 1:1 mixture of TBTCl and MBTCl. The values of the three mixture samples are consistent with the calibration line (Fig. 2), showing that the FWHM of the Lorentzian function provides the organic extent for the Sn species in environmental samples.

Similar analyses were applied to environmental materials, the anti-fouling paint, and NIES CRM No. 12. We could obtain XANES spectra for NIES CRM No. 12 containing only 10.7 ppm of Sn, suggesting that the detection limit of the fluorescent XANES can reach the ppm level, which could be sufficiently sensitive for Sn speciation in some sediments and biological samples. From the FWHM of the environmental samples, it was shown that tributyl or tetrabutyl compounds are the main Sn species in the anti-fouling paint, which is consistent with the fact that TBT is the main Sn species in the paint. The organic extent of Sn in NIES CRM No. 12 is about 1, suggesting that inorganic species are the main Sn component in the sample. The analyses of the environmental samples indicate that the present method can be used for Sn speciation in solid materials such as sediments, biocides, and biological samples.

Compared with chromatographic methods, it is difficult to obtain the precise concentration ratio of various butyl-, phenyl-, and methyl-substituted compounds by the present XANES method. However, it has often been noted that there are large discrepancies between different studies on the concentrations of organic and inorganic Sn species in environmental samples using conventional chromatographic methods. It is considered that the present method can be more reliable in terms of accuracy, since the method does not require any complex pretreatment procedures that may induce various errors in chromatographic analyses. Although the XANES method cannot give the precise concentration of each organotin compound, direct observation using XANES will be helpful for estimating roughly the ratio of organic and inorganic tin compounds in environmental samples.

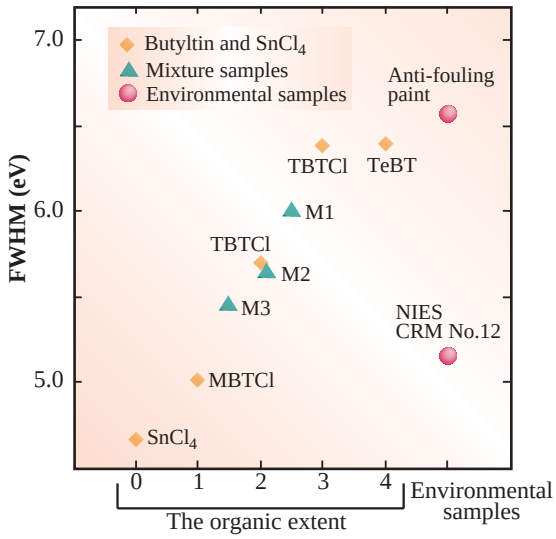

Fig. 2. Relationship between the FWHM of the Lorentzian function in the simulation of Sn *K*-edge XANES spectra and the organic extent (= the average number of butyl groups bound to Sn). The results for the mixture samples (M1, M2, and M3) are also plotted. The FWHM values of the anti-fouling paint and NIES CRM No. 12 are indicated at the right-hand section.

Yoshio Takahashi

Dept. of Earth and Planetary Systems Science, Hiroshima University

E-mail: takahasi@geol.sci.hiroshima-u.ac.jp

References

[1] Y. Takahashi *et al.*: Environ. Sci. Technol. **38** (2004) 1038.
[2] Y. Takahashi *et al.*: Anal. Sci. **19** (2003) 891.
[3] Y. Takahashi *et al.*: Chem. Lett. (2002) 366.
[4] N. Sakakibara, Y. Takahashi, Y. Yamaguchi, K. Shibata and T. Uruga: Chem. Lett. (2004) 264.
[5] Y. Takahashi *et al.*: Anal. Chem. (2004) - in press.

Changes of Chemical States of Toxic Metals in Aquatic Sediments by Bacteria

The implementation of Pollutant Release and Transfer Register (PRTR) obliged us to report the total amount of chemical substances, such as toxic metals, released into the atmosphere, hydrosphere and soil. The total amount of these substances that have been released into the environment due to human activity is now becoming clear. However, the chemical state changes of toxic metals have not been clarified. We should clarify the behavior of toxic metals in the environment to ensure safety against damage due to toxic metal contamination, because the toxicity of a metal depends on its valence or combined states.

In many cases, microorganisms have assumed a vital role in the chemical state changes of metals. The use of microorganisms is expected to lead to the development of environmental restoration technologies by revealing the biological reaction pathway of metals.

Recently, a selenate reduction bacterium, *Sulfurospirillum barnesii* [1], was isolated from a freshwater sediment. *S. barnesii* has the ability to reduce selenic acid [Se(VI)] under anaerobic conditions, using organic acid as an electron donor.

We present here the chemical state changes observed for selenium by X-ray absorption fine structure (XAFS), focusing our attention on the reduction ability of *S. barnesii* to reveal the behavior of selenium in a biological reactive process.

We used a DSM 10660 strain [2] (= ATCC 700032 strain) for *S. barnesii*, cultivated in a 500 ml sealed bottle with *Sulfurospirillum* II medium containing 83 mg/l Se(VI). Cultivation was carried out at constant temperature (30°C) under anaerobic conditions with the injection of inert gases (N_2/CO_2).

XAFS measurement was carried out at beamline **BL01B1** with a two-crystal Si(111) monochromator. XAFS spectra of *S. barnesii* culture were collected in the fluorescence mode using a Ge 19-element solid-state detector.

Figure 1 shows Se *K*-edge XANES spectra of *S. barnesii* culture and reference materials. A peak due to metallic selenium [Se(0)] was clearly observed in the spectra after 28, 37, 43, 53 and 66 hours. Also, a peak due to tetravalent selenium [Se(IV)] was observed in the same spectra. This result shows that the reduction pathway from Se(VI) to Se(0) by *S. barnesii* goes through Se(IV).

To estimate the chemical composition of selenium in each moment, we calculated the ratio of each chemical states by the curve-fitting method using the spectra of the reference materials. The result is shown in Fig. 2. The change of the chemical composition of selenium indicates that Se(VI) constantly decreases with increasing *S. barnesii* growth rate. In this case, although a rate-limiting step of the reduction pathway from Se(IV) to Se(0) occurred for 20 hours after seeding, the reduction of Se(VI) to Se(IV) proceeded constantly. Thus, from the above finding, it is assumed that the reduction of Se(VI) to Se(IV) by *S. barnesii* is faster than that of Se(IV) to Se(0) under such a high selenium concentration (83 mg/l selenium).

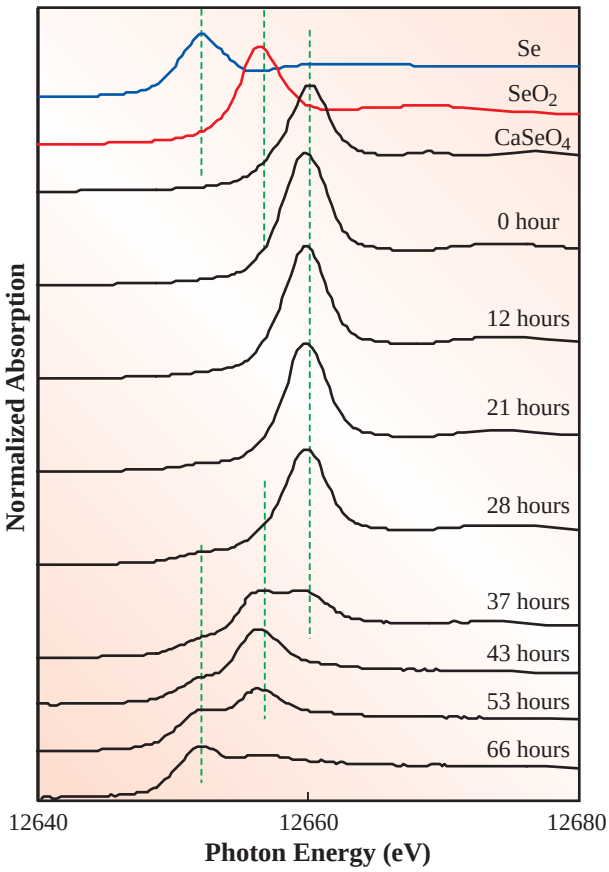

Fig. 1. Se *K*-edge spectra of culture after 0, 12, 21, 28, 37, 43, 53 and 66 hours from seeding *S. barnesii*, along with Se, SeO_2 and $CaSeO_4$ for reference.

The results also indicate that selenium released in to the hydrosphere is immobilized as metallic selenium by anaerobic bacteria, such as *S. barnesii*, which have the ability to reduce selenium. Figure 3 shows pattern diagrams of dynamics of selenium in aquatic sediments. If we can accelerate the growth of selenium reduction bacteria, and keep them in high density, we will be able to effectively render selenium harmless.

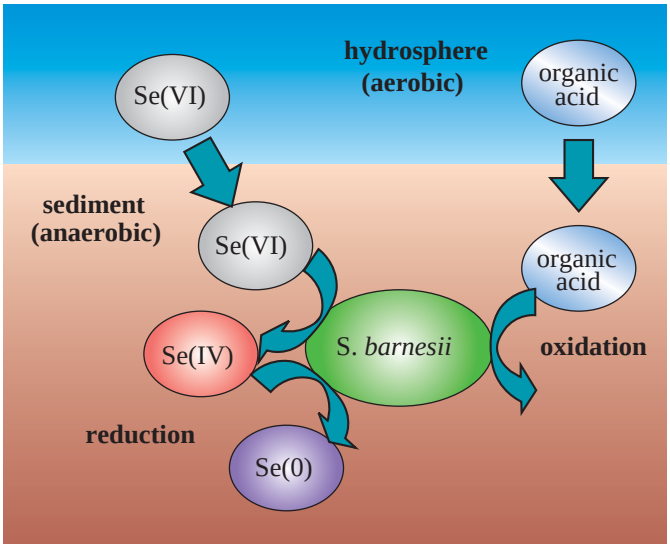

Fig. 3. Pattern diagrams of dynamics of selenium in aquatic sediments.

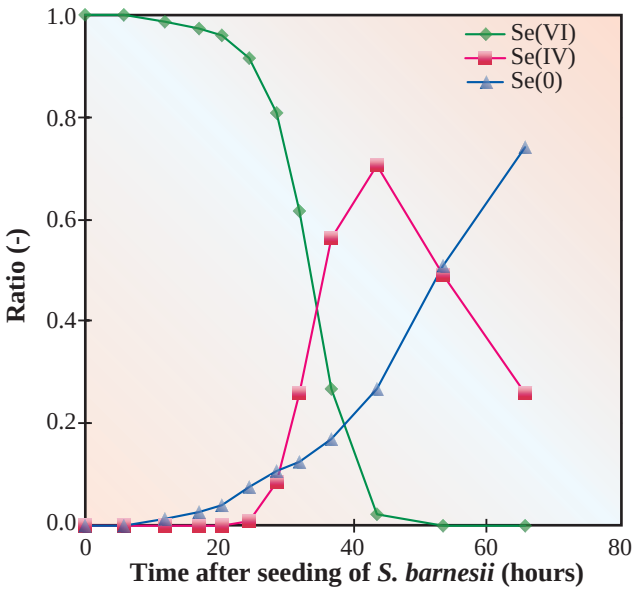

Fig. 2. Change in chemical composition of selenium with time. (Result of calculation by the curve-fitting method using the spectra of reference materials).

Shigeki Fujiwara[a], Norizo Saito[b] and Yasuhiro Konishi[b]

(a) JFE Engineering Corporation
(b) Osaka Prefecture University

E-mail: fujiwara-shigeki@jfe-eng.co.jp

References

[1] R.S. Oremland *et al.*: Appl. Environ. Microbiol. **65** (1999) 4385.
[2] DSMZ List of Media: (http://www.dsmz.de/media/med771.htm).

Monitoring Trace Amounts of Lead and Arsenic Adsorbed under Environmental Conditions by XAFS Combined with Fluorescence Spectrometry

The risk of trace amounts of metals in environmental water to human health has been pointed out [1]. The regulations of metal concentration in water are becoming more severe: e.g., 100 ppb for lead and 10 ppb for arsenic. Co-precipitation and adsorption are promising methods for the removal of trace amounts of metals in water. Information on the removed metal site structure and the chemical state is crucial in the assessment of the removal effectiveness for the most hazardous valence state of metals.

X-ray absorption fine structure (XAFS) has become widely used with the state-of-the-art technology of synchrotron radiation and advanced X-ray detectors to monitor the local structure of noncrystalline and heterogeneous/hybrid materials. However, there are still experimental difficulties in measuring at high-energy resolution the absorption edge of the trace amount of an element in samples containing a high concentration of heavy element(s).

In this account, 0.12 wt% Pb adsorbed from a 100 ppb aqueous solution and 0.20 wt% As adsorbed from a 200 ppb arsenite solution were monitored by the XAFS combined with a high-energy-resolution fluorescence spectrometer [2]. The energy resolutions were 0.3 eV at 5 keV and 1.1 eV at 8 keV. The latter value includes the contribution of the beamline [3]. These values are smaller than the core-hole lifetime widths of Pb L_3 (5.81 eV) and As K (2.14 eV). Thus, the advantages of the method applied in this account are (i) the removal of lifetime broadening [4], (ii) reasonable signal/background ratio, and that (iii) the method is free from the problems associated with photon-counting losses.

The X-ray fluorescence from Pb adsorbed on $Mg_6Fe_2(OH)_{16}(CO_3)\cdot 3H_2O$**(1)** was analyzed by a Rowland-type spectrometer (radius 220 mm) equipped with a Johansson-type cylindrically bent Ge(555) crystal and a scintillation counter at beamline **BL10XU** [5]. The spectrometer was tuned at 10551.5 eV (Pb $L\alpha_1$ emission), and the obtained Pb L_3-edge X-ray absorption near-edge structure (XANES) spectra are shown in Figs. 1(a-c). Based on the comparison of the rising edge and post-edge peak energies, spectrum a for Pd adsorbed from the 1.0 ppm solution resembled only that for $2PbCO_3\cdot Pb(OH)_2$ (Fig. 1(g)). Figures 1(b,c) for Pb adsorbed from a 100 ppb solution resembled each other. The rising edge position shifted from –1.1 to –1.3 eV compared to Fig. 1(a). Figures 1(b,c) resembled only those of PbY zeolite (Fig. 1(d)), Pb mordenite or Pb-ZSM-5. Pb^{2+} ions replace the protons or Na^+ sites of zeolites.

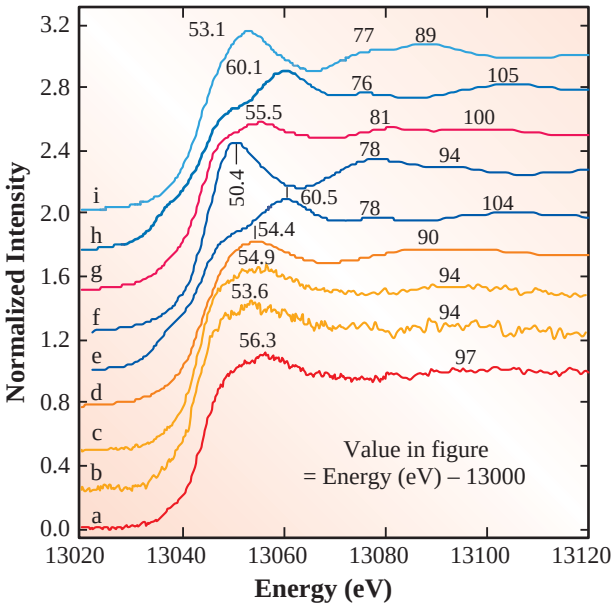

Fig. 1. Normalized Pb L_3-edge XANES spectra for Pb^{2+} on **1** measured utilizing a secondary fluorescence spectrometer **(a – c)**. The Pb content was 1.0 wt% adsorbed from a 1.0 ppm Pb^{2+} solution **(a)** and Pb 0.30 wt% **(b)** and 0.12 wt% **(c)** adsorbed from a 100 ppb solution. XANES spectra for PbY zeolite **(d)**, PbO **(e)**, $Pb(NO_3)_2$ **(f)**, $2PbCO_3\cdot Pb(OH)_2$ **(g)**, $Pb_6O_4(OH)_4$ **(h)**, and $PbCO_3$ **(i)** were measured in the conventional transmission mode.

An unresolved shoulder peak was observed at 13049 eV in Figs. 1(a-c). A similar peak was also observed for $2PbCO_3\cdot Pb(OH)_2$ (Fig. 1(g)). No shoulder peak appeared in this region for PbY (Fig. 1(d)).

In summary, most of the Pb^{2+} coagulated as a eutectic mixture of $PbCO_3$ and $Pb(OH)_2$ on **1** in the adsorption from a 1.0 ppm solution. In contrast, in the adsorption from a 100 ppb solution, the major Pb phase was ion-exchanged Pb^{2+} via surface reaction A.

$$-OH + Pb^{2+} \rightarrow -OPb^{+} + H^{+} \qquad (A)$$

A shoulder peak at 13049 eV suggests a minor contribution from the coagulated eutectic mixture of $PbCO_3$ and $Pb(OH)_2$ on **1**. The interpretation of this difference that depends on the Pb concentration is illustrated in Fig. 2. The surface of **1** has a buffering effect and the pH value in the proximity of **1** becomes 7 – 8 due to the effect of coagulant chemicals released through a slight dissolution of **1** [5]. In the pH region, a forward reaction of B proceeds from a 1.0 ppm solution.

$$Pb^{2+} + nCO_3^{2-} + 2(1-n)OH^- \rightarrow nPbCO_3 \bullet (1-n)Pb(OH)_2 \qquad (B)$$

In the adsorption from a 100 ppb Pb^{2+} solution, equilibrium shifted to the left-hand side of equation B. The ratio of free Pb^{2+} in the solution dramatically increased, and thus the, ion exchange reaction (equation A) dominantly proceeded. Hence, the major species of ion-exchanged Pb^{2+} and the minor phases of the coagulated eutectic mixture of $PbCO_3$ and $Pb(OH)_2$ were detected (Figs. 1(b,c)).

The As *K*-edge XANES spectra were also measured similarly to the Pb L_3-edge spectra described above. The fluorescence spectrometer was tuned to 10544.3 eV (As $K\alpha_1$ emission). Samples of 0.48 – 0.20 wt% As adsorbed from 16 ppm of arsenate, 16 ppm of arsenite, and 200 ppb of arsenite aqueous solutions were studied (Figs. 3(d-f)) on an Fe-impregnated montmorillonite $(Na_{1.5}Ca_{0.096}Al_{5.1}Mg_{1.0}Fe_{0.33}Si_{12}O_{27.6}(OH)_{6.4})$**(2)** [3]. The three spectra resembled one another. The strong peak positions in the post-edge region were very close to that for the spectrum of $KH_2As^{V}O_4$ (Fig. 3(c)) rather than that for the spectrum of $As^{III}_2O_3$ (Fig. 3(b)). Thus, the observed oxidation of trace amounts of arsenite upon adsorption on **2** to arsenate is important in the preservation of the environment because arsenate affects far less human health than arsenite.

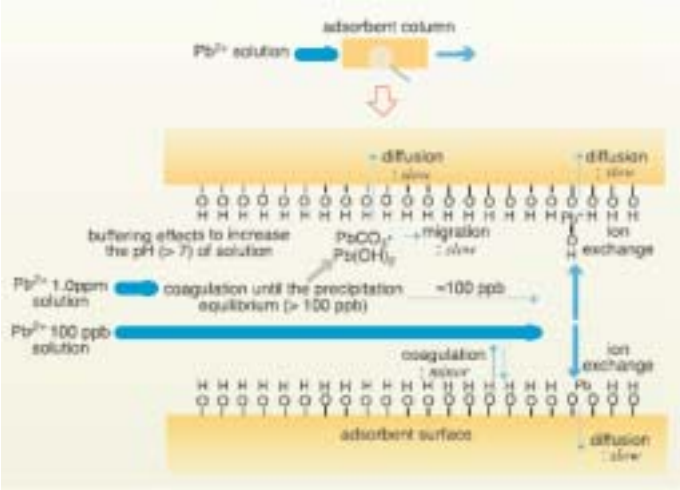

Fig. 2. Pb^{2+} adsorption mechanism on **1** from 1.0 ppm and 100 ppb aqueous Pb^{2+} solutions.

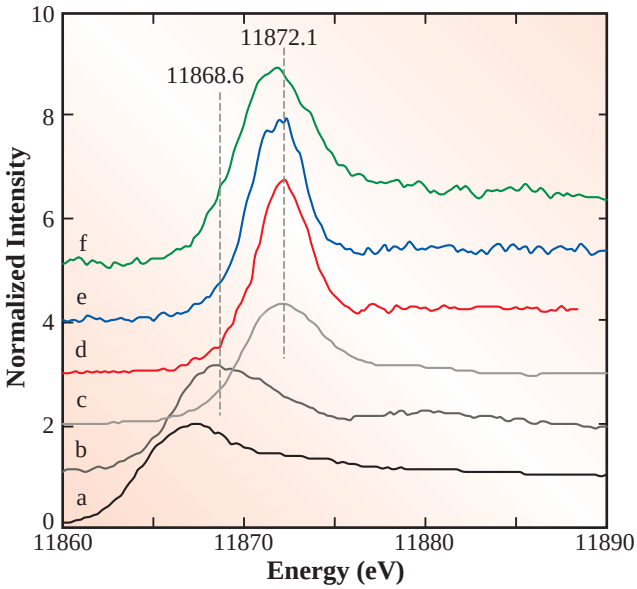

Fig. 3. Normalized As *K*-edge XANES spectra for As metal **(a)**, As_2O_3 **(b)**, KH_2AsO_4 **(c)**, and As adsorbed on **2** (Fe 15.3 wt%, **d** – **f**) from solutions of 16 ppm of KH_2AsO_4 **(d)**, 16 ppm of As_2O_3 **(e)**, and 200 ppb of As_2O_3 **(f)**. Spectra **(d** – **f)** were measured utilizing a high-energy-resolution fluorescence spectrometer. The spectra **(a** – **c)** were measured in the conventional transmission mode.

Yasuo Izumi

Tokyo Institute of Technology

E-mail: yizumi@chemenv.titech.ac.jp

References

[1] http://www.who.int/water_sanitation_health/en/
[2] Y. Izumi *et al.*: J. Electron Spectrosc. Relat. Phenom. **119** (2001) 193.
[3] Y. Izumi, F. Kiyotaki, T. Minato, D. Masih and Y. Seida: Phys. Scr. - in press.
[4] Y. Izumi and H. Nagamori: Bull. Chem. Soc. Jpn. **73** (2000) 1581.
[5] Y. Izumi *et al.*: Anal. Chem. **74** (2002) 3819.

INDUSTRIAL APPLICATIONS

In this section, six carefully selected experiments successfully accomplished in the industrial field in 2002B and 2003A are presented.

The very interesting experiments referred in this section were achieved using the following five different beamlines; that is, two experiments were achieved using the engineering science research beamline, BL19B2, and four experiments, using the contract beamline for industrial consortium ID, BL16XU, the magnetic materials beamline, BL39XU, the structural biology II beamline, BL40B2, and the single crystal structure analysis beamline, BL02B1.

The first experiment is about an *in situ* study of rubbers for a studless tire that can run on ice or snow by refraction contrast imaging which provides a visual information (BL19B2), the second experiment involves the X-ray scattering measurement and X-ray absorption spectroscopy of a CVD-RAM material which provide useful information for the development of high-speed phase change devices (BL19B2), the third experiment is about a study of the oxide/Si interface for an international technology roadmap of a semiconductor (ITRS) and a complementary metal oxide semiconductor (CMOS) by X-ray crystal truncation rod (XCTR) scattering (BL16XU), the fourth experiment is about a study of a Co/Pt multilayer for recording media by X-ray magnetic circular dichroism (XMCD) (BL39XU), the fifth experiment is about an *in situ* small-angle X-ray scattering study of a polymer material (BL40B2) and the sixth experiment involves the strain analysis of a thermal barrier thick coating using high-energy X-ray (BL02B1). The remarkable articles shown in this section can be used as good models for material researchers.

Tokihiko Okamoto

Dynamic Observation of Contact Behavior between Rubber for Tires and Ice by Refraction Contrast Imaging

Studded tires were abolished in 1994 due to environmental problems, such as dust and noise pollution, in Japan. In order to run on ice or snow safely, winter tires called studless tires have been developed and sold. In recent years, many studless tires are available in the market. Studless tires make the surface of an icy road very smooth when they slip on the road, resulting in an icy road with a very low friction coefficient. In addition, the friction between a studless tire and ice is related to the characteristics of the ice, e.g., the crystal structure, the size, the dielectric constant and the concentration of impurities [1,2]. Also, the frictional heat generated between a studless tire and an icy road dissolved the surface of the icy road, and water serves as a lubricant [3]. These friction behaviors become complex under the conditions of the boundary and the fluid lubrication. Nihei *et al.* have reported about the effects of the surface roughness of a studless tire [4]. According to their report, when the surface roughness was about 50 μm, the friction coefficient became maximum, and they expected that water is probably removed due to surface unevenness. Therefore, a systematic investigation and a detailed analysis of these behaviors are required to improve the performance of studless tires. In this study, we observed and investigated the contact behavior between the rubber for tires and ice.

The *in situ* observation of their behaviors by X-ray refraction contrast imaging caused by the reflection effect was carried out at the third hutch of beamline **BL19B2**. A continuous X-ray from the synchrotron radiation source was monochromatized to 20 keV by a Si(311) double crystal monochromator. In order to perform time-resolved observation, the X-ray detector adopted was a CCD camera with a pixel size of 10 μm (C4880, Hamamatsu Photonics K.K). The CCD camera was coupled with the optical lens and the phosphor screen. The distance between the sample and the X-ray CCD detector was determined to be about 2 m using the formula [5], $\Delta X = (\lambda L)^{1/2}$, where ΔX is the space resolution of detection, λ the X-ray wavelength, and L the distance from the sample to the detector. The beam diffuser made by rotating a sandpaper was installed at the first hutch in order to remove interference patterns, probably caused by Be windows. The compression-testing machine equipped with a high-precision cooling function was prepared (Fig. 1). Rubbers of different surface roughnesses were obtained using various kinds of sandpaper based on the JIS standard. The surface roughnesses of the rubbers were ~ 20 μm, ~ 45 μm, ~ 60 μm and ~ 90 μm. The rubbers prepared were of $2^{l} \times 15^{w} \times 3h^{h}$ mm^3. The X-ray refraction contrast imaging data was stored during the process of compressing the sample at a speed of 5 mm/min until the load reached 2 kg/cm^2.

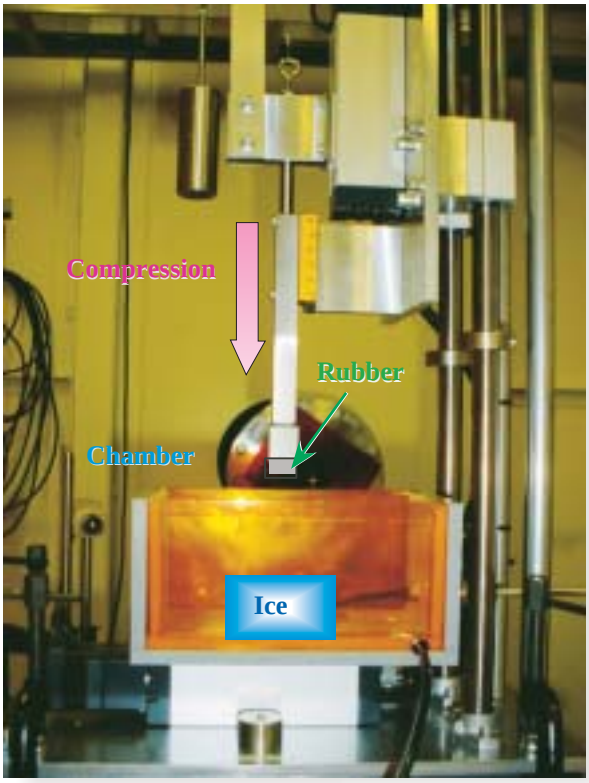

Fig. 1. Compression-testing machine equipped with a high-precision cooling function.

The images of the contact behavior between rubbers of different surface roughnesses and ice are shown in Fig. 2. When the surface roughness is about 20 μm, the rubber and ice are completely in contact, and there is almost no clearance. The dewatering effect could not be acquired at this surface roughness. As the surface roughness increases, the clearance increases due to surface unevenness, and then it seems that passages for dewatering would be formed. On the other hand, when the surface roughness is very large, the friction coefficient is small because of the drastic decrease in the contact area. Thus, it is very important to observe *in situ* contact behaviors between the rubbers and ice in order to improve the performance of studess tires.

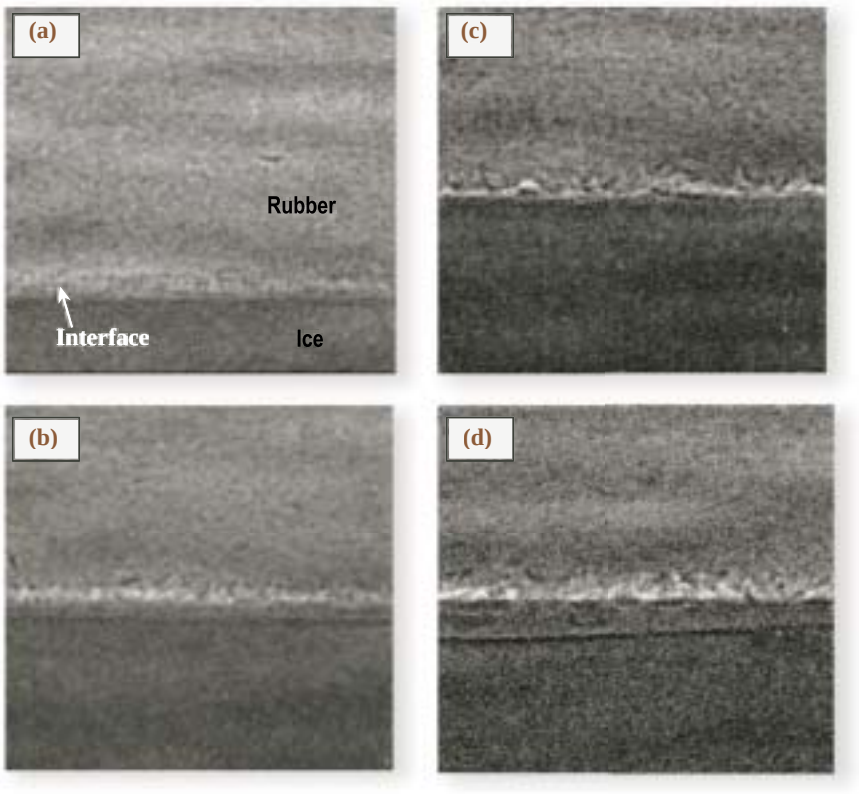

Fig. 2. X-ray refraction contrast images under the condition of ice and rubbers contact. The surface roughnesses of the rubbers are **(a)** 20 μm, **(b)** ~ 45 μm, **(c)** ~ 60 μm and **(d)** 90 μm.

Hiroyuki Kishimoto

Material & Process Technology Research Dept.,
SRI Research and Development Ltd.

E-mail: h-kishimoto.az@srigroup.co.jp

References

[1] M. Nihei *et al.*: Jidousha Gijutsu Kai Ronbunsyu **25** (1994) 141.
[2] M.A. Rist: J. Phys. Chem B **101** (1997) 6263.
[3] M. Nihei *et al.*: Jidousha Gijutsu Kai Ronbunsyu **28** (1997) 89.
[4] M. Nihei *et al.*: International Tribology Conference (1998).
[5] Y. Suzuki *et al.*: SPIE Proc. **13** (1999) 3770.

High-Speed Phase Change in GeTe-Sb_2Te_3 Pseudobinary Compound, a Superior DVD-RAM Material

In a rewritable phase-change optical disk such as a DVD-RAM (digital versatile disc - random access memory), information is recorded using the change in optical property, such as reflectivity or transmissivity, that results from the phase transformation of the material between the crystal (erase) and amorphous (record) states. Currently, the best-known phase-change material is the GeTe(1-x)-Sb_2Te_3(x) pseudobinary compound, in which the reversible structural change can be induced in a very brief time of 10 ns. The crystallization speed of this compound is very fast, which contributes to the shortening of the erasing time, and extremely high-speed rewriting can be realized. To clarify this high-speed phase-change mechanism, the crystal and amorphous structures of this pseudobinary compound has been studied for several years by powder diffraction, extended X-ray absorption fine structure (EXAFS), and grazing incidence X-ray scattering (GIXS) measurements using synchrotron radiation at beamlines **BL02B2** and **BL19B2**.

X-ray diffraction measurements revealed that this compound crystallizes into a single phase with a simple NaCl-type structure ($Fm\bar{3}m$) as the metastable state, upon laser annealing (erasing operation) over a wide composition range of GeTe from 100 mol% to at least 50 mol% (Fig. 1). Te occupies the 4(a) sites (Cl sites) and Ge and Sb locate randomly at the 4(b) sites (Na sites) [1].

EXAFS measurements of the amorphous compound (x = 0, 1/7, 1/5, 1/3, and 1/2) showed that Ge, Sb, and Te are about four-, three-, and two-fold coordinated, respectively, and these coordination numbers were almost constant and independent of the pseudosbinary composition (x). In addition, the amorphous compound had a specific coordination feature. The analyzed coordination numbers (n(x)) of Ge, Sb, and Te to each other are shown in Fig. 2. From this figure, the following relations can be derived. (i) Te-Te pairs are rarely present in this pseudobinary amorphous compound. In other words, Te is surrounded by only Ge or Sb. (ii) Sb bonds more easily to Te than to Ge or Sb. For example, it is estimated that when one Sb atom is doped into amorphous GeTe (x – 0), the Sb atom, which is three-fold coordinated, is surrounded by about two Te atoms but by only one Ge. (iii) Ge bonds to the three kinds of atoms with almost equal probabilities. These suggest that two kinds of atomic pairs, Ge-Te and Sb-Te, exist in this pseudobinary amorphous

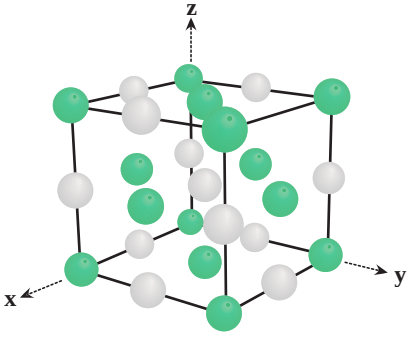

Fig. 1. The crystal structure of laser-crystallized GeTe-Sb_2Te_3 metastable phase shown schematically in perspective. Green circles show atomic positions for Te. Gray circles show those for Ge or Sb. The lattice constant, a, is about 6 Å.

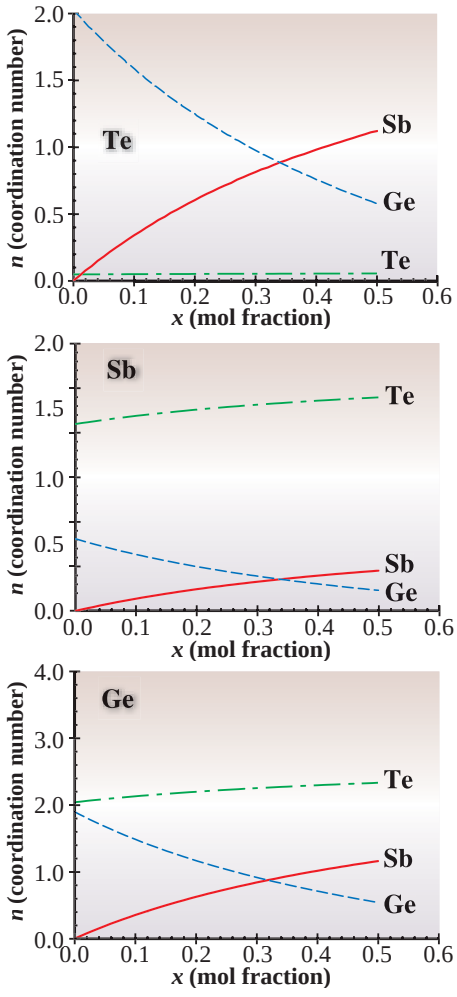

Fig. 2. Determined coordination numbers of the atoms surrounding Te (top), Sb (middle) and Ge (bottom). n and x in the figures indicate coordination number and mol fraction of Sb_2Te_3 in the GeTe-Sb_2Te_3 pseudobinary system, respectively.

compound to a greater extent than if they were coordinated completely at random. These two pairs constitute the structural frame in the crystal phase of this compound; as seen in Fig. 1, only two kinds of bond pairs, Ge-Te and Sb-Te, exist in it. It is consequently presumed that this amorphous compound already has atomic arrangements with the characteristics seen in its crystalline state. When thermal energy is added to the amorphous (recording) mark by laser irradiation, these pairs act as crystallization nuclei and trigger the arrangement of atoms into an NaCl-type structure.

Figure 3 shows the electron radial distribution functions (RDF) for $GeSb_2Te_4$ (x=1/2) and $Ge_2Sb_2Te_5$ (1/3) amorphous films, which were derived by using the GIXS intensities up to the wave number of about 12 $Å^{-1}$. The patterns of these RDFs are very similar to each other and clearly indicatea medium-range order; in the patterns we can see three distinct peaks indicating atomic pair distributions at the distances of r = 2.8, 4.2, and 6.2 Å. Figure 4 shows the RDF calculated for the crystal structure of $GeSb_2Te_4$ (indicated by bars) with that observed for its amorphous state. It can be seen that the positions and the amplitudes of the three RDF peaks of the amorphous phase are near those of the 1st (r = 3 Å and CN = 6), 2nd (4.2 Å and 12) and 5th (6.7 Å and 24) atomic pairs in the crystalline phase. Here, CN means the number of atoms at the i^{th} coordination shell in the crystal (see Fig. 1). It was, however, difficult to find the peaks corresponding to the radial distances of the 3rd (5.2 Å and 8) and 4th (6.0 Å and 6) atomic pairs in the crystalline phase. We then divided the RDF of the amorphous film into six single Gaussian peaks (shown by dashed curves in Fig. 4) by least squares fitting. The synthesized curve (thin solid curve) showed good agreement with the observed RDF profile. The third observed peak consists of three single peaks at r – 5.7, 6.2 and 6.9 Å, which are presumed to correspond to the 3rd, 4th and 5th atomic pairs of the crystal structure. These results suggest that the local structure of this pseudobinary amorphous compound bears the structural characteristics of its crystalline phase to a large extent [3].

We have seen that the crystal and amorphous phases of the GeTe-Sb_2Te_3 pseudo-binary phase-change material have very similar atomic arrangements to each other over a wide composition range. It is believed that when an amorphous mark is given energy by laser irradiation to erase a record, this structural similarity between the two phases enables the phase change to occur with only a slight atomic movement, which results in rapid phase transformation.

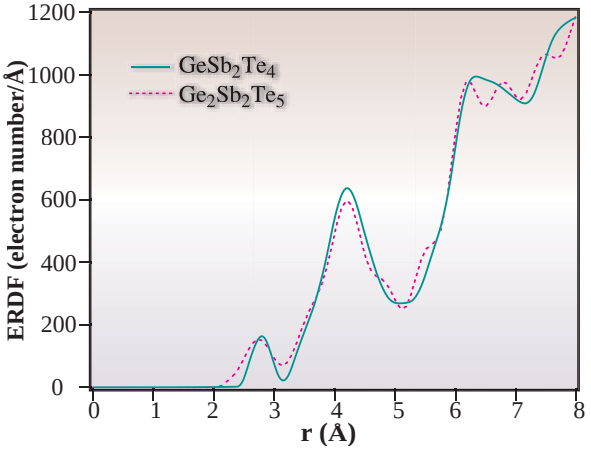

Fig. 3. The electron radial distribution functions (RDFs) of the amorphous films of $GeSb_2Te_4$ (solid line) and $Ge_2Sb_2Te_5$ (dashed line).

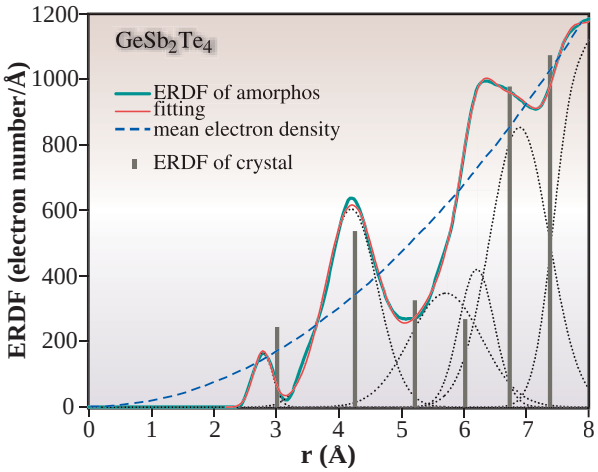

Fig. 4. The electron radial distribution function (RDF) of the amorphous film of $GeSb_2Te_4$ (indicated by thick line). The bars indicate the calculated RDF of the crystal structure of $GeSb_2Te_4$.

Toshiyuki Matsunaga[a], Noboru Yamada[b] and Masugu Sato[c]

(a) Characterization Technology Group, Matsushita Technoresearch, Inc.
(b) Storage Media Systems Development Center, Matsushita Electric Industrial Co.
(c) SPring-8 / JASRI

E-mail: matsunaga.toshiyuki@jp.panasonic.com

References

[1] T. Matsunaga and N. Yamada: Jpn. J. Appl. Phys. **41** (2002) 1674.
[2] T. Matsunaga, N. Yamada and M. Sato: submitted in Phys. Rev. B
[3] M. Sato *et al.*: 2003 MRS Fall Meeting Proc. (Boston in USA, 2003).

Atomic Displacement at the Gate Oxide / Si Interface Evaluated by X-ray CTR Scattering

Driven by the demand for higher electric performances as assessed in the International Technology Roadmap of Semiconductor (ITRS), complementary metal oxide semiconductor (CMOS) devices have been scaled down continuously. As a result, the thickness of SiO_2-based gate oxide is approaching atomic dimensions and the requirement of the electric properties for the gate oxide is becoming increasingly severe. As shown in Fig. 1, a typical thickness of gate oxides for 90-nm-node CMOS transistors is 1.1 nm, which corresponds to only four SiO_2 molecular layers. For the achievement of CMOS devices with such ultrathin SiO_2, nitrogen must be incorporated into the gate oxide to suppress boron penetration from the polycrystalline-Si gate into the underlying channel region, and to decrease gate leakage current. Controlling the depth profile of nitrogen in the gate oxide is a key issue since an excessive amount of nitrogen at the gate oxide/Si interface generates fixed charge and an interface level, which lead to the degradation of the electric properties and reliability of the gate oxide. To fabricate the CMOS devices with high electric performance and high reliability, the evaluation techniques for the gate-oxide/Si interface structure with nitrogen incorporation in an atomic scale has been desired but have not been realized.

Crystal truncation rod (CTR) scattering is a surface X-ray diffraction which is particularly sensitive to the structure of surfaces and thin films [1-3]. CTR scattering is a continuous scattering perpendicular to the surface because the Laue condition is relaxed to a non-integer Miller index in the vertical direction due to the abrupt termination of the crystal periodicity at the surface. The intensity of CTR scattering contains information on the structure of the surface atoms through the interference with the scattering amplitude from the substrate. In this work, we developed an evaluation technique of the interface atom displacement (IAD), expressed by δc, using CTR scattering, which is sensitive to the interfacial atom structure, particularly for nitrogen distribution. IAD is defined as the vertical displacement of the topmost Si atoms from the expected position for crystalline Si at the interface.

Based on the calculation of kinematical diffraction for the interface model with IAD, we found that δc introduces asymmetry of the CTR peak profile. By measuring the asymmetry, we can evaluate δc from the measured CTR profiles. We developed an analytical program, which can be used to evaluate δc based on the optimization of the measured CTR profile using the IAD model.

Since the intensity of CTR scattering is very weak compared to the bulk diffraction peak, high flux X-rays are required for the measurement. We carried out the CTR measurement using the newly installed four-circle diffractometer at the undulator beamline **BL16XU**. In the experiment, the X-ray wavelength of 0.116 nm was selected using a double-crystal monochromator. For the detection of X-rays diffracted from samples, an Si (111) analyzing crystal was used to improve the angular resolution. We measured theSi (11L) CTR scattering for the gate oxides formed on the Si(100) substrate by the rocking measurement

non-integer Miller index in the vertical direction due to the abrupt termination of the crystal periodicity at the surface. The intensity of CTR scattering contains information on the structure of the surface atoms through the interference with the scattering amplitude from the substrate. In this work, we developed an evaluation technique of the interface atom displacement (IAD), expressed by δc, using CTR scattering, which is sensitive to the interfacial atom structure, particularly for nitrogen distribution. IAD is defined as the vertical displacement of the topmost Si atoms from the expected position for crystalline Si at the interface.

Based on the calculation of kinematical diffraction for the interface model with IAD, we

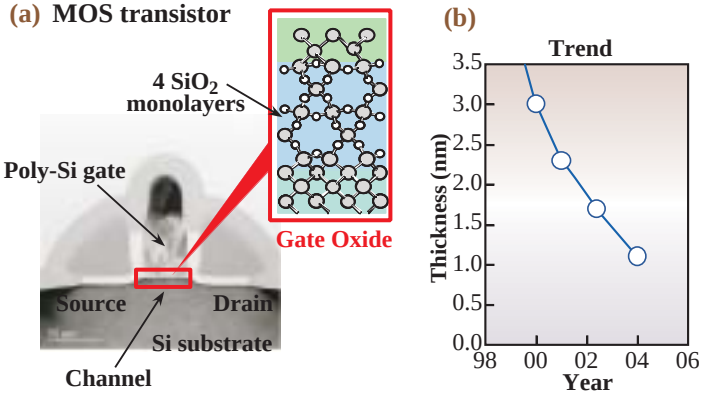

Fig. 1. TEM image of MOS transistor **(a)** and trend of gate oxide thickness **(b)**. The gate oxide has become thinner year by year. In 2004, the thickness of the gate oxide for the 90 nm technology node reached 1.1 nm.

found that δc introduces asymmetry of the CTR peak profile and that by using the relation, we can evaluate δc from the measured CTR profiles. We developed an analytical program, which can be used to evaluate δc based on the optimization of the measured CTR profile using the IAD model.

Since the intensity of CTR scattering is very weak compared to the bulk diffraction peak, high flux X-rays are required for the measurement. We carried out the CTR measurement using the newly installed four-circle diffractometer at the undulator beamline **BL16XU**. In the experiment, the X-ray wavelength of 0.116 nm was selected using a double-crystal monochromator. For the detection of X-rays diffracted from samples, an Si (111) analyzing crystal was used to improve the angular resolution. We measured the Si (11L) CTR scattering for the gate oxides formed on the Si(100) substrate by the rocking measurement based on the ω scan. After subtracting the background scattering from each rocking curve, the integrated intensity was obtained. Figure 2 shows the results of (11L) CTR scattering for samples with 1.1-nm-thick gate oxide processed under two nitridation conditions. The intensity corresponds to the square of the scattering factor in the model calculation.

By applying the analytical program, we successfully reproduced the measured data, as shown by the solid lines in Fig. 2. As a result, δc was As a result, δc was determined with the accuracy of 0.0005 nm. The obtained δc for samples A and B were −0.013 nm and +0.010 nm, respectively, as shown in Fig. 3. A positive value of δc means the displacement of interface Si atoms toward the gate oxide and the negative value means displacement toward the Si substrate. For the SiO_2 sample without nitridation, δc is usually close to zero. After evaluating δc for the various nitridation samples, we found that δc distributed between −0.03 nm and +0.03 nm is strongly correlated with the nitridation procedure and like temperature and time. By evaluating δc from the measured CTR profile, we could readily observe the slight difference in the nitrogen contribution at the interface.

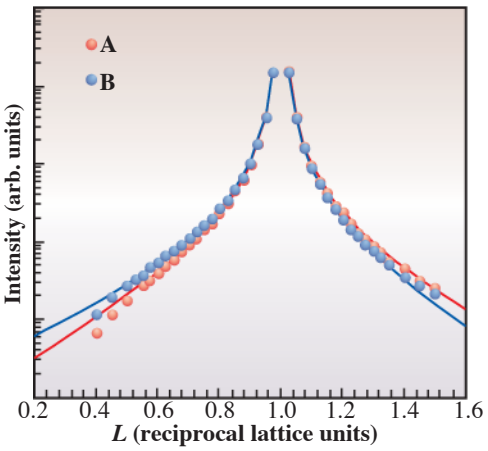

Fig. 2. The experimental results of the Si(11L) CTR scattering intensity for the gate oxides processed under two different nitridation conditions. These two profiles show the different peak asymmetries that are reproduced well by using the IAD model, as shown by the solid lines.

The electric measurements have been performed for the corresponding gate structures and gate leakage current and carrier mobility were found to have a close relation to δc. These results may be due to the fact that δc is related to the nitrogen distribution and the chemical bonding at the interface that sensitively reflects the electric performance.

In summary, atomic displacement at the SiO_2/Si interface has been successfully evaluated by applying the IAD model to the CTR scattering data, and its close relation with the electric properties was observed. This new technique provides a parameter, δc, that sensitively reflects the nitrogen distribution at the gate oxide/Si interface and that can be used to determine the optimum nitridation condition of a gate oxide with superior electric properties.

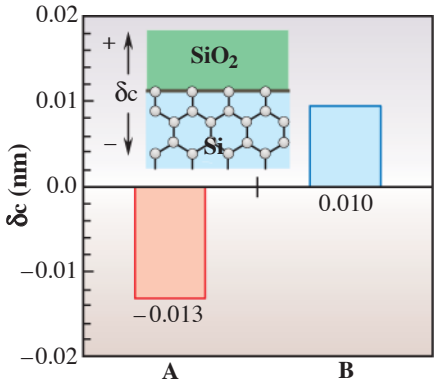

Fig. 3. Displacement of interfacial atom, δc, obtained from the analysis. In sample A, δc has negative value, but in sample B, δc has a positive value, which reflects that the difference in the interface structure corresponds to the different nitridation conditions.

Shuichi Doi and Naoki Awaji

Fujitsu Laboratories Ltd.

E-mail: doi.shuuichi@jp.fujitsu.com

References

[1] I.K. Robinson: Phys. Rev. B **33** (1986) 3830.
[2] I. Takahashi *et al.*: J. Phys. Condens. Matter **5** (1993) 6525.
[3] N. Awaji *et al.*: App. Phys. Lett. **74** (1999) 2669.

Spontaneous Magnetic Moment of Pt in Perpendicular Magnetic Recording Media

The hard disk drive (HDD) that stores a large amount of information for computers and networks is becoming a crucial device for information technology. The essential figure of merit for the HDD is the areal density of the recorded bits on a disk, which contributes to large capacity, small size, and low cost simultaneously. At present, the areal density exceed 100 Gbits per square inch. This density corresponds to a bit area of only 80×80 nm^2. However, the areal density increase is approaching saturation due to the physical limitation of the thermal decay of recorded bits. As element permanent magnets that represent recorded bits become smaller and smaller with the areal density increase, thermal energy overwhelms the anisotropy energy that maintains the direction of recorded magnetization.

Perpendicular magnetic recording [1] is the key technology to overcome this limit. The Co/Pt multilayer film described here is one of the most promising candidate disk material for perpendicular recording, which was originally developed for magneto-optical recording [2]. It has a layered structure consisting of alternative deposited Co and Pt layers whose thicknesses are both on the subnanometer scale. The film exhibits a strong perpendicular magnetic anisotropy caused by interfacial anisotropy between the Co and Pt layers. This high anisotropy is advantageous for high-density recording disks to ensure a good thermal stability of the recorded bits. In this experiment, the study of the magnetic behavior of Pt was carried out. The Co/Pt multilayer exhibits a very high anisotropy. In particular, the magnetism of Pt at the interface of Co was studied.

The addition of Pt to Co based alloy enhances magnetic anisotropy. Therefore, Pt is widely used for disks. On the other hand, Pt addition sometimes increases media noise. Since media noise depends on film microstructure, Pt atoms may modify the magnetic grain structure. The atomic magnetic behavior of Pt is interesting from this viewpoint, as well.

Samples are prepared by sputtering deposition. The film structure is shown in Fig 1. The number of Co/Pt deposition pairs is usually more than ten; however in this experiment, one Pt film and Co film were layered. Co 15 nm in thickness was deposited without any additive elements on the Ti seed layer, followed by the deposition of Pt films of various thicknesses. The Pt thicknesses were 0.2, 0.5, 1 and 2 nm. No passivation layer was deposited on it.

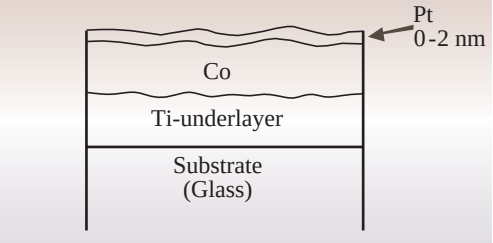

Fig. 1. Schematic of layer structure of prepared samples of Co/Pt layered disk.

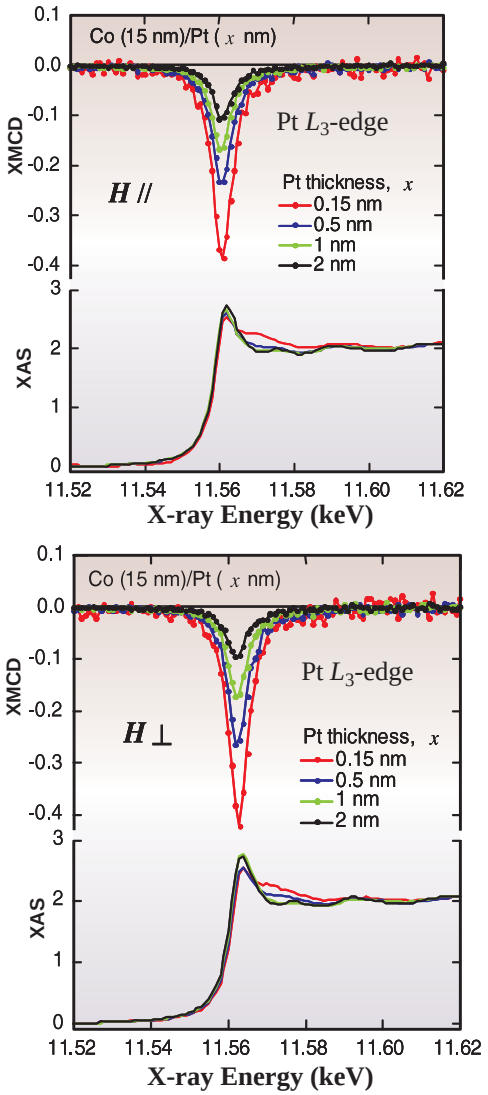

Fig. 2. XMCD spectra at the Pt L_3 edge of Pt in Co/Pt films of different Pt thicknesses, compared with spin-averaged XAS spectra. Applied fields are in-plane (upper) and perpendicular (lower).

XMCD experiments on the Pt $L_{2,3}$ edges were carried out in the fluorescence mode at beamline **BL39XU**. Monochromatic X-rays were incident on a Co/Pt sample perpendicularly to the film plane. A magnetic field was applied in the perpendicular direction to the sample plane so as to measure the perpendicular 'hysteresis loop'. The maximum field was 20 kOe to attain saturation magnetization. The M_S of Co is approximately 1420 emu/cm^3, therefore the field of 20 kOe is greater than the demagnetization field, $4\pi M_S$, that was sufficient to magnetically saturate the sample. Applied in-plane field was also measured to compare the two hysteresis loops, and to observe magnetic anisotropy. The intensities of fluorescent X-rays were detected using a silicon drift chamber, which confirms that total count rates as high as 105 cps and the efficient separation of Pt $L_{\alpha1}$ and $L_{\alpha2}$ lines from the elastic scattering mainly originate from the substrate.

Figure 2 shows the observed XMCD spectra of Co/Pt films of different Pt thicknesses for in-plane (upper) and perpendicular (lower) applied fields. The spin-averaged XAS spectra of the samples are compared in the bottom of each figure. The XMCD and XAS amplitudes were scaled per unit Pt thickness. The two sets of spectra are almost identical, which means no magnetic anisotropy of the magnetism of Pt is present. The Pt sample of 0.2 nm thickness shows the largest XMCD amplitude, which is 20% of that in the case of the XAS edge jump. XMCD amplitude decreases with increasing Pt thickness, indicating that Pt magnetization decreases with the distance from the interface with Co.

With the help of the magneto-optical sum rules, we estimated the magnetic moment of the Pt 5*d* electrons as a function of distance from the Co/Pt interface as shown in Fig. 3. The amount of magnetic moment per hole exhibits an almost exponential decay, in which the maximum number is 0.4 μ_B / hole for a Pt atom in contact with Co atoms at the interface. This spontaneous moment is close to that of Ni. The change in Pt moment m(x) with Pt thickness x was well reproduced by an exponential function, $m(x) = m_0 * \exp(-x/d)$, with a characteristic thickness d = 0.4 nm, which characterizes the effective range of hybridization between Co and Pt. The relatively large magnetic moment of Pt will affect the macroscopic magnetic characteristics such as saturation magnetization, M_S, of the Co/Pt multi-layered film.

From the viewpoint of the nanostructure of CoCrPt alloy films, the moment of Pt can adversely affect the magnetic isolation of CoCr gains. Since the Pt atoms in CoCr are not localized in grains, the polarized Pt atoms at grain boundaries magnetically connect the grains. The XMCD measurement contributes to the nanotechnology of magnetic disks.

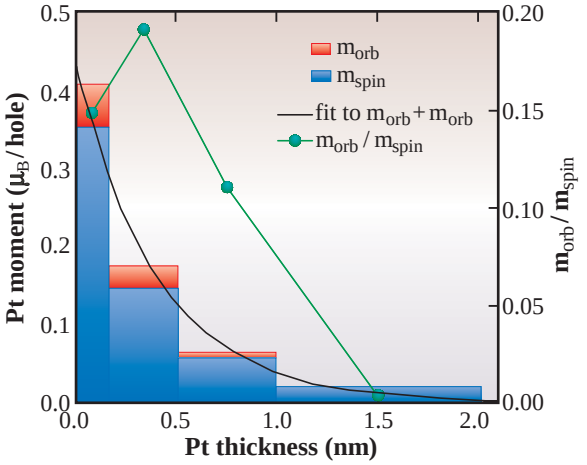

Fig. 3. Spontaneous magnetic moment of Pt atoms as a function of thickness of the Co interface. Morb (top of the bars) and Mspin (bottom of the bars) are orbit and spin moments, respectively. The black exponential decay line is the fit curve to the measurement.

Hiroaki Muraoka[a] and Motohiro Suzuki[b]

(a) Research Institute of Electrical Communication, Tohoku University
(b) SPring-8 / JASRI

E-mail: muraoka@riec.tohoku.ac.jp

References

[1] S. Iwasaki: IEEE Trans. Magn. **20** (1984) 657.
[2] W.B. Zeper *et al.*: IEEE Trans. Magn. **25** (1989) 3764.

In Situ Small-Angle X-ray Scattering Experiment in Melt Spinning of High-Density Polyethylene

The effect of flow on the structure formation in polymeric melt under non-isothermal conditions has been attracting attention in both academic and industrial points of view. Fiber spinning is a process that primarily imposes extensional deformation on polymeric melt at the spinline during rapid cooling. In the industrial point of view, it is very important to elucidate the structure formation in the spinning process because the structure has a large effect on the properties of the obtained fibers. The structure formation in the spinning process is very complex because many phenomena (crystallization, phase separation, glass transition and so forth) occur in the process. An *in situ* experiment on the spinning process will provide fruitful information on the structure formation; however, the intensity of the X-ray beam of a conventional laboratory source is very weak for the experiment because the diameter of the spinning fiber is very thin; in the order of tens of microns. Therefore, synchrotron radiation is useful for a small sample such as a spinning fiber. An *in situ* X-ray scattering experiment on spinning process by synchrotron radiation [1] was carried out at HASYLAB, Hamburg, by Japanese and German researchers for the first time: although, this type of *in situ* experiment has not been carried out in Japan. We attempted an *in situ* small-angle X-ray scattering (SAXS) on the melt-spinning at SPring-8 and this may be the first trial of such an experiment in synchrotron facilities in Japan.

High density polyethylene (HDPE) was used as a sample in this experiment. The X-ray scattering experiments were carried out at beamline **BL40B2**. The custom-made spinning apparatus used in the *in situ* X-ray experiment is shown in Fig. 1. The apparatus has a vertical movement system that adjusts the position of the spinning fiber to the X-ray beam with an accuracy higher than 10 μm. Moreover, the distance from the nozzle to the incident X-ray beam can be changed along the spinline. A melt polymer was extruded from a small hole and drawn with take-up rollers. The energy of the incident X-ray was 8 keV (wavelength λ = 0.155 nm) and the scattered X-ray from the fiber was recorded on an imaging plate system.

Figure 2 shows the series of SAXS patterns obtained at different positions in the spinline. The distance L from the nozzle to the incident X-ray beam is depicted on the left top of each SAXS pattern. As L increased, the scattered intensity parallel to the fiber increased at first (L = 100 mm) and subsequently decreased (L = 300 mm). Moreover, the scattering angle dependence of the scattered intensity parallel to the fiber changed with L. We analyzed the scattered intensity as a function of the scattering vector q using a scattering theory [2] of a paracrystal model for oriented lamellar microdomains and obtained a model for the structure formed in the spinline. Highly oriented lamellar crystals were grown in the direction

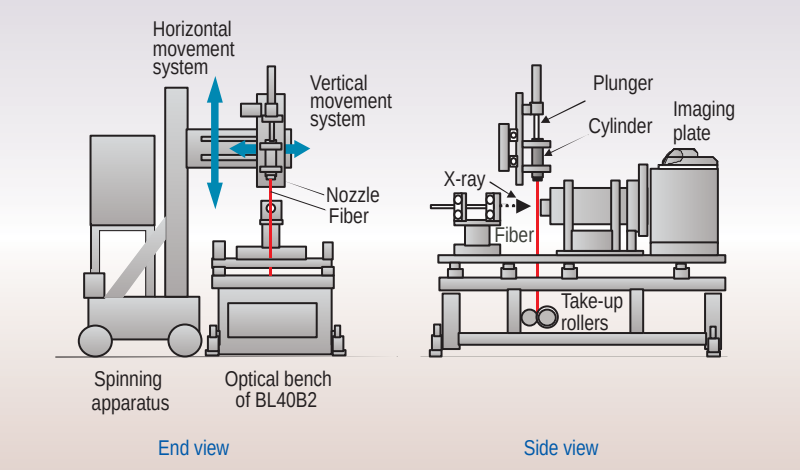

Fig. 1. Schematic representation of the spinning apparatus for *in situ* small-angle X-ray scattering in BL40B2.

for the structure formed in the spinline. Highly oriented lamellar crystals were grown in the direction parallel to the fiber. The average thickness of the lamellar crystals and the average frequency of density fluctuations concerning the lamellar crystals and amorphous regions are depicted in the figure. Moreover we should note the other feature of the scattering pattern indicated by an arrow "S." This is a "streak" pattern indicating the formation of a structure oriented parallel to the fiber. Voids or extended chain crystals can be attributed to the structure giving rise to the streak pattern; however, we cannot fix either of them from the SAXS results. It should be note that the intensity of the streak pattern became weak from L = 100 mm to 300 mm. This suggests that the structure giving rise to the steak pattern was smeared by the lamellar structure. We are going to elucidate the structure formation in the spinline by more detailed analysis of the scattered intensity and by electron microscopy of the fiber obtained in the *in situ* experiment in SPring-8.

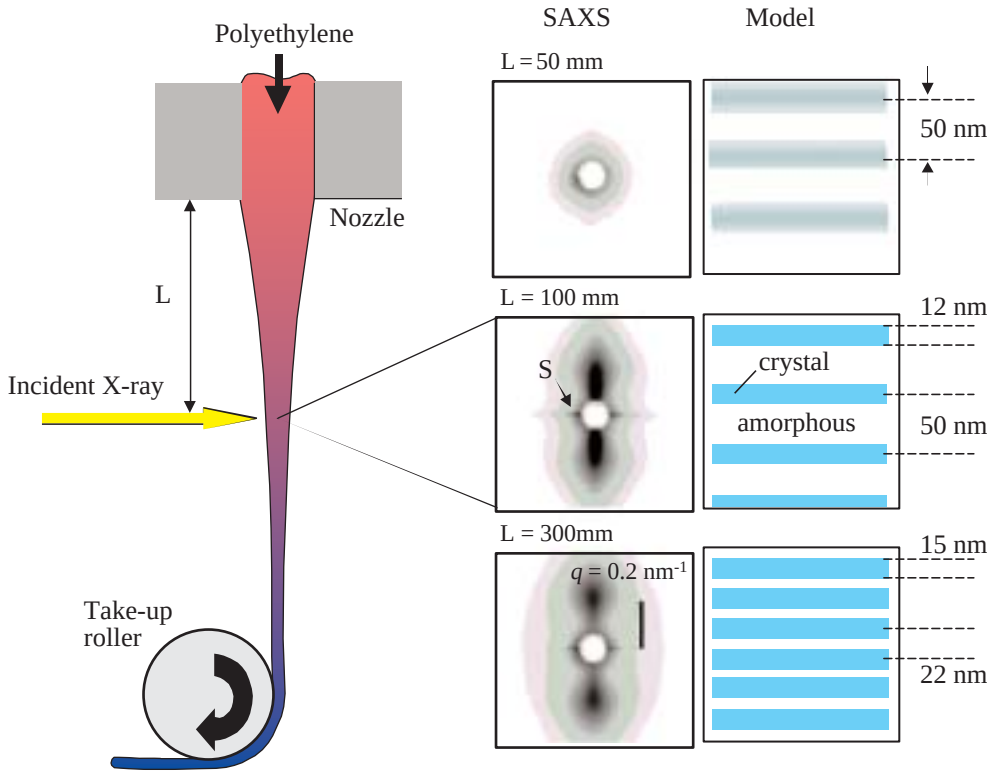

Fig. 2. *In situ* SAXS patterns obtained in the spinline. L is the distance from the nozzle to the incident X-ray beam. SAXS patterns inserted in this figure are taken at L = 50, 100 and 300 mm. A structure model derived from the analysis of the q dependence of scattered intensity parallel to the fiber is depicted on the right side of each SAXS pattern.

Hiroki Murase[a], Masaru Kotera[b] and Katsuhiko Nakamae[b]

(a) TOYOBO Research Center Co., Ltd.
(b) SPring-8 / JASRI

E-mail: hiroki_murase@kt.toyobo.co.jp

References

[1] Y. Hirahata *et al.*: Polymer **23** (1996) 5131.
[2] S. Sakurai *et al.*: J. Appl. Crystal. **24** (1991) 679.

Measurement of Strain Distribution in Thermal Barrier Coating using Hard X-rays

The thermal efficiency of gas turbine engines increases with combustion temperature. Recently, the combustion temperature of gas turbine engines has become much higher than the melting point of their metallic parts, and their thermal efficiency has risen above 50%. A thermal barrier coating (TBC) enables such high-temperature combustion. Commonly, TBCs consist of a top coating and a bond coating as shown in Fig. 1. For the bond coating, NiCoCrAlY powders are plasma-sprayed on the substrate of a Ni-based superalloy. The top coating is made of plasma-sprayed zirconia, this ceramic top coating protects the components of the gas turbine engine from high-temperature damage. The molten zirconia collides with the substrate, flattens and solidifies suddenly, so that the top coating contains many pores and microcracks. The residual stress in the TBC is generated by many factors, such as the mismatch of thermal expansions between the top and bond coatings, thermally grown oxide (TGO) and interface roughness. Many types of residual stress promote the spallation of TBCs, and the spallation of the top coating results in the melt-down of the gas turbine engine. Therefore, the measurement of the spalling stress is very important for the improvement of coating technology.

A distribution of the residual stress in the TBC has been analyzed using computer simulations because there is no method of measuring the internal stress nondestructively. The residual stress can be measured with conventional X-rays. The energy of the X-rays, however, is low and its penetration depth is very shallow, for example the penetration depth of Cr-Kα is 3 μm for zirconia. Only the in-plane stress, σ_1, is measured with low-energy X-rays. A $2\theta - \sin^2\psi$ method is used for measuring the in-plane stress [1]. ψ is the angle between the normal direction to the surface of a specimen and the diffraction plane. The shift in the diffraction angle, 2θ, is proportional to the stress, therefore, the in-plane stress, σ_1, can be calculated from the gradient of the $2\theta - \sin^2\psi$ diagram.

On the other hand, high-energy synchrotron X-rays have a large penetration depth, so that diffractions with high-energy X-rays contain the diffraction from a deep position. Therefore, the residual stress near the interface between the top and the bond coating can be measured with high energy X-rays. In particular, it is noted that the out-of-plane stress, $\sigma_1 - \sigma_3$, can be measured by the $\sin^2\psi$ method with high energy X-rays. Low-energy X-rays are used for the measurement of the in-plane stress, σ_1, and also high-energy X-rays are used for the measurement of the out-of-plane stress, $\sigma_1 - \sigma_3$. From the results measured with low and high-energy X-rays, the spalling stress, σ_3, can be estimated. This method is called the hybrid method.

Figure 2 shows the distribution of the spalling stress using the hybrid method. The spalling stress in the top coating with exposure time 0 h is small from the surface to the interface between the top and bond coatings. The spalling stress with oxidization is small beneath the surface but increases steeply near the

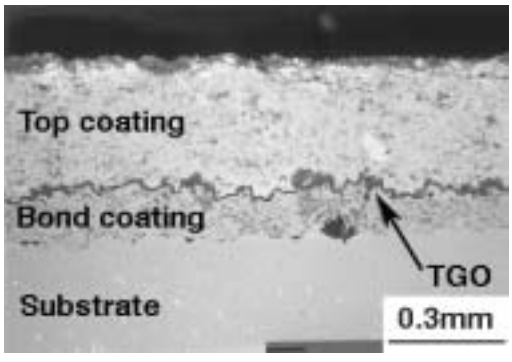

Fig. 1. Cross section of TBC with exposure at 1373 K for 1000 h. TGO is thermally grown oxide and promotes the spallation of the top coating.

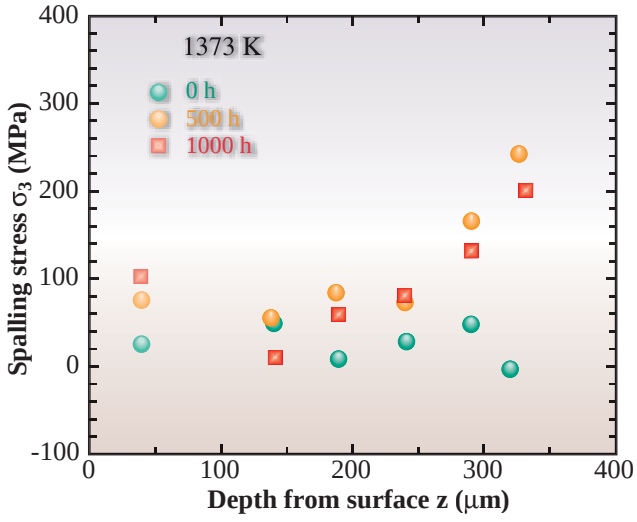

Fig. 2. Distribution of spalling stress evaluated by hybrid method. Specimens were exposed in atmosphere at 1373 K for 0, 500 and 1000 h. Thickness of top coating is approximately 350 μm.

interface. Actually, a spalling crack is initiated near the interface. The distribution of the spalling stress estimated by the hybrid method corresponds to the phenomenon of the spallation of the oxidized TBCs. Comparing the spalling stress oxidized TBC with non-oxidized TBC, the TGO promotes the spallation of the top coating. The convex part of the bond coating was more oxidized as shown in Fig. 1. The roughness of the bond coating creates the adhesion effect of the top coating but promotes the spalling stress and the non-uniform growth of the TGO. It is very important to control the TGO and the interface roughness. The TGO does not grow uniformly and the undulation of the interface between the top and the bond coating complicates the stress state. The measurement of the spalling stress is very important to evaluate the spallation.

The hybrid method is very useful for measuring the spalling stress of the TBC. However, a long experimental time is required because many specimens with surface removal have to be prepared and measured by the $\sin^2\psi$ method. Since the experimental shift in the synchrotron radiation facility is limited, it is necessary to reduce the experimental time. Therefore, a strain scanning method is expected as a method of speeding up the experiment.

Figure 3 illustrates the optics of the strain scanning method. As shown in the figure, a gauge volume is determined by the divergent and receiving slits. The position of the gauge volume is scanned by moving the sample stage. The distribution of the strain is evaluated by the shift in diffraction angle.

In our previous experiment by the strain scanning method, the measured peak angle shifted with the increase in the depth of the gauge volume. This was caused by interfering with the gauge volume with the surface of the TBC. In order to solve this problem, strict collimation is made by attaching an analyzer in front of the counter, and the correct strain can be obtained. LiF (200), Ge (111) and Cu (111) analyzers were examined for the strain scanning method. As a result, the LiF analyzer is the most suitable for the strain scanning method. The Ge analyzer showed a strict collimation but reduced the diffraction intensity. The Cu analyzer did not have a good collimation and the peak shift appeared. The LiF analyzer, however, had a deep penetration depth for high-energy X-ray, so that it was difficult to adjust the LiF analyzer. The strain scanning method will be established by improving the mount of the LiF analyzer. The out-of-plane strain can be measured by a reflection configuration as shown in Fig. 3, and also a transmission configuration is needed for measuring the in-plane strain, therefore, very high brightness is an advantage, i.e., an undulator.

Recently, large-penetration-depth and high-brightness hard synchrotron radiation X-rays have been highlighted and an international workshop on hard synchrotron X-rays for texture and strain analysis was held [2]. It is useful to apply high-energy synchrotron X-rays to strain analysis. To make a standard for measuring the stress with high-energy synchrotron X-rays, a new project was started by VAMAS-TWA20 [3]. Japan has been requested to cooperate in this project as a member.

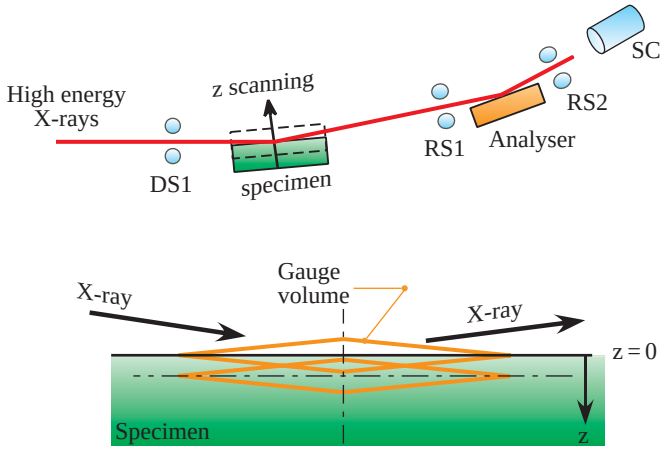

Fig. 3. Optics for strain scanning method and gauge volume. Strain distribution can be measured by scanning the sample stage.

Kenji Suzuki[a] and Keisuke Tanaka[b]

(a) Faculty of Education and Human Sciences, Niigata University
(b) Department of Mechanical Engineering, Nagoya University

E-mail: suzuki@ed.niigata-u.ac.jp

References

[1] V. Hauk: Structural and Residual Stress Analysis by Nondestructive Methods, p. 139 (1997), Elsevier, Amsterdam.
[2] Abstract booklet, International Workshop on Hard Synchrotron X-rays for Texture and Strain Analysis, DESY, Hamburg (2003).
[3] http://www.vamas.org/

INSTRUMENTATION & METHODOLOGY

The development of new science is strongly related to the development of new experimental techniques or new instrumentation. High-quality synchrotron radiation from SPring-8 has opened new scientific fields. In this section, new instrumentation and methodology are introduced.

SPring-8 has succeeded in solving the high heat-load problem to beamline components, optical elements ,and X-rays and vacuum ultraviolet radiation is provided for a various experiments. Now the energy region is extended to the soft X-ray regime. Using a helical undulator and YB_{66} double-crystal monochromator, the 1 – 3 keV region has been covered at BL15XU. On the other hand, the development of detectors suited for higher energy regions continues. A free air ionization chamber is found to be a useful absolute intensity monitor even above 50 keV by employing the linear polarization of synchrotron radiation. An area detector for high energy X-rays, the YAP imager, which has 128×128 pixels has been developed and successfully applied to a temperature-dependent diffraction experiment.

In addition to the above-described new instruments, new experimental methods have developed by fully utilizing the high performance of SPring-8. A new high-throughput experimental method made non-resonant magnetic scattering as a practical tool to study the magnetic structure. High-resolution X-ray microdiffraction using zone plate clarified the special non-uniformity of the strain and the period in a multi-quantum well. X-ray microtomography has been successfully applied to the observation of micropores, which evidenced the unidirectional solidification of the Al-In alloy and the formation of porous Al by electrochemical etching. The last is the development of a Talbot interferometer for phase imaging, which showed air bubbles in a plastic sphere clearly.

Masaharu Nomura

Performance of YB_{66} Double-crystal Monochromator for Dispersing Synchrotron Radiation

The crystal growth technique of YB_{66} was developed originally by Tanaka and Kamimura's group of the National Institute for Materials Science (NIMS) [1]. YB_{66} has a lattice plane (4 0 0) that is large (0.586 nm) and suitable for dispersing soft X-ray [2], which cannot be covered easily by grating monochromators. Synchrotron radiation technology has developed rapidly and has been introduced as a third-generation light source for the past ten years. Although the problem of a high heat load from third-generation light sources has not yet been overcome in the dispersion by a YB_{66} crystal, a great demand for executing an experiment using a high-resolution and high-brilliance soft X-ray light source still remains. In addition, one of the important specifications of beamline **BL15XU**, which has been developed by NIMS, is the capability of obtaining monochromatic light of optional wavelength on a sample between 0.5 keV and 60 keV. YB_{66} is known to have an energy resolution ($\Delta E/E$) of about 5×10^{-4} and is more resistant to synchrotron radiation damages than other crystals (Beryl, Quartz, InSb) [2] applicable in the same energy region. Thus, the beamline monochromator with YB_{66} is the most suitable for BL15XU [3] at SPring-8, which is a third-generation light source in the 1 - 2 keV range and the first of its kind in the world.

The YB_{66} crystal (10 mm^H × 20 mm^V × 1 mm^T) used in this study was a commercial product (Crystal Systems Inc.). The crystal surface which is parallel to a diffracting plane was polished by a lapping machine and by hand. An indirect cooling system using a Ni-coated holder made of Cu was used as shown in Figs. 1(a) and 1(b) [4]. The YB_{66} crystal was set on the holder using liquid InGa after pretreating of the contact surface, ultrasonic washing for 15 min with acetone and preheating for 2 hours at 110°C.

The soft X-ray used in this study was generated by a helical undulator. This type of undulator has the characteristics that higher harmonics distribute mostly outside an axis of X-ray, and thus, the heat load of the crystal due to higher order lights can be reduced to some extent. In this study, the characteristics of synchrotron radiation dispersion from the helical undulator operating at an electron energy of 8 GeV and an injection current of 100 mA were studied. The schematic drawing of the experimental configuration is shown in Fig. 2.

For the estimation of the source condition which dominated the heat load at the crystal surface, thermal analysis by the finite element method was performed. Rocking curves were measured by rotating the $\Delta\theta$ axis of the first crystal, and the photon flux passing through this monochromator was measured by an Si PIN photodiode.

The most suitable energy region for the YB_{66} crystal was the 1 - 2 keV range. It is also possible, but not easy, to use this crystal up to 3 keV or higher, because there are absorption edges of Y (L_1-edge 2373 eV, L_2-edge 2156 eV and L_3-edge 2080 eV). From the results of measurement, the FWHM of the 4 0 0 reflection is plotted as a function of photon energy ranging from 0.15 eV at 1.1 keV to 0.42 eV at 2.1 keV as shown in Fig. 3. The FWHM of the YB_{66} crystal obtained is superior to that obtained at SSRL [5]. The footprint on the crystal at SSRL, 1.5 mm^H ×15 mm^V [5], was significantly larger than that obtained by us, 0.07 mm^H ×1 mm^V. The effective divergence of our beam originating from the helical undulator being smaller than that of SSRL is the main reason that our FWHM value was superior to that obtained at SSRL.

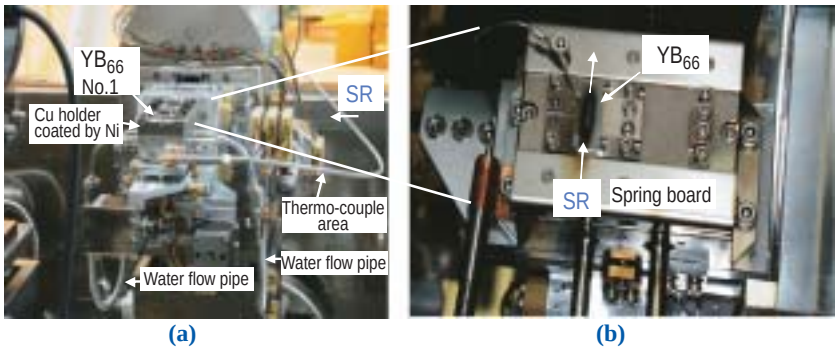

(a) (b)

Fig. 1. **(a)** Installation of the YB_{66} crystal on the holder of the monochromator in BL15XU. First, YB_{66} crystal is set on the Ni - coated Cu holder. InGa is placed in the interface between the YB_{66} and Ni-coated Cu holder. A thermo-couple is attached to the front surface of YB_{66}. Ni-coated Cu holder is cooled by water. **(b)** Top view of the YB_{66} crystal. The size of YB_{66} crystal is 10 mm^H × 20 mm^V × 1 mm^T. The front surface near the edge was pressed down by two points using the spring board of the holder.

The photon flux passing through the monochromator of BL15XU measured at the sample position at a stored current of 100 mA by a Si PIN photodiode under vacuum is shown in Fig. 4. The photon flux ranged from 6×10^8 photons/sec/100 mA at 1.1 keV to 5×10^9 photons/sec/100mA at 2 keV, almost the same as that obtained at SSRL [5]. Even we attenuated the thermal load from the undulator, a photon flux as high as 10^9 photons/sec/100mA measured at the sample position was obtained.

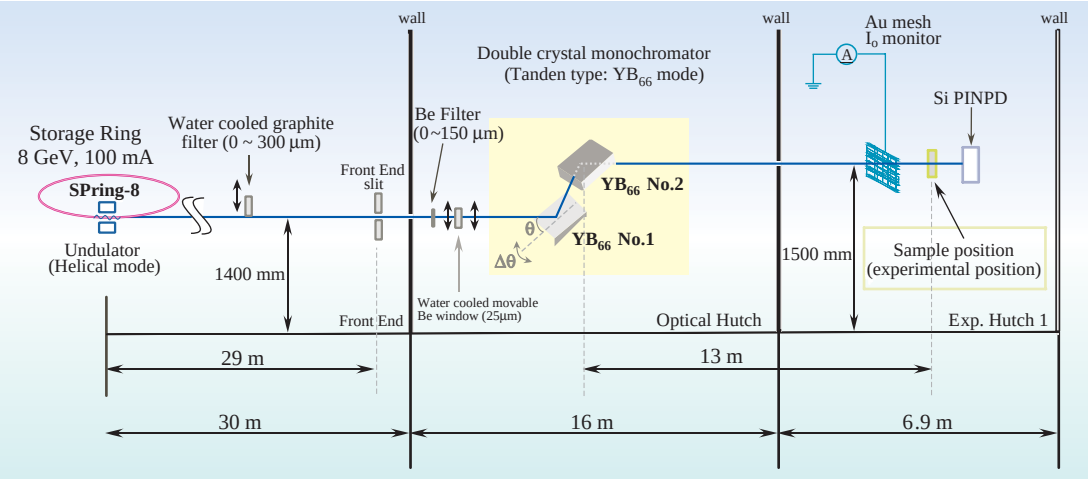

Fig. 2. Outline of the experimental configuration to the first experimental hutch of beamline BL15XU at SPring-8. A tandem type monochromator consists of two monochromators which can select the analyzed crystal from Si, YB_{66}, and multilayer. In the 1 - 2 keV range, we adopted the YB_{66} crystal for dispersing synchrotron radiation.

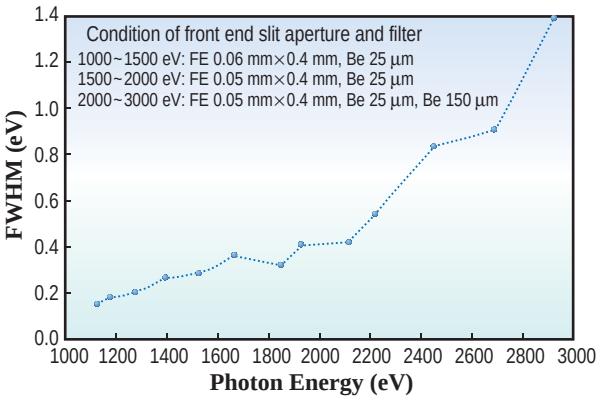

Fig. 3. Energy resolution obtained from the FWHM of the rocking curve of the YB_{66} 4 0 0 reflection as a function of photon energy ranging from 0.15 eV at 1.1 keV to 0.42 eV at 2.1 keV.

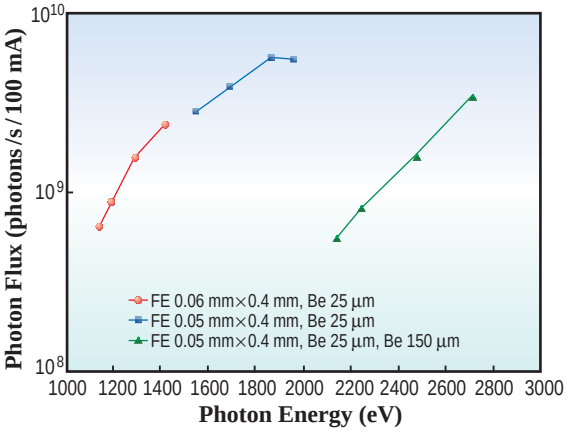

Fig. 4. Photon flux passing through the monochromator at the ring current of 100 mA. It was measured at an experimental position by a Si PIN photodetector as a function of photon energy for the front end slit size and filter conditions as parameters.

Masaru Kitamura[a] and Sei Fukushima[b]

(a) Toshiba Co., Manufacturing Engineering Center
(b) Harima Office, National Institute for Materials Science

E-mail: himajin@spring8.or.jp

References

[1] A.G. Slack *et al.*: Phys. Rev. B **4** (1971) 1714.
[2] T. Tanaka *et al.*: J. Cryst. Growth **73** (1985) 31.
[3] M. Kitamura, H. Yoshikawa, T. Mochizuki, A.M. Vlaicu, A. Nisawa, N. Yagi, M. Okui, M. Kimura, T. Tanaka and S. Fukushima: Nucl. Instrum. Meth. Phys. Res. A **497** (2003) 550.
[4] M. Kitamura *et al.*: SPring-8 User Experimental Report No. 7 (2001A), JASRI, C01A15XU-2000N, p. 236.
[5] J. Wong *et al.*: J. Synchrotron Rad. **6** (1999) 1086.

A Portable Absolute-Intensity Monitor for High-Energy Synchrotron Radiation

An attractive advantage of SPring-8 is that a monoenergetic photon beam up to 100 keV energy region is available at bending-magnet beamlines. High-energy X-rays with an excellent energy resolution are not available by conventional X-ray machine and non-large-scale synchrotron radiation facilities. For applications of a unique photon beam, an absolute intensity monitor becomes an important tool; however, this type of monitor had not been realized.

In SPring-8, several parallel-plate free-air ionization chambers of different sizes are used as monitors, which has the advantage of robustness, easy handling and suffering no radiation damage even under long irradiation. The mechanism is simple; electrons emitted at photon interaction ionize the air and parallel electrodes collect the ions and electrons produced. The photon intensity can be calculated from the output current, which corresponds to the dose in the sensitive volume. For the measurement of the absolute intensity, electrons have to lose all the energy in the collecting volume because in the condition of no electron loss the conversion formula from dose to intensity is available. To attain the condition, the electrode separation has to be larger than the twofold of the maximum distance of electron traveling in principle. That is, the separation has to increase with the energy and so the necessary value reaches 27-cm at 100 keV. On the other hand, if the wide plate separation were used for high-intensity photons in SPring-8, a tremendously high voltage would be required to suppress the recombination.

Here, it should be noted that electrons are emitted by two kinds of interactions: photoelectric and Compton effect. While the energy of photoelectrons is almost the same as that of photons, the Compton recoil electrons have much lower energies; the maximum energies for 50 and 100 keV photons are only 8.2 and 28 keV, respectively. Conveniently enough, with increasing photon energy, the proportion of the ionization by photoelectrons decreases rapidly.

Furthermore, synchrotron radiation from bending magnets is linearly polarized on the horizontal plane; thus, photoelectrons are preferentially emitted on the horizontal plane as shown in Fig. 1. Therefore, most photoelectrons do not hit electrodes if they are placed horizontally. On the other hand, Compton electrons are emitted forward on the vertical plane; however, the energies are low enough. Thus, in high-energy region, the reduced photoelectric effect and linear polarization can be expected to decrease electron loss remarkably even not using such a wide plate separation. The narrow separation will increase the electric field, which will make the chamber applicable to high-intensity synchrotron radiation [1].

For detailed physical simulation, a Monte-Carlo electron/photon transport code, EGS4 [2], was used.

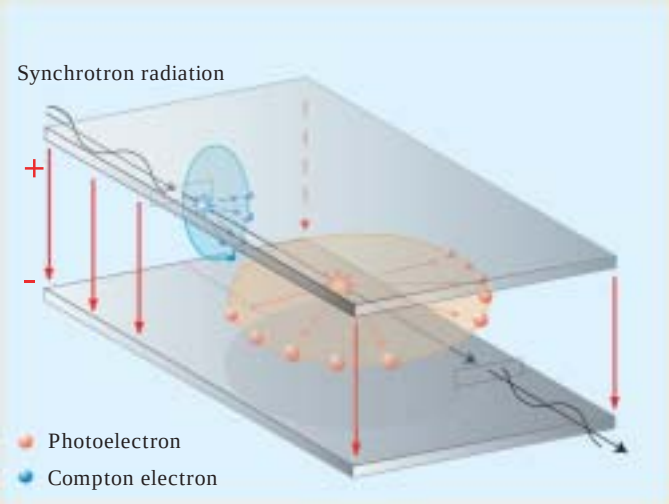

Fig. 1 Schematic of the electron motion produced in air of the monitor. Photoelectrons have almost the same energy as incident photons and some are emitted at a large angle with respect to the beam axis. Linear polarization, however, increase the magnitude of emission on the horizontal plane. By contrast, Compton electrons have a much lower energy when emitted on the vertical plane.

In the Monte-Carlo method, a random sampling method is used to determine the interaction probability, the particle direction, the energy after the interaction, and so forth. Linear polarization was considered in the calculations. For the electron loss, absorbed energies in the air at the plate separations of 8.5 cm and infinity were calculated, and the ratio of these two values was used as the collection efficiency: The difference between the ratio and unity equals the proportion of electron loss. Figure 2 shows the calculated result. The electron loss became within 3.3% even at 80 - 190 keV and beam size dependence was not observed between the 1- and 10-mm square beams. Without linear polarization, the electron loss increased to 4 - 5% between 70 and 150 keV. The reason for the decrease in electron loss at 150 keV is the decreased occurrence of the photoelectric effect.

For experimental confirmation, the photon intensity measured with the ionization chamber with an 8.5 cm plate separation was compared with that measured with a Si-PIN photodiode at **BL20B2** and **BL38B1** beamlines. The photodiode has been calibrated with a total absorption calorimeter [3]. The result is also shown in Fig. 2 as the ratio of both values. The ratio equaled unity within 3% and the dependence of the collection efficiency on the photon energy agreed with the EGS4 result. That is, the deviation from unity at 80 - 150 keV is due to the electron loss from electrodes.

In conclusion, a portable photon intensity monitor with an uncertainty of 3% for high-energy synchrotron radiation has been developed. While the interelectrode distance of 8.5 cm is much shorter than the twofold electron range at 150 keV, that is, 53 cm, sufficiently low electron loss was confirmed. The ionization chamber can be carried easily from one beamline to another to monitor the photon intensity.

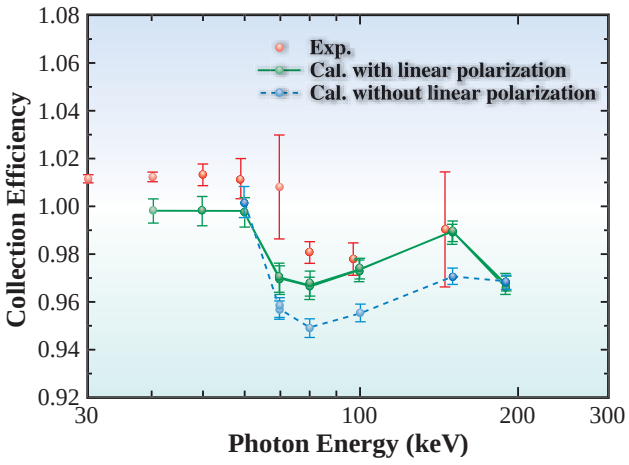

Fig. 2 Collection efficiency measured and calculated by considering linear polarization. Both values almost agreed with each other: the decrease between 80 and 150 keV is due to the electron loss. Without linear polarization, collection efficiency became clearly smaller between 70 and 150 keV.

Nobuteru Nariyama

SPring-8 / JASRI

E-mail: nariyama@spring8.or.jp

References

[1] N. Nariyama, N. Kishi and S. Ohnishi: Nucl. Instrum. Meth. A **524** (2004) 324.
[2] W.R. Nelson *et al.*: SLAC-265 (1985).
[3] H. Nakashima *et al.*: Nucl. Instrum. Meth. A **310** (1991) 696.

YAP Imager, an Area Detector for High-Energy X-ray Photons

High-energy X-ray beams are outstanding scientific resources of third-generation synchrotron radiation facilities. They provide a powerful means of investigating the internal structures of thick or high-Z samples, local atomic structures of non-crystalline materials, and substances containing heavy elements. However, the detection of high-energy X-ray photons is not straightforward because they penetrate through and scatter in all detection media. High-density inorganic crystals with constituents of high-Z values are, therefore, widely used. With a single body CsI(Tl) scintillator attached to a diffractometer, the structure factor of a given sample can be measured by a slit scan method, which however, is highly time-consuming. To be more efficient, an advanced area detector is needed, which should be fast enough to resolve the individual high-energy X-ray photons arriving for background rejection.

In this respect, cerium-doped yttrium aluminum perovskite ($YAlO_3$:Ce, often abbreviated YAP(Ce)) is a promising scintillator, because its decay time (~ 28 nsec) is ten times faster than that of a NaI(Tl) scintillator, however, its light yield is 40% that of a NaI(Tl) scintillator. Its density (5.35 g/cm^3) is as high as that of germanium, and the wavelength of maximum emission (360 nm) is sufficiently blue to illuminate wavelength-shifting fibers as explained below [1].

By assembling 16384 elements of YAP(Ce) crystals, a 2D matrix of [128 × 128] has been fabricated at the SPring-8 facility as a detection media of an advanced high-energy X-ray area detector, called "YAP imager," (Fig. 1) [2,3]. Each crystal element is 1 mm×1 mm×6 mm. There are 128 wavelength-shifting fibers attached to the 128 columns (x-coordinate) on the top surface of the 2D array, and another 128 wavelength-shifting fibers attached to the 128 rows (y-coordinate) on the bottom surface. The 128 fibers of both coordinates are bundled into 8 groups, and are guided to their own photomultipliers. The photomultiplier has sixteen segmented anodes that position-sensitize its photocathode into 4 × 4 regions. The sixteen fibers in each group are attached to their own assigned regions.

When high-energy X-ray photons are absorbed in a YAP(Ce) crystal element, scintillation photons are induced (see Fig. 2). These scintillation photons emitted at an acceptance angle enter the corresponding wavelength-shifting fibers on both coordinates. By entering the fibers, the scintillation photons are absorbed and reemitted into the wavelength region from 390 nm to 450 nm. The red-shifted scintillation photons in each coordinate will travel through the fiber, and reach one of the segmented anodes. The arrival location of the incident X-ray photon on the 2D YAP crystal matrix can be uniquely identified by detecting the signals induced on segmented anodes on both coordinates. The scintillation pattern induced on the 2D crystal matrix is thus projected both coordinates. Due to the finite acceptance angle and wavelength-shift efficiency, only a few scintillation photons will reach the photomultipliers, so that the YAP imager does not give energy information of the

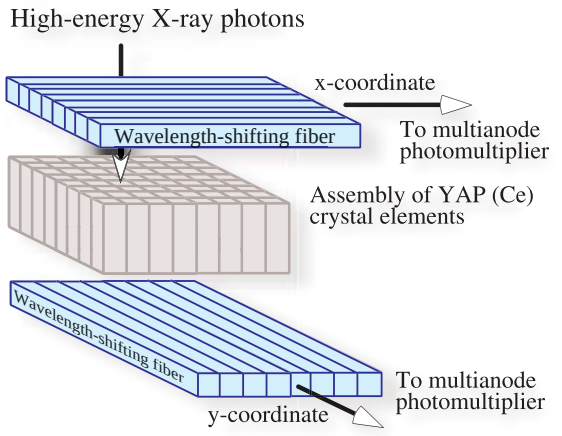

Fig. 1. Diagram explaining 2D YAP crystal assembly and wavelength-shifting fibers attached.

Fig. 2. Photograph of YAP Imager fabricated at the SPring-8 facility.

incoming X-ray photons. At the cost of losing the energy information, however, the YAP imager immediately digitizes the arrival locations of incoming X-ray photons on its 2D crystal matrix with a spatial resolution of 1mm × 1mm. This early digitization allows the YAP imager to be operated at a high counting rate with the dedicated readout system described below.

The X-ray attenuation length of a YAP crystal becomes equal to the thickness of the present 2D YAP crystal matrix at approximately 120 keV, where the matrix absorbs 63% of incoming X-ray photons. Although absorption efficiency increases as the X-ray photon energy decreases, the number of scintillation photons generated in the crystal elements decreases at the same time, making the overall detection efficiency from 60 keV up to 120 keV to be nearly constant at approximately 60%. The position dependence of overall detection efficiency was observed over the detection area, presumably due to the structural irregularities remaining in the crystal matrix, the wavelength-shifting fibers, and the multianode photomultipliers. Flood field images obtained by detecting tungsten X-ray fluorescence are analyzed together with experimental data to eliminate this non-uniformity.

In the present data acquisition system, the 128 segmented anode signals on both coordinates are degenerated into 16 unified signals by combining all the *n*-th segmented anode signals into an *n*-th single signal. Also eight dynode signals of the photomultipliers for both coordinates are sent to the data acquisition system. The dynode signals identify which photomultiplier is fired, and the degenerated anode signals which segmented anode is fired, thus providing sufficient information to determine the arrival location of X-ray photons. In this wiring scheme, the total number of signals to be processed is drastically reduced to forty eight, which is less than 0.3% of the total number of crystal elements assembled. To efficiently encode degenerated anode signals and dynode signals into position information, a high-speed logic processing module, called the "position encoder," has been developed as the central module in the data acquisition system for the YAP imager [4].

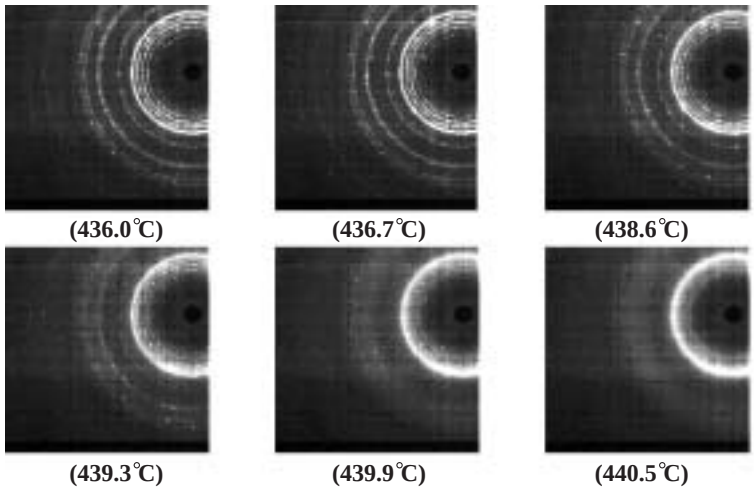

Fig. 3. A series of Zn diffraction patterns visualized with the YAP imager while Zn was undergoing the phase transition at approximately 438.6℃.

One of the important applications of the YAP imager is the *in situ* observation of two-dimensional diffraction patterns formed by a sample undergoing phase transition. A Zn powder sample in a glassy carbon cell was placed in an electric furnace, and was positioned on the diffractometer of the high-energy X-ray diffraction beamline **BL04B1**. By using the 113.4 keV monochromatic X-ray beam, a series of Zn diffraction patterns were observed while Zn was changing its phase from crystal to liquid or from liquid to crystal at approximately 438.6°C (Fig. 3). Because of the excellent detection efficiency of the YAP imager system, only 60 sec of the exposure time was sufficient for the present case. The YAP imager is now ready for performing various types of time-resolved imaging at a high-energy X-ray region beyond 100 keV.

Katsuya Hirota, Hidenori Toyokawa and Masayo Suzuki

SPring-8 / JASRI

E-mail: toyokawa@spring8.or.jp

References

[1] S. Baccaro *et al.*: Nucl. Instrum. Meth. A **361** (1995) 209.
[2] A. Gorin *et al.*: Nucl. Instrum. Meth. A **510** (2003) 76.
[3] K. Hirota, H. Toyokawa, M. Suzuki, T. Kudo, M. Nomachi, Y. Sugaya, M. Yosoi, A. Gorin, I. Manuilov, A. Riazantsev, and K. Kuroda: Nucl. Instrum. Meth. A **510** (2003) 83.
[4] K. Hirota *et al.*: Nucl. Instrum. Meth. A **513** (2003) 187.

A New Method of Non-Resonant X-ray Magnetic Scattering

Non-resonant X-ray magnetic scattering (NRXMS) is a very promising technique in studying the magnetic structure of small samples, such as microcrystals and/or thin films [1]. Since X-rays are an electromagnetic wave, they are sensitive to magnetic as well as to charge distributions in condensed matter. In addition, orbital angular momentum ***L*** and spin angular momentum ***S*** scatter X-rays differently, which provides a way of separating the ***L*** and ***S*** contributions to magnetization experimentally. Brilliant X-rays from a third-generation synchrotron radiation source make up quite a small cross section generated by NRXMS.

The X-ray susceptibility of matter, including magnetic effects, needs to be treated as a tensor [2]. Indeed, magnetic scattering can be discriminated from charge scattering by the polarization analysis of scattering processes. The polarization of X-rays is analyzed using a suitable analyzer crystal, which gives rise to scattering at 90°. A polarization analyzer eliminates polarization parallel to its own scattering plane; at the same time, the remaining polarization is considerably suppressed because the scattering factor and the Debye-Waller factor take a small value with the scattering at 90°. Then, the scattered intensity from a sample will be considerably reduced by the diffraction process on an analyzer crystal. In order to overcome the intensity loss by the analyzer crystal, we have developed a new polarization analysis technique without using an analyzer crystal [3].

Figure 1(a) shows a schematic view of the experimental setup with a conventional polarization analyzer. In this case, the linearly polarized synchrotron radiation and vertical scattering plane are fixed. The polarization of the scattered X-rays from a sample is analyzed by rotating an analyzer crystal around the axis which is parallel to the scattered X-rays. On the other hand, in our new technique a variable scattering plane is employed instead of an analyzer crystal, where a sample crystal also plays the role of an analyzer crystal and the linearly polarized synchrotron radiation is kept fixed. A schematic of the inclined scattering plane geometry is seen in Fig. 1(b). In this figure, ϑ represents the inclination angle of the scattering plane from the vertical plane.

The polarizations perpendicular and parallel to the scattering plane are defined as the σ and π polarizations, respectively. The amplitude of linearly polarized synchrotron radiation is parameterized as $\boldsymbol{E}(\vartheta) = E(\hat{\boldsymbol{e}}_\sigma \cos\vartheta + \hat{\boldsymbol{e}}_\pi \sin\vartheta)$, where $\hat{\boldsymbol{e}}_\sigma$ and $\hat{\boldsymbol{e}}_\pi$ are the polarization vectors. One can consider the new technique to be the manipulation of an incident polarization. The inclination angle dependence of the charge scattering intensity is given by $\boldsymbol{I}_c(\vartheta) \propto \cos 2\vartheta + [(1+\cos 2\theta)/(1-\cos 2\theta)]$. Similarly, that of the magnetic scattering intensity is written as $\boldsymbol{I}_m(\vartheta) \propto \cos(2\vartheta + \alpha) + B$ where B is the baseline and α the phase shift arising from the off-diagonal element of the X-ray susceptibility tensor. Figure 2 shows the inclination angle dependence of the charge and magnetic scattering intensities. It is apparent that the two scattering processes exhibit respective ϑ-dependences. Therefore, the magnetic scattering can be discriminated from the charge scattering without using an analyzer crystal.

In order to demonstrate the validity of the new technique, we have conducted NRXMS experiments

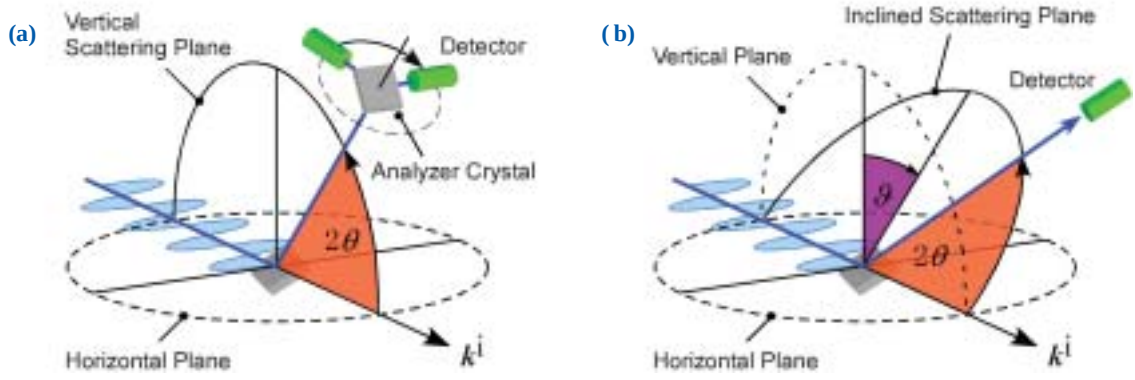

Fig. 1. **(a)** Schematic view of the experimental setup with the conventional polarization analyzer. $\boldsymbol{k}^i$ is the incident wavevector and 2θ is the scattering angle. **(b)** A schematic view of the inclined scattering plane geometry. ϑ is the inclination angle of the scattering plane from the vertical plane.

on the rare earth metal dysprosium, which has a helical magnetic structure in the temperature range between 89 K and 179 K. The single-crystal sample was disk-shaped, 5 mm in diameter and 1 mm thick and had its *c*-axis of a hexagonal lattice normal to the surface of the disk. The experiments were carried out at beamline **BL46XU** using a six-circle diffractometer. The incident photon energy was 20 keV and a NaI(Tl) scintillation detector was used. The sample was mounted on the cold head of a closed-cycle helium refrigerator.

As the sample was cooled below the Néel temperature, magnetic reflections were observed as satellites of the fundamental reflections along the c^* direction. Figure 3 shows the inclination angle dependence of the intensity of the $00\bar{8}$ satellite reflection normalized by the 008 fundamental reflection. The normalization by the close Bragg reflection was necessary because it was almost impossible to keep an identical sample volume illuminated by the incident X-ray beam, particularly through a blind shroud. Measurements were performed with a sample temperature of 120 K. The inclination angle dependence shown in the figure cannot be explained by the charge scattering that has an intensity maxima with ϑ – 0°. The solid curve in the figure, which represents the intensity variation expected for the simple basal plane spiral with L/S = 2, coincides with the experimental result very well.

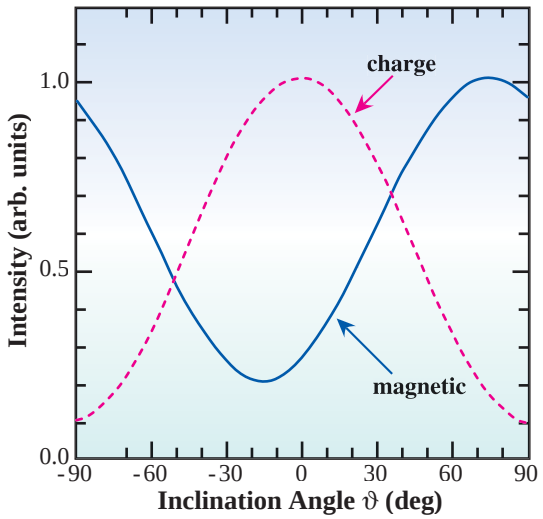

Fig. 2. Inclination angle dependence of scattering intensities. The charge scattering will show a similar dependence to the dashed curve. The magnetic scattering is followed by the phase shift shown as a solid curve.

Consequently, it was confirmed, by the new technique, that the $00\bar{8}$ satellite reflection is indeed the magnetic reflection.

In conclusion, we have developed a new polarization analysis technique without using an analyzer crystal. Thereby, the diffraction data of magnetic scattering can be collected in a short time. Our technique fully conserves the capability to separate the *S* and *L* contributions to magnetization and is applicable not only to NRXMS but also to resonant X-ray scattering.

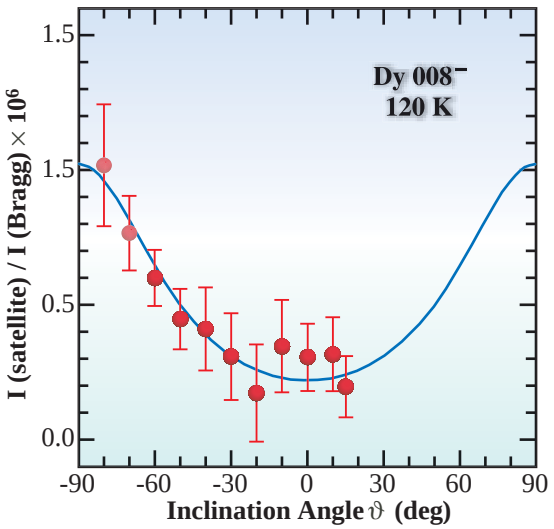

Fig. 3. Inclination angle dependence of the intensity of the $00\bar{8}$ satellite reflection normalized by the 008 fundamental reflection at T = 120 K. The solid curve represents the result of fitting with $L(K)/S(K)$ = 2.

H. Ohsumi

SPring-8 / JASRI

E-mail: ohsumi@spring8.or.jp

References

[1] See for example: Synchrotron Rad. News **14**, No. 5 (2001).
[2] M. Blume and Doon Gibbs: Phys. Rev. B **37** (1988) 1779.
[3] H. Ohsumi, M. Mizumaki, S. Kimura, M. Takata and H. Suematsu: Physica B **345** (2004) 258.

High-resolution X-ray Microdiffraction System for Characterizing Selectively Grown Layers Using a Zone Plate Combined with a Narrow Slit

A microdiffraction system using a zone plate (ZP) is suitable for characterizing selectively grown semiconductor epitaxial layers and multi-quantum-well (MQW) structures [1,2]. This is because the hard X-ray microbeam produced by a ZP has both a sub-micrometer beam size and a relatively low angular divergence of the sub-mrad order. Using such a system, we were able to measure the lattice strain distribution in InGaAsP metal-organic vapor-phase epitaxy (MOVPE) layers selectively grown on 3- and 4-μm-wide InP stripe regions with a strain sensitivity of about 1×10^{-4} [2]. Although this strain sensitivity was fairly good, further improvement was desired to enable more precise strain measurements.

We have therefore developed a new high-resolution microdiffraction system [3], which enabled high-resolution X-ray microdiffraction experiments. The system (Fig. 1) was set up at beamline **BL24XU** using a newly developed apparatus for hard X-ray microimaging and microdiffraction [4]. The monochromatized beam (15 keV) was focused using a phase ZP, which was fabricated by NTT Advanced Technology. The diameter, outermost zone width, tantalum absorber thickness, and focal length of the ZP were, respectively, 180 μm, 50 nm, 800 nm, and 108.9 mm at a photon energy of 15 keV. A platinum 20-μm-diameter pinhole was used as an order-sorting aperture (OSA). To suppress the beam divergence, a 5-μm-wide slit was placed in front of the ZP. Since only one part of the ZP was used, the beam divergence became smaller as shown in Fig. 1. The center of the slit was off-placed from the ZP center so that the OSA would eliminate unfocused and going straight beams. The focused beam that passed through the OSA enabled us to perform high-resolution X-ray microdiffraction experiments using a precise $\theta - 2\theta$ goniometer with sub-100-nm-resolved *XYZ* sample-positioning stages.

We measured the focused beam size using the knife-edge scan method. The result was 0.32 μm horizontally and 1.3 μm vertically at the full width at half maximum. The measured photon flux at the sample position was about 1×10^7 photons/s at 100 mA. The horizontal angular divergence of the focused beam, estimated by measuring a Si 400 rocking curve, was about 70 μrad.

To confirm the capabilities of this system, we measured the spatial non-uniformity of the strain and the period in as-grown InGaAsP multi-quantum-well (MQW) structures selectively grown by MOVPE (see the inset of Fig. 2). Three rocking curves were taken at the center position and positions ±0.5 μm from the center position of the 1.8-μm-wide stripe region.

The measured rocking curves are shown in Fig. 2. The log of the diffraction intensity was plotted *versus* $\Delta q/q_{InP} = \Delta\theta \cot\theta_B$ in percentages (×100), where $\Delta\theta = \theta - \theta_B$ is the goniometer angle relative to the InP 400 Bragg peak angle. Also, $q_{InP} = 2\pi/d_{InP}$ is the momentum transfer, where d_{InP} is the lattice spacing of the InP 400 diffraction. In all rocking curves, the 0th- and ±1st-order satellite peaks of the MQW superlattice were clearly observed in addition to a

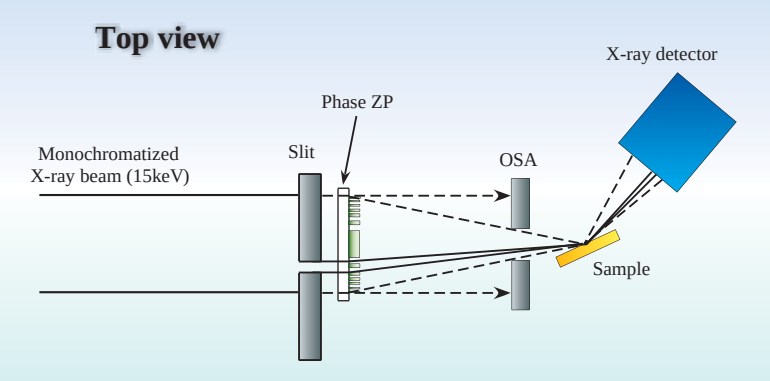

Fig.1. Schematic figure of the experimental arrangement. The monochromatized beam was focused by using a phase zone plate (ZP).

strong InP 400 peak at $\Delta q/q_{InP} = 0$. Since $\Delta q/q_{InP} = -\Delta d/d_{InP}$ from the Braggs' law, the strain perpendicular to the surface was directly determined from the 0th-order peak position. Also, the MQW period is proportional to the inverse of the separation between adjacent satellite peaks. We found that the spatial non-uniformity of the strain and the period in the MQW structure, i.e., the magnitude of the strain near the stripe edges, was greater than that at the stripe center, and the period near the stripe edges was longer than that at the stripe center. This indicates that the surface migration from the stripe edge to the stripe center is insufficient under these growth conditions [5].

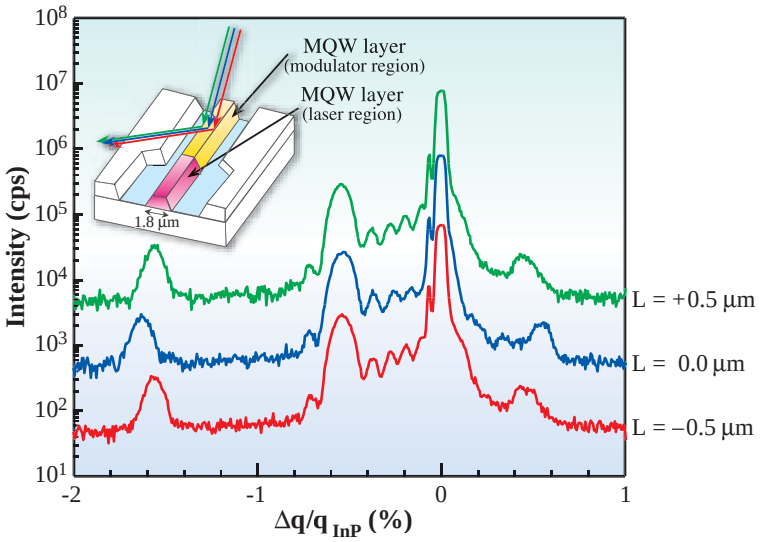

Fig. 2. A series of rocking curves taken at 0.5 μm intervals across the stripe region. The log of the diffraction intensity was plotted against $\Delta q/q_{InP}$. Note that the curves are vertically displaced for clarity.

Shigeru Kimura

SPring-8 / JASRI

E-mail: kimuras@spring8.or.jp

References

[1] Z. Cai *et al.*: Appl. Phys. Letters **75** (1999) 100.
[2] S. Kimura *et al.*: J. Jpn. J. Appl. Phys. **41** (2002) L1013.
[3] S. Kimura, Y. Kagoshima, T. Koyama, I. Wada, T. Niimi, Y. Tsusaka, J. Matsui and K. Izumi: Proc. of the SRI 2003, p.1275.
[4] Y. Kagoshima *et al.*: Proc. of the SRI 2003, p. 1263.
[5] Y. Sakata *et al.*: J. Cryst. Growth **208** (2000) 130.

Observation of Micropores by X-ray Computerized Microtomography: Fabrication of Porous Al with Deep Pores by Al-In Monotectic Solidification and Electrochemical Etching

Porous materials have potential for various practical applications because of their characteristic features. These include large surface area with respect to their volume, permeation of fluids, ability to hold fluids in their pores, and high strength to weight ratio. We have proposed a novel process for fabricating porous media in which deep pores are regularly aligned [1]. The process consists of two parts. The first part is the solidification process under a magnetic field to produce an aligned structure in which the minor phase with a rod shape is regularly aligned in the matrix phase. The second part is the electrochemical dissolution of the minor phase. A three-dimensional (3D) observation is strongly required to evaluate the aligned structure and the electrochemical dissolution process. X-ray computerized tomography with a high spatial resolution enables the observation of the aligned structure and the pores fabricated by the electrochemical dissolution process.

The X-ray computerized microtomography was performed at beamline **BL47XU** [2]. A monochromatized X-ray (15keV) was used to obtain a sufficient intensity and contrast for an X-ray transmitted through Al-In alloy specimens. The format of the transmission X-ray images was 1000 × 1018 pixels and the effective pixel size was 0.5 μm × 0.5 μm. The exposure time for every transmitted image was 1.5 s. Reconstructed images were obtained using 750 transmission images. The present configuration allowed a 3D observation with a spatial resolution of 2 μm.

The aligned structures have been produced by the unidirectional solidification of monotectic alloys such as Al-In, Al-Bi and Cu-Pb [3,4]. As compared to the eutectic alloys that are well known to form the aligned structure during the solidification, the growth condition to form the aligned structure is extremely limited in the monotectic alloys. However, the monotectic alloys have a significant advantage in fabricating the porous media. Since the minor phase precipitates as the liquid state during the monotectic solidification, any anisotropy due to the crystal structure does not distort the aligned structure. Thus, it is desired to extend the growth condition for the aligned structure of the monotectic alloys.

Al-10at% In alloys were unidirectionally solidified under a magnetic field of 10 T. The imposition of the static magnetic field during the unidirectional solidification successfully achieved the aligned rod-like structure even at the hypermonotectic composition (10at% In). Figure 1 shows the reconstructed image of the Al-In alloy solidified under a magnetic field of 10 T. The constituent phases (Al and In phases) were identified by the linear absorption coefficients of the reconstructed images. The X-ray computed microtomography shows that the continuous In rods with diameters of 10 - 20 μm are regularly aligned parallel to each other. Moreover, the In rods were reduced to be less than 1 μm in diameter by plastic deformation techniques because of the high ductility of the Al and In phases.

On the basis of the X-ray computed microtomography, a growth model for the monotectic alloys under a magnetic field has been proposed [1]. The In phase nucleates at the solidifying front during the solidification. The In liquid droplets can be pushed by the solidifying front [3,4]. When the diameter of a pushed droplet exceeds a certain value, the droplet is engulfed by the front. The sequence of nucleation, pushing and engulfment results in the distribution of the In droplet in the matrix during the conventional solidification. The imposition of the high magnetic field reduces the melt flow around the droplet and consequently

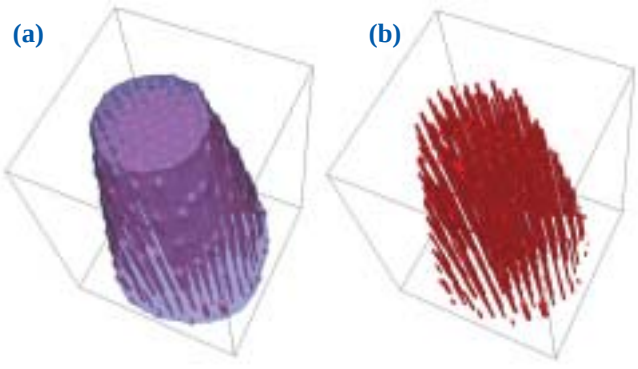

Fig. 1. 3D images of the Al-10at%In alloys which were unidirectionally solidified at a growth rate of 2.7 μm/s under a magnetic field of 10 T. **(a)** Image of the specimen used for the CT observation (Al matrix is semitransparent) and **(b)** In rods aligned in the Al matrix. The size of the 3D images is 380 × 380 × 500 μm^3. Blue: Al; Red: In.

enhances the engulfment of the In liquid phase. As a result, the cooperative growth of the Al and In phases produces the aligned structure.

A 10% HNO_3 aqueous solution was used for the electrochemical dissolution. As shown in Fig. 2, the electrochemical dissolution at a constant potential of −0.1 V for 12 h successfully removed the In rods from the matrix. However, the depth of the pores cannot be observed by SEM. Figure 3 shows the reconstructed 3D image of the Al-In alloys after the electrochemical dissolution for 24 h. Deep pores whose depth is more than 500 μm are produced by the electrochemical dissolution of the In rods. Deeper pores can be fabricated by the same procedures. Pores with a diameter less than 1 μm were also fabricated using the specimens reduced by the plastic deformation.

The computed microtomography using a hard X-ray and a high-resolution detector at SPring-8 significantly contributed to the fabrication of the porous media with deep pores. This technique will be widely applicable to evaluate microstructures of micro- and nanofabrications in various fields.

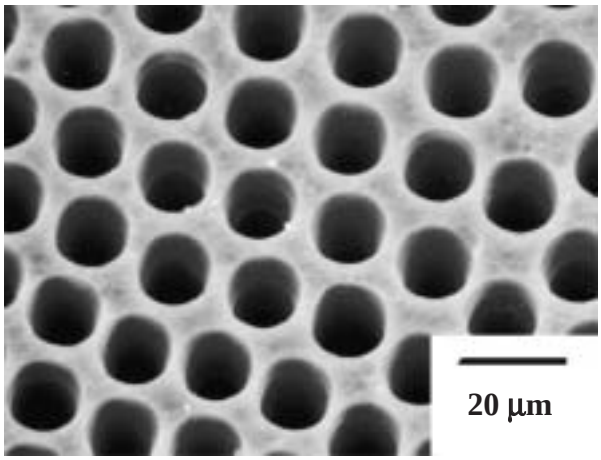

Fig. 2. SEM image of the porous Al produced by the electrochemical dissolution of the unidirectional solidified Al-10at%In alloy (growth rate: 2.7 μm/s; magnetic field: 10 T).

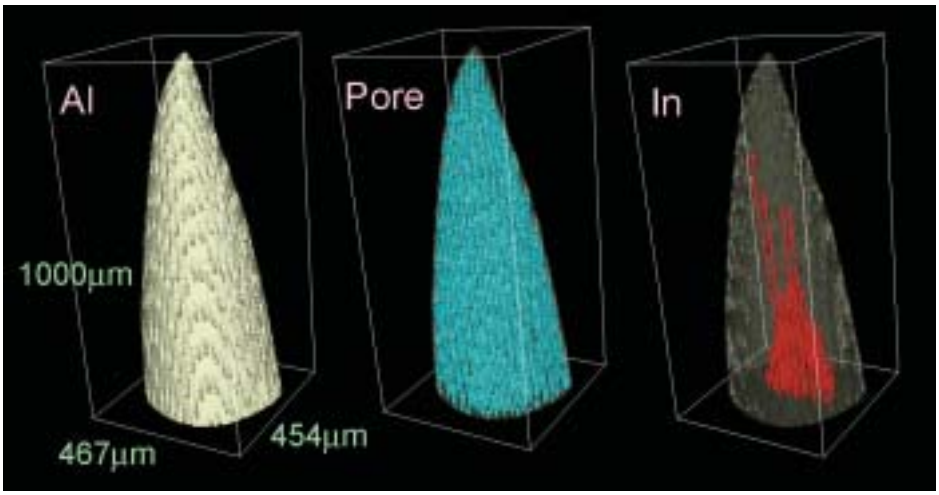

Fig. 3. 3D images of the porous Al produced by the electrochemical dissolution (24 h) of the unidirectional solidified Al-10at% In alloy. The size of the 3D images is 467×454×1000 μm^3.

Hideyuki Yasuda

Osaka University

E-mail: yasuda@ams.eng.osaka-u.ac.jp

References

[1] H. Yasuda, I. Ohnaka, S. Fujimoto, A. Sugiyama, Y. Hayashi, M. Yamamoto, A. Tsuchiyama, T. Nakano, K. Uesugi and K. Kishio: Materials Lett. **58** (2004) 911.
[2] K. Uesugi *et al.*: Nucl. Instrum. Meth. Phys. Res. A **467-468** (2001) 853.
[3] A.Kamio *et al.*: Mater. Sci. Eng. A **146** (1991) 105.
[4] B.K.Dhindaw *et al.*: Metall. Trans. A**19** (1988) 2839.

X-ray Talbot Interferometry for Phase Imaging

Using phase information is a key in the modern X-ray image science. Biological soft tissues can be observed without using contrast media, and various phase-sensitive X-ray imaging methods have been reported so far. We have proposed and demonstrated X-ray Talbot interferometry (XTI) as a novel and simple phase-sensitive imaging method, three-dimensional imaging with which is also feasible [1,2].

XTI is based on the Talbot effect by a transmission grating. The Talbot effect is a self-imaging phenomenon observed at specific distances downstream from a grating illuminated coherently. For instance, although no contrast is detected just behind a phase grating, the pattern of the grating becomes visible at a distance determined by the wavelength of illumination and the period of the grating. The image is called the 'self-image'. It should be noted that the self-image is deformed when a sample is placed in front of the grating due to the refraction at the sample.

XTI employs another grating (G2) as shown in Fig. 1. The position of G2 is selected so that the self-image of G1 is formed on G2. A moiré pattern showing the self-image deformation is observed by the superposition of the self-image and G2. The contrast generated by XTI corresponds to the differential phase shift caused by a sample.

We prepared transmission gratings by forming gold stripes on thin glass plates by optical lithography. The height of stripes of G1 was 1.25 μm so that the $\pi/2$ phase shift was generated for 0.1 nm X-rays maximizing the contrast of the self-image. The height of stripes of G2 was 8 μm, which was a marginal value attained by optical lithography, so that the amplitude modulation power of G2 was as high as possible. Figure 2(a) shows an image obtained by XTI for a plastic sphere 1.2 mm in diameter. Structures seen in the sphere are air bubbles. Using a phase-shifting technique, the differential phase shift caused by a sample could be calculated from multiple images acquired by displacing G2 against G1 as indicated by an arrow in Fig. 1. A resultant image mapping the differential phase shift is shown in Fig. 2(b). Because the phase shift can be obtained by integrating Fig. 2(b) as shown in Fig. 2(c), a three-dimensional image mapping the refractive index (Fig. 2(d)) could be reconstructed from images such as Fig. 2(c) measured in multiple projection directions by rotating a sample (phase tomography). A phase tomogram maps the refractive index difference, and the noise level of the tomogram was 5×10^{-9} (standard deviation), which corresponds to the detection limit of the density deviation of 4 mg/cm^3.

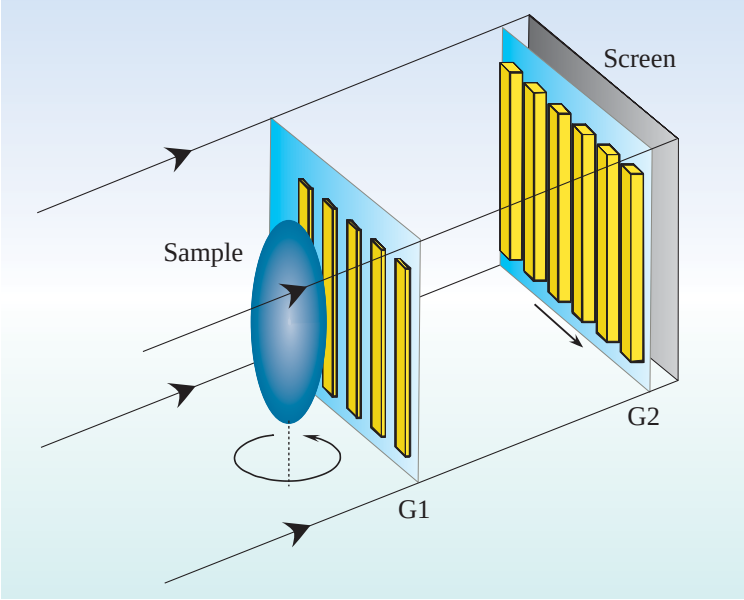

Fig. 1. Setup of an X-ray Talbot interferometer. Transmission gratings (G1 & G2) are aligned with a separation corresponding to the distance at which the Talbot effect by G1 occurs. A contrast corresponding to the differential phase caused by a sample placed in front of G1 is observed behind G2.

One advantage of XTI is that no crystal optics is used. This implies that a divergent X-ray beam with a broad energy band is available, provided that its partial spatial coherency is assured to some extent. Therefore, XTI would be practical with X-ray sources other than synchrotron radiation sources.

However, a technical problem to be solved for future applications is the fabrication of a better amplitude grating for G2. Because of high penetration power of hard X-rays, patterning with a high aspect ratio should be attained. The LIGA process would be a suitable technique for overcoming this difficulty, and a preliminary study for fabricating such a grating for XTI is in progress.

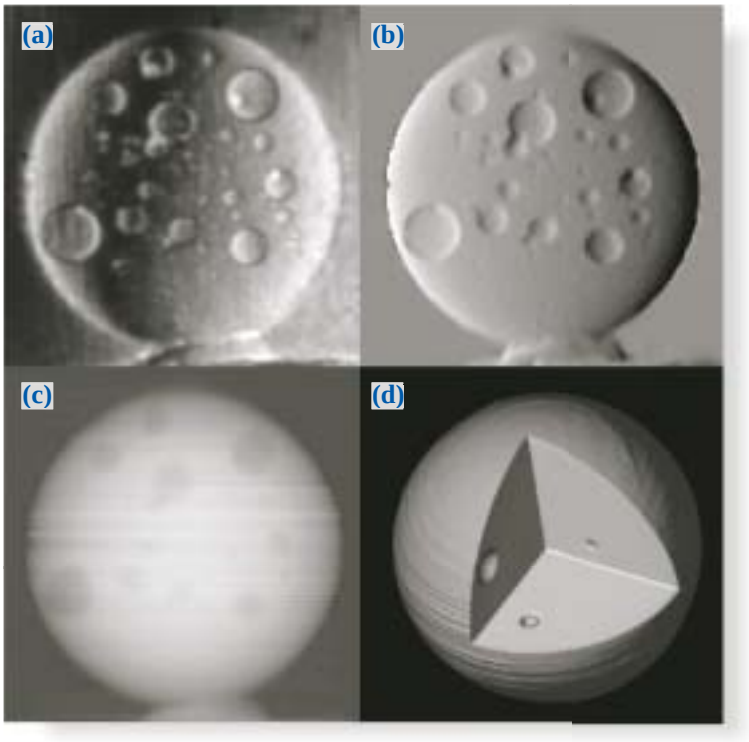

Fig. 2. Images obtained for a plastic sphere 1.2 mm in diameter: **(a)** a raw image generated by the X-ray Talbot interferometer, **(b)** an image mapping the differential phase shift measured by the phase-shifting technique, **(c)** a phase map obtained by integrating **(b)**, and **(d)** a three-dimensional rendering view of the data reconstructed by phase tomography. Structures seen in the sphere are air bubbles.

Atsushi Momose

Graduate School of Frontier Sciences,
The University of Tokyo

E-mail: momose@exp.t.u-tokyo.ac.jp

References

[1] A. Momose *et al.*: Jpn. J. Appl. Phys. **42** (2003) L866.
[2] A. Momose, S. Kawamoto, I. Koyama, Y. Hamaishi, K. Takai and Y. Suzuki: AIP Proc. **705** (2004) 1259.

Nuclear Physics

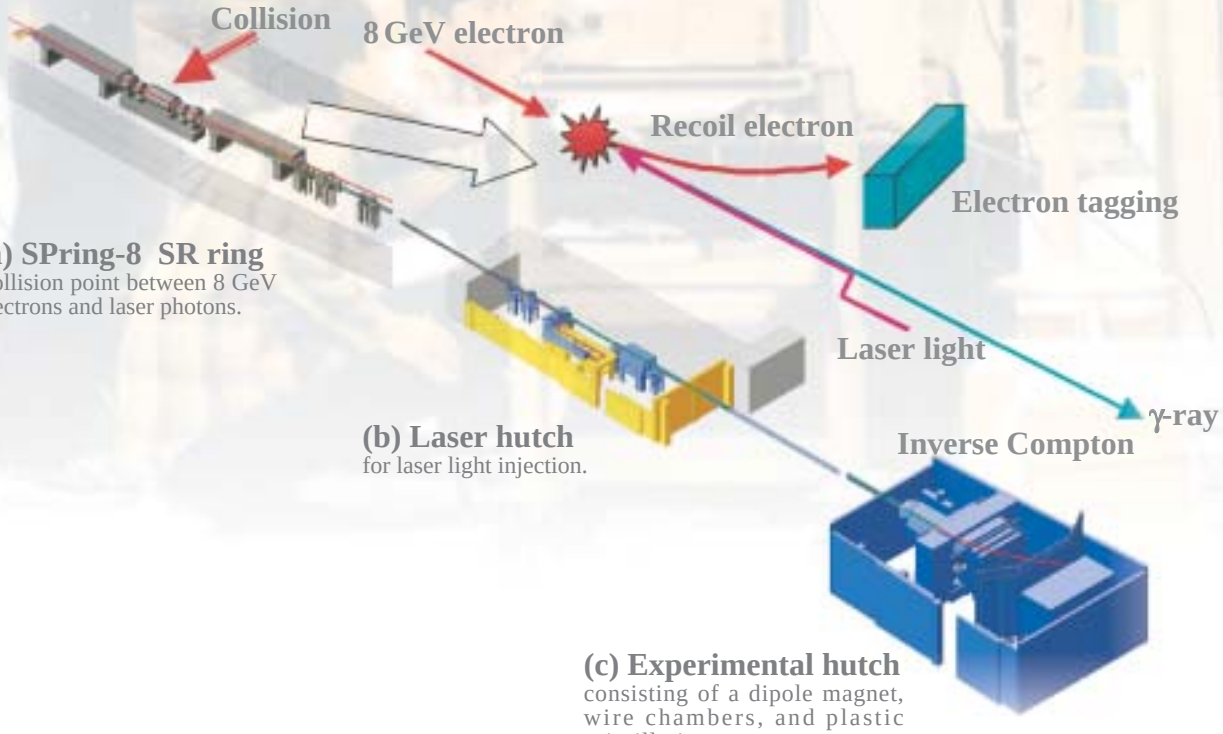

(a) SPring-8 SR ring
Collision point between 8 GeV electrons and laser photons.

(b) Laser hutch
for laser light injection.

(c) Experimental hutch
consisting of a dipole magnet, wire chambers, and plastic scintillation counters.

Evidence for $S = +1$ Pentaquark Baryon in Photoproduction from the Nucleon

Quarks are ultimate building blocks of subatomic particles although an isolated quark has never been observed. According to the quantum chromodynamics (QCD), each quark can have three colors; red, blue, or green. Only the colorless combination (superposition) of quarks can travel freely as a particle. An example of such a combination is a proton, which is made of two 'u' quarks and one 'd' quark. The relatives of a proton which are made of three quarks are called baryons. A particle consisting of one quark (q) and one anti-quark ($\bar{q}$) is called a meson. Note that an anti-quark can have the anti-colors; magenta ('anti-red'), violet ('anti-green'), or yellow ('anti-blue') so that a $q\bar{q}$ pair can be colorless. Mesons and hadrons together form a particle type called hadrons.

There were no clear experimental evidences for the existence of a hadron with a quark configuration rather than three quarks (three anti-quarks) or a $q\bar{q}$ pair, although QCD does not forbid the existence of other combinations such as $q\bar{q}\,q\bar{q}$ or $qqqqq\bar{q}$. The absence of the hadron state with more than three quarks was one of the big mysteries in particle physics for decades.

Recently, we, the LEPS collaboration at beamline **BL33LEP**, have found evidence for a pentaquark state ($qqqq\bar{q}$) with the strange quark number $S = +1$ (Fig. 1).

A baryon state with $S = +1$ cannot be made of three quarks since they must contain one anti-strange ($\bar{s}$) quark. To make the baryon number equal to 1, the minimal quark configuration should be $qqqq\bar{s}$, where q stands for a 'u' quark or a 'd' quark.

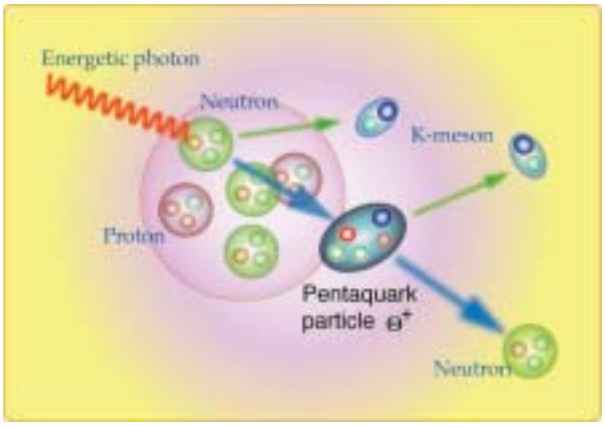

Fig. 1. Production of the pentaquark particle studied by the LEPS collaboration.

In 1997, Diakonov, Petrov and Polyakov studied anti-decuplet baryons using the chiral soliton model [1]. The mass splittings of the established octet and decuplet were reproduced with an accuracy of 1% in this model, and the lightest member of the anti-decuplet with $S = +1$, which we now call Θ^+, was predicted to have a mass of 1530 MeV and a total width of less than 15 MeV. The $S = +1$ baryon in this mass region has not been searched in the KN scattering experiments in the past because the momenta of kaons are too high, as pointed out in Refs. [1,2]. This fact together with the very narrow predicted width motivated us to search for evidence of the Θ^+ at the LEPS facility.

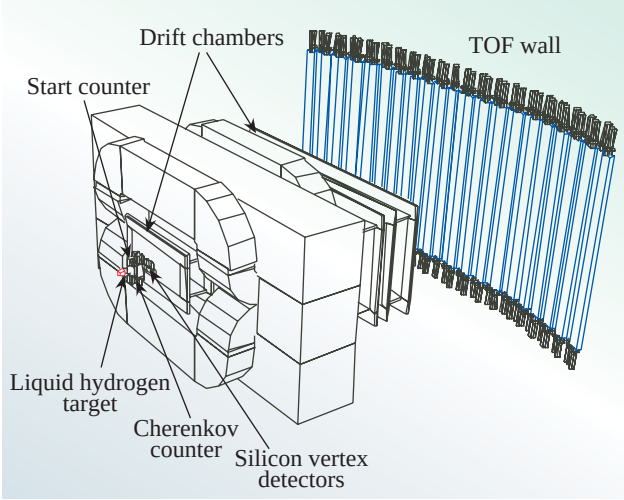

Fig. 2. The LEPS detector. It analyzes the momentum and velocity of charged particles in forward angles.

The laser-electron photon (LEP) beam is generated by backward-Compton scattering of laser photons with the 8 GeV electrons [3]. The maximum energy of the beam is currently 2.4 GeV, which is well above the threshold for $s\bar{s}$ production. Figure 2 shows a schematic drawing of the LEPS detector. For the determination of the momentum of a charged particle, tracking counters were placed before and after a 0.7 T magnet. A time-of-flight (TOF) scintillator array was positioned 3 m behind the dipole magnet to measure the velocity of a charged particle. The mass of a charged particle was reconstructed from the momentum and velocity information.

A 0.5-cm-thick plastic scintillator (SC) located 9.5 cm downstream from the 5-cm-thick liquid-hydrogen (LH_2) target ensured that at least one charged particle is produced in the LH_2 target. For the Θ^+ search at LEPS, the events from the SC were used to study the events generated from neutrons in the carbon nuclei at the SC, by searching for baryon resonances with the strangeness quantum number $S = +1$ in the K^- missing mass spectrum in the $\gamma n \to K^+K^-$ reaction [4]. Since the LH_2 target contained no neutron, events from the LH_2 target were used to estimate the background spectrum.

Figure 3 shows the K^- missing mass distribution of the signal sample. A prominent peak at 1.54 GeV (1540 MeV) is found. The broad background centered around 1.6 GeV is most likely due to non-resonant K^+K^- production and the background shape in the region above the peak has been fitted by a distribution of events from the LH_2. The upper limit for the width was determined to be less than 25 MeV. The observed narrow peak strongly indicates the existence of an $S = +1$ resonance which may be attributed to the exotic 5-quark baryon proposed as the Θ^+.

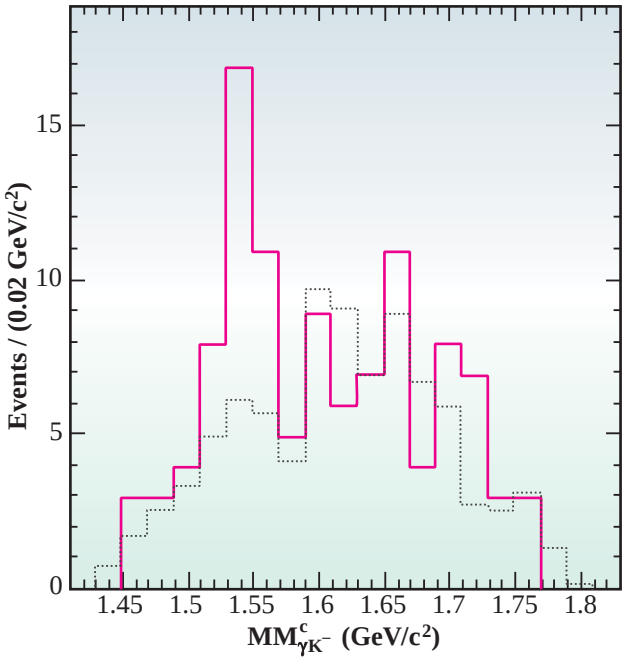

Fig. 3. K^+ missing mass spectrum for the signal sample (solid histogram) and for events from the LH_2 (dotted histogram) [4].

Soon after a result on the Θ^+ was announced by the LEPS collaboration, it was confirmed by experiments at ITEP [5], Jefferson Lab [6], and ELSA [7]. All experimental results indicate that the width of the $S = +1$ baryon, which is now called Θ^+, is very narrow. The both measured mass and which are in good agreement with a prediction by Diaknov *et al*. Intensive theoretical investigation of the Θ^+ is in progress. Further experimental efforts to determine the spin and parity of the Θ^+ are crucial.

Takashi Nakano

Research Center for Nuclear Physics

E-mail: nakano@rcnp.osaka-u.ac.jp

References

[1] D. Diakonov *et al.*: Z. Phys. A **359** (1997) 305.
[2] M. Polyakov *et al.*: Eur. Phys. J. A **9** (2000) 115.
[3] T. Nakano *et al.*: [LEPS Collaboration], Nucl. Phys. A **684** (2001) 71c.
[4] T. Nakano, D.S. Ahn, J.K. Ahn, H. Akimune, Y. Asano, W.C. Chang, S. Daté, H. Ejiri, H. Fujimura, M. Fujiwara, K. Hicks, T. Hotta, K. Imai, T. Ishikawa, T. Iwata, H. Kawai, Z.Y. Kim, K. Kino, H. Kohri, N. Kumagai, S. Makino, T. Matsumura, N. Matsuoka, T. Mibe, K. Miwa, M. Miyabe, Y. Miyachi, M. Morita, N. Muramatsu, M. Niiyama, M. Nomachi, Y. Ohashi, T. Ooba, H. Ohkuma, D.S. Oshuev, C. Rangacharyulu, A. Sakaguchi, T. Sasaki, P.M. Shagin, Y. Shiino, H. Shimizu, Y. Sugaya, M. Sumihama, H. Toyokawa, A. Wakai, C.W. Wang, S.C. Wang, K. Yonehara, T. Yorita, M. Yoshimura, M. Yosoi and R.G.T. Zegers: [LEPS Collaboration], Phys. Rev. Lett. **91** (2003) 012002.
[5] V.V. Barmin *et al.*: [DIANA Collaboration], Phys. Atom. Nucl. **66** (2003) 1715.
[6] S. Stepanyan *et al.*: [CLAS Collaboration], Rev. Lett. **91** (2003) 252001.
[7] J. Barth *et al.*: [SAPHIR Collaboration], arXiv:hep-ex/0307083.

Accelerators Frontiers

Beam Performance and Upgrades of the Storage Ring

Orbit Stability

In 2002, it was accomplish the suppressing of chamber vibration in quadrupole magnets reducing drastically the fast variation of the beam orbit in the storage ring [1]. However, the slow drift of orbit is still large. The beam orbit moves slowly within ±10 μm, which generates about 1.5 μrad in angle of the photon beam axis at the worst case. From the observation of the orbit drift, we found that the shortage of degrees of freedom in the steering phase causes this drift. After many orbit correction steps, the higher order distortion of the orbit is created. The periodic correction was carried out using the twenty-four air-core-type steering magnets with high resolution and low hysteresis. We therefore investigated the possibility of using normal horizontal and vertical steering magnets (six horizontal and vertical steering magnets are usually installed in each Chasman-Green cell) to increase the available number of steering in the correction. The problem is the poor resolution of field setting, which is two orders worse than that of the air-core-type steering magnets. To reduce the field setting errors while using the normal steering magnets, we investigated the magnets' hysteresis. Results show that the hysteresis is not so large and the resolution of the field setting can be drastically improved by increasing the resolution of the current setting in the power-supplies.

On the other hand, when many steering magnets are used in the correction, the photon beam axis of each beamline is necessary for keeping all the axes constant. To this end, to ensure the absolute transverse positions of the attached BPMs which are installed upstream and downstream of insertion devices (IDs), we have designed a set of new chambers equipped with BPM. The readouts from BPMs define the corresponding photon axis. Three sets of new BPM chambers have been installed in three ID straight sections and their performances is being investigated. The GUI program for the periodic orbit correction has also been modified to consider all photon axes of ID beamlines. The new algorithm will be in service in May 2004.

Top-up Operation

The top-up operation maximizes research activities in a synchrotron radiation (SR) facility by an effectively infinite beam lifetime and high photon beam stability. We have been improving the SPring-8 accelerators to achieve the ideal top-up operation. Since autumn 2003, we have been injecting the beams keeping the photon beam shutters opened and ID gaps closed. We are developing a bunch-by-bunch feedback system to reduce further the beam loss with all the ID gaps fully closed by lowering the operating chromaticity. The top-up operation with constant stored current is scheduled in May 2004. This operation requires two key conditions. One is a perturbation-free injection, which never perturbs users' experiments by exciting the oscillation of stored beams. Figure 1 shows effective beam size variations due to the beam injection before improvements, which are measured at a beam diagnosis beamline by the X-ray beam profile monitor. The betatron

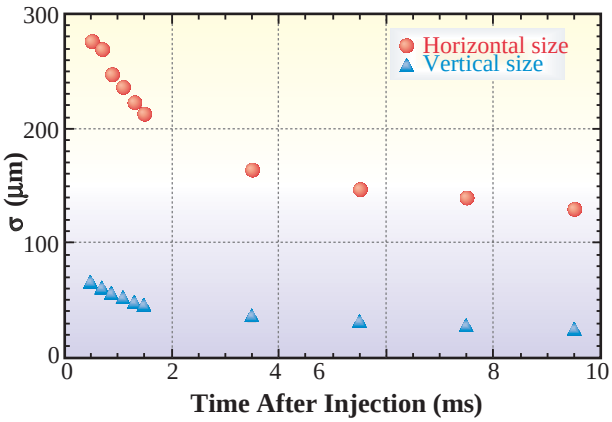

Fig. 1. Horizontal and vertical beam size variations due to the beam injection before improvements.

functions are 2.1 m and 27.8 m in horizontal and vertical directions, respectively. The other is a loss-free injection, which prevents demagnetization of permanent magnets comprising of IDs through the lost electron bombardment.

In order to reduce the amplitude of the horizontal oscillation, we have adjusted the magnetic field shape of four injection bump magnets to close the bump orbit. Since the eddy current at the end plates of magnets mainly causes the similarity break of the field shape, the four bump magnets were replaced by the new ones having the nonmetal end plates to reduce the effect of the eddy current [2]. We also developed a scheme for suppressing the horizontal oscillation induced by the nonlinearlity of sextupole magnets. This scheme can make the oscillation amplitude negligibly smaller than the horizontal beam size, down to a few tens microns by a simple optimization of sextupole strengths in the injection bump [3]. These reduced the horizontal oscillation down to one-third of the stored beam size. Figure 2 shows the time variation of the horizontal oscillation amplitude of the stored beam.

The vertical oscillation of the stored beam is excited depending on the amplitude of the injection bump, which reveals that the tilt of the bump magnets causes the vertical oscillation.

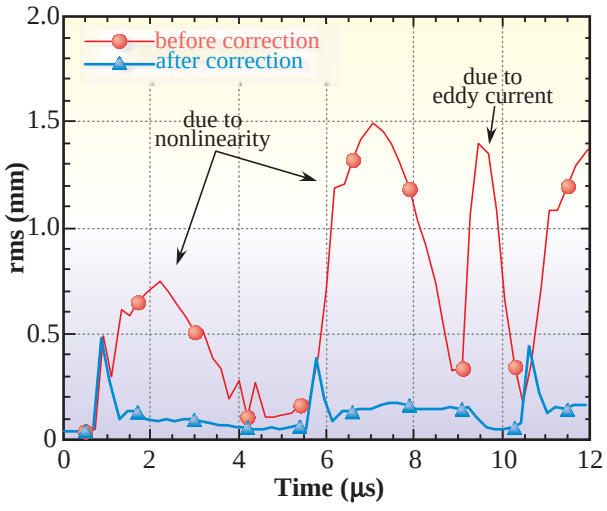

Fig. 2. Horizontal oscillation amplitude of stored beam measured using turn-by-turn monitor.

By adjusting the tilt angle of bump magnets properly, the vertical oscillation was reduced by one-third. For the remaining vertical oscillation, the feedforward correction was applied with a single pulse corrector. These two countermeasures reduced the vertical oscillation down to two-thirds of the stored beam size. As a result of the above suppression treatments, the variation of monochromatized beam intensity has became less than 10% at the experimental station during the beam injection.

For the loss-free injection, beam collimators were installed upstream of the beam transport line from the booster synchrotron. The horizontal tail of the injection beam is usually cut at $\pm 1\sigma$ and the core part of the beam is only injected to the storage ring. This realized the injection efficiency of nearly 100% under the restricted gap condition of in-vacuum IDs [4].

Bunch-by-bunch feedback

Transverse beam instabilities are one during the most serious problems during the operation of the SPring-8 storage ring, and to suppress them, a large chromaticity was introduced to the ring optics. However, this large chromaticity imposes a serious restriction on the ring operation and it is difficult to optimize ring parameters for recently requested advanced operation modes, such as top-up, high-current and low-energy modes. To dissolve this large chromaticity, a bunch-by-bunch feedback system (BBF) is developed and its introduction to user operation is scheduled at the start of 2004. The BBF is another method for curing instabilities and this measures the positions of bunches and kicks them back bunch-by-bunch, turn-by-turn. A block diagram of the BBF system is shown in Fig. 3.

Compared with similar systems in other facilities, our BBF system has several advantages: low-noise high-resolution position detection and digitization, and nearly one-order- lower cost by using of FPGAs instead of DSPs for digital signal processing. To reduce the noise of the system, a fast and high-resolution strip-line monitor was developed and slow but high-

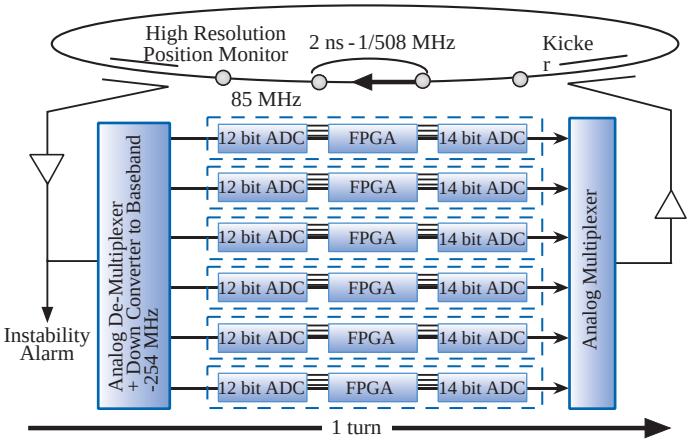

Fig. 3. Schematic block diagram of the bunch-by-bunch feedback system.

resolution ADCs were employed with the help of a newly invented analog de-multiplexer. The diagnosis system of the BBF and the instability detection and alarm system were also developed.

Accelerator Diagnosis Beamlines

X-ray imaging observation of the electron beam using a zone plate X-ray beam profile monitor [5] is in progress at the accelerator diagnosis beamline #1 (BL38B2). The focused image of the electron beam was successfully obtained. Figure 4 shows an example of images of the electron beam of the SPring-8 storage ring observed using this monitor. The operation conditions of the ring are as follow: low-emittance optics, multi-bunch filling, beam current of 100 mA, and all ID gaps fully open. On the basis of preliminary calibrations of the X-ray zooming tube, the horizontal and vertical beam sizes (1σ) were roughly 120 μm and 15 μm, respectively. Equipments for use in SR experiments on accelerator components were installed in the optics hutch of BL38B2. The installed equipments are a vacuum chamber for irradiation experiments of photon absorbers, metal filters for controlling irradiating SR intensity, and Be windows through which white X-ray radiation exits into the atmosphere. For example, radiation damage of insulators of quadrupole magnets was studied using white radiation in the atmosphere.

Construction of the accelerator diagnosis beamline #2 (BL05SS) is in progress. In 2003, the UHV components of the front end were installed in the accelerator tunnel. The radiation shielding hutches were built on the experimental hall. BL05SS has a straight section of the storage ring, where IDs for light sources can be installed. Mechanical design of the vacuum chamber for the ID straight section and conceptual design of IDs have been started.

The study of the production of γ-ray photons with energies of the order of 10 MeV is in progress in BL38B2 and BL05SS. The γ-ray photons are generated *via* backward Compton scattering of optically pumped far-infrared laser photons by electrons of the storage ring.

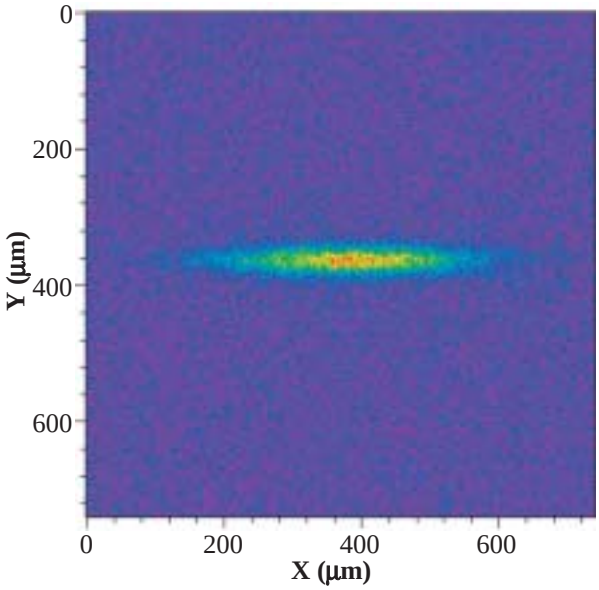

Fig. 4. Example of images of the electron beam of the storage ring observed using the zone plate X-ray beam profile monitor.

Installation of 10T Superconducting Wiggler for Beam Tests

There are some demands for γ-rays in the energy range from a few hundred keV to several or ten MeV. Use of high-energy photons of about a few hundred keV to 500 keV will become possible in Compton scattering experiments. Intense low-energy positron beams can be produced via the electron-positron pair-production process by γ-rays. To generate such γ-rays, a 10 T superconducting wiggler (SCW) was proposed [6], a prototype machine fabricated in Budker INP [7] and was tentatively installed in the storage ring in August 2002, and beam tests were carried out [8]. Figure 5 shows a photograph of the SCW installed in the storage ring. Basic parameters of the SCW are listed in Table I.

Table I. Basic parameters of the SCW (design values)

Number of Poles:	3
S/C Wire:	Nb_3Sn and NbTi
Maximum Field:	10 T
Stored Energy at 10T:	400 kJ
Weight:	1000 kg
Length:	1 m
Pole Gap:	42 mm
Beam Chamber:	65 mm(H) × 20 mm(V)

After ramping up the magnetic field of SCW to 9.7 T, we could successfully store a beam in the storage ring. The stored current was limited to 1 mA to avoid high heat load on photon absorbers and radiation damage to accelerator components. We then measured beam parameters such as horizontal beam size (Fig. 6), bunch length and tune shift affected by the strong magnetic fields. The results agreed well with calculations based on the measured magnetic field distribution of the SCW. We also measured a spectrum of high-energy SR using the NaI(Tl) scintillator and a photomultiplier at the SCW peak field of 9.5 T. The data was taken at an extremely low beam current of about 8 pA and we could see a reasonable agreement between the experimental data and simulations.

After the beam tests, the SCW was removed from the storage ring and is now in the test bench. When we consider its effects on the stored beam together with the high heat load, it is not easy to use the SCW during user operation. Nevertheless, the applications of high-energy γ-rays generated by the SCW are interesting and important, and we are now looking for a possible way of using the SCW for actual applications.

Fig. 5. Photograph of the SCW.

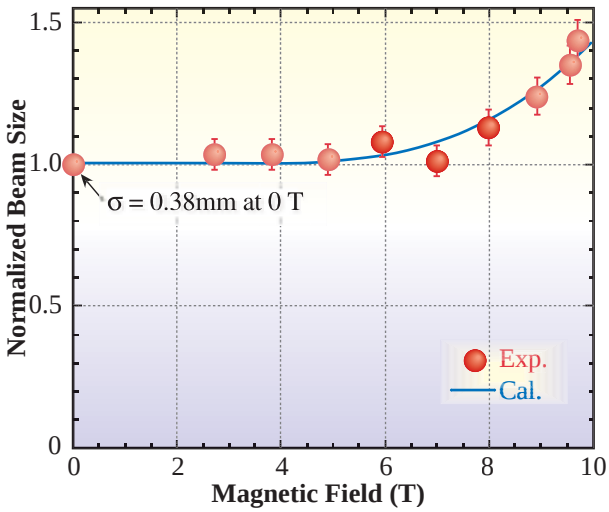

Fig. 6. Horizontal beam size normalized by a value at 0 T.

HOM-damped Re-entrant Quasi-half-cell RF Cavity for the SPring-8 Storage Ring [9]

The RF cavity parasitic narrow-band coupling impedances of higher order resonant modes (HOMs) cause coupled-bunch instabilities (CBIs) harmful for storing an electron beam. In order to cope with CBIs, the bell-shaped single-cell RF (BSR) of SPring-8 cavities was designed to have lower HOM coupling impedances than the threshold coupling impedance of CBI at a beam current of 100 mA and delivered with systematic modification in their inner size, two frequency tuners and precisely temperature-controlled cooling water [10]. However, a large increase in beam current reduces the threshold coupling impedance of CBI and becomes difficult for the BSR cavities. Therefore, in preparation for the future reinforcement of beam current, a new RF cavity with lower HOM coupling impedances than those in the BSR cavity was designed and its RF properties were examined by the MAFIA frequency-domain simulation. The newly designed RF cavity has a higher beam accelerating shunt impedance of the TM010 mode than that in the BSR cavity and 3 structures for suppressing CBIs: a re-entrant quasi-half-cell body, HOM skew-imposing ports (SKIPs) and a grooved-beam pipe (GBP). To confirm the designed RF performance of the re-entrant quasi-half-cell RF (RQR) cavity, an aluminum model cavity shown in Fig. 7 was fabricated and the low-power RF measurement was carried out. The measured resonant frequency, Q-value, and R/Q of the TM010 mode in the aluminum model cavity were about 506.9 MHz, 19000 and 200 Ω, respectively. Table II shows the measured RF properties in the model cavity with SKIPs and GBP. These measured values were approximately similar to those obtained by the MAFIA calculations, and the HOM damping performance of the RQR cavity with SKIPs and GBP was verified by the measurement.

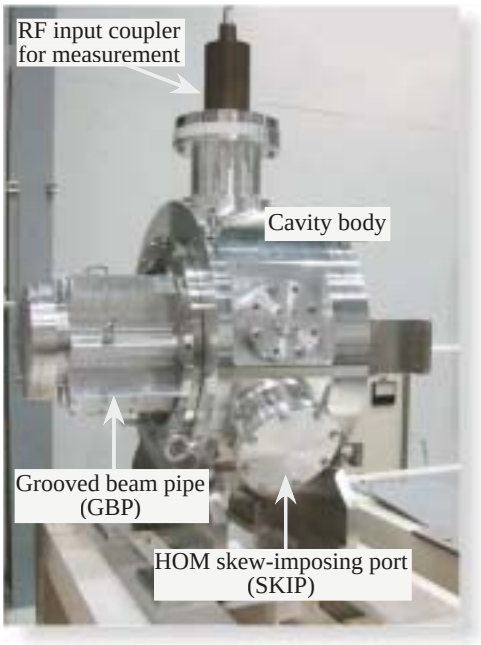

Fig. 7. RQR model cavity made of aluminum.

Table II. Measured RF properties of the principal resonant modes in the aluminum model RQR cavity with SKIPs and GBP

mode	frequency [MHz]	Q	coupling coefficients
TM010	506.903 (506.855)	19200 (19800)	2.9
TM110-L	810.888 (816.810)	400 (500)	0.1
TM110-H	819.598 (825.757)	400 (400)	0.1
TM011	919.330 (913.144)	12700 (15600)	7.5
TM111-L	1142.981 (1145.318)	600 (900)	0.2
TM111-H	1145.211 (1149.825)	600 (800)	0.3

Developments and Upgrades of Linac

Accelerator stabilization

A klystron modulator used for the SPring-8 linac employs the de-Q'ing type voltage regulation technique. In this kind of circuit, an induction voltage regulator (IVR) coarsely adjusts a dc high voltage and the following de-Q'ing trigger circuit finely controls the charging voltage of a PFN. If the dc high voltage could not sufficiently stabilized, the de-Q'ing circuit cannot accurately regulate the PFN voltage. We recently observed a maximum voltage variation of 5% throughout a day in a 400 V ac line at the SPring-8 site. The de-Q'ing circuit cannot sufficiently suppress the PFN voltage variation caused by this large line variation, which often results in negligible klystron's RF-power and phase variations. Therefore we have reexamined the entire regulation circuit to improve the IVR control. The improved controller coarsely regulates the IVR's output voltage in order to maintain the variation within ±1%. This improved regulation consequently reduced the previous long-term variation to 0.03% rms throughout a week, which corresponded to the RF power and phase variation of about 0.08% rms and 0.2 degrees rms, respectively.

Reduction of dark currents

The SPring-8 linac accelerates electron beams by dark currents from a gun or accelerating structures, as well as main electron beams with a pulse width of 1 or 40 ns. These dark currents can be the background of an electron beam injection into a booster synchrotron, and then it consequently spoils the purity of a single bunch circulating in the storage ring. The 1 GeV dark currents originate mainly from two components: electron emissions from a gun grid and field emissions in accelerating cavities of the injector section. We have first tried to reject the former emission currents using a beam deflector [11] before it is accelerated by linac's buncher cavities. The deflector itself is composed of a rectangular chamber with two parallel-plate electrodes inside it, as shown in Fig. 8. The 180 keV electron beam is horizontally deflected with an angle of 110 mrad when a pulsed electric field of 7 kV is applied between both electrodes; then, it is blocked by an iris plate placed 150 mm downstream.

We have measured the purity of the single bunched beam stored in the 8 GeV storage ring by a photon counting technique. Figure 9 shows the charge distributions around the main bunch circulating in the storage ring when the deflector is in or out of operation. These experimental results clearly prove that the deflector has filtered out the faint charges around the main bunch, which were observed when the deflector was not in operation.

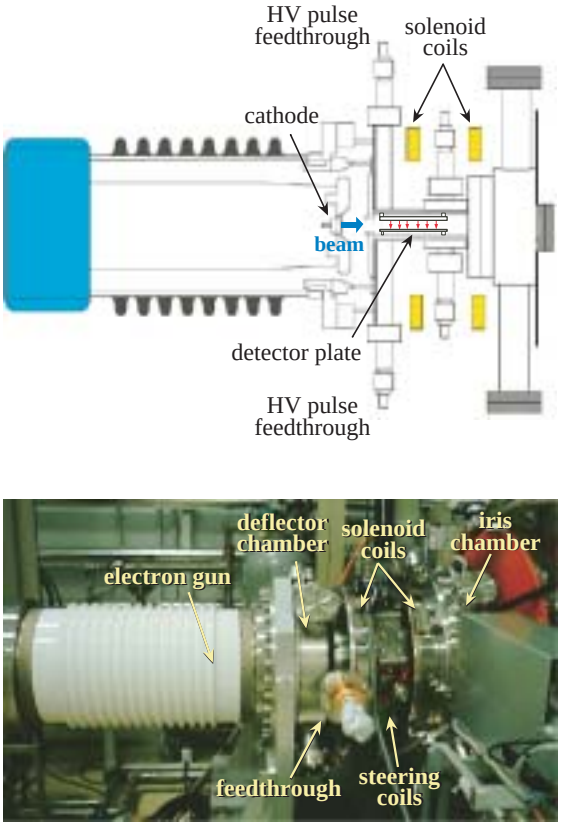

Fig. 8. Electron gun and beam deflector.

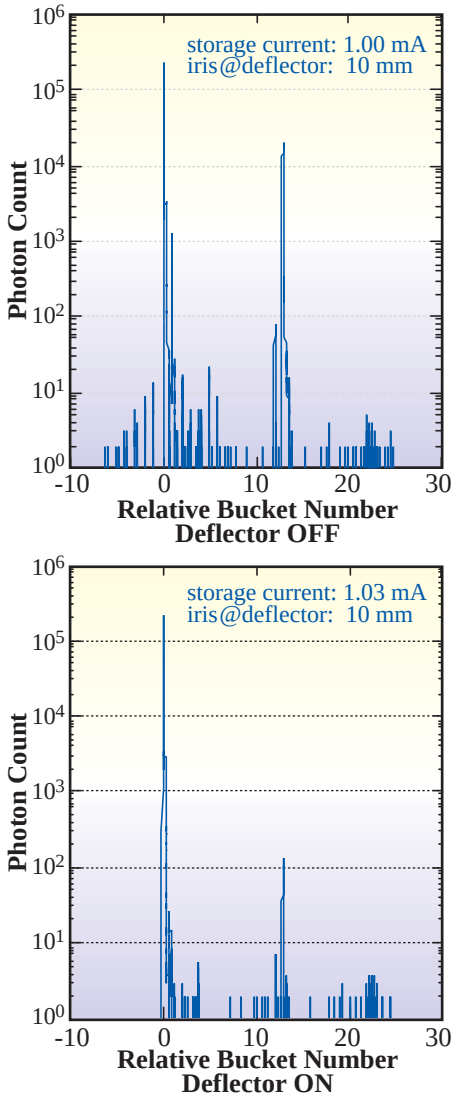

Fig. 9. Charge distribution of the single bunch beam stored in the 8-GeV storage ring.

RF gun development

We have started the development of a cartridge-type photocathode in collaboration with Hamamatsu Photonics and the University of Tokyo [12]. The cartridge-type photocathode, which is manufactured in a factory, is expected to have reproducible high quantum efficiency (QE) and be easy to handle even in small laboratories. The first prototype is a Cs_2Te cathode encapsulated in a glass cartridge, as shown in Fig. 10. A revolver system, which can hold four cartridges, is attached to a cathode plate of an RF gun cavity. The procedure for charging the cavity with a cathode plug is as follows: A coaxial mover slides a cartridge out of the revolver and then a Kovar foil sealing the cartridge is broken by a pair of cutters similar to a bird's bill. An inner rod of the mover pushes the cathode plug out of the cartridge and mounts it into a cathode-plug hole of the cavity. Conditioning and high-field tests have been carried out on the prototype cartridges. The maximum accelerating field reached 90 MV/m, however, the QE of the photocathode deteriorated from 3% to 1% in one day. We are improving the fabrication method of the photocathode surface to control the deterioration of the QE. A new cathode will be tested in 2004.

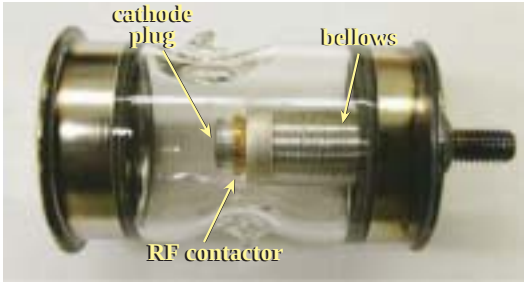

Fig. 10. Prototype cathode cartridge.

References

[1] S. Matsui *et al.*: JJAP **42** (2003) L338.
[2] T. Ohshima: Proc. of the 14th Symposium on Accel. Sci. and Techn., Tsukuba (2003) 223.
[3] H. Tanaka *et al.*: submitted to Phys. Rev. E.
[4] K. Fukami *et al.*: to be presented in the APAC 2004, Gyeongju, Korea.
[5] S. Takano *et al.*: Proc. 14th Symposium on Accel. Sci. and Tech., Tsukuba (2003) 491.
[6] A. Ando *et al.*: J. Synchrotron Rad. **3** (1996) 201.
[7] M. Fedurin *et al.*: Nucl. Instrum. Meth. A **448** (2000) 51; M. Fedurin, *et al.*, *ibid.* A **470** (2001) 34.
[8] K. Soutome *et al.*: Proc. of 2003 Particle Accelerator Conference, Portland (2003) 250; M. Shoji *et al.*, *ibid.*, (2003) 782.
[9] H. Ego: Nucl. Instrum. Meth. A **516** (2004) 270.
[10] H. Ego *et al.*: Nucl. Instrum. Meth. A **383** (1996) 325; H. Ego *et al.*, *ibid.* A **400** (1997) 195.
[11] T. Kobayashi *et al.*: Proc. of EPAC 2002, Paris (2002) 2685.
[12] J. Sasabe *et al.*: Proc. of FEL 2003, Tsukuba.

Haruo Ohkuma, Hiroto Yonehara, Hirofumi Hanaki and Noritaka Kumagai
SPring-8 / JASRI

Facility Status

The operation statistics since the facility was opened to users are shown in Fig. 1. In 2003, the SPring-8 storage ring was operated on four- or five-week period for one operation cycle. The total operation time of the accelerator complex was 5419.5 hours. Of those hours, 72.4% (3926.0 hours) were available to the users. The injection time and the down time due to failure accounted for 0.7% (39.2 hours) and 3.9% (208.5 hours) of the operation time, respectively; a great loss of user time was due to one major failure in October 2003. A crack and hole were made on the side-wall of the vacuum chamber for a beam injection point, because the aborted electron beams of about 100 mA hit the inner side-wall of the vacuum chamber. Consequently, the broken injection vacuum chamber was removed and replaced by a reserved one. As a result, the user time of 119.5 hours was cancelled for the failure and recovery works. The remaining 23.0% (1245.8 hours) was dedicated to: (i) the machine and beamline study, (ii) the machine and beamline tuning, (iii) the commissioning of new photon beamlines.

The operation modes of three different filling patterns were delivered to the user time; 37.2% in the multi-bunch mode operation, 50.8% in the several bunch mode such as 203-bunch mode (203 equally spaced bunches), 29 equally spaced 11-bunch trains, and the remaining 12.0% in the hybrid filling mode such as a 2/21-partially filled multi-bunch with 18-isolated bunches. For the hybrid filling mode, 1 or 1.5 mA is stored in each isolated bunch. An isolated bunch purity of better than 10^{-10} is routinely being delivered.

Table I presents a summary of the useful beam parameters of the storage ring. In November 2002, the low emittance optics was introduced to the user time by breaking the achromatic condition. After the above mentioned failure, however, the ring optics went back to the former HHLV optics, because in case of the low emittance optics the aborted beam hits the injection vacuum chamber just like concentrated fire.

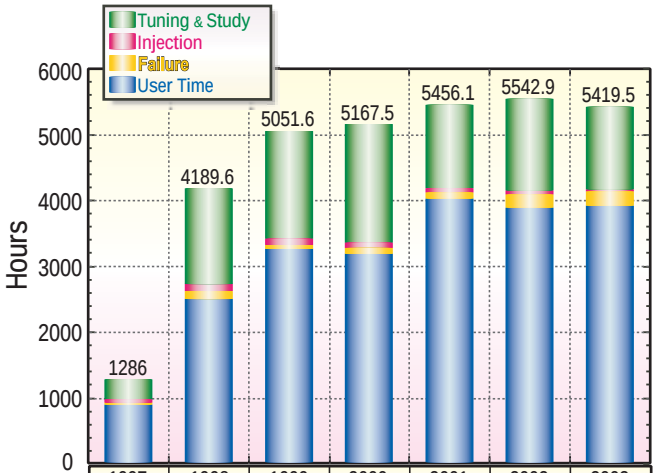

	1997	1998	1999	2000	2001	2002	2003
Tuning & Study (Accel. & BL)	304	1457.6	1624.2	1815	1276.5	1394.9	1245.8
Injection	50	110	95.2	70.4	59.3	60.8	39.2
Failure	26	110	57.2	88.7	87.1	190.5	208.5
User Time	906	2512	3275	3193.4	4033.2	3896.7	3926

Fig. 1. Operation statistics since the facility was opened to users.

Table I. Beam parameters of SPring-8 storage ring

	HHLV Optics	Low Emittance Optics
Tunes (ν_x / ν_y)	40.15 / 18.35	40.15 / 18.35
Current[mA]: single bunch	13	10
multi bunch	100 (120[*1])	100
Bunch length (FWHM) [psec]	32	34
Horizontal emittance[nm·rad]	6.3[*2] / 6.6[*3]	3.1[*2]
Vertical emittance[pm·rad]	16.9[*3]	8.7[*3] / 3.9[*4]
Coupling [%]	0.26[*3]	0.28[*3] / 0.13[*4]
Beam size[mm]: (σ_x / σ_y)[*5]		
Long ID section	381 / 13.4	283 / 11.4
ID section	397 / 8.5	289 / 7.2
BM section	149 / 21.0	103 / 15.2
Beam Divergence[mrad]: ($\sigma_{x'}$ / $\sigma_{y'}$)[*5]		
Long ID section	16.1 / 1.2	11.9 / 0.81
ID section	15.9 / 1.9	11.7 / 1.3
BM section	57.4 / 0.78	53.8 / 0.68
Operational Chromaticities: (ξ_x / ξ_y)	+7 / +6 (+2 / +2)[*6]	+8 / +8
Lifetime[hr]: 100 mA (multi bunch)	~ 150	~ 97
1 mA (single bunch)	~ 24	~ 9
Dispersion distortion[mm]:horizontal (rms)	24	9.3
vertical (rms)	1.1[*7]	1.1[*7]
Orbit stability (tune harmonics)[mm]:		
horizontal (rms)	–	1.3
vertical (rms)	–	0.35

[*1] Maximum stored beam current at machine study.
[*2] Measured by a pulse bump and scraper, [*3] two dimensional interferometer, and [*4] two photon correlation.
[*5] Assuming that 0.26% coupling for "HHLV" and 0.2% coupling for "Low Emittance Optics"
[*6] With bunch-by-bunch feedback. [*7] With correction by 24 skew Q's.

BEAMLINES

SPring-8 beamlines are categorized into four groups as listed below:

(1) Public Beamlines
(2) Contract Beamlines
(3) JAERI / RIKEN Beamlines
(4) Accelerator Beam Diagnosis

The public beamlines are constructed by JAERI and RIKEN with government grants, and are open for public use. This category of public beamlines includes three R&D beamlines, which were constructed for the purpose of developing new devices and beamline equipment such as optical elements, detection systems, and so forth. Used mainly by SPring-8 staff, the R&D beamlines are also open to public. Now 25 public beamlines (22 X-ray beamlines, two soft X-ray beamlines and one infrared beamline) are operational and available for public use.

The contract beamlines are, on the other hand, facilities that are installed, owned, operated and maintained by universities, companies and other organizations. Beamline contractors can use their beamline almost exclusively. Hyogo Prefecture took the lead in the contract beamline construction. Industrial Consortium, National Synchrotron Radiation Research Center (NSRRC, Taiwan), Institute for Protein Research (Osaka Univ.), Research Center for Nuclear Physics (RCNP, Osaka Univ.), National Institute for Materials Science and Pharmaceutical Consortium followed in that order. NSRRC was the first to construct foreign contract beamlines (BL12B2 and BL12XU) at SPring-8. Currently those nine contract beamlines are all in operation.

The JAERI/RIKEN beamlines are those constructed by JAERI and RIKEN for the exclusive use to promote their own research activities although 20% of beamtime is reserved for public use. Four JAERI and six RIKEN beamlines have already been constructed and one of the RIKEN beamlines, BL17SU, is in commissioning. RIKEN BL19LXU is the only one long undulator beamline and can provide the highest brilliance. Experimental stations of BL22XU and BL23SU are located at RI Laboratory and dedicated to research utilizing radioactive isotopes and actinide materials. BL26B1 and BL26B2 are beamlines used for high throughput protein crystallography following the human genome project. BL29XU has two experimental stations, one located in the experimental hall, and the other at the end of the 1 km beamline. Dedicated to studying the characteristics of the electron beam accumulated in the storage ring, the accelerator beam diagnosis beamlines are currently under the exclusive use of the JASRI accelerator group.

All 62 beamlines that SPring-8 can accommodate (34 insertion devices, 4 long undulators, 23 bending magnets and 1 infrared) are shown in the Beamline Map (Fig. 2). As of March 11, 2004, one beamline (BL17SU) is in the phase of commissioning. Including the two accelerator beam diagnosis beamlines, we have 47 beamlines, about 75% of full capacity (Table II).

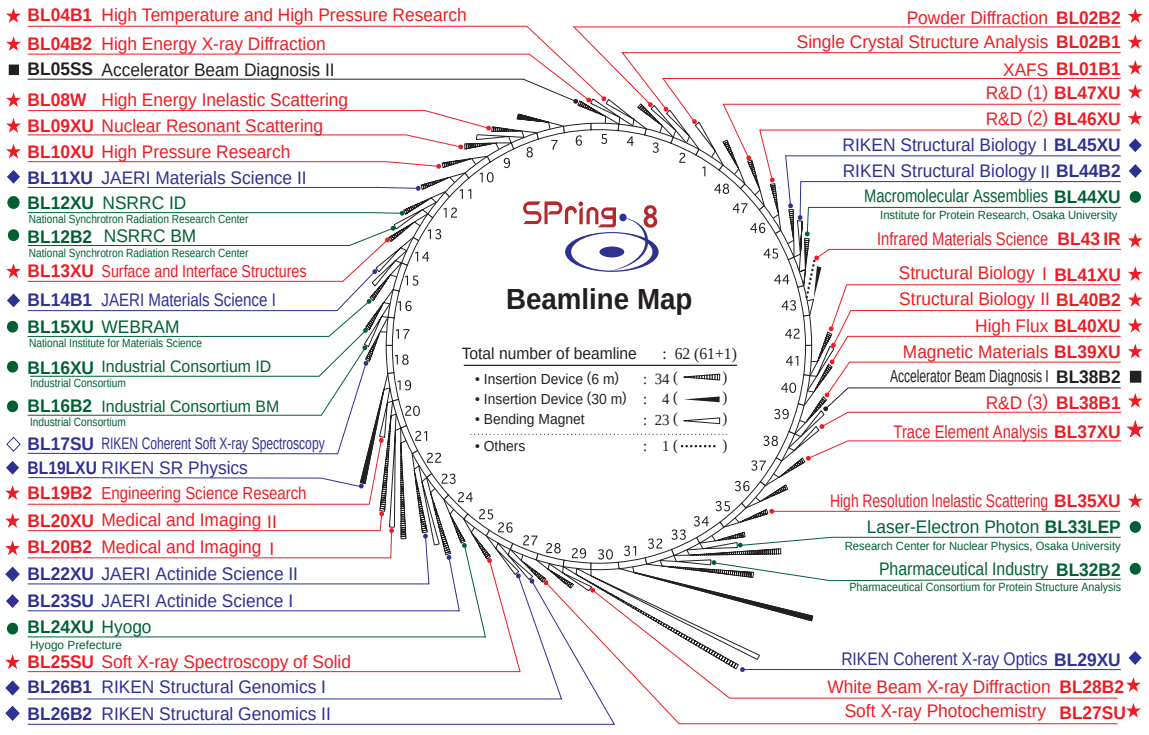

Fig. 2. Beamline Map.

Table II. List of beamlines

BL #	Beamline Name	(Public Use)	Areas of Research
★ Public Beamlines			
BL01B1	XAFS	(Oct. 1997)	XAFS in wide energy region (3.8 to 113 keV). XAFS of dilute systems and thin films.
BL02B1	Single Crystal Structure Analysis	(Oct. 1997)	Single crystal structure analysis in X-ray wide energy range. Precise X-ray diffraction analysis of the lattice or charge modulation originated from the phase transition at low temperatures.
BL02B2	Powder Diffraction	(Sep. 1999)	Accurate structure analysis of crystalline materials using powder diffraction data. Structural aspects of phase transition. *Ab initio* structure determination by powder diffraction. Rietveld refinements.
BL04B1	High Temperature and High Pressure Research	(Oct. 1997)	Determination of phase relation. Equation of state of mantle. Viscosity of melts. Kinetics of mineral transformation. Rheology of mantle minerals. Structure of melts and glasses at high pressures.
BL04B2	High Energy X-ray Diffraction	(Sep. 1999)	Structural analysis of glass, liquid, and amorphous materials. X-ray diffraction under ultra high-pressure. Precise single crystal structure analysis
BL08W	High Energy Inelastic Scattering	(Oct. 1997)	Magnetic Compton scattering. High-resolution Compton scattering. High-energy Bragg scattering. High-energy fluorescent X-ray analysis.
BL09XU	Nuclear Resonant Scattering	(Oct. 1997)	Lattice dynamics by using nuclear inelastic scattering. Time domain Mössbauer spectroscopy, especially under the extreme conditions. Coherent X-ray optics using nuclear resonant scattering. Nuclear excitation by electron transition (NEET). Surface structures and residual strain analysis.
BL10XU	High Pressure Research	(Oct. 1997)	Structure analysis and phase transitions under ultra high pressure (DAC experiment). Earth and planetary science.
BL13XU	Surface and Interface Structures	(Sep. 2001)	Atomic-scale structure analysis of a crystal surface, an ultra-thin film and a nanostructure. Surface structure analysis under thin-film growth. Analysis of nanostructures grown at a vacuum/solid, liquid/solid, and solid/solid interface.
BL19B2	Engineering Science Research	(Nov. 2001)	XAFS in wide energy region. Residual stress measurement. Structural analysis of thin film, surface and interface. Powder diffraction. X-ray imaging.
BL20XU	Medical and Imaging II	(Sep. 2001)	Microimaging: Scanning microscopy. Imaging microscopy. Microtomography. X-ray holography and other experiments on X-ray optics and developments of optical elements. / Medical application: Microangiography. Refraction-enhanced imaging. Radiation therapy. / Ultra-small angle scattering.
BL20B2	Medical and Imaging I	(Sep. 1999)	Medical research: Microradiography, microtomography and refraction-contrast imaging on biological specimens and small animals. / Imaging techniques: Evaluation and development of various kinds of optical elements for novel imaging techniques.
BL25SU	Soft X-ray Spectroscopy of Solid	(Apr. 1998)	High resolution photoemission. Photoelectron diffraction and holography. Magnetic circular dichroism in the core absorption (MCD). Photoelectron emission microscope (PEEM).
BL27SU	Soft X-ray Photochemistry	(May 1998)	Industrial research: Growth of thin film of functional material. Micro-fabrication by functional material etching. / Atomic and molecular spectroscopy: Search of novel photochemical processes. High resolution atomic and molecular electron spectroscopy. Complete determination of electronic decay channel. Dissociation dynamics of inner-shell excited molecules. Site-specific dissociation processes of isolated molecules. / Surface analysis and solid state physics: Search of electronic structures of solids and nanolayers. Elucidation of electronic state of molecule on surface.
BL28B2	White Beam X-ray Diffraction	(Sep. 1999)	White X-ray diffraction. Time-resolved energy-dispersive XAFS (DXAFS) for studies of chemical and/or physical reaction process.
BL35XU	High Resolution Inelastic Scattering	(Sep. 2001)	Dynamics of materials including phonons. Glass transitions. Liquid dynamics. Diffusion. Methods of investigation for inelastic X-ray scattering (IXS) and nuclear resonant scattering (NRS).
BL37XU	Trace Element Analysis	(Nov. 2002)	X-ray microbeam spectrochemical analysis. Ultra trace element analysis. High energy X-ray fluorescence analysis.
BL38B1	R&D (3)	(Oct. 2000)	XAFS. R&D of optics and detector. Monochromatic data collection for routine macromolecular crystallography.
BL39XU	Magnetic Materials	(Oct. 1997)	X-ray magnetic circular dichroism (MCD) spectroscopy. Element-specific magnetometry. X-ray emission spectroscopy and its magnetic circular dichroism. Resonant or non-resonant magnetic scattering.
BL40XU	High Flux	(Apr. 2000)	Time-resolved diffraction and scattering experiments. X-ray speckle. X-ray fluorescence trace analysis.
BL40B2	Structural Biology II	(Sep. 1999)	Macromolecular crystallography. Small angle X-ray (solution) scattering.
BL41XU	Structural Biology I	(Oct. 1997)	Macromolecular crystallography.
BL43IR	Infrared Materials Science	(Apr. 2000)	Infrared microspectroscopy. Magneto-optical spectroscopy. Infrared surface science. Absorption and reflection spectroscopy. Time-resolved experiments with pulsed laser and SR (pump and probe).
BL46XU	R&D (2)	(Nov. 2000)	R&D of insertion devices. Resonant and non-resonant magnetic scattering structural analysis.
BL47XU	R&D (1)	(Oct. 1997)	R&D of microtomography and microbeam technique.

BL #	Beamline Name	(First Beam)	Areas of Research
	● Contract Beamlines		
BL12XU	NSRRC ID (NSRRC)	(Dec. 2001)	Elementary electronic excitations, quasiparticle behaviors, and electron-correlation effects in correlated electron systems by high resolution non-resonant or resonant inelastic X-ray scattering. Local electronic structure of molecular solids of low-Z elements (e.g., biomaterials) by high resolution near-edge X-ray Raman scattering. Phase transitions under high-pressure, low and high temperatures. Materials science by high-resolution X-ray absorption and emission spectroscopy. X-ray physics and optics.
BL12B2	NSRRC BM (NSRRC)	(Oct. 2000)	X-ray absorption spectroscopy. Powder X-ray diffraction. High resolution X-ray scattering. Protein crystallography.
BL15XU	WEBRAM (National Institute for Materials Science)	(Jan. 2000)	Highly precise characterization of advanced materials: High resolution X-ray photoemission microscopy. Study and analysis for synthesis process of thin films assisted with X-ray irradiation. High energy excitation X-ray photoelectron spectroscopy. High resolution X-ray emission spectroscopy. Highly precise X-ray powder diffraction study and ultra-small angle scattering.
BL16XU	Industrial Consortium ID (Industrial Consortium)	(Oct. 1998)	Characterization of thin films for VLSI and magnetic devices, catalysts, functional materials, and structural materials.
BL16B2	Industrial Consortium BM (Industrial Consortium)	(Oct. 1998)	Characterization of industrial materials, such as metal and oxide films, semiconductor crystals by XAFS, topography and other methods.
BL24XU	Hyogo (Hyogo Prefecture)	(May 1998)	Structure analysis of small bio-crystals for industry. Surface/interface analysis of metallic materials for industry by fluorescent X-ray analysis and strain measurements. Surface/interface analysis during metal-organic chemical vapor deposition by grazing incidence X-ray diffraction. Microbeam formation studies for materials and life science.
BL32B2	Pharmaceutical Industry (Pharmaceutical Consortium)	(Apr. 2002)	Protein structure analysis for structure-based drug design: Design and optimization of new leading compounds based on pharmacodynamic action mechanism elucidated at the molecular level which obtained from a detailed interaction analysis of receptor-drug complexes.
BL33LEP	Laser-Electron Photon (Osaka University)	(Jun. 1999)	Meson photoproduction from nucleon and nucleus. Photoexcitation of hyperons, nucleon resonances, and other exotic states. Photonuclear reactions. Beam diagnoses. Test and calibration of detectors with GeV photon beam.
BL44XU	Macromolecular Assemblies (Osaka University)	(May 1999)	Crystal structure analysis of biological macromolecular assemblies (e.g. membrane protein complexes, protein complexes, protein-nucleic acid complexes, and viruses).
	◆ JAERI Beamlines		
BL11XU	JAERI Materials Science II	(Oct. 1998)	Nuclear resonant scattering. Surface and interface structure with MBE. Inelastic scattering. XAFS.
BL14B1	JAERI Materials Science I	(Dec. 1997)	Materials science at high pressure. Structure physics.
BL22XU	JAERI Actinide Science II	(May 2002)	Materials science at high pressure. Resonant X-ray scattering (activity at RI laboratory).
BL23SU	JAERI Actinide Science I	(Feb. 1998)	Surface chemistry with supersonic molecular beam. Biophysical spectroscopy. Photoelectron spectroscopy (activity at RI laboratory). Magnetic circular dichroism (activity at RI laboratory).
	◆ RIKEN Beamlines		
BL17SU	RIKEN Coherent Soft X-ray Spectroscopy	(Sep. 2003)	Spectroscopic study on multiply charged ions: Photoabsorption study on multiply charged ions. Fundamental research for X-ray astronomy using synchrotron radiation. / High resolution photoemission spectroscopy: Angle-resolved photoemission (ARPES) study using soft X-rays to observe 'bulk' band structure. *In situ* ARPES measurement on strongly-correlated transition-metal oxide thin films fabricated by laser MBE method. / Soft X-ray emission spectroscopy for solid and biological samples: Soft X-ray emission study on transition metal compounds to study electronic correlations in solids. Study of the electronic structure of biological samples by soft X-ray emission spectroscopy.
BL19LXU	RIKEN SR Physics	(Oct. 2000)	Any research field requiring the highly brilliant X-ray beam.
BL26B1/B2	RIKEN Structural Genomics I & II	(Apr. 2002)	Structural genomics research based on single crystal X-ray diffraction.
BL29XU	RIKEN Coherent X-ray Optics	(Dec. 1998)	X-ray optics, especially coherent X-ray optics.
BL44B2	RIKEN Structural Biology II	(Feb. 1998)	Laue macromolecular crystallography.
BL45XU	RIKEN Structural Biology I	(Jul. 1997)	Time-resolved structures of non-crystalline biological materials such as protein, nucleic acid solutions, membrane, muscle, and micelle system under various conditions by small-angle scattering and diffraction technique.
	■ Accelerator Beam Diagnosis		
BL05SS	Accelerator Beam Diagnosis	(Mar. 2004)	Accelerator beam diagnostics. R&D of accelerator components.
BL38B2	Accelerator Beam Diagnosis	(Sep. 1999)	Accelerator beam diagnostics. R&D of accelerator components. Production of MeV γ-ray photons.

User Operation

Statistics

SPring-8 invites research proposals twice a year and submitted proposals are reviewed at the SPring-8 Proposal Review Committee (PRC). For 2002B, the PRC approved 472 proposals from 751 proposals and 563 from 733 for 2003A. The total of little more than 4,000 hours of beamtime was allocated to successful applicants from 2002B through 2003A.

SPring-8 user operation results for the period from 1997B to 2003A are shown in Table III. This table shows user beamtime available to users and the numbers of users and experiments conducted at both public and contract beamlines, which are also illustrated in Fig. 3. The results in the table and the figure include the numbers of experiments using reserved beamtime and priority research proposals.

Research Term	User Time (hours)	Public BL		Contract BL	
		Experiments	Users	Experiments	Users
1997B: 1997.10 - 1998.03	1,286	94	681		
1998A: 1998.04 - 1998.10	1,702	234	1,252	7	
1999A: 1998.11 - 1999.06	2,585	274	1,542	33	467
1999B: 1999.09 - 1999.12	1,371	242	1,631	65	427
2000A: 2000.02 - 2000.06	2,106	365	2,486	100	794
2000B: 2000.10 - 2001.01	1,558	382	2,370	88	620
2001A: 2001.02 - 2001.06	2,381	473	2,915	102	766
2001B: 2001.09 - 2002.02	1,893	486	3,277	114	977
2002A: 2002.02 - 2002.07	2,093	543	3,246	110	1,043
2002B: 2002.09 - 2003.02	1,893	538	3,508	143	1,046
2003A: 2003.02 - 2003.07	2,244	632	3,777	172	1,347
TOTAL	21,088	4,263	26,685	934	7,487

Table III. SPring-8 user operation results.

In 2002B and 2003A, SPring-8 provided users with 1,893 and 2,244 hours of beamtime in four and five operation cycles, respectively. As for 2002B, 3,508 individuals used the public beamlines in 538 separate experiments, while 1,046 individuals used the contract beamlines in 143 experiments. In 2003A, 3,777 individuals used the public beamlines in 632 separate experiments, while 1,347 individuals used the contract beamlines in 172 experiments. From October 1997, when SPring-8 was opened to the public, through 2003A, a total of 34,172 public and contract beamline users conducted 5,197 experiments.

Figures 4 and 5 indicate the numbers of selected proposals by affiliation of applicants and by research fields from 1997B to 2003A. As can be seen from the charts, as for the classification by affiliation, universities have accounted for approximately 70% and other organizations have made up the rest almost equally. The percentage of approved proposals from overseas was 4% for 2002B and 6% for 2003A. The ratio of Life Science, Diffraction & Scattering and the others has been 1:1:1 since the inauguration of SPring-8. The ratio of XAFS, Spectroscopy and Method & Instrumentation, all of which are categorized as “the others,” has also been 1:1:1.

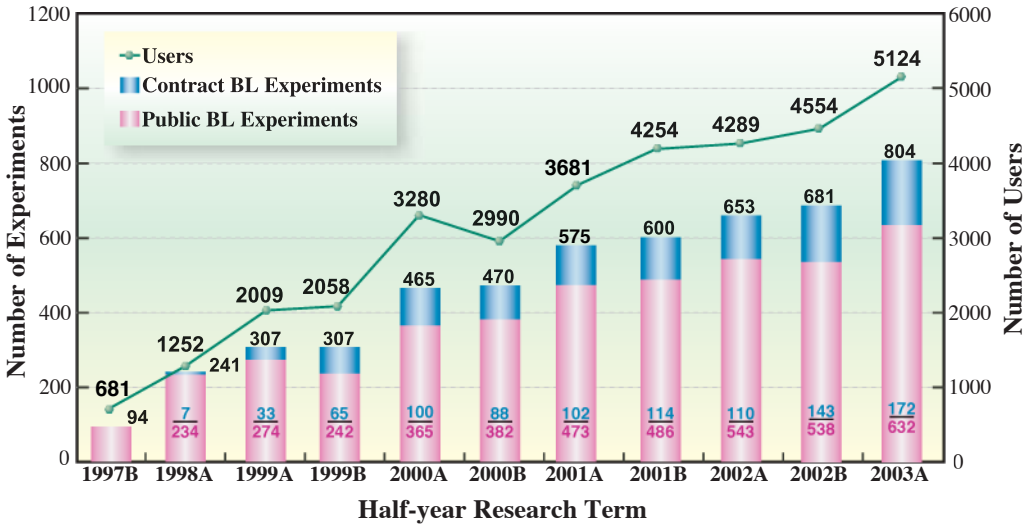

Fig. 3. Number of users and experiments conducted.

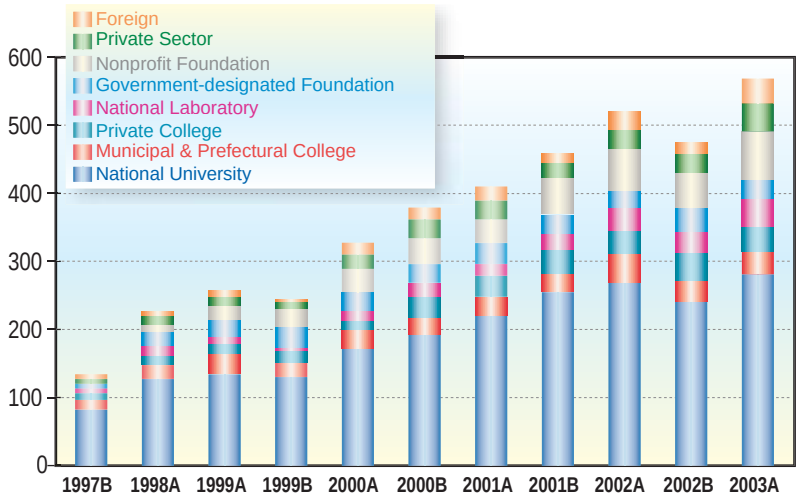

Fig. 4. Number of selected proposals by affiliation of applicants (public beamlines).

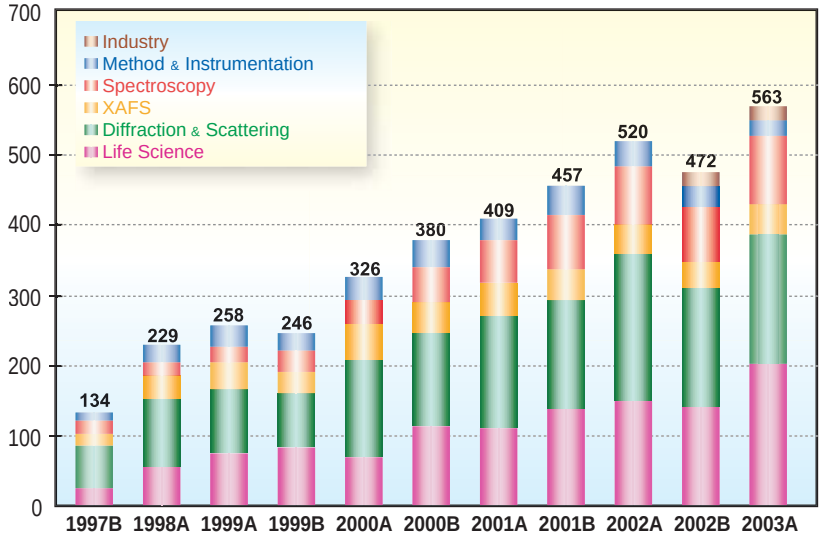

Fig. 5. Number of selected proposals by research fields (public beamlines).

Priority Research Proposal

Until FY2002, there were only general and long-term proposals and the proposals using beamtime reserved for JASRI. In FY2003, the new scheme for the management of public beamlines was established, based on the report on SPring-8 by the governmental review committee. The report called on SPring-8 to further promote the use of public beamlines to produce more research results. The important point of the report was to launch the Priority Research Program. The new scheme is shown in Table IV. As can be seen from the table, beamtime not exceeding 50% is allocated to the Priority Research Proposals and proposals using beamtime reserved for JASRI, so that more than 50% of the total user beamtime is guaranteed for general and long-term proposals.

The scheme for Priority Research Program is intended to make the best use of SPring-8 and produce more research results. The Priority Research Proposals are tentatively categorized into the following three groups:

- Priority Field Proposal,
- Power User Proposal and
- Strategy Proposal.

Details of each proposal are provided below.

Priority Field Proposal

JASRI designates research fields which are expected to produce excellent research results or fields of strategic significance. The Priority Field Proposals are further categorized into three subgroups: Nanotechnology Support, Protein 500 and Industrial Use. These proposals are reviewed before General Proposals at the review committees designated for each priority field. The outline of each priority research field is as follows:

Nanotechnology Support

This research field is to support the development in nanotechnology, using 11 beamlines at SPring-8. Nanotechnology Support at SPring-8 had already started in 2002 under the Nanotechnology Researchers Network Project (Nanonet Project) of MEXT (Ministry of Education, Culture, Sports, Science and Technology) and was consolidated into the Priority Research Program in FY2003. In 2002B and 2003A, a total of 120 proposals were selected from 183 submitted proposals. This Project is valid until FY2006.

Protein 500

Just as Nanotechnology Support, Protein 500 at SPring-8 started shortly after MEXT launched the Protein 3000 Project in 2002 as a post-human genom program to analyze 3,000 kinds of protein structures and was taken over as the Priority Field Program in FY2003. Under the Project, three of SPring-8 structural biology beamlines are assigned to analyze 500 kinds of protein structures, and 30% of their beamtime is allocated every year. In 2002B and 2003A, a total of 141 proposals were selected. This Project is valid until FY2006.

Industrial Use

As part of industrial use, the Trial Use Program originally ran from 2001B to 2002A, for the purpose of attracting new users to SPring-8, mainly from industries and restarted as one of the Priority Field Proposals in 2003A. In 2003A, 14 Trial Use proposals were selected from 17 proposals; Since 2001B, 36 proposals were selected from 39 proposals.

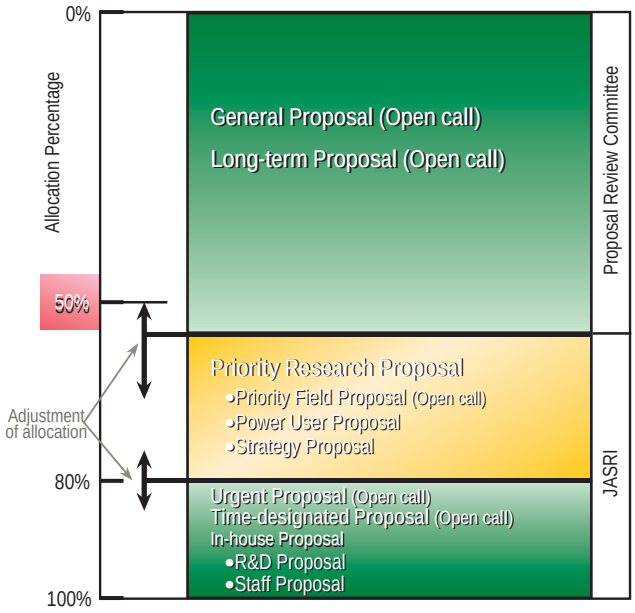

Table IV. New beamtime allocation scheme for public beamlines.

Power User Proposal

This category refers to proposals of user groups who have full knowledge of beamline instrumentation and are highly likely to produce outstanding research results in the future also. Such user groups are designated as Power Users (PUs) by JASRI and expected to provide support for general users. In return for their support, up to 20% of beamtime of relevant beamlines can be used by the PUs. First such PUs are to be designated for 2003B.

Strategy Proposal

Strategy Proposals are expected to contribute to promoting research at SPring-8 including the development of new technologies necessary for the facility operation. JASRI will conduct such research by itself or jointly with other organizations.

Long-term Proposal

Separately from General Proposals, SPring-8 has created a system for the long-term use of beamlines, where beam access is guaranteed for up to three years. This system aims to further promote research that is expected to produce outstanding results in the field of science and technology, to pave the way for

new research areas and research methodology and to help improve the technology for industrial base significantly by making the best use of SPring-8 characteristics. In 2003A, one proposal was selected from four proposals; The total of eight proposals have been selected from 27 proposals since 2000B.

Industrial Research

As well as the promotion of research activities in the field of basic science, the contribution to the reinforcement of the technological base in industry has been one of the main pillars of the SPring-8 Project. The coordinator system, introduced in FY2000 to support industrial use mainly through consultation, is a case in point. Equally important is the Trial Use Program. This program aims to revitalize local industries and to create and promote new industries. Public beamline BL19B2, Engineering Science Research Beamline, built to promote SR use by industries, is the main beamline used for the Trial Use Program. There are three contract beamlines, which were constructed by Industrial Consortium and Pharmaceutical Consortium, for the use by the consortium members. In addition to the above, workshops and training courses are to be noted. These courses are intended for a variety of research fields and SR instrumentation and were attended by a total of 1,150 industrial users from FY2000 through FY2002.

Proprietary Research

Users conducting proprietary research are charged beamtime fees. Proprietary research is essential when users have commercially confidential information in their experiment or sample and do not want to disclose their research results. In 2002B, 14 proprietary experiments were performed at public beamlines and 24 at contract beamlines; In 2003A, 14 experiments were conducted at public beamlines and 23 experiments at contract beamlines. During the period from 1999B, when the system was introduced, to 2003A, a total of 142 experiments have been carried out at both public and contract beamlines. The Pharmaceutical Consortium has spent about 75% of their beamtime on proprietary research at their contract beamline, BL32B2.

Research Results

SPring-8 users are not charged for non-proprietary research as long as they submit an experiment report within sixty days after their experiments. When their results are disclosed in scientific journals or any other form of publication, the project leaders are required to report to JASRI and have the results registered with JASRI. As of September 30, 2003, the number of refereed publications is 1,296 (928 for public use, 120 for contract beamlines and 232 for JAERI and RIKEN beamlines; The results at two or more beamlines are counted at each beamline.)

Budget and Manpower

SPring-8 consisting of accelerators, beamlines and facilities for users, was constructed by the JAERI/RIKEN Project Team during the period from 1991 through 1997 at the total cost of about 110 billion yen. In 1994, JASRI was designated by the Law regarding Promotion of Common Use of the Synchrotron Radiation Facility (SPring-8) as the Organization for the Promotion of Synchrotron Radiation Research to be responsible for managing SPring-8. As a result, the SPring-8 research complex has been formed by JAERI Kansai Research Establishment, RIKEN Harima Institute and JASRI. JASRI has been entrusted by JAERI and RIKEN with the

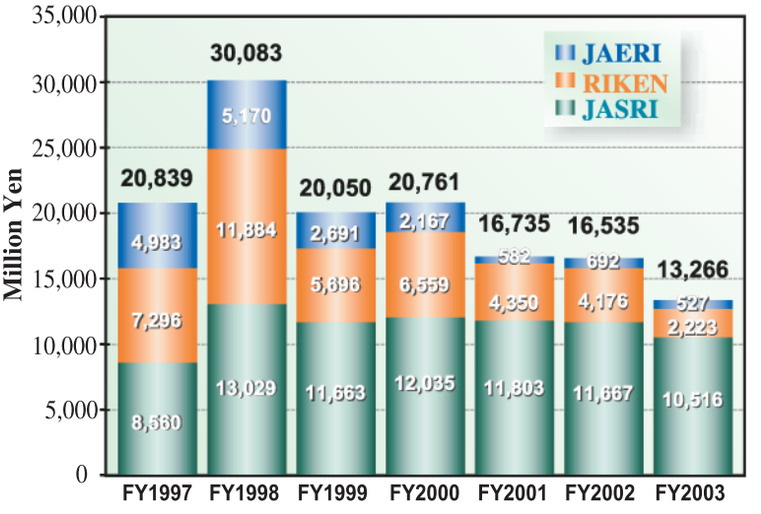

Figure 6

operation, maintenance, improvement, upgrading, R&D and safety management of SPring-8 as well as the technical support for the new beamline construction since the construction of main facilities and buildings at SPring-8 was completed and the public use started in 1997.

About 94% of the total budget of JASRI comes from the Government through JAERI and RIKEN to be appropriated for the above-mentioned missions of JASRI and the remaining 6% comes directly from the Government in the form of a grant for user support. Figure 6 illustrates the budget at SPring-8. It shows that the total budget for JASRI for FY2003 was 10,516 million yen and the total budgets for JAERI and RIKEN were 527 million yen and 2,223 million yen, respectively. As can be seen from the figure, the budgets for JAERI and RIKEN have reduced since FY2001. It is because the construction such as utility facilities is approaching completion, meanwhile construction of beamlines is stopped due to lack of budget.

In FY2002, the total number of JASRI staff was 463. The total number of SPring-8 staff amounts to 1,051 when the number of staff at JAERI Kansai Research Establishment and RIKEN Harima Institute is combined with the number of JASRI staff. The numbers of staff by the types and fields of employment are illustrated in Fig. 7.

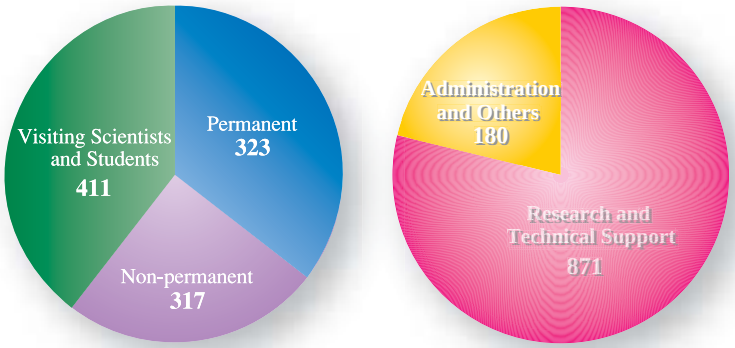

	by Type			by Field		Total
	Permanent	Non-permanent	Visiting Scientists and Students	Research and Technical Support	Administration and Others	
JASRI	220	128	115	327	136	**463**
JAERI	42	26	7	67	8	**75**
RIKEN	61	163	289	477	36	**513**
	323	**317**	**411**	**871**	**180**	**1,051**

Fig. 7. Manpower at SPring-8: JASRI, JAERI, RIKEN (FY2003)

Organization

As mentioned earlier in the Budget and Manpower, the SPring-8 research complex is composed of JASRI, JAERI Kansai Research Establishment and RIKEN Harima Institute (see the organization charts Fig. 8 - 10), all of which are on site. While JAERI and RIKEN conduct their own research at SPring-8, JASRI is entrusted by the two with the operation, maintenance, improvement, upgrading, R&D and safety management of SPring-8. Since SPring-8 is a facility open to the public, user support is also one of the important tasks of JASRI. The organization that JASRI has formed to accomplish those missions is shown in Fig. 8. As can be seen from the organization chart, JASRI consists of the Synchrotron Radiation Research Laboratory, the Administration Sector and the SPring-8 Safety Office.

January 1, 2004.

SPring-8 Organization

Japan Synchrotron Radiation Research Institute (JASRI)

President Y. Ihara
Vice President K. Nagara, A. Kira
Managing Exec. Director H. Ohno, M. Yamada
Exec. Director S. Kikuta, M. Nagata

Director General
A. Kira

Deputy
S. Kikuta

Synchrotron Radiation Research Laboratory

- **Accelerator Div.** — N. Kumagai
  - Operation & Beam Dynamics — H. Ohkuma
  - Linear Accelerator — H. Hanaki
  - Circular Accelerator — H. Yonehara
  - Control — R. Tanaka
- **Beamline Div.** — S. Kikuta, T. Ishikawa
  - Insertion Device & Front End — H. Kitamura
  - Optics & Transport Channel — S. Goto
  - Control — R. Tanaka
  - Instrumentation Development — N. Yagi
  - Technical Support — I. Nishida
- **Materials Science Div.** — H. Suematsu
  - User Support I — S. Komiya
  - Materials Structure I — M. Takata
  - Materials Structure II — J. Mizuki
  - Spectroscopy I — H. Suematsu
  - Spectroscopy II — K. Kobayashi
- **Life & Environmental Science Div.** — T. Ueki
  - User Support II — T. Ueki
  - Structure Biology — M. Yamamoto
  - Life Science — N. Yagi
  - Microimaging / Analysis — Y. Suzuki
- **Facilities & Utilities Div.** — K. Sezaki

Administration Sector — O. Ichimaru

- General Affairs Div. — M. Inoue
- Finance Div. — Y. Terakado
- Planning Div. — O. Ichimaru
- User Administration Div. — T. Matoba
- Public Relations Div. — M. Hara

SPring-8 Safety Office — J. Tada

Figure 8

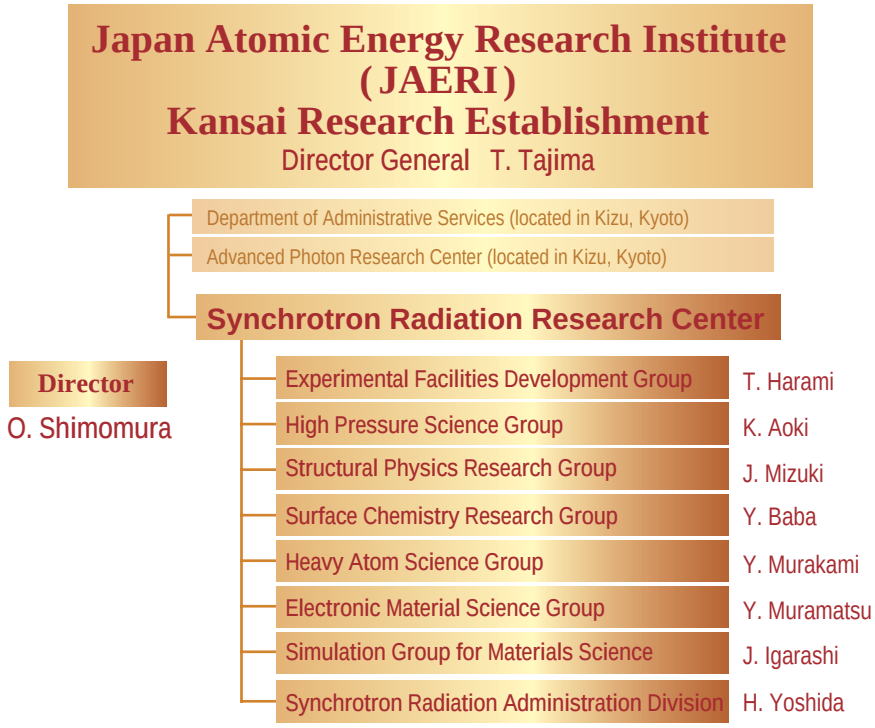

Figure 9

Figure 10

International Conferences and Workshops

The International Conferences and Workshops sponsored by SPring-8 (JASRI, JAERI, RIKEN) held in 2002 and 2003 are listed below.

6th Harima International Forum on Structural Organization of Macromolecular Assembly
January 13 - 16, 2002

24th Advanced ICFA Beam Dynamics Workshop on Future Light Sources
April 30 - May 4, 2002

5th International Workshop on 30 m Long Straight Section on the use of Coherent Soft X-rays from Super - Brilliant Sources -
May 10 - 12, 2002

Japan-Hungary Seminar on Physics in Modern Science and Technology - Frontier of Photon Science -
May 15, 2002

1st Annual Meeting of Structural-Biological Whole Cell Project of *Thermus thermophilus* HB8
July 26 - 27, 2002

International Workshop on Photoionization (IWP 2002)
August 22 - 26, 2002

7th Harima International Forum on Structure and Properties of Disordered Materials
September 5 - 7, 2002

5th SRRTNet Workshop on Interface Between Theory, Computation and Experiments
October 15 - 16, 200

7th International Workshop on Accelerator Alignment (IWAA 2002)
November 11 - 14, 2002

International Workshop on Beam Orbit Stabilization 2002 (IWBS 2002)
December 4 - 6, 2002

LEPS 2003 Workshop on Science and Technology of LEPS in the Medium High Energy Region
March 3 - 4, 2003

8th Harima International Forum on Structural Biology of Biological Machinery
March 19 - 21, 2003

SCW Workshop on Generation of High-Energy Synchrotron Radiation using a Super Conducting Wiggler and Its Applications
March 24 - 25, 2003

2nd Annual Meeting of Structural-Biological Whole Cell Project of *Thermus thermophilus* HB8
August 22 - 26, 2003

RIKEN/BBSRC Symposium Japan-UK Protein Structure Biology
September 11 - 12, 2003

International Workshop on High-pressure Mineral Physics and Geochemistry: Interaction of Plate, Mantle, and Core, and Global Circulation of the Earth Material
September 13 - 15, 2003

Workshop on Beam Physics 2003
October 13 - 15, 2003

JAERI International Workshop on X-Ray Scattering and Electronic Structure
December 11 - 12, 2003

Users' Meeting

The Users Meeting sponsored by SPring-8/JASRI held in 2002 and 2003 are listed below

6th SPring-8 Symposium
September 10 - 11, 2002

6th Workshop of Experimental Techniques at SPring-8
December 18 - 20, 2002

7th SPring-8 Symposium and Workshop of Experimental Techniques at SPring-8
November 12 - 14, 2003

Editor
Seishi Kikuta
SPring-8 / JASRI

Editing & Layout
Marcia M. Obuti-Daté
SPring-8 / JASRI

Printing
ROKKO Publishing & Sale Co.

J A S R I
Library and Information
Users Administration Division

1-1-1 Kouto, Mikazuki-cho, Sayo-gun
Hyogo 679-5198 • JAPAN
Tel. +81-(0)791-58-2797 Fax. +81-(0)791-58-1869

frontiers@spring8.or.jp
http://www.spring8.or.jp/

July 2004

SPring-8

Japan Synchrotron Radiation Research Institute
1-1-1 Kouto, Mikazuki-cho, Sayo-gun, Hyogo 679-5198 JAPAN
http://www.spring8.or.jp